UNIVERSITY OF SOUTHAMPTON
Faculty of Engineering and Physical Sciences
Aerodynamics and Flight Mechanics

Computational Modelling of Particle Tribocharging in Small, High-Speed Cyclones

by

Daniel Neal Powell
ORCiD: 0000-0001-6877-2734

A thesis submitted for the degree of
Doctor of Philosophy

June 2022

UNIVERSITY OF SOUTHAMPTON

ABSTRACT

FACULTY OF ENGINEERING AND PHYSICAL SCIENCES
AERODYNAMICS AND FLIGHT MECHANICS
Doctor of Philosophy

COMPUTATIONAL MODELLING OF PARTICLE TRIBOCHARGING IN SMALL, HIGH-SPEED CYCLONES

by Daniel Neal Powell

Small, high-speed cyclones are used in domestic vacuum cleaners to separate sub-micron sized particulates from an air stream using no moving parts. The complex fluid flow within the cyclone is turbulent and highly-swirling, with small sub-micron particles encountering and responding to fluid structures of a wide spatial and temporal range. The process of particle separation in these cyclonic devices is not well-known and accurate numerical prediction of separation efficiency remains a computationally expensive task. In addition to this, particles are known to exchange charge through collisions, in a process known as tribocharging, which can cause smaller particles to agglomerate into larger structures. This thesis aims to develop a computationally inexpensive particle model able to predict the transport of particle charge which is valid in this highly-swirling flow for small particles.

Models of particle tribocharging in the literature have only been validated for particles many orders of magnitude larger than those of interest here. Novel experiments were performed where sub-micron particles were aerodynamically focused to impact a metal plate using an aerosol beam. The results validated the physics of charge transfer at these small scales, with an equilibrium level for the voltage on the plate reached which charged analogous to a capacitor charging circuit. These measurements provided estimates of tune-able constants for a simple capacitor-like tribocharging model from the literature.

Capturing collisions between particles in a Lagrangian reference frame is prohibitively expensive computationally, therefore an Eulerian particle model was chosen which can deal with collisions efficiently. The Equilibrium Eulerian method for computing the Eulerian particle velocity field for low Stokes number particles was validated in an analytical Taylor-Green flow. This flow field features fluid gradients and strong streamline curvature, with the length and velocity scales matched with the smallest turbulent scales in a representative cyclone. Strengths and weaknesses of the model were assessed in this challenging flow field, with an Eulerian sub-model for the transport of particle charge implemented.

A large eddy simulation of a small, high-speed cyclone was performed with high wall resolution. Flow rates and pressure drop were matched to experimental evidence and partially resolved turbulent structures were observed along the cyclone walls. Lagrangian particle tracking provided a separation efficiency which matched experiment except for the smallest $0.1\mu m$ particles. Particles were observed travelling in distinct streaky bands by the walls which matched video evidence obtained experimentally. The Eulerian particle model provided an excellent match to the Lagrangian particle result for separation efficiency, with banding of large $1\mu m$ particles by the walls able to be captured, matching both the Lagrangian particles and experiment. The transport of charge and resulting electric field in the cyclone showed significant tribocharging occurring at the cone tip of the cyclone and by the walls which is novel. This work is expected to inform future cyclone design to improve the separation efficiency of small particles.

Contents

Declaration of Authorship

I, Daniel Neal Powell, declare that the thesis entitled "Computational Modelling of Particle Tribocharging in Small, High-Speed Cyclones" and the work presented in the thesis are both my own and have been generated by me as the result of my own original research. I confirm that:

1. This work was done wholly or mainly while in candidature for a research degree at this University;
2. Where any part of this thesis has previously been submitted for a degree or any other qualification at this University or any other institution, this has been clearly stated;
3. Where I have consulted the published work of others, this is always clearly attributed;
4. Where I have quoted from the work of others, the source is always given. With the exception of such quotations, this thesis is entirely my own work;
5. I have acknowledged all main sources of help;
6. Where the thesis is based on work done by myself jointly with others, I have made clear exactly what was done by others and what I have contributed myself;
7. None of this work has been published before submission

Signed:

Date:

Acknowledgements

I would like to thank my supervisor, Prof. John S. Shrimpton for his greatly appreciated patience and expertise throughout this project. From Dyson, I would like to thank Ricardo Gomiciaga and Tom Grimble for support in setting up experiments and interesting discussions on cyclones and Jeff Joiner for technical assistance with the machining and construction of the experimental rig. Last but not least I would like to thank Emma, who has been an invaluable source of support for me throughout this work.

This work was supported by the EPSRC centre for Doctoral Training in Next Generation Computational Modelling grant EP/L015382/1 and by Dyson who both provided experimental data and allowed use of their facilities to perform the experimental work. The author acknowledges the use of the IRIDIS High Performance Computing Facility, and associated support services at the University of Southampton, in the completion of this work.

Nomenclature

Latin Symbols

a	Taylor-Green flow parameter
a_b	Bottom neighbour face coefficient
a_B	Bottom neighbour coefficient
a_e	East neighbour face coefficient
a_E	East neighbour coefficient
a_h	Cyclone inlet height
a_{nb}	Neighbour coefficient
a_n	North neighbour face coefficient
a_N	North neighbour coefficient
a_P	Central coefficient
a_s	South neighbour face coefficient
a_S	South neighbour coefficient
a_t	Top neighbour face coefficient
a_T	Top neighbour coefficient
a_w	West neighbour face coefficient
a_W	West neighbour coefficient
A	Area
A_c	Contact Area
b	Cyclone inlet width
b_α	Explicit source term in linear system
B	Cone tip diameter
B_1	Charge model constant 1
B_2	Charge model constant 2
B_B	Log-law constant
c	Mass fraction
C	Capacitance
$\mathcal{C}$	Collision operator
C_1	Collision frequency of one particle
C_{11}	Collision frequency between two like-particles
C_{12}	Collision frequency between two particles 1 and 2
C_C	Cunningham slip correction factor
C_D	Coefficient of drag
C_{i2}	Second matrix invariant
C_{i3}	Third matrix invariant
C_p	Specific heat at constant pressure
C_r	Rankine vortex constant
C_s	Smagorinsky constant
C_v	Specific heat at constant volume
C_w	WALE constant
d	Distance

d_H	Hydraulic diameter
d_p	Particle diameter
D	Cyclone diameter
D_e	Vortex finder diameter
D_α	Diffusion coefficient of α
e	Charge of an electron
e_t	Internal energy
E	Electric field strength
E_b	Electric field strength for air breakdown
E_g	Total energy
f	Normalised phase space distribution function
f_c	Shaking frequency
f_f	Friction factor
f_p	Fraction of particles
f_s	Scattering coefficient
F	Force
g	Acceleration due to gravity
g_0	Dense packing function
h	Cyclone top height
H	Cyclone total height
H_e	Heaviside step function
i	Current
I	Identity matrix
I_1	Empirical correlation 1
I_2	Empirical correlation 2
I_e	Interpolation factor
I_{int}	Integral from Hertzian theory
J	Term in the WALE model
k	Turbulent kinetic energy
k_B	Boltzmann constant
k_C	Particle count
k_t	Thermal conductivity
l	Length
l_η	Kolmogorov length scale
L_s	Mixing length
L_x	Axial flux of axial momentum
L_θ	Axial flux of angular momentum
l	Length
L	Particle separation
m	Mass
M	Separation efficiency exponent
M_n	The nth central moment
M_w	Molecular weight
n	Particle number density
N	Total number
P	Pressure
$\mathcal{P}$	Penetration
q	Charge (intensive)
q_h	Heat flux
Q	Charge (extensive)
Q_c	Q-criterion
Q_e	Equilibrium charge
r	Particle position vector

R	Radius of curvature
R_0	Resistance
R_a	Gas constant for air
R_f	Flow rate ratio
R_{scaled}	Scaled residual
S	Vortex finder length
S_c	Explicit source term
S_α	Source term for α
S_n	Number density source term
S_p	Implicit part of linearised S_ϕ
S_{mag}	Strain rate magnitude
t	Time
t_L	DRW timescale
t_τ	Integration dummy time variable
T	Temperature
u	Fluid speed
v	Particle speed
V	Volume
V_c	Voltage
w	Relative speed between particle and fluid
x	Displacement
y	Height
Y	Young's modulus
z	z-coordinate
Z_p	Particle electrical mobility

Greek Symbols

α	Volume fraction
β	Collision frequency function
γ	Ratio of specific heats
Γ	Collision term
δ_c	Charge transfer cut-off distance
δ_r	Boundary layer thickness
Δ	Local grid scale
ΔP	Pressure drop
ΔV	Cell volume
ϵ	Turbulent dissipation rate
ϵ_m	Permittivity of medium
ζ	Normally distributed random variable
ζ_f	MEE interpolation factor
η	Separation efficiency
θ	Angle
θ_f	Variable determining MEE interpolation factor
κ	Von Karman constant
λ	Mean free path
λ_s	Eigenvalue
μ	Dynamic viscosity

ν	Kinematic viscosity
ξ_{relax}	Relaxation factor
Ξ	Uniformly distributed random variable
π	Pi
ρ	Density
ρ_e	Charge per unit volume
σ	Surface charge density
σ_0	Equilibrium charge density
σ_g	Geometric standard deviation
Σ	Summation
τ	Time scale
τ_e	Eddy lifetime
τ_w	Wall shear stress
ϕ	Work function
ϕ_d	Dilution
ϕ_e	Electric potential
ϕ_F	Fermi level
χ	Poisson's ratio
ψ	Variable
Ψ	Coefficient in Taylor-Green MEE velocity

Brackets and Superscripts

$\bar{\ }$	Time average
$\hat{\ }$	Spatial average
$\tilde{\ }$	Favre average
$\langle\rangle$	Ensemble average
$\dot{\ }$	Temporal derivative
$+$	Wall normalised
$*$	Dimensionless
$'$	Fluctuating part
i, j, k	Grid point indices
n	Current time step
T	Matrix transpose
v	Eulerian particle derivatives

Subscripts

0	Reference value
1	Particle 1
2	Particle 2
50	50% separation efficiency
A	Area
c	Contact
dr	Drift
e	Equilibrium
f	Fluid
F	Face
g	Geometric

i, j, k	Tensor indices
in	Inlet
K	Kinetic
m	Mixture
mag	Magnitude
out	Outlet
p	Particle
s	Dimensionless for free-molecular
SA	Surface area
sh	Sheath flow
t	Turbulent
v	Vortex finder
w	Wall
x	Cartesian x-direction
y	Cartesian y-direction
z	Cylindrical Axial component
η	Kolmogorov scale
τ	Time scale
∞	Free-stream

Tensor/Vector Notation

A_i	Area vector
D_i	Electric displacement vector
$\frac{D}{Dt}$	Material derivative $\frac{D}{Dt} = \frac{\partial}{\partial t} + u_j \frac{\partial}{\partial x_j}$
E_i	Electric field strength
g_i	Acceleration due to gravity vector
h_i	Turbulent diffusive flux of volume fraction
$\boldsymbol{i}, \boldsymbol{j}, \boldsymbol{k}$	Unit vectors in Cartesian geometry
$\boldsymbol{k}_a$	Non-orthogonal vector
$\boldsymbol{k}_n$	Runge-Kutta n^{th} stage vector
$\boldsymbol{n}$	Unit normal vector
S_{ij}	Strain rate tensor $S_{ij} = \frac{1}{2}\left(\frac{\partial u_i}{\partial x_j} + \frac{\partial u_j}{\partial x_i}\right)$
u_i	Fluid velocity vector
v_i	Eulerian particle velocity vector
V_i	Lagrangian particle velocity vector
w_i	Relative velocity vector
$\boldsymbol{W}$	$\tau_p \boldsymbol{g}$
x_i	Eulerian position vector
X_i	Lagrangian position vector
$\boldsymbol{Z}$	State vector holding position and velocity
δ_{ij}	Kronecker delta (equal to 1 if i=j, else equal to 0)
ϵ_{ijk}	Permutation symbol (equal to zero for repeating indices)
τ_{ij}	Deviatoric stress tensor
Ω_{ij}	Vorticity tensor
∇	Nabla $\frac{\partial}{\partial x}\boldsymbol{i} + \frac{\partial}{\partial y}\boldsymbol{j} + \frac{\partial}{\partial z}\boldsymbol{k}$ for 3D Cartesian
∇_V	Velocity space nabla $\frac{\partial}{\partial V_x}\boldsymbol{i} + \frac{\partial}{\partial V_y}\boldsymbol{j} + \frac{\partial}{\partial V_z}\boldsymbol{k}$ for 3D Cartesian

Chapter 1

Introduction

1.1 Project Aim

The aim of this industrially-sponsored project is to create a computationally inexpensive particle model with a charge sub-model to be able to predict the separation efficiency of a cyclone. Cyclones have been used in a variety of industries to separate particulates from a fluid stream. These include reducing the amount of sand and black powder in the natural gas industry [1], air filtration [2] and in the petro-chemical industry [3]. These cyclonic separators are an attractive method for separation as they have no moving parts, are reliable and have low operating costs [4]. Their basic principle of operation relies on the particle-laden flow entering the cyclone being spun around and the more dense particle phase experiencing a higher centrifugal force than the carrier fluid [5]. These particles travel towards the walls, losing momentum and allowing them to be collected by the bin or hopper at the base [1]. This principle is known to not give the full picture of separation as particles re-entrain back into the flow [6] and very small particles are able to bypass the main vortex and escape through the vortex finder situated at the top [7]. The flow speed by the cone tip of these small cyclones may be high enough for compressibility effects to be important and are thus designated “high-speed”. The full mechanism by which cyclones separate the particulate phase from the carrier fluid is still not well understood due to the complexity of the interactions between the strongly turbulent flow and the particles [8].

Cyclones are used as part of a complex separation system in Dyson domestic vacuum cleaners. Within these products, the dust entering the system is first exposed to a vortex flow in a large bin and then passed through a fine-mesh; thus capturing the larger clumps of dust and household waste. The remaining flow is then passed through an array of small cyclones which inertially separate the larger remaining particles. Particles which are unable to be separated by the cyclones are passed through a high-efficiency particulate air (HEPA) filter (which European standards require an efficiency of ≥ 0.995 for particles with diameter $d_p = 0.3\mu m$ [9]), after which the flow exits the device and re-enters the local atmospheric environment. Simple diagrams of these separation stages are provided in Figure 1.1. Before the use of cyclones in domestic vacuum cleaners, the dust was passed through a bag which acted as a replaceable filter and back out to atmosphere. These bags required frequent replacement from the user and would experience a rise in pressure drop across it as it became caked in particulates. This increase in pressure drop results in a loss of suction at the cleaner head. Cyclonic vacuum cleaners resulted in no need for the user to purchase bags and provided no loss of suction during use of the device.

Improving cyclone separation efficiency helps to prolong the life of the downstream filtration media, as the cyclones will capture more particles which decreases the amount of particulate matter reaching the filters. This results in monetary savings from reducing the regeneration frequency of the filters and/or the overall filtration media in the product. If less filtration media is required, the overall vacuum cleaner product can be made both smaller and lighter; the importance of which has increased significantly with the uptake of handheld battery-powered devices which are predicted to replace the traditional, heavier, wired products [10].

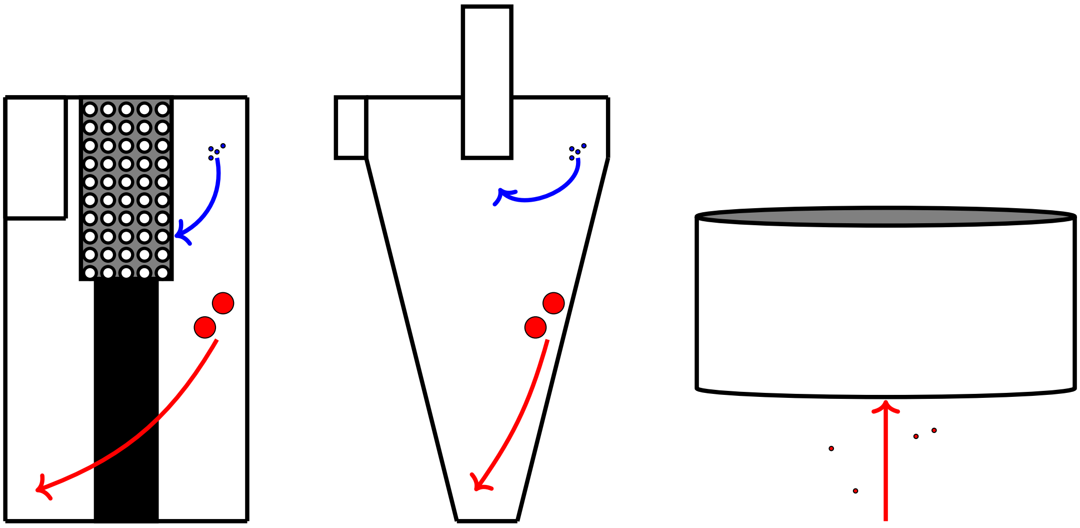

Figure 1.1: The three main separation stages in a modern cyclonic vacuum cleaner in order from left to right: the bin, the cyclone and the filter. Red particles symbolise those which are separated at the current stage, with blue particles escaping the separation process. Arrows show indicative trajectories for the respectively coloured particles.

1.2 The Research Problem

Simple models used to predict cyclone separation efficiency neglect much of the rich physics present in the cyclone such as the effects of turbulence on the particles, the presence of the boundary layer and collisional interactions between particles and the cyclone walls. More complex models of this system commonly involve the use of computational fluid dynamics (CFD) to predict the Eulerian fluid flow field and to model the turbulence. This flow field is used to calculate the trajectories for the discrete Lagrangian particles and from these the separation efficiency can be estimated. The accuracy of the CFD flow field is expected to correlate with the accuracy of the particle trajectories. Computing accurate flow fields involves very fine numerical grids/meshes and is computationally expensive. Simulation of highly-swirling flow remains a difficult challenge to correctly model [11].

A frame from a video showing the dust travelling through a small, high-speed cyclone experimentally is shown in Figure 1.2, with the cyclone approximately $66mm$ in height. In this video provided by Dyson, the dust is shown to move in bands of differing speeds dependent on the distance from the wall. This evidence suggests the boundary layer and secondary fluid structures are influencing the particle trajectories, which ultimately determine the separation efficiency. This phenomenon is not considered in simple separation efficiency models for cyclones and a more complex analysis is required.

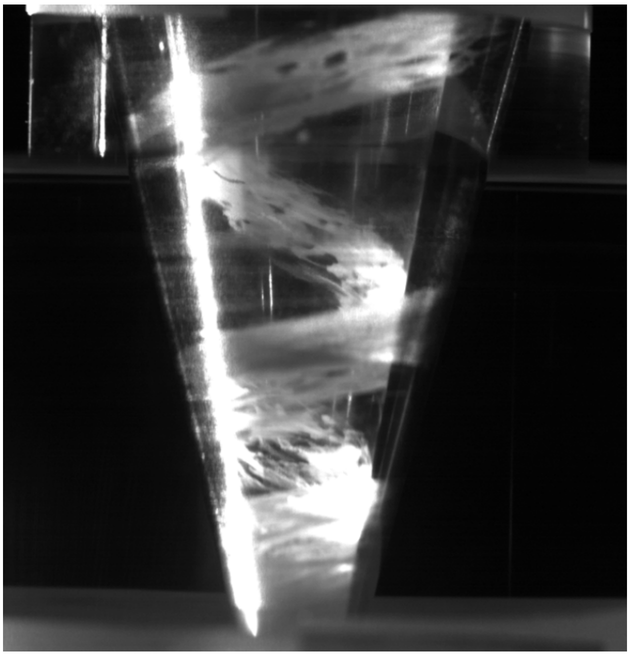

Figure 1.2: Still frame from a video provided by Dyson showing silica-based dust from Powder Technology Inc. in the air flow through a small, high-speed cyclone. The dust is travelling in discrete bands by the cyclone walls with streak-line patterns visible.

In these bands close to the wall, particles may collide with each other. If particle collisions are considered, the expense of modelling the Lagrangian particulate phase (which is independent of the cost of computing the Eulerian fluid phase) increases further. This prevents representative numbers of particles from being tracked in the cyclone, for which we must resort to tracking small statistical samples of particles which may not provide an accurate representation of the system. These particle collisions occur with each-other and with the cyclone walls, exchanging charge during contact in a process known as tribocharging [12]. This electrical charging of particles by frictional contact has been observed for cyclones used in vacuum cleaners [13]. The subject to this day remains ambiguous, with the mechanism of charge transfer not fully understood [14], disagreements in the literature [15] and experiments having poor repeatability [16]. This presence of charge on the particle surface may contribute to the formation of powder particle assemblies, in a process known as agglomeration [17]. These agglomerates may then be large enough to be efficiently separated by the cyclone.

The particle sizes studied for tribocharging in the literature are as small as $100\mu m$ for single-particle collisions [18], with particles smaller than this only studied as bulk powder experiments. Models of the charging process are built on the contact between two particles and have been validated for these large $d_p \geq 100\mu m$ particles. There is a gap of several orders of magnitude in particle diameter in the literature to what is required in this work. In addition to the charge measurements, the tribocharging models applied to larger particles have not been validated at these small scales of $d_p \leq 1\mu m$. Novel experiments at this size range are performed in this work to both validate the charging physics for small particles and to provide the necessary model constants in the tribocharging model.

To capture the charging behaviour of particles requires involving collisions. As this is too computationally expensive, this motivates the use of an alternate framework for the Lagrangian particulate phase: an Eulerian treatment. In this framework, information regarding individual particles is lost and instead the dispersed particulate phase is modelled as a continuum [19], much like the carrier fluid phase. Some form of additional closure is required, which will aim to be simple enough such that the Eulerian method is computationally cheap and able to capture the relevant physics. One such Eulerian particle model, the Equilibrium Eulerian (EE) model [20], was validated in the academic case of isotropic turbulence. Applying this model to a swirl-dominated flow has not been validated, therefore this validation is performed in this work on an analytical Taylor-Green flow field which consists of counter-rotating eddies. The flow and particle scales in this Taylor-Green flow are matched to the case of particles in the turbulent eddies in the cyclone to provide a useful source of validation for the Eulerian model. This Eulerian particle phase allows the effects of collisions to be modelled as a diffusion, with particle charge treated as a scalar which is transported by the particle flow field. This allows predictions of the charge distribution in the cyclone to be made which can give an indication as to where agglomeration and electrical breakdown in air may occur.

1.3 Geometry and Scales

From the cyclone geometry and the state of the flow entering the cyclone, the scales of the problem can be defined. These scales, which at first are expressed dimensionally, are converted to a dimensionless form. The conclusions drawn from the work not only apply to this specific cyclone, but to any system with matching dimensionless quantities. The cyclone in this context represents an application of the research into particle modelling in highly-swirling flows.

1.3.1 Cyclone Geometry and Inlet Conditions

A 2D vertical slice down the centre of the cyclone is shown in Figure 1.3, with the key geometric parameters labelled. The rectangular inlet to the cyclone, of height a_h and width b, is visible in the top left of the diagram. The vortex finder of diameter D_e, which protrudes into the cyclone body by a length S, is seen at the top of the cyclone and is where the cleaned fluid leaves the separation device. The body diameter of the cyclone is given by D, with the total height provided by H and the height of the top section denoted by h. At the base of the cyclone is the cone tip of diameter B, which is where captured particles leave and are collected into a bin or hopper. These key geometric lengths are provided in Table 1.1.

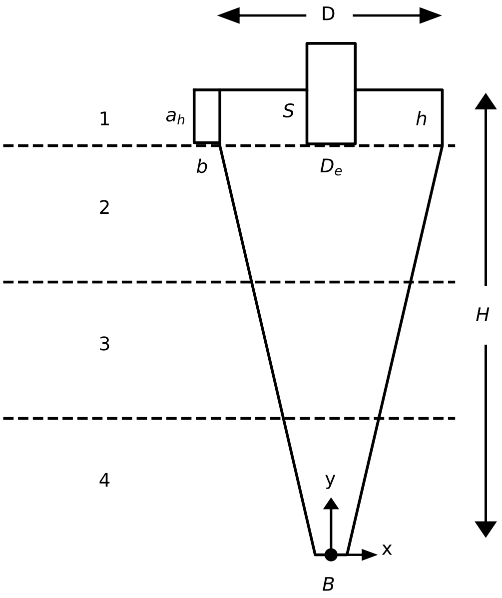

Figure 1.3: Geometry with the coordinate origin shown by the filled black circle. The dashed lines separate out the sections of the cyclone numbered 1 to 4. The top section (from $y = H$ to $y = H - h$) is the part of the cyclone without taper and the remaining three sections are of equal height divisions (going down in increments of $\frac{H-h}{3}$). The positive z-axis goes out of the page, in the opposite direction of flow entering the cyclone through the inlet.

Dimension	**Dimension/D**
a_h	0.322
b	0.115
B	0.143
D_e	0.217
h	0.340
H	2.832
S	0.329

Table 1.1: Key geometric values for the cyclone ($D = 23.3mm$). This geometry, provided by Dyson, is representative of cyclones found in domestic vacuum cleaners.

The dashed horizontal lines in Figure 1.3 represent a splitting of the cyclone into 4 volumes: a top section and 3 tapered conical sections. The walls in the top section have a constant radius and is where the inlet flow meets the swirling cyclone flow. For the tapered conical sections, the flow speeds up as the outer diameter decreases and in section 4, the flow reverses direction. These changes in the flow at the different sections allow analysis into how both the fluid and particle statistics vary as a function of the outer swirl radius later in this work.

The operational volumetric flow rate entering the cyclone provided is $7.5 \times 10^{-4} m^3/s$ [13] which for air at standard atmospheric conditions (which will be assumed henceforth) equals a mass flow rate of $\dot{m}_f = 9.2 \times 10^{-4} kg/s$ and a bulk mean inlet speed of $\bar{u}_0 \approx 37m/s$. The pressure drop of the cyclone ΔP, defined as the drop in static pressure P across the cyclone [11], at this flow rate is $\Delta P = 5kPa$.

1.3.2 Fluid Scaling

The mixing of momentum due to turbulence and the state of the boundary layer is governed by the Reynolds number [21]

$$Re = \frac{\rho_f u l}{\mu_f} = \frac{ul}{\nu_f}, \tag{1.1}$$

where ρ_f is the fluid density, u is a characteristic velocity, l is a characteristic length and μ_f and ν_f are the fluid dynamic and kinematic viscosities respectively. For simple pipe flows, the characteristic velocity is the bulk flow velocity and the length is taken as the pipe diameter. The characteristic length scale of the cyclone remains an open question; Hoekstra argued that the body diameter is most appropriate as it is the swirling flow of the cyclone itself which is of main interest [22]. The characteristic velocity is commonly set as the bulk inlet velocity u_0, which is assumed to be the same as the outer swirl velocity of the cyclone. The cyclone Reynolds number is shown in Eq. 1.2 and for the cyclone considered is $Re_D \approx 56,000$ (computed *a posteriori* from the CFD results of Chapter 5), which is lower than other cyclones in the literature [1, 2, 23, 24]. As the range of turbulent lengths scale with the Reynolds number, the possibility of resolving most of the scales of turbulence using large eddy simulation (LES) appears plausible and is explored in Section 2.1.1.

$$Re_D = \frac{\rho_f u_0 D}{\mu_f} \tag{1.2}$$

The swirling nature of the flow can be characterised by a dimensionless constant known as the swirl number, Sw, which is the ratio of the axial flux of angular momentum L_θ to the axial flux of axial momentum L_x multiplied by the equivalent nozzle radius, which in the case of a cyclone is the vortex finder radius $\frac{D_e}{2}$ [25]

$$Sw = \frac{L_\theta}{L_x \frac{D_e}{2}}. \tag{1.3}$$

Swirlers used in combustion chambers with swirl numbers above 0.6 create recirculation zones in the flow to promote uniform mixing of the air and fuel mixture [26]. The swirl number is location dependent in a cyclone which makes this quantity difficult to determine. A geometric swirl number which is constant for a given cyclone geometry has been defined as [27]

$$Sw_g = \frac{\pi D D_e}{4 a_h b}. \tag{1.4}$$

A derivation of the geometric swirl number is provided in Appendix A. Cyclones used in industry typically have geometric swirl numbers of between 1.5 and 4 [3], the swirl number of the cyclone (from Eq. 1.4) considered here is $Sw_g = 4.6$ (1 d.p.) which indicates that this cyclone is highly-swirling compared to other cyclones and swirlers in the literature.

The high swirl in the cyclone results in the formation of recirculation regions in the flow. For a straight pipe exit, the critical swirl number for this instability is $Sw \approx 0.6$ [27], the same value as observed for swirlers used in combustion chambers. Above this swirl number, as Reynolds number is increased, additional instabilities such as vortex breakdown and the precessing vortex core (PVC) occur. The PVC is a large 3D, time-dependent instability where the vortex core precesses about the vertical axis; the frequency of which is linearly proportional to the volumetric flow rate [28]. The conical geometry of the cyclone is able to provide a stabilising effect on the vortex core, however if the instability is strong enough the vortex core can attach itself to the outer cyclone walls [29]. This can reduce the separation efficiency significantly due to the re-entrainment of particles by the walls [11]. This time-dependent PVC phenomenon is a major part of the cyclone flow field and is ignored in simple cyclone separation and fluid models. This suggests the need for high-resolution CFD to accurately capture the cyclone flow field both in space and time.

The pressure drop for a given cyclone geometry ultimately determines the fluid flow field. This is because a specific value of ΔP specifies a unique inlet mass flow rate $\dot{m}_{in}$ (or vice-versa) which sets the Reynolds number of the flow. This relationship expressed in terms of the volumetric flow rate is approximately $\Delta P \propto \dot{V}^2$, which comes from the conversion of static pressure to dynamic pressure by the cyclone [11]. It is this pressure conversion by the vortex core which leads to the (at first seemingly counter-intuitive) result that cyclones with rough walls, high particle mass loadings and/or long lengths *decrease* the pressure drop [11].

The equations of motion of the fluid phase in the cyclone are governed by the usual Navier-Stokes equations for fluid flows [11]. These are a set of partial differential equations (PDEs) with non-linear terms and as such, analytical solutions only exist for the simplest of flows. Obtaining an analytical flow field for the cyclone is not possible and either an approximate numerical solution or experimental data is sought instead. Numerically solving the Navier-Stokes equations directly for a representative cyclone is not computationally feasible as a consequence of the fine grids required to capture the smallest turbulent eddies in the flow. As the turbulent dissipation rate is expected to scale as $\epsilon_f \approx \frac{u_0^3}{l_0}$, where u_0 and l_0 are representative values for the large geometric scales, the ratio of the largest to the smallest scales in 1D can be estimated as [30]

$$\frac{l_0}{l_\eta} \approx Re^{\frac{3}{4}}, \tag{1.5}$$

with l_η denoting the Kolmogorov length scale. The Kolmogorov scales can be estimated using dimensional analysis as [30]

$$l_\eta = \left(\frac{\nu_f^3}{\epsilon_f}\right)^{\frac{1}{4}}, \tag{1.6}$$

$$\tau_\eta = \sqrt{\frac{\nu_f}{\epsilon_f}}, \tag{1.7}$$

$$u_\eta = \left(\epsilon_f \nu_f\right)^{\frac{1}{4}}. \tag{1.8}$$

The mesh resolution required to capture the Kolmogorov scales in a direct numerical simulation (DNS) of a representative swirling flow is prohibitively expensive. To provide rough numerical estimates for the number of computational cells/nodes required, consider a 3D box of isotropic turbulence on a uniform grid. The ratio of the large scales (size of the domain) to the small Kolmogorov scales is expected to scale as $\frac{l_0}{l_\eta} \approx Re^{\frac{9}{4}}$, where the grid spacing Δx is expected to be of the order of l_η. Using the Reynolds number based on the cyclone body diameter and assuming a uniform mesh, the number of grid points required is expected to be $\approx Re_D^{\frac{9}{4}} \approx 5 \times 10^{10}$ which is 4-5 orders of magnitude more than those used in the literature in Section 2.1.1.

Due to the computational cost of DNS, the turbulence must be modelled instead. An accurate model is required to capture this high swirl and anisotropic turbulence in cyclones [31]. The most common turbulence models in use for cyclone CFD are incompressible Reynolds-averaged Navier-Stokes (RANS) models. These models involve a Reynolds decomposition which splits the variables in the incompressible Navier-Stokes equations into a mean component and a fluctuating component. For a variable $\psi(\boldsymbol{x}, t)$, the Reynolds decomposition is [32]

$$\psi(\boldsymbol{x}, t) = \overline{\psi}(\boldsymbol{x}) + \psi^{'}(\boldsymbol{x}, t), \tag{1.9}$$

where $\overline{\psi}$ and $\psi^{'}$ represent the mean and fluctuating component of ψ respectively. The mean component is commonly calculated as the time average which is given by [19]

$$\overline{\psi}(\boldsymbol{x}) = \frac{1}{T}\int_t^{t+T} \psi(\boldsymbol{x}, t)dt. \tag{1.10}$$

This is the average of ψ over a time interval T. If the flow is not statistically stationary, time averaging must be replaced by ensemble averaging defined as [32]

$$\left\langle \psi(\boldsymbol{x}, \boldsymbol{t}) \right\rangle = \frac{1}{N}\sum_{n=1}^{N} \psi(\boldsymbol{x}, t), \tag{1.11}$$

where N is the number of flow realisations which must be large enough such that the fluctuating effects are negligible. The fluctuating part has a mean of zero for both the temporal and ensemble average. After the Reynolds decomposition, the equations of motion for the fluid are then appropriately time or ensemble averaged and the RANS equations are produced [32]. A consequence of this averaging process is that an additional term appears in the momentum equation known as the Reynolds stress tensor. This involves the fluctuating components and requires an additional model to close the set of equations. Simple eddy-viscosity closures, such as the k-ϵ model, are known to inaccurately model tangential velocities and over-predict turbulent viscosities in swirling flows [33]. These simple models treat the effects of the turbulence as an additional viscosity, whose value is obtained by solving one or more transport equations. Most modern published cyclone CFD uses a Reynolds stress model (RSM) [34] which is better suited at capturing the anisotropy of the turbulence in these complex flows [35, 36].

In RSM, transport equations are solved for the components of the Reynolds stress tensor $\rho_f \overline{u_i' u_j'}$ and the turbulent dissipation rate [32]. In 3D, this amounts to an additional 7 PDEs to be solved in the domain in addition to the mean flow equations. Within the transport equations for the Reynolds stresses, additional closures are required for terms such as the pressure-strain and turbulent diffusion [32]. The RANS equations with RSM provide a stiffer set of equations than simple turbulence models and are known to converge slowly [32]. It is also useful to stress that RSM, as with all RANS models, does not directly compute any of the turbulent scales. These turbulent eddies are missing and Lagrangian particles tracked in such a flow will not see any turbulent structures.

Another approach to turbulence modelling which is able to directly capture part of the turbulent scales is LES. Here, instead of time-averaging (Eq. 1.10) the Navier-Stokes equations, a spatial filter is applied, defined as [19]

$$\hat{\psi}(\boldsymbol{x}, t) = \frac{1}{V} \int_V \psi(\boldsymbol{x}, t) dV, \tag{1.12}$$

where V is the volume of integration. In compressible flows, densities are Favre averaged by [19]

$$\tilde{\psi}(\boldsymbol{x}, t) = \frac{\int_{V_k} \rho_k \psi_k(\boldsymbol{x}, t) dV}{\int_{V_k} \rho dV}. \tag{1.13}$$

LES directly solves the Navier-Stokes equations for scales larger than the cut-off filter width and models the flow below this filter width. The motivation for this method is based upon Kolmogorov's hypotheses and the turbulent cascade. The larger energy-containing eddies are directly computed, with the small eddies (which are assumed to have a universal form) estimated using a sub-grid scale (SGS) model. When a simple eddy-viscosity model is used to model the effects of the unresolved scales, the rate of transfer of energy to the residual motions approximately equals the turbulent dissipation rate to give [30]

$$\epsilon_f \approx \nu_t \hat{S}_{mag}, \tag{1.14}$$

where ν_t is the turbulent viscosity estimated from the SGS model and $\hat{S}_{mag}$ is the resolved strain rate magnitude where [30]

$$S_{mag} = \sqrt{2 S_{ij} S_{ij}}, \tag{1.15}$$

with the strain rate tensor defined as [30]

$$S_{ij} = \frac{1}{2} \left(\frac{\partial u_i}{\partial x_j} + \frac{\partial u_j}{\partial x_i} \right). \tag{1.16}$$

Of particular interest in this work are the boundary layers of the fluid by the walls of the cyclone. From the experimental evidence in Figure 1.2, particles appear to be moving in bands close-to or in the boundary layers. These boundary layers are expected to differ from the well-studied flat plate boundary layer due to the curvature of the geometry and intense swirl. The majority of cyclones operate at high Reynolds numbers and therefore have turbulent boundary layers. These are less prone to separation over curved surfaces than their laminar counterparts [37] due to the mixing between layers. For a concave surface such as the flow inside a cyclone, the curvature produces a favourable pressure gradient which keeps the boundary layer attached to the wall.

Although the concave curvature has a stabilising effect on separation, it has a destabilising effect just outside of the wall which promotes the growth of secondary flow structures. One of these features are known as Görtler vortices and are due to the occurrence of centrifugal forces arising from disturbances in a concave boundary layer [38]. The onset of these Görtler vortices can be predicted from a dimensionless parameter known as the Görtler number, G_θ, defined as [39]

$$G_\theta = \frac{u_\infty \delta_r}{\nu_f} \sqrt{\frac{\delta}{R}}. \tag{1.17}$$

Here u_∞ is the free stream velocity, $\delta_r = \sqrt{\frac{\nu_f x}{u_\infty}}$ is related to the boundary layer thickness, R is the radius of curvature and x is the distance from the leading edge. Görtler structures have been observed experimentally throughout the boundary layer and extending to approximately twice the Blasius boundary layer thickness away from the wall [40]. A crude approximation of the Görtler number for the boundary layer at the top of the cyclone body just after the inlet can be calculated by assuming $u_\infty \approx U_0 = 37m/s$ and by setting both R and x equal to $\frac{D}{2}$. This results in an approximate Görtler number of $G_\theta = 13$. Görtler vortices are typically observed when $G_\theta = 8$ [39] and therefore these boundary layer structures are expected to be present in the cyclone.

1.3.3 Particle Scaling and Regimes

The particulate phase is composed of many individual particles. A Reynolds number based on the particle diameter, Re_p, henceforth known as the particle Reynolds number can be defined as

$$Re_p = \frac{\rho_f |\boldsymbol{u} - \boldsymbol{V}|\, d_p}{\mu_f}, \tag{1.18}$$

where $\boldsymbol{V}$ is the particle velocity. This particle Reynolds number describes the state of the flow around the particle. The forces on the particle arising from the fluid arise from integrating both the pressure and shear force distribution over the particle [41]. This task becomes simpler if the particles are assumed to be spherical. Then, the diameter of the particle, d_p, completely defines the size of the particle and the mass of the particle is given by

$$m_p = \frac{\pi}{6} \rho_p d_p^3, \tag{1.19}$$

where ρ_p is the particle density. For particles sufficiently small, a point-particle approximation is made which means the volume of the particle is considered negligible. This is only valid when $d_p << L$, where L is the smallest length scale in the fluid. If Stokes flow is assumed ($Re_p << 1$), the flow around the particle is analytical and given by the Maxey-Riley equation [42]. This contains a variety of force-contributions; many of which become negligible by assuming that the density ratio between the particles and the carrier fluid is large ($\frac{\rho_p}{\rho_f} >> 1$) [43] and is discussed in more detail in Section 2.1.2. This only remaining force from the Maxey-Riley equation is the Stokes drag force, given by [44]

$$\boldsymbol{F}_{\text{drag}} = 3\pi\mu_f d_p \left(\boldsymbol{u}((\boldsymbol{x} = \boldsymbol{X}), t) - \boldsymbol{V}(t)\right), \tag{1.20}$$

where the fluid velocity is evaluated at the point particle current location. A useful substitution is to define a particle relaxation time as

$$\tau_p = \frac{\rho_p d_p^2}{18\mu_f}, \tag{1.21}$$

which defines an inertial time scale for the particle [45]. It can be shown to be the time constant in the relative velocity vs time exponential decay for a particle acted on solely by drag. By normalising τ_p with a representative fluid time scale τ_f, we produce the Stokes number [46]

$$Stk = \frac{\tau_p}{\tau_f}. \tag{1.22}$$

The Stokes number is a dimensionless number characterising the ability of a particle acting under Stokes drag to follow fluid streamlines. If $Stk << 1$, particles rapidly accelerate to follow fluid streamlines and act as fluid tracers. Conversely if $Stk >> 1$, particles tend to ignore the fluid due to their large inertia and act as “billiard balls”. In a turbulent flow, the fluid timescale is representative of the smallest turbulent eddies seen by the particle (Eq. 1.7).

When the particle diameter d_p is comparable to the fluid mean free path λ_f, the fluid flow around the particles is said to be in the free molecular regime [45]. For $d_p >> \lambda_f$, the fluid phase behaves as a continuum as in the usual treatment of fluid dynamics. This continuum criterion in general is characterised by the Knudsen number [47]

$$Kn = \frac{\lambda_f}{d_p}, \tag{1.23}$$

with $Kn << 1$ indicating the fluid flow around the particle behaves as a continuum. For particles with length scales comparable to the fluid mean free path, the fluid motion around the particle is no longer considered a continuum and the drag force is altered due to slip of the gas at the particle surface [48]. This is rectified in the Stokes drag equation by the introduction of a Cunningham slip correction factor [49]. This is directly incorporated into the definition of τ_p as

$$\tau_p = \frac{\rho_p d_p^2 C_c}{18\mu_f}, \tag{1.24}$$

where C_c is given by [48]

$$C_c = 1 + \frac{\lambda_f}{d_p}\left(2.514 + 0.8e^{-\frac{0.55 d_p}{\lambda_f}}\right). \tag{1.25}$$

The Cunningham slip correction factor is shown for the particles applicable to this thesis in Figure 1.4, showing that the smallest particles have a drag force ≈ 2.95 times smaller acting on them without correction. The discrepancy is less pronounced for the larger $1\mu m$ particles, however the error is around 17% and thus this correction is necessary for all particle sizes considered here.

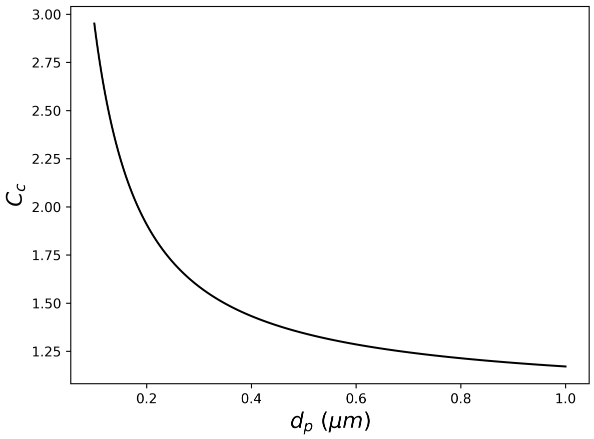

Figure 1.4: Cunningham slip correction factor for particle diameters in the range $0.1\mu m \leq d_p \leq 1\mu m$ with an air mean free path of $68nm$ [50].

The motion of the individual particles are governed by Newton's second law, which provides a coupled set of first order ordinary differential equations (ODEs) describing the particle trajectories. For particles acted upon solely by Stokes drag, the equations of motion for a single particle become

$$\frac{d\boldsymbol{V}}{dt} = \frac{\boldsymbol{u} - \boldsymbol{V}}{\tau_p}, \tag{1.26}$$

$$\frac{d\boldsymbol{X}}{dt} = \boldsymbol{V}, \tag{1.27}$$

where $\boldsymbol{X}$ is the position vector of the particle.

We have briefly discussed the effect of the fluid on the particles, however the particles may influence the fluid and even other particles. The strength of the different levels of coupling between the phases are determined by the volume fraction α and the mass fraction c. The volume fraction is defined as the volume occupied by the particulate phase per unit volume [46] and the mass fraction is defined as the mass of the particulate phase in a unit volume normalised by the total mass of particles and fluid in that volume [46]. These two quantities are related for a monodisperse aerosol by the particle and fluid densities

$$c = \frac{m_p}{m_{tot}} = \frac{\alpha\rho_p}{\alpha\rho_p + (1-\alpha)\rho_f}. \tag{1.28}$$

Two-way coupling, when both the fluid and particle phases influence each other, is commonly considered important when $c > 1 \times 10^{-3}$ [51]. The presence of small particle Stokes number in this regime increases the turbulent dissipation from an increased particulate phase surface area, with larger values of Stokes numbers increasing the production of turbulent kinetic energy due to vortex shedding on the particles [52]. At large volume fractions, particle-particle collisions begin to affect the behaviour of the particulate phase. A useful graphical illustration of the different regimes adapted from Elghobashi [52] is shown in Figure 1.5.

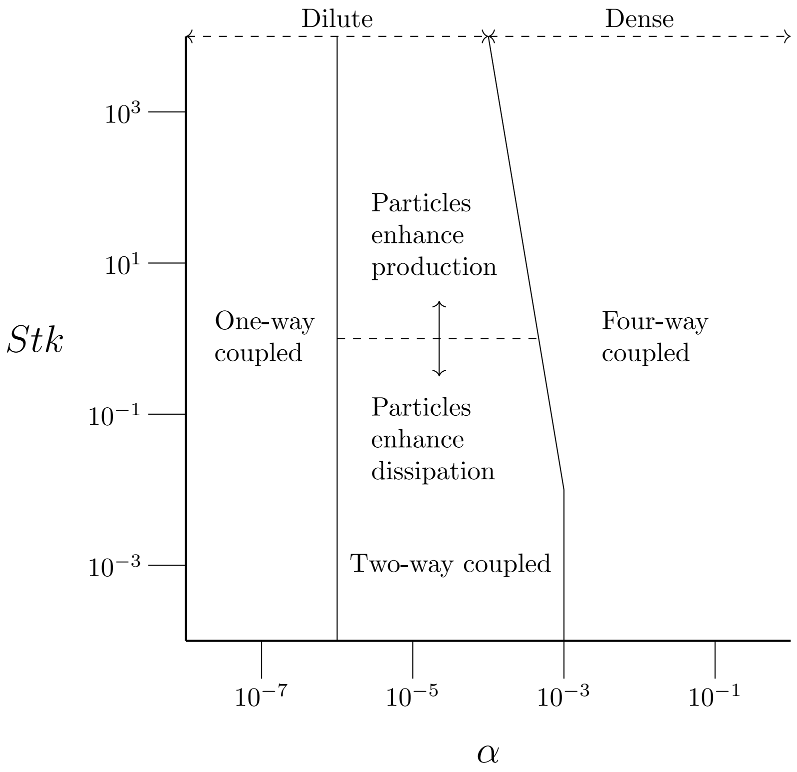

Figure 1.5: Particle regimes as a function of volume fraction and Stokes number at $Re \approx 1 \times 10^4$ adapted from Elghobashi [52].

Experimentally, particles are seen to accumulate at the walls of a cyclone and therefore volume fractions are expected to be higher in the near-wall region. This increases the likelihood of two particles colliding with each other by the walls, which is characterised by the collision frequency, C_{12}. This is defined as the number of collisions between two particles per unit volume per unit time [45]

$$C_{12} = \beta n_1 n_2, \tag{1.29}$$

where β is the collision frequency function and n_1 and n_2 represent the number densities of particulate phase 1 and 2 respectively [53] (for a monodisperse aerosol $n_1 = n_2 = n$). The number density, or particle concentration, is the number of particles per unit volume [47]. For a monodisperse aerosol composed of spherical particles, it is related to the volume fraction by

$$n = \frac{\alpha}{V_p} = \frac{6\alpha}{\pi d_p^3}. \tag{1.30}$$

A collision frequency function may be defined for different mechanisms causing particles to collide. One such mechanism is Brownian motion which arises from frequent collisions between the particle and fluid molecules due to the thermal energy of the fluid [54]. The classical analysis by Einstein assumed that particles move independently of each other, the motion of a particle in consecutive time intervals is independent and the average energy of a particle in each coordinate axis is $\frac{1}{2}k_B T_f$ [55], where k_B is the Boltzmann constant. A key result is that the mean square displacement of a particle after time t is given by

$$\overline{\boldsymbol{X}^2} = 2D_{\mathrm{lam}}t, \tag{1.31}$$

where D_{lam} is the laminar (Brownian) diffusion coefficient. This diffusion coefficient is given by the Stokes-Einstein relation [54]

$$D_{\mathrm{lam}} = \frac{k_B T_f}{3\pi\mu_f d_p}. \tag{1.32}$$

The original theory proposed by Einstein considered a dilute particle suspension, with each particle assumed to be in an infinite fluid. Batchelor generalised this to the case of a homogeneous suspension where particles are close enough to each other to interact hydrodynamically [56]. The Brownian collision frequency function in this case between two particles of differing diameters is given as [45]

$$\beta_{\text{Brownian}} = \frac{2k_B T_f \left(d_{p,1} + d_{p,2}\right)^2}{3\mu_f d_{p,1} d_{p,2}}, \tag{1.33}$$

which for a monodisperse suspension yields [45]

$$\beta_{\text{Brownian}} = \frac{8k_B T_f}{3\mu_f}. \tag{1.34}$$

This equation assumes that the diffusion coefficient is given by the Stokes-Einstein relation and remains constant (which is not true for particle separations below λ_f [45]). For particles travelling through a shear layer in a fluid, collisions may occur due to their relative motion. For a simple 1D laminar shear ($u = u(y)$), the collision frequency function is [45]

$$\beta_{\text{lam}} = \frac{4}{3}\left(\frac{d_{p,1}}{2} + \frac{d_{p,2}}{2}\right)^3 \frac{du}{dy}. \tag{1.35}$$

This equation predicts increasing collision rate for larger particles and larger velocity gradients. Particles may collide in a turbulent flow due to their inertia from an accelerating eddy. The classical solution from Saffman and Turner assumes that the turbulence is isotropic and that the particle Stokes numbers are low ($Stk << 1$) [57]

$$\beta_{\text{turb}} = 1.3\sqrt{\frac{\epsilon_f}{\nu_f}}\left(\frac{d_{p,1}}{2} + \frac{d_{p,2}}{2}\right)^3, \tag{1.36}$$

where ϵ_f is the turbulent dissipation rate. This equation is of a similar form to the laminar shear, with the fluid velocity gradient expressed in terms of the Kolmogorov scales of turbulence. This model is derived from dimensional analysis and assumes that collisions are occurring over length scales smaller than l_η [45].

These three models can be representative of the contribution to the total collision frequency function for their respective physics (Brownian motion, laminar shear, turbulence). This collision frequency is pivotal in calculating the charge exchange due to collisions in Section 2.2. The relative contribution of each of these sets of physics for particles in a cyclone may be seen as a function of particle diameter. By using both mean and maximum values of the fluid statistics in a cyclone (calculated *a posteriori* from the CFD results in Chapter 5), the significance of each set of physics can be determined. This is shown in Figure 1.6.

From these graphs, is clear that Brownian motion has the weakest contribution towards collisions for all but $0.1\mu m$ particles colliding with similar-sized particles. Both the contribution of laminar and turbulent shear have the same form as their respective equations have the same form. The collision frequency function for particle-particle collisions is dominated by the turbulent eddies and/or large velocity gradients in a cyclone, with larger particles more likely to experience collisions. The velocity gradient for the 1D laminar shear model was replaced with the strain rate magnitude as the cyclone flow is 3D. As the cyclone flow is swirling and turbulent, the modified laminar shear model appears to capture the contribution to collision frequency due to small turbulent structures in the flow and from mean flow structures. The model for collision frequency due to turbulent shear is not necessary when employed in a high-resolution LES and will therefore be excluded in this work as the laminar shear model will be able to capture the majority of the turbulent structures in the flow.

The particulate phase challenging the cyclone is a polydisperse silica-based test dust supplied by Powder Technology with a density of $\rho_p = 2650 kg/m^3$. From the experimental separation efficiency data provided by Dyson, the range of particle diameters of interest in this work is from $0.1\mu m \leq d_p \leq 1\mu m$ which at the smallest size represents particles which are not separated by the cyclone to the largest sized particles which are completely removed by the cyclone. The particle mass flow rate entering the cyclone is $\dot{m}_p = 1.33 \times 10^{-6} kg/s$ [13].

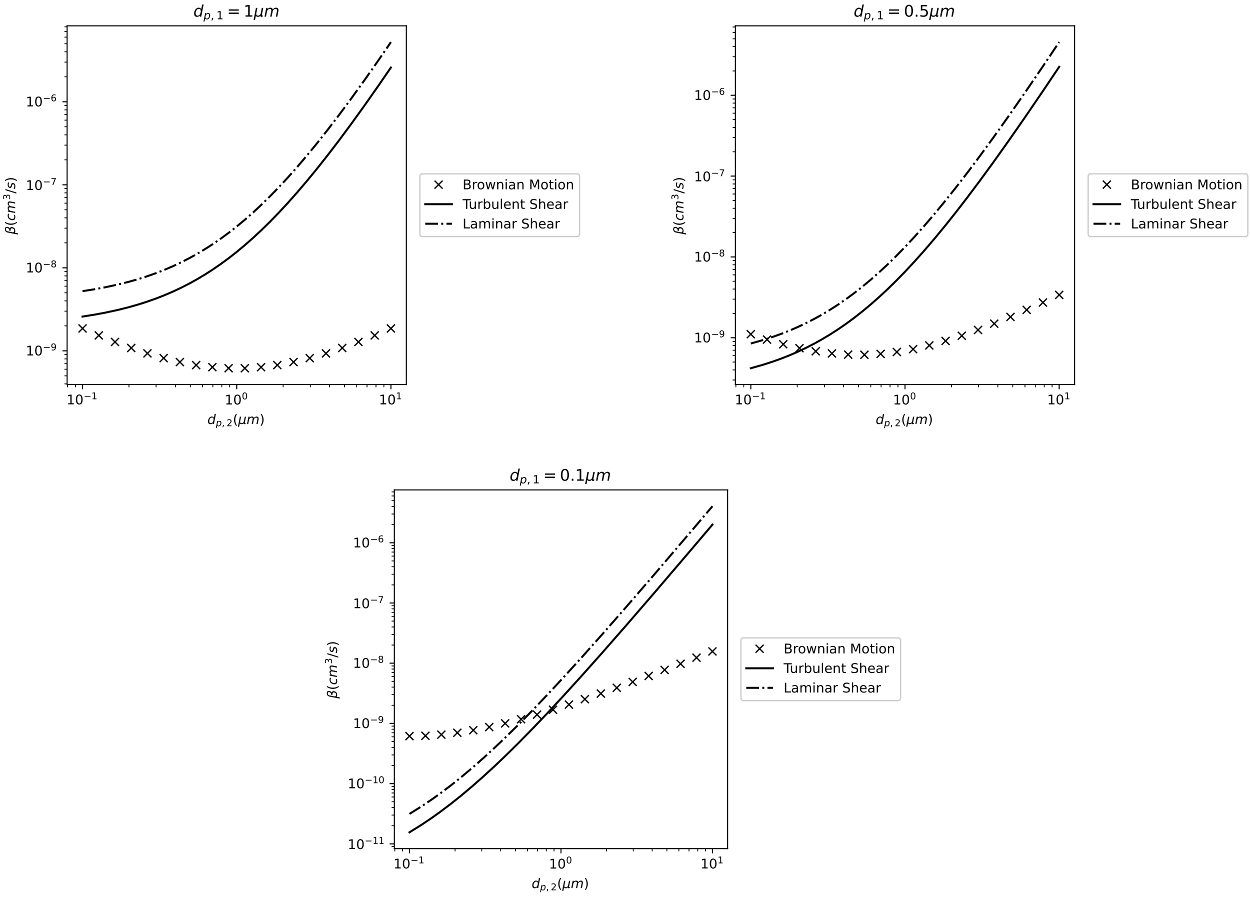

Figure 1.6: Collision frequency functions against collisional particle diameter ($d_{p,2}$) for three representative diameters of particles ($d_{p,1}$) in a small, high-speed cyclone. The collision frequency functions were calculated using the volume-weighted averages of time-averaged variables from the cyclone CFD in Chapter 5. Explicitly these are $\bar{\nu}_f \approx 1.53 \times 10^{-5} m^2/s$, $\bar{\mu}_f = 1.7894 \times 10^{-5} kg/ms$, $\bar{T}_f \approx 298K$, $\bar{\epsilon}_f \approx 2190 m^2/s^3$ and the mean fluid strain rate was used in place of the laminar shear velocity gradient as $\bar{S}_{mag} \approx 23570/s$.

1.4 Fundamental Tribocharging Physics

Tribocharging, triboelectric charging and triboelectrification are the names given to the process by which charge is exchanged by different materials from physical contact [58]. Electric charge is generated if a net imbalance of charge remains on the surface of the materials post-contact [59]. Large amounts of charge building up creates large voltages that can suddenly discharge, causing fire and explosions [60]. In a particle-laden flow, charge may be exchanged when particles collide with each other, or with the walls. This can lead to particles agglomerating into larger particles or cause particles to break-up into smaller fragments; thus affecting the separation efficiency of devices such as a cyclone. The fundamental aspects of the charging process is provided here for the reader, who may be unfamiliar with this subject. In addition, the influence of magnetic fields is assumed to be negligible and thus the theory of electrostatics applies [61].

Metals are structured with positive ions located below the surface of the material, with a sea of electrons on the surface. These electrons are not bound to any single molecule and are therefore able to flow freely and give metals their electrical conductor properties. This means that any charge acquired on a metal surface can flow away to earth. Insulating materials such as silica test dust on the other hand, do not possess a sea of electrons in their structure. Therefore any charge acquired or removed on the insulator's surface tends to stay there. When two neutrally charged materials come into contact and exchange charge, one material acquires a positive charge whilst the other becomes negatively charged. The resultant polarity after contact between two frictional materials can be found by considering the position of both materials on the triboelectric series [62]. This is an empirical list of materials ordered by their tendency to acquire a positive charge after contact with the most positively-charging materials situated at the top of the list [63].

A hypothesis for the cause of tribocharging for metal-metal surfaces was put forward by Volta as an effect of contact, where friction aids in increasing the number of contact points [64]. As materials are not completely smooth, friction occurs at these imperfect contact sites which is where charge may transfer. From this it can be reasoned that faster rubbing of materials will increase the rate of charge transfer. This was extended by Helmholtz who viewed the charge obtained post impact as originating from a double layer formed during contact [64]. This double layer is due to the contact potential difference between the two metals, which arises from the difference in work functions, ϕ, between the two materials.

The work function of a surface is given by the difference between the energy of an electron at rest in a vacuum and the Fermi level ϕ_F (electrochemical potential) of the material [65]

$$\phi = -e\phi_e - \phi_F, \tag{1.37}$$

where e is the charge of an electron and ϕ_e is the scalar electric potential which is related to the electric field strength $\boldsymbol{E}$ by [61]

$$\boldsymbol{E} = -\nabla\phi_e. \tag{1.38}$$

The electric field strength is the force a unit positive charge would experience in the presence of an electric field. The charge per unit volume ρ_e is given by [61]

$$\nabla \cdot \boldsymbol{D} = \rho_e, \tag{1.39}$$

where $\boldsymbol{D}$ is the electric displacement vector which is related to the permittivity of the medium ϵ_m and the field strength by [61]

$$\boldsymbol{D} = \epsilon_m \boldsymbol{E}. \tag{1.40}$$

Combining Eqs. 1.38, 1.39, and 1.40 yields the Poisson equation [61]

$$\nabla^2\phi_e\left(\boldsymbol{x}\right) = -\frac{\rho_e\left(\boldsymbol{x}\right)}{\epsilon_m}. \tag{1.41}$$

Placing two different materials next to each other will create an electric field between both material surfaces due to this difference in work functions (also known as a double layer). This field means that there is a difference in electrical potential between the two surfaces, similar to the two plates of a capacitor. This analogy has formed the basis of more complete models of triboelectrification and this idea is illustrated in Figure 1.7.

The charge-storing ability of the plates of a capacitor is characterised by its capacitance C, defined as the amount of charge Q that can be stored on a material for a given voltage V_c. For a parallel plate capacitor, it can be defined as [66]

$$C = \frac{\epsilon_m A}{d} = \frac{Q}{V_c}, \tag{1.42}$$

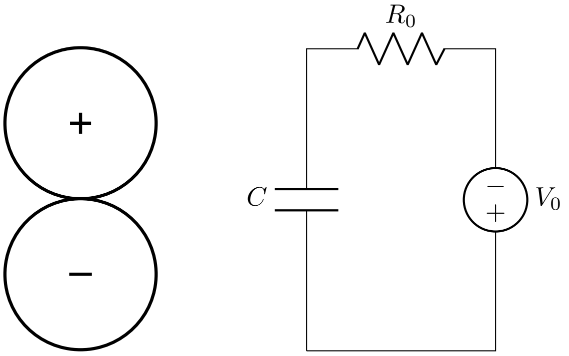

Figure 1.7: Analogous capacitor circuit model of contact between a positively charged and negatively charged particle. The charging circuit has a perfect voltage source of V_0, a resistor with resistance R_0 and a capacitor with capacitance C.

where ϵ_m is the permittivity of the material between the plates, A is the area of one plate and d is the distance between the plates. The current flowing through the circuit is the time rate of change of charge given by [61]

$$i = \frac{dQ}{dt}. \tag{1.43}$$

Using this, we may express the current (Eq. 1.44) and voltage (Eq. 1.45) across a capacitor by the integral and differential equations

$$i = C\frac{dV_c}{dt}, \tag{1.44}$$

$$V_c = \frac{1}{C}\int i\,dt. \tag{1.45}$$

The increasing charge on a capacitor is due to the build-up of electrons on the negatively-charged plate. The charge of an electron was first measured by Millikan in his famous oil drop experiment [67] which showed that charge at the lowest scales is discrete and given by

$$Q = Ne, \tag{1.46}$$

where N is the number of electrons and the charge of a single electron is defined to be $e = 1.602176634 \times 10^{-19}C$ exactly [68]. The physics of charge transfer is explained well for metals, however for insulating materials the problem becomes more difficult. Henry considered the potential of an insulator to be nonsensical as it varies from point to point and is dependent on neighbouring charges [58]. He also stated that the identity of the charge carriers are unknown except in the case of metal/metal contacts where the charge carriers are most certainly electrons [58].

Fukada attempted to extend the theory to insulating materials by rubbing two specimens together and measuring the charge of each at an electrode [69]. As the specimens were different shapes, the results did not include the absolute value of the charge and instead the results were ordered into a triboelectric series for all materials tested. This suggested that the separation of electrons between two materials is determined by free electrons produced during contact by either an unknown abrasion process or local heating filling the electron "traps" in the double layer. The material with more electron traps will accept more electrons and hence become negatively charged. The electron emission by heat from frictional contact is known as thermionic emission and the mechanism is essentially the same as photoelectric emission.

The photoelectric effect has provided evidence for the particle-like nature of light. Einstein hypothesised that light acts as a particle during the photoelectric effect and interacts with a single electron on the surface of the metal [70]. If the energy E of the photon is greater than the work function, then photoelectric emission may take place [71]. This effect is shown graphically in Figure 1.8.

Thermionic electron emission therefore provides a link between tribocharging and the material work function. This link also provides strong evidence that the charge carriers for insulators are electrons which Henry was unable to evidence.

Early work on tribocharging showed that the macroscopic phenomena of materials charging through contact is linked to the electron level. These electrons can transfer from one material to another during contact due to a double-layer formed that is analogous to the plates of a capacitor and the process could be modelled as a capacitor-resistor circuit. The factors affecting the rate of charge transfer, the limits of charge on particles and resultant polarity have since been studied in the literature and are presented in Section 2.2.1.

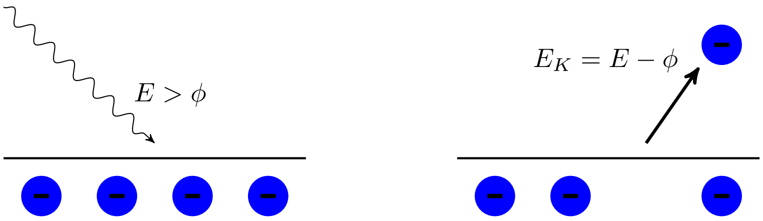

Figure 1.8: Photoelectric emission of a single electron on a metal plate with work function ϕ from interacting with a photon of energy E. The resulting kinetic energy of the particle E_K is the difference between the initial photon energy and the work function of the metal.

1.5 Summary and Structure of Thesis

From the geometry and operating conditions, it is clear that this is a multi-scaled problem. Lengths vary 6 orders of magnitude, from $10^{-1}m$ down to $10^{-7}m$. The vortex core speed is roughly expected to be twice the inlet speed and may cause compressibility effects for the fluid. The mass flow rate of the fluid is roughly 3 orders of magnitude greater than for the particles, of which there are at least a trillion entering the cyclone every second. Resolving all these length scales or considering each and every particle individually is not computationally feasible. As the particles are small, these may be considered as point particles which do not disturb the fluid flow around them. This limits the smallest fluid scales to those of the smallest eddies present, which are suitable candidates to be modelled, rather than directly resolved as will be shown in Section 2.1.1. For the particles, only a representative sample will be possible for individual Lagrangian particle tracking. In this work, a model for treating the entire particulate phase as a separate fluid in an Eulerian framework is presented. This loses information relating to individual particle trajectories, however it is computationally efficient and the particle mass flow rates in the model will be able to match operational conditions. The Eulerian model can also be prescribed in a simple way by utilising the low Re_p and Stk expected for the particles.

There are 3 main bodies of work in this thesis: particle charging, the Eulerian model and the cyclone flow field. The current state of the literature into these fields are presented in Chapter 2. From this literature review, the choice of how to computationally model the cyclone flow field can be decided and suitable models for the particle charging and Eulerian model can be deduced. The gaps in the literature, mainly the missing charge information for small particles and relevant validation of the Eulerian model, can be identified. From this, novel research to extend the body of knowledge in these areas can be performed.

The first body of new work begins in Chapter 3 with particle charging experiments performed on sub-micron particles. These experiments allow the results and key models made for larger particles in the literature to be validated for these small particle sizes. The experiments additionally allow the estimation of key model parameters needed in charge models to be able to compute the charge transfer from impact numerically.

The second stage of work is the validation of the Eulerian model in an analytical flow field in Chapter 4. The flow field features strong streamline curvature, with the scales matched to the turbulent length scales in the cyclone. This permits an in-depth analysis of the model in a representative, simpler flow field. The model is compared against results obtained by tracking Lagrangian particles in the same flow, with the strengths and weaknesses of the model identified.

The final stage of work concerns the cyclone itself in Chapter 5. A CFD model of the cyclone is presented with high wall resolution. Lagrangian particle tracking is compared against experimental evidence for separation efficiency to justify the particle and fluid modelling assumptions. These are compared to the results of the Eulerian model applied to the cyclone, with predictions concerning the transport of particle charge through the cyclone.

The main results of this thesis are then outlined in the conclusion in Chapter 6 and suggestions for future work are presented. Additional information is provided in the appendices.

Chapter 2

Literature Survey

In this chapter, the current knowledge from literature relevant to this thesis is presented. This begins with a review of the literature surrounding the cyclone flow field from experiment and determining the separation efficiency of a cyclone in Section 2.1. Problems involving measuring the highly-swirling flow and the accuracy of simple models are examined. From this, the state of more advanced CFD cyclone models are analysed with strengths and weaknesses compared to experimental evidence. Current work with models of the particulate phase in cyclones, used to better estimate separation efficiency compared to simpler models, is critiqued. This informs the modelling choices to produce an accurate fluid flow field to track the particulate phase through the cyclone in Chapter 5.

The effects of charge are then considered. Models of this phenomena have been developed for larger particles than those of interest in this work, which sets the scene for novel particle charge experiments to validate these models at small sizes in Chapter 3.

Finally, an alternative framework for describing the particulate phase is presented; an Eulerian framework. These Eulerian methods for particulate phases offer a computationally efficient way to model collisions which would not be feasible in Lagrangian models. The Eulerian method is derived from the governing Lagrangian equations such that any Eulerian model is consistent with the Lagrangian physics explored earlier. The Eulerian model is then validated in Chapter 4, where the cyclone turbulent scales are mimicked in an analytical flow field.

2.1 Separation Prediction Methods

From the basic operating principle of cyclones, the swirling fluid is used to separate out particles in the flow due to the larger centrifugal forces imparted on the particles from the carrier fluid. Knowledge of this fluid flow field in the cyclone is needed in order to calculate these particle trajectories and to estimate separation efficiency. The focus of the majority of the literature surrounding cyclones is on the effect of the geometry on the performance of the cyclone [72]. The two key performance metrics are the static pressure drop across the cyclone ΔP, and the separation efficiency η [73]. The separation efficiency is defined as [11]

$$\eta = 1 - \frac{m_{p,\text{out}}}{m_{p,\text{in}}}, \tag{2.1}$$

where $m_{p,\text{out}}$ and $m_{p,\text{in}}$ are the total mass of particles exiting and entering the cyclone respectively. Separation efficiencies are determined experimentally through the use of a particle counter both upstream and downstream of the cyclone [74]. Pressure drops are measured from the difference in pressures at tappings on the cyclone inlet and outlet pipes [75].

The fluid flow in the cyclone is complex due to the high levels of 3D swirl and the presence of turbulent structures [36]. Flow measurement techniques such as pitot-static tubes and hot-wire anemometry are intrusive and disturb the flow pattern [11]. The flow field has been experimentally visualised using techniques such as particle image velocimetry (PIV) and laser Doppler anemometry (LDA). Both involve injecting small tracer particles which have a very low Stokes number (Eq. 1.22) and are able to faithfully follow fluid streamlines into the flow. These two methods are considered non-intrusive and are assumed not to disturb the flow through measurement.

PIV involves imaging the positions with a high speed camera [76]. Liu *et al.* used PIV to measure the instantaneous cylindrical velocity components in the cylindrical, conical and cone tip regions of the cyclone [75]. The flow was measured at Reynolds numbers between $6.5 \times 10^4 \leq Re_D \leq 1.4 \times 10^5$, for a cyclone with a geometric swirl number of $Sw_g = 2.45$. The time-averaged flow pattern in the cyclone was found to resemble a Rankine vortex (discussed in Appendix B), with the velocity profile found to be independent of Reynolds number when normalised by the inlet velocity. The inner rigid body vortex velocity profile was independent of the axial location, whilst the outer irrotational vortex had a small increase in speed moving vertically down the axial direction. These measurements were taken in two perpendicular, vertical planes through the centre of the cyclone. A full, 3D picture of the cyclone flow field was unable to be determined experimentally.

LDA measures the scattering of light by the tracer particles and measuring their Doppler shift to provide the velocities at the particle locations. Hoekstra *et al.* used LDA to measure the fluid velocity in the conical section of a cyclone at $Re_D = 1.2 \times 10^5$, with swirl numbers of $1.79 \leq Sw_g \leq 3.15$ by varying the vortex finder diameter [3]. Measurements of the velocities in the vortex core lacked resolution due to the low particle concentrations in this region and measurements could only be taken in small volumes and not the complete domain. The PVC was found to dominate the core region and introduced pseudo-turbulent fluctuations in the velocity measurements. The stresses in the free-vortex region were found to be anisotropic and the velocity profile of the boundary layer was not visible due to the low near-wall resolution.

As is usual with complex systems such as the cyclone, simplified models have been developed to roughly estimate the performance characteristics of the system. For cyclones, the particle separation efficiency is the key performance metric which is ultimately determined by the particle trajectories through the turbulent, highly-swirling flow. These models commonly ignore the unsteadiness and turbulence present in the flow and idealise the swirling fluid as a Rankine vortex (Eq. B.1). The two most common modelling approaches towards cyclone separation efficiency are force-balance (equilibrium-orbit) and time-of-flight models [11].

The standard, most commonly used force-balance model was derived by Barth [77]. This model considers particles travelling on the edge of the vortex core, where the fluid velocity is greatest. For the Rankine vortex, this would be where $|\boldsymbol{r}| = R$. In the frame of reference of the particle, the two forces seen by the particle are a centrifugal force pushing the particle towards the outer walls and a drag force pulling the particle towards the centre of the cyclone. The magnitude of the centrifugal force is given by [11]

$$|\boldsymbol{F}_{cent}| = \frac{2m_p|\boldsymbol{u}_t^2|}{D_e}, \tag{2.2}$$

where $\boldsymbol{u}_t$ is the fluid tangential velocity (assumed equal to the particle tangential velocity). The Stokes drag (Eq. 1.20) pushing the particle towards the cyclone centre is provided by the radial component of the fluid velocity $\boldsymbol{u}_r$. Equating these two forces provides the particle diameter where both forces balance as

$$d_{p,50,Barth} = \sqrt{\frac{9\mu_f D_e|\boldsymbol{u}_r|}{\rho_p|\boldsymbol{u}_t^2|\,C_c}}. \tag{2.3}$$

This provides a simple estimate of the cut-diameter of a cyclone $d_{p,50}$, defined as the particle diameter which has a 50% chance of being separated [11]. The inclusion of the Cunningham slip correction factor (Eq. 1.25) makes this equation implicit, which requires solution through iteration. The main difficulty in applying this model is determining the tangential and radial components of the fluid velocity on the edges of the vortex core. By using CFD, these velocity components are able to be accurately determined and a cut-size can be estimated using Barth's model in Chapter 5.

Conversely, time-of-flight models compare the time taken by a particle to reach the cone tip to the time taken to impact the wall from the inlet [11]. This model assumes that the cyclone is cylindrical with no taper and near to the wall, the fluid velocity is equal to the inlet velocity. The time taken for a particle to swirl down to the cone tip is

$$t_{bottom} = \frac{\pi D N_s}{u_{in}}, \tag{2.4}$$

where N_s is the number of spirals down the cyclone the particle performs. For the radial motion towards the walls from the inlet, the particle is assumed to be moving at terminal velocity and there is no radial component to the fluid velocity. From equating forces as with Barth's model, a representative time to impact the wall by traversing the inlet width can be estimated as

$$t_{wall} = \frac{bD}{2\tau_p C_c u_{in}^2}, \tag{2.5}$$

where the Cunningham slip factor has been included again due to the small particle sizes. Equating the two times provides the classic time-of-flight estimate of the cut-off diameter as

$$d_{p,50,Rosin} = \sqrt{\frac{9b\mu_f}{\pi N_s u_{in} \rho_p C_c}}. \tag{2.6}$$

This model is implicit with the inclusion of the Cunningham slip correction factor. The difficulty in using this model is determining N_s, which is commonly estimated from experience [11]. The assumptions of this time-of-flight model, including the constant body diameter of the cyclone, are obviously incorrect. The estimation of the wall impact time by using the inlet width as the characteristic length is a major inaccuracy with the model, as is assuming the velocity profile close to the wall as a uniform inlet velocity. The assumptions made using the force-balance approach, whilst a great simplification of reality, are not as extreme as for the time-of-flight model and therefore Barth's model is preferable.

Altmeyer *et al.* compared the predictions of various cyclone separation efficiency models, including Barth's, to experimental data [78]. In their work, they amalgamated several models together to attempt to use the "best" estimate for a given flow regime. They found the cut-size was poorly predicted at low inlet velocities ($Re_D \leq 4 \times 10^4$) but improved with increased inlet velocity. The worst prediction of cut size overestimated $d_{p,50}$ by approximately a factor of 3. The forms of the separation efficiency curves obtained using various models (apart from Barth's which only calculates a cut-size) did not faithfully match the experimental form observed. Such simple separation efficiency models are therefore best suited as a rough initial guess for $d_{p,50}$ and not as a definitive estimation.

Once an estimate of $d_{p,50}$ is acquired, either by a model like Barth's (Eq. 2.3) or from experimental data, a functional form of the separation efficiency curve can be plotted. A curve known to fit many cyclone geometries well [11] is given by [79]

$$\eta(d_p) = \frac{1}{1 + \left(\frac{d_{p50}}{d_p}\right)^M}, \tag{2.7}$$

where M is commonly set to 6.4, however lower values of M have been found to better fit most cyclones [11]. The functional form of the separation efficiency curve from the cyclone is plotted in Figure 2.1, with the cut-off diameter estimated by linear interpolation of the experimental results and the exponent found to be $M \approx 6.3$ from least-squares regression. The functional form qualitatively fits the experimental results provided by Dyson very well, with the largest discrepancies occurring around the small $0.1\mu m$ particles. For these small sizes, the results are noisy and likely due to agglomeration of the small particles into larger structures which are able to be separated.

With experimental measurements unable to provide the full picture and simple separation efficiency models failing to provide accurate results, an approximate numerical solution is sought for instead. Finding a numerical solution of the fluid PDEs for a complex geometry such as a cyclone is commonly done by using the Finite Volume

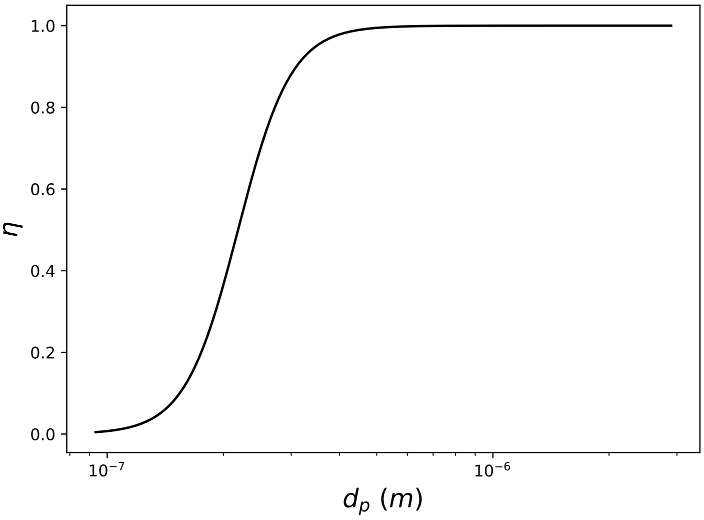

Figure 2.1: Experimental separation efficiency results for the cyclone using the fitted functional form. The R^2 value of the model fit to raw experimental data is 0.988 (to 3 significant figures).

Method (FVM) [32]. This involves splitting the domain into small control volumes and solving the integral form of the discretised PDEs over each control volume. As these equations are PDEs, boundary conditions (BCs) are required for a solution. The cyclone walls are given the no-slip condition. The most common choice of inlet/outlet boundary conditions are a velocity inlet and pressure outlet specification. The velocity (or mass flow rate) at the inlet is commonly known either *a priori* or from experiment and the outlet is specified at zero static pressure.

2.1.1 Turbulence Modelling

The LDA performed by Hoekstra *et al.* was used to assess the accuracy of turbulence models used in cyclone flow. They compared the mean experimental tangential and axial velocity components to predictions obtained from $k-\epsilon$, RNG $k-\epsilon$ and RSM [3]. The $k-\epsilon$ and RNG $k-\epsilon$ both predicted unrealistic velocity distributions; with the standard $k-\epsilon$ predicting a solid-body rotation only instead of the Rankine-like profile observed experimentally. The RNG $k-\epsilon$ provided a better experimental match, however it also predicted the predominantly solid-body rotation similar to the standard model for all but the largest swirl numbers explored. RSM provided the correct form of the velocity profile for all swirl numbers investigated, however the size of the vortex core and the magnitude of the maximum tangential velocities did not faithfully match experiment. In spite of this, many researchers have continued to use RSM to model the flow field in a cyclone [1, 23, 36, 35, 80, 81, 82, 83, 84].

Although less popular, LES has been applied to the fluid flow within a cyclone [85]. In recent years, it has begun to overtake RSM as the choice of turbulence model for cyclones. An extensive search of cyclone LES studies from the literature are therefore explored in order to inform the CFD in Chapter 5 and in particular, how to validate the simulation.

Shalaby *et al.* compared an LES with Smagorinksy SGS model with Lagrangian particle tracking to experiment. The normalised tangential and axial velocity profiles provided the correct form to experiment and the difference in pressure drop between the numerical model and experiment was around 2% [86]. This flow field was used to track particle trajectories and estimate a separation efficiency curve, which closely resembled the experimentally derived separation curve, with a small systematic error observed with the LES over predicting the separation efficiency. This systematic difference was more pronounced with decreasing particle diameter. These results were produced for a geometry where $Sw_g = 3.14$ at Reynolds numbers of $Re_D \approx 7 \times 10^5$. A laminar inlet velocity profile was assumed, even though the inlet Reynolds number was $Re_0 \approx 1.4 \times 10^5$.

The flow field in the cyclone has been shown to be insensitive to the inlet velocity profile by Derksen who performed LES with a Smagorinsky SGS model using the Lattice Boltzmann Method on the classical Stairmand cyclone geometry at $Re_D \approx 3.3 \times 10^4$ and $Sw_g = 6.04$ [87]. Derksen argued that this insensitivity is due to the region where the inlet flow merges with the cyclone flow. Here, the fluid rapidly forgets about the conditions in the upstream inlet pipe. Derksen also showed that the bin/hopper at the base of the cyclone must be included in the CFD model, otherwise the LES overestimates the intensity of the swirl in the vortex core. This study utilised 7.7×10^6 lattice cells, the largest from other cyclone work to the author's knowledge, however 45% of these cells were outside the main cyclone geometry.

Shukla *et al.* compared Lagrangian particle tracking in a RANS model with a RSM to an LES with a dynamic Smagorinksy SGS model. They found the prediction of both the velocity fluctuations and separation efficiency for small particles was poor using RSM and that LES provided good agreement with experiment [8]. They suggested that the improved accuracy for separation efficiency of small particles using LES was greatly influenced by the more accurate capture of the velocity fluctuations.

Misiulia *et al.* performed LES of a small cyclone with a diameter less than half of the cyclone considered in this work ($0.41D$) [88]. They used a dynamic Smagorinsky SGS model and looked at pressure drops in the range $1Pa \leq \Delta P \leq 25,000Pa$, with the largest pressure drops requiring the finest mesh of 3.65×10^6 cells. This is a pressure drop 4 times greater than the cyclone considered here. The time step for this largest ΔP case was $\Delta t = 5 \times 10^{-7}s$. The only validation performed was to compare pressure drops and flow rates to experiment. A fitted curve of pressure drop as a function of volumetric flow rate was obtained from experiment (with an R^2 value of 0.9974 indicating a very good fit) and the maximum discrepancy between the LES and experiment was below 10.3%, however this was deemed acceptable [88]. Discrepancies of this magnitude between numerical results and experiment have additionally been seen for pressure drop validation studies [89], although these results were using an RSM turbulence model.

It is also of note that a DNS of a small hydrocyclone was performed by Zhu *et al.* for $Sw_g = 2.93$ and $Re_D \approx 500, 1000, 2000$ in studies consisting of 2.6×10^6 cells [90, 91]. The Reynolds number of the inlet flow (which is smaller than Re_D) in these cases means that the inlet flow is laminar. The onset of unsteady flow was observed at $Re_D \approx 1000$ and the velocities in these cases were not high enough to produce an air core.

The DNS studies by Zhu *et al.* found vortical wall structures in their unsteady cases which they identified as Görtler vortices [91]. From Lagrangian tracking in these flows, they found that separation efficiency improved at higher Reynolds numbers from both a combination of higher tangential velocities and a larger number of Görtler vortices being generated. The Görtler vortices in the cyclone were visualised from plots of vorticity and vector plots of the fluid velocity along a 2D slice of the cyclone and were found to have the usual "mushroom-like" structure due to the pairs of counter-rotating vortices in this laminar boundary layer.

Wang *et al.* studied a supersonic DNS of a concave turbulent boundary layer where the Görtler instability contributed to the formation of large stream-wise roll structures in the boundary layer [92]. In a turbulent boundary layer, definitively identifying these structures as Görtler vortices is impossible [92], even in a simple geometry. The instabilities associated with the concave curvature were seen to reduce u^+ compared to the flat plate result beginning at $y^+ \approx 8$, with the size of the structures growing larger than the boundary layer thickness based on 99% of the free-stream velocity. The growth of structures arising from Görtler vortices has been observed in other work to grow up to twice the boundary layer thickness [40, 93]. The response of particles to these flow structures is discussed in Section 2.1.2.

Experimental data obtained for the cyclone flow field in the boundary layer by the walls is difficult to obtain. As shown by the DNS of Zhu *et al.*, CFD provides a useful research tool for determining this flow. Studies at representative turbulent Reynolds numbers for cyclones do not either state, nor appear to care for, the near-wall resolution. The focus for high-fidelity work is usually on capturing the vortex core and the PVC phenomena. By accurately capturing the vortex core, the pressure drop is able to be closely matched to experiment as the effect of the vortex core is an order of magnitude greater than the walls on the pressure drop [11]. The effect of near-wall turbulent structures on particles in cyclones at high speeds remains an open topic.

In addition to the choice of turbulence model, the geometry of the connective piping to the cyclone may affect the flow field within the cyclone. Schmidt *et al.* investigated the effect of the outlet pipe geometry on the cyclone swirl velocity using a hybrid turbulence model of LES for the vortex core region with RANS by the walls at $Re_D = 1 \times 10^6$ [94]. They found that short outlet pipes strongly under predicted the levels of swirl in the cyclone compared to experiment. A sufficiently long outlet pipe prevents this feedback, even with bends in the outlet geometry and reversed flow occurring at the outlet. Though they did not explicitly disclose the lengths of the outlet pipes used, figures in their paper can be used to estimate lengths of the short, medium and long outlets as $\approx 0.364H$, $\approx 0.727H$ and $\approx 1.455H$ respectively. This is a useful result to inform the cyclone CFD geometry in Chapter 5.

Validation of cyclone CFD in the literature commonly consists of comparing tangential velocity profiles across a horizontal section to experimental evidence [95, 84, 96, 97, 98, 99], with some accrediting "good fits" with discrepancies of approximately 10% [88, 100, 89, 96]. For the cyclone geometry provided by Dyson, there is no available experimental velocity profile data for this design. The general shape of the tangential velocity profile normalised by the inlet velocity can be compared to various differing geometries from the literature. This checks that the profile is as expected and agrees with known trends of cyclone performance as is common in the literature, such as both increased tangential velocities and thinner vortex cores as Swirl number is increased [3]. As experimental separation efficiency data has been provided, this can be used as a supplementary form of validation, provided the computational modelling of the particulate phase through the cyclone is accurate. This is explored in the following section.

2.1.2 Uncharged Particle Physics and Modelling

In this section, we consider the particles to be laden in a fully turbulent flow and neglect any physics relating to charge. The forces acting on the spherical particles are examined and models of these forces from literature are discussed. The simplifications of the particle equation of motion for the small, heavy particles considered here are presented.

In Section 1.3.3, assuming Stokes flow is valid, the fluid forces acting on a single spherical particle are given by the Maxey-Riley equation [42]. This includes effects of flow curvature from a non-uniform flow, following Esteban, this can be neglected for point particles and simplifies to the Basset, Boussinesq and Oseen (BBO) equation [43]

$$m_p \frac{d\boldsymbol{V}}{dt} = \boldsymbol{F}_{\text{drag}} + \boldsymbol{F}_{\text{pressure}} + \boldsymbol{F}_{\text{added}} + \boldsymbol{F}_{\text{Basset}} + \boldsymbol{F}_{\text{weight}}, \tag{2.8}$$

with $\boldsymbol{F}_{\text{drag}}$ given by Eq. 1.20. The pressure gradient force arises from local pressure gradients evaluated along the trajectory and is given by

$$\boldsymbol{F}_{\text{pressure}} = \frac{\pi}{6} d_p^3 \nabla P. \tag{2.9}$$

The added mass, or virtual mass force is due to the particle displacing fluid as it accelerates as

$$\boldsymbol{F}_{\text{added}} = \frac{\pi}{12} \rho_f d_p^3 \frac{d\boldsymbol{w}}{dt}, \tag{2.10}$$

where $\boldsymbol{w} = \boldsymbol{u} - \boldsymbol{V}$ is the relative velocity vector. The Basset force is the most complicated of these forces and arises due to the lagging development of the boundary layer around the particle to provide

$$\boldsymbol{F}_{\text{Basset}} = \frac{3}{2} d_p^2 \sqrt{\rho_f \mu_f \pi} \left(\int_0^t \frac{1}{\sqrt{t - t_\tau}} \frac{d\boldsymbol{w}}{dt_\tau} dt_\tau + \frac{\boldsymbol{w}_0}{\sqrt{t}} \right). \tag{2.11}$$

Finally the particle weight is given as

$$\boldsymbol{F}_{\text{weight}} = \frac{\pi}{6} \rho_p d_p^3 \boldsymbol{g}. \tag{2.12}$$

For large density ratios ($\frac{\rho_p}{\rho_f} >> 1$), all of these forces apart from Stokes drag and the particle weight are negligible from dimensional analysis in previous work by the author [101]. The particle weight can also be shown to be negligible in the high-speed cyclone flow by a simple comparison with drag. For a particle spinning around the top of the cyclone (of radius $R = \frac{D}{2}$) at the inlet speed $V_t \approx u_0$, the ratio of centripetal acceleration ($\frac{V_t^2}{R}$) to gravitational acceleration $|\boldsymbol{g}| = 9.81$ is approximately 1.175×10^5. It should also be added that this is a conservative estimate as particles traversing in the vortex core are expected to travel over twice as fast around a radius ≈ 5 times smaller.

An additional force on a small particle arises in shear flows known as the Saffman Lift force due to a difference in velocity seen across the particle [102]. This force has been known to accelerate particles away from walls in thin micro-capillary tubes in aerosol beams towards the centreline [103, 104]. This was generalised to 3D flows as [105]

$$F_{\text{saffman},i} = \frac{0.8647 \pi \rho_f d_p^2 \nu_f^{\frac{1}{2}} S_{ij}}{(S_{lk} S_{kl})^{\frac{1}{4}}} \left(u_j - V_j\right). \tag{2.13}$$

This force is usually considered small for particles larger than a micron, however it may be significant in the boundary layer of the cyclone where sharp velocity gradients are present. The particles of interest in this work are also sub-micron, for which the Saffman Lift force may have an appreciable result on particle trajectories. This effect of this force in a cyclone has been examined by Xiadong *et al.* who found that this force increased the separation efficiency for small particles and reduced their residence time in the cyclone [106]. Their work was performed using idealised analytical flow fields for the tangential, radial and axial velocity components with fluctuations superimposed to mimic the effect of turbulence. The differences with the inclusion of Saffman lift were small, however the flow field used does not contain any turbulent structures which may be present close to the walls and are expected to influence particle trajectories. The particle diameters examined ranged from $\approx 5\mu m$ to $250\mu m$ [106] which are much larger than those considered in this thesis, for which this force is expected to be more significant as the particle acceleration due to Saffman lift is proportional to $\frac{1}{d_p}$. The results were also not compared to any experimental evidence. The effects of the inclusion of this force for sub-micron particles in a high-speed cyclone may be significant, thus its effect will be determined in the high resolution CFD flow field in Chapter 5.

From Section 1.3.3, the ability for particles to follow fluid streamlines is governed by the Stokes number. Using the turbulent length scales of a flow, the Stokes number determines the response of the particle to these turbulent eddies. The distribution of particles in isotropic turbulence as a function of Stokes number has been measured by various authors, with particles observed computationally to collect around eddies in a process known as preferential accumulation [107, 108, 109]. These simulations involved a fully periodic fluid domain discretised on a uniform mesh. A pseudospectral method was employed to simulate the isotropic turbulence and point-particles were tracked in a Lagrangian frame of reference assuming low Re_p [110]. The fluid velocity at the particle location is interpolated from neighbouring points [107]. The simulations were one-way coupled, in which the fluid affects the particles through the drag force and the effects of particles on the fluid are considered negligible. Particle-particle interactions are also ignored [109]. This effect is most pronounced for a Stokes number of $Stk \approx 1$ [110]. These particles are seen to be centrifuged out of regions of locally high vorticity and collect in regions of locally high strain.

From Section 2.1.1, it is expected that turbulent structures such as Görtler vortices are present in the cyclone boundary layer. The particle response to these structures is characterised by the Stokes number. In the cyclone DNS by Zhu *et al.*, the separation efficiency was seen to increase with increasing numbers of Görtler vortices [91]. Large Stokes number particles were insensitive to these structures and were separated as usual. Fine particles with small Stokes numbers can be captured by the flow and transported into the core of the Görtler vortices. As these unsteady structures move from the wall towards the central cyclone axis, they transport these particles away from the wall. In their DNS, which had no air core, the axial velocity by the cone tip is directed downwards and so these particles were able to leave the cyclone into the bin. At higher Re where a fully developed PVC exists, this argument may not be valid. The Görtler vortices would still be expected to aid in the transport of small particles away from the walls, however this effect on their separation efficiency is unknown.

The transport of particles from regions of high to low turbulent intensity is known as turbophoresis [111]. This is observed in anisotropic turbulence and results in increased wall deposition of particles. This effect is due to particles obtaining a large fluctuating velocity component in a region of high turbulent intensity, which allows the particle to enter a region where the turbulent intensity is not high enough to supply the particle with sufficient momentum such that it can return to its original position [112]. From the experimental evidence provided in Figure 1.2, the wall migration of particles in the turbulent cyclone flow is expected to contribute to the visible particles bands.

Having discussed the physics of small, heavy particles in turbulent flows, we now discuss how these are modelled computationally. The motion of small particles in turbulent flows is commonly modelled by assuming Stokes drag to be the only force on the particles and for the particles to be one-way coupled. This requires numerically integrating Eqs. 2.79 and 1.27 together to provide an estimate of the particle trajectory, given an initial condition for velocity and position. A myriad of numerical methods exist to solve such a problem. In tracking particles in isotropic turbulence, high-order schemes are in common use such as a third-order Runge-Kutta scheme [110, 113]. In particle-laden cyclone flow, many authors have not stated how they have integrated the particle trajectories [35, 72, 4, 114, 115]. The choice of time step for the integration of particle trajectories and the number of particles needed to be tracked for statistically stationary results in a cyclone is missing from the literature.

In tracking Lagrangian particles in a CFD flow field, the particles can only respond to turbulent structures which are resolved in the numerical model. In RANS models all the turbulent structures are time-averaged away and in LES only the larger scales are present in the flow. The effects of the unresolved scales on the particles is commonly ignored [35, 80]. Simple models have been produced to mimic the effects of the unresolved scales on the particles in a stochastic manner by adding a random contribution to the fluid velocity seen by the particle. One such model is the discrete random walk (DRW) model [31]. For LES, time and velocity scales can be estimated using the mixing length L_s (Eq. F.10) and the resolved strain rate magnitude as

$$t_L \approx \frac{1}{\hat{S}_{mag}}, \tag{2.14}$$

$$\sqrt{\overline{u'^2}} \approx \frac{L_s}{t_L}. \tag{2.15}$$

These are representative of the largest unresolved eddies in the flow. The fluctuating velocity components are computed by [31]

$$u^{'} = \zeta\sqrt{\overline{u'^2}}, \tag{2.16}$$

where ζ is a normally distributed random variable. The velocity fluctuation is assumed to be the same in all directions. The length of time for which this fluctuating velocity component is active is given by

$$t_{\mathrm{eddy}} = \min\left(\tau_e, t_{\mathrm{cross}}\right), \tag{2.17}$$

where τ_e is the eddy lifetime and t_{cross} is an estimate of the eddy crossing time given by

$$t_{cross} = -\tau_p \ln\left(1 - \left(\frac{L_e}{\tau_p|\boldsymbol{u}-\boldsymbol{v}|}\right)\right). \tag{2.18}$$

There are two common methods to calculate τ_e: the first keeps it constant as [31]

$$\tau_e = 2t_L, \tag{2.19}$$

with the second option varying it randomly as

$$\tau_e = -t_L \ln(\Xi), \tag{2.20}$$

where Ξ is a uniform random number drawn between 0 and 1. This model has been applied to particles in cyclones but validation and assessment of the accuracy of the model in this case has not been determined [31, 116].

From Figure 1.6, Brownian motion may be significant for small $0.1\mu m$ particles. The effects of Brownian motion can be computer modelled as a white noise process as [105]

$$\boldsymbol{F}_{\mathrm{Brownian}} = \boldsymbol{\zeta}\sqrt{\frac{2m_p k_B T_f}{\tau_p \Delta t_p}}, \tag{2.21}$$

with $\boldsymbol{\zeta}$ representing a random number vector where $\boldsymbol{\zeta} \sim N(0,1)$ and Δt_p is the particle time step.

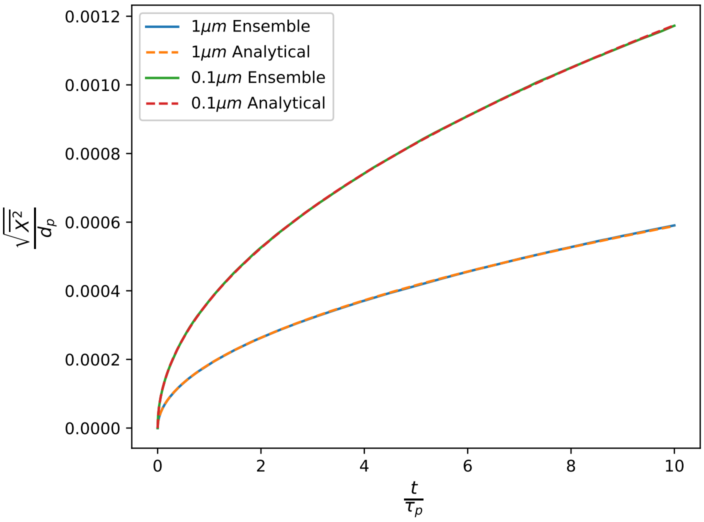

Figure 2.2: Ensemble-averaged RMS 1D particle displacements due to the Brownian motion model (Eq. 2.21) acting on fluid tracers for $1\mu m$ and $0.1\mu m$ particles with $T_f = 300K$.

To check that this model provides the correct dispersive behaviour, 1×10^5 particles were tracked for 1000 time steps, where $\Delta t = \frac{\tau_p}{100}$ and the ensemble average of the particle displacements at each time step were compared to the solution predicted by Eq. 1.31. This was performed by initialising a stationary particle at the origin for each realisation. An acceleration due to the Brownian force (Eq. 2.21) is then calculated and then multiplied by the time step. This is added to the previous particle velocity. The new velocity is then multiplied by the time step and added to the previous position to provide the new particle position, in a similar way to a first-order Euler integration scheme [117]. Figure 2.2 shows this for both the largest and smallest particles relevant to this work and excellent agreement with the theoretical prediction from Eq. 1.31 is attained. Both the computer model and theory of Brownian motion predicts larger mean square displacements relative to the particle diameter for smaller particles as expected.

In wall-bounded flows, an assumption for the particle-wall interaction must be made. Particles may assume to be trapped on impact with a wall and be counted as separated or to reflect off the wall either elastically or inelastically. Bogodage and Leung have discussed the choices in the literature and found trapped boundary conditions for both the cyclone walls and bin over-predict the separation efficiency but this choice remains unclear [72].

The particles are commonly tracked in a frozen fluid flow field; representing a single fluid realisation in time. Tracking the particles with an unsteady flow field becomes significantly more expensive and is commonly not performed. Particles are injected on the inlet plane of the CFD domain uniformly spaced [72], with some authors found not to disclose the number of particles tracked [81].

2.1.3 Separation Prediction Methods Conclusion

The cyclone flow field is complex, 3D, turbulent, highly-swirling and difficult to measure experimentally. Various simplified models for the cyclone cut size exist in the literature, however the equilibrium orbit model from Barth has the most reasonable assumptions and can be used alongside a functional relationship to provide rough estimates of separation efficiency, if accurate fluid velocities in the vortex core are known.

To more accurately determine the cyclone flow field, CFD with an appropriate turbulence model can be employed. Simple RANS eddy-viscosity models are unable to appropriately capture the swirling flow and RSM is the most commonly used as it is able to capture the correct form of the velocity profile for a wide range of swirl numbers. Given a computed CFD flow field, Lagrangian particles can be tracked through the domain to obtain more accurate estimates of separation efficiency compared to simple models and the trajectories can provide useful insight into the separation process. For accurate particle tracking, the mean flow field along with the instantaneous turbulent fluctuations also need to be accurate. LES provides a more realistic flow field which includes the larger turbulent scales being directly computed compared to RSM which poorly captures the fluctuations in the fluid velocity field.

From the large density ratio, sub-micron diameter and small particle Reynolds numbers hypothesised, Stokes drag with Cunningham slip correction is expected to be the dominant force acting on the dilute particulate phase. The effect of Saffman lift, which has been shown to be appreciable for sub-micron particles in shear flows, requires further investigation. Simple stochastic models of both Brownian motion and the effects due to the unresolved turbulent scales exist and exhibit the correct behaviour. The significance of these forces on the separation efficiency of a small, high-speed cyclone are investigated in Chapter 5.

2.2 Particle Charging

The literature surrounding particle tribocharging is uncertain and conflicting [58, 14]. Many authors report opposite results for similar experimental set-ups and there exist different theories as to how charge is transferred on contact. Key charge measurements from the literature are presented in Section 2.2.1 to highlight important phenomena present and to provide a first insight into the scales of the problem. The literature review concludes with presenting the evolution of key models created to model tribocharging and to determine their suitability to model particle tribocharging in small, high-speed cyclones.

2.2.1 Experimental Data

Section 1.4 looked at the fundamental theory surrounding tribocharging which centres around the transfer of electrons during contact between two materials. This chapter looks at the measurements made on tribocharging which gives insight into the physics of charge transfer; these being the factors that affect the rate of charge transfer, whether a maximum charge level can exist on a material surface and predicting the polarity after contact. For particle charging in a cyclone, this information is needed for sub-micron insulating particles to enable a suitable tribocharging model to be determined.

A study of small 0.25 to $15\mu m$ diameter particles statically charging from dispersing into a cloud was performed by Kunkel, who reported that homogeneous dusts had no net resulting charge [118]. This means that if this charge distribution is measured in bulk, it will be incorrectly concluded that no charge is present. This is useful information for tribocharging experiments in Chapter 3. Kunkel also found no correlation between size and polarity and concluded that the charge transfer from two particles occurs during separation of contact [118]. Charge transfer by separation has a clear link with frictional charging; more aggressive friction results in a greater charge transfer. Later work by Matsuyama *et al.* (in Section 2.2.4) further highlights the difference in charge transfer during separation, indicating that the entire process from contact to separation is complex.

Davies showed that charge density produced on a dielectric surface by contact with a metal is dependent on the metal work function [119]. From this he produced a triboelectric series of some insulating materials based on their work functions measured experimentally. This list was in accordance with previous triboelectric series and the only insulator work function measured previously was in reasonable agreement with this [119]. This work evidenced that electrons are the charge carriers in insulators. By being ordered into a triboelectric series by work function, the charging characteristics of insulators could be predicted using models originally designed for metal-metal contacts.

Lowell investigated the contact electrification of metals and found strong agreement with representing the contact as a capacitor circuit and that the charge transferred is determined by the equalisation of Fermi levels on contact [120]. Lowell looked at polymer-metal charging from different contacts and predicted an equilibrium charge dependent on the work function of the metal [121]. This equilibrium charge is equivalent to the saturation of charge on the plates of a capacitor in an electrical circuit. This suggests that knowledge of the equilibrium charge, along with the speed of charging can completely define the charging process for a contact. Lowell also found that the transfer of material on contact is not the primary mechanism for tribocharging [122]; further evidencing the validity of electron transfer.

To understand the tribocharging behaviour of insulators, single particle impacts of a polymer on a metal plate were performed in detail by Matsuyama *et al.* From these experiments, Matsuyama formally introduced a condenser model of particle charging [123] and then extended the model to create the "charge-relaxation" model [124] (both covered in Section 2.2.4), a simple model of the experiment is shown in Figure 2.3.

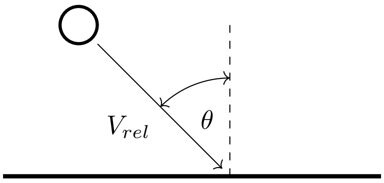

Figure 2.3: Diagram of Matsuyama's experiment of a single particle impacting a metal plate with relative speed V_{rel} and angle θ. The dashed line is normal to the metal plate.

The experiment consisted of firing particles out of a pneumatic gun, measuring the initial charge of the particle using a Faraday cage pre-impact and then measuring the charge transferred to the metal plate during impact using an electrometer connected to the plate. Although it was not possible to control the initial charge of the particles, it was simple to change the angle of the plate relative to the particle. The initial charge on the

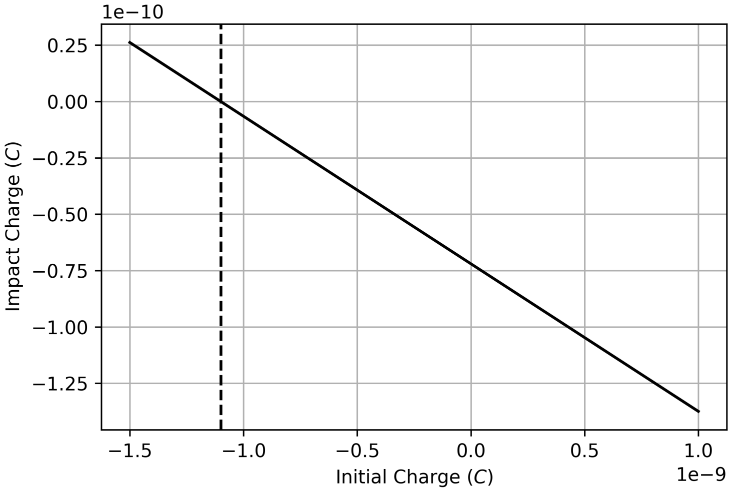

Figure 2.4: Example data from Matsuyama's single impact experiments [123] for Teflon particles striking an Aluminium plate. The dashed vertical line represents the equilibrium charge ($Q_e \approx -110pC$).

polymer particles varied from around $-1000pC$ to $500pC$ for both materials considered (Teflon and Nylon-66), the impact speed V_{rel} varied between $7-18m/s$ and the angle was varied between $0-60°$ [123]. The results showed that the impact charge varied linearly to the initial charge of the particle, with the x-intercept (Q_e) indicating the equilibrium charge where no charge transfer takes place with the metal plate. This trend is shown graphically in Figure 2.4.

The impact speed and angle are related to the normal speed by

$$V_n = V_{rel}\cos(\theta). \tag{2.22}$$

Changing the normal impact speed (and therefore θ or V_{rel}) has no effect on the equilibrium charge [123]. This suggests that material properties govern the equilibrium charge rather than the conditions at contact. These were originally performed using particles with a diameter of a few millimetres and were later repeated with particles as small as $100\mu m$ which are several orders of magnitude larger than the dust considered in this work.

Tribocharging has also been studied in pharmaceutical fields by authors such as Ghadiri who has also collaborated with Matsuyama and repeated the impact charging experiments [125]. Pharmaceutical powders are very fine and prone to tribocharging which can affect the quality of the end product. As these particles are so small, only simple experiments such as shaking (Figure 2.5) have been performed [126]. These experiments have shown that the saturation/equilibrium charge is independent of shaking frequency [126] and Bi *et al.* showed that particle size affects the charge build-up [127]. These results, which are obtained for particles smaller than the single particle experiments, also suggest that the equilibrium charge of a particle is independent of the conditions of impact. Impact conditions only affect the speed of charging.

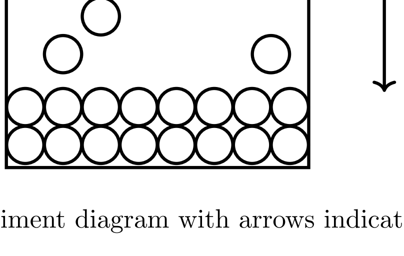

Figure 2.5: Powder shaking experiment diagram with arrows indicating the direction of displacement.

The effect of humidity on tribocharging has also been examined. It has been found that high humidity levels $> 80\%$ result in particles unable to hold their charge on the surface as they discharge to the water in the air [128]. Lower humidity levels allowed particles to hold a greater amount of charge and this regime change depended on the material along with the polarity of the resultant charge [128]. This gives an estimate of the maximum allowable humidity level for the experiments in Chapter 3.

Alois looked at tribocharging in aerosolised oxides with diameters between around $0.1\mu m$ and $40\mu m$, covering the range considered in this report [129]. In this work a model was proposed based on electron transfer by using the absolute generalised relative electronegativity. This quantity is related to the electronegativity and was permissible to be used here as the chemical composition of the contacting surfaces was known *a priori*. The experimental set-up consisted of rapidly decompressing a chamber at ambient pressure into a near vacuum through an injector tube, which the particles will collide with and subsequently tribocharge. The charge exchanged between the injector and particles was measured by integrating the voltage between the injector and vacuum housing over time and dividing by the resistance of the circuit. The results found that the charge/mass ratio of particles had two regimes: a $\frac{1}{r_p}$ dependence was found for particle diameters larger than $1.5\mu m$ and a negative linear trend for particles smaller than $1.5\mu m$. This regime transition sits within the range of test dusts considered in this report and the smaller particle trend was explained by agglomeration.

The results from Alois *et al.* also found that results were very consistent at low humidities and varied considerably at high humidities. This was explained by the adhered water forming bridges at the contact points, significantly increasing the effective contact area and the conditions at the surface [129]. The effects of humidity will be assumed to be negligible in any model considered.

The size ranges currently studied in literature for particle tribocharging are shown in Figure 2.6. There exists a large gap in the knowledge as particles become smaller than $\approx 50\mu m$. The fundamental physics needs to be verified at the scales pertinent to this work. This requires experiments to be performed in Chapter 3. From the literature, it is clear that single particle experiments will not be possible for the desired size range and that experiments will have to be performed on many particles; with the underlying physics of single-particle charging inferred from these results.

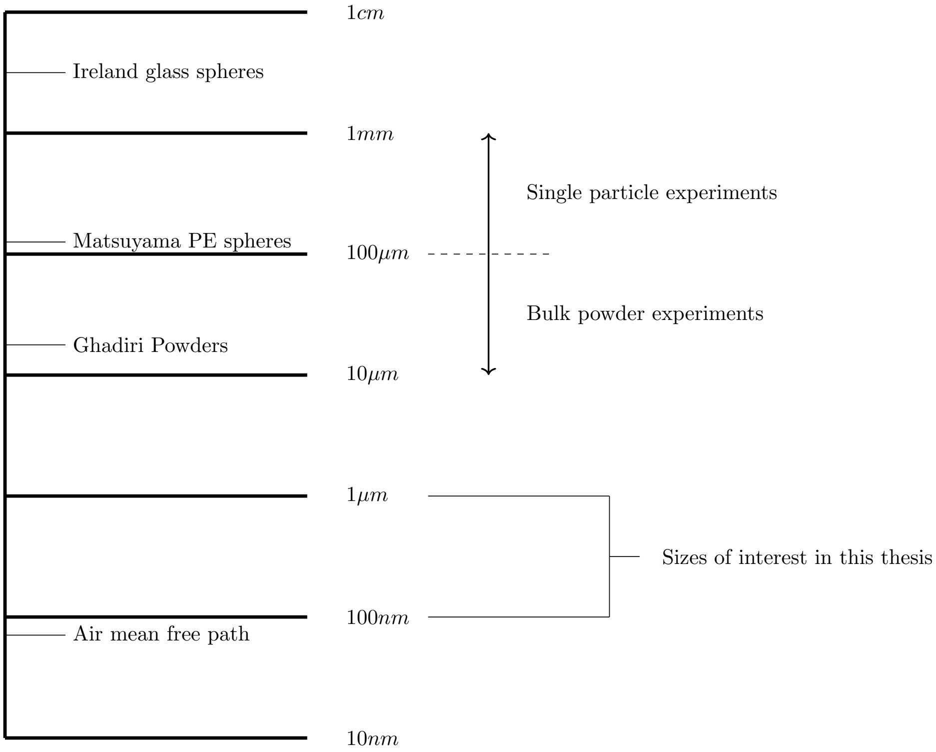

Figure 2.6: Diagram of different sizes considered in the most pertinent literature for this report.

This section has shown the conflicting results from different authors surrounding polarity. The construction of a triboelectric series has been shown to be an effective way to determine the resultant polarity when two different materials contact. There exists a maximum charge level that a particle can hold which is influenced by humidity. Low humidity levels do not significantly change the maximum charge (saturation charge) attainable by a particle, however high levels of humidity cause the particle to discharge to the adhered water on the surface. Capacitor models for charge transfer on contact have also been shown to accurately capture the charging process for large particles, however the physics has not been verified for sub-micron particles. These findings will be used to access the suitability of tribocharging models for small particles.

2.2.2 Aerodynamic Focusing of Sub-Micron Particles

Single particle experiments, such as the plate-impact set-up by Matsuyama *et al.* have provided an excellent way of characterising the charging properties of very large particles. Controlling single particles in the range of diameters $0.1\mu \leq d_p \leq 1\mu m$ for the same set of experiments is too difficult. Tribocharging experiments in this size range have instead been performed on bulk powders, with little control over the conditions of particle impact. The experiments performed by Alois *et al.*, performed on the particle sizes of interest, provided some level of control over the small particles by pulling them into a vacuum chamber.

Vacuums have been used by Israel and Friedlander to produce well-defined beams of sub-micron particles known as aerosol beams. An aerosol beam is formed by expanding a high-pressure reservoir through a converging nozzle in a low pressure chamber [130]. The particles have more inertia than the carrier fluid and are therefore unable to follow the fluid streamlines which results in the particles maintaining their rectilinear motion. Aerosol beams are used to inject particles into mass spectrometers [45] and particle counting devices and are therefore ideal for controlling the motion of small particles. The mass flow rate through the choked nozzle for a given fluid is a function of only the nozzle area and stagnation values (Eq. 2.23). For air ($R_a = 287 Jkg^{-1}K^{-1}$, $\gamma = 1.4$) at standard conditions ($T_0 = 293.15K$, $P_0 = 101235Pa$) the pressure ratio $\frac{\Delta P}{P_0}$ needed for choked flow is 0.528 [41], where ΔP is the pressure drop across the nozzle. If the back pressure is reduced further, the beam velocity is unaffected and this can create a well-defined nozzle velocity for a beam that is not susceptible to pressure variations. The resistance to pressure fluctuations is especially useful when using vacuum pumps and airlines as there will always be inherent unsteadiness by the air/vacuum supplies and the choked nozzle provides a near-constant output. Assuming isentropic flow, the choked mass flow rate is given by [131]

$$\dot{m}^* = \frac{P_0}{\sqrt{R_a T_0}} A^* \sqrt{\gamma} \left(\frac{\gamma + 1}{2} \right)^{-\frac{\gamma+1}{2(\gamma-1)}}, \tag{2.23}$$

where A^* is the nozzle area at the throat. The mass flow rate as a function of pressure drop is provided in Figure 2.7.

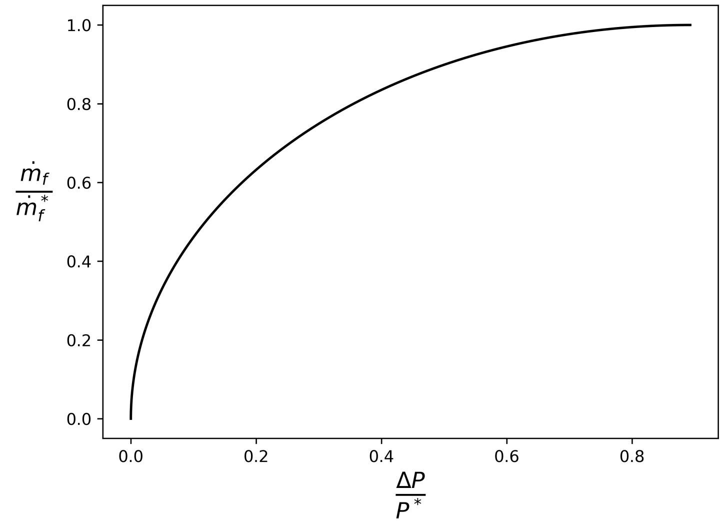

Figure 2.7: Fluid mass flow rate as a function of pressure drop, normalised by their respective choked conditions for air at standard conditions.

The velocity of the aerosol beam downstream was determined theoretically by assuming free molecular flow in the stagnant low pressure chamber [132]. Following Dahneke and Friedlander, the equation of motion in 1D for a spherical particle decelerating under drag is [132]

$$m_p \frac{dV}{dt} == \frac{\pi}{8} \rho_f d_p^2 V^2 C_D. \tag{2.24}$$

By defining the dimensionless parameters

$$V_s = \frac{V}{\sqrt{\frac{2R_a T_f}{M_w}}}, \tag{2.25}$$

$$x_s = -\frac{x}{\frac{4}{3}\frac{\rho_p}{\rho_f} d_p}, \tag{2.26}$$

where M_w is the molecular weight of the gas, a dimensionless equation of particle motion can be derived as

$$\frac{dV_s}{dx_s} = V_s C_D\left(V_s\right). \tag{2.27}$$

The drag coefficient in terms of this dimensionless velocity is given by [133]

$$C_D(V_s) = \frac{e^{-V_s^2}}{\sqrt{\pi} V_s^3}\left(2V_s^2 + 1\right) + \frac{4V_s^4 + 4V_s^2 - 1}{2V_s^4}\operatorname{erf}(V_s) + \frac{2\sqrt{\pi}}{3V_s} f_s, \tag{2.28}$$

where f_s is a scattering coefficient with $0 \leq f_s \leq 1$ and erf is the error function defined as [134]

$$\operatorname{erf}(V_s) = \frac{2}{\pi}\int_0^{V_s} e^{-t^2} dt. \tag{2.29}$$

This theoretical model predicts that particles will have a well-defined stop distance given by [132]

$$x_{stop} = \frac{4}{3}\frac{\rho_p}{\rho_f} d_p x_{s,stop}, \tag{2.30}$$

where $x_{s,stop}$ is the dimensionless stop distance obtained by integrating Eq. 2.27 from the boundary condition $V_s(0) = 0$. For monodisperse aerosol beams Dahneke and Friedlander showed agreement of the theoretical model with experiment, with the beams exhibiting a well-defined stop distance which was proportional to the particle diameter. For polydisperse beams, the agreement with experiment was only approximate, possibly due to collisions between various particle sizes in the beam [132]. Finally, their results indicated that $f_s = 0.4$ gave the best fit to experiment.

An aerosol beam is suitable to focus sub-micron particles experimentally. This set-up is able to allow analogous experiments to the plate-impact set-up by Matsyuama *et al.*, with a beam of particles impacting the plate instead of a single particle. The deformation due to impact with the plate can be modelled using a Hertzian contact model.

2.2.3 Hertzian Contact Model

Various models for particle tribocharging have been suggested in the literature which have been based on experimental evidence. These models all assume that the area formed when two materials come into contact is known. A common way of modelling the contact of particles is using Hertzian theory which allows the contact area and contact time to be computed. This theory makes the following assumptions [135]:

- The surfaces of both spheres are smooth, continuous and frictionless
- The contact area is small compared to the size of the bodies
- Each solid can be considered to behave as an elastic half-space by the contact zone
- The gap h between the undeformed surfaces can be approximated by an expression of the form $h = Ax^2 + By^2$

The first assumption enables a smooth solution where energy is conserved. The second assumption means that small strains can be assumed and therefore the linear stress-strain relations can be applied. The third assumption means that the deformation occurs at the contact region for both bodies and the fourth assumption requires parabolic surface profiles. An illustration of Hertzian contact is shown in Figure 2.8.

The contact force between two materials is given by [136]

$$F_{\text{hertz}} = \frac{4Y_c r_a^3}{3r}, \tag{2.31}$$

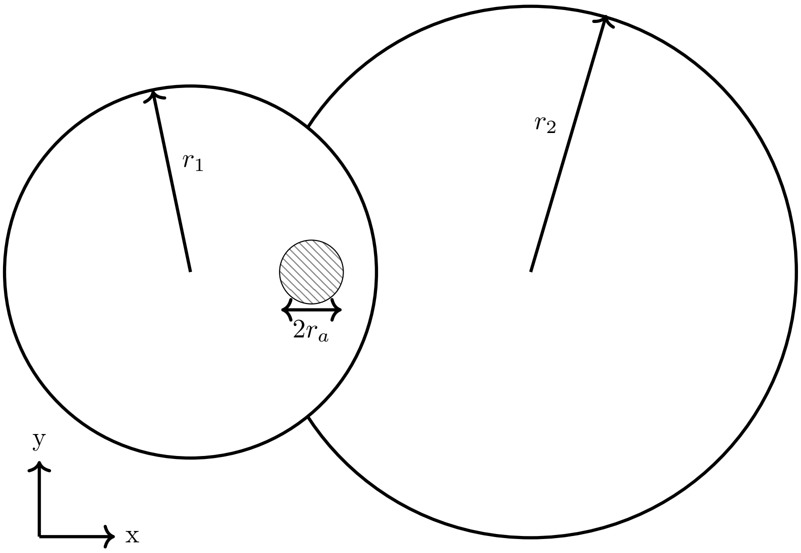

Figure 2.8: Diagram of Hertzian contact between two spheres or radius r_1 and r_2 producing a contact area of radius r_a.

Parameter	Value
Diameter	$0.1\mu m$
Density	$2650kg/m^3$
Young's modulus	$7.13 \times 10^{10}Pa$
Poisson's ratio	0.17
Relative impact velocity	$37m/s$

Table 2.1: Simulation parameters used to produce the dimensionless plot in Figure 2.9. The particle properties are from the silica test dust introduced in Section 1.3.3.

where the reduced radius of curvature can be calculated by [135]

$$\frac{1}{r} = \frac{1}{r_1} + \frac{1}{r_2}, \tag{2.32}$$

where r_1 and r_2 are the radii of particles 1 and 2 respectively. The contact modulus is calculated using [135]

$$\frac{1}{Y_c} = \frac{1-\chi_1^2}{Y_1} + \frac{1-\chi_2^2}{Y_2}, \tag{2.33}$$

where Y is the Young's modulus, χ is Poisson's ratio and the subscripts 1 and 2 refer to particles 1 and 2 respectively. The contact radius is related to the reduced radius of curvature and penetration d by [136]

$$r_a = \sqrt{rd}. \tag{2.34}$$

This simple model allows the deformation of two objects contacting to be calculated from the radius, Young's modulus, Poisson ratio and impact force only. For a spherical particle impacting a flat plate, the reduced radius of curvature is equal to the particle radius. This is attractive from the point of view of a discrete element method (DEM) code which has been implemented to calculate contact areas. It is important to note that during the contact process, the contact area varies. To fully resolve the contact process for sub-micron particles, very small time steps are needed. The mean or maximum contact area during an impact is therefore more suitable to use for a charge model; especially one that is to be used in a CFD code. The variation of non-dimensional contact area with normalised contact time is shown in Figure 2.9 with the simulation parameters given in Table 2.1, representing a $0.1\mu m$ particle impacting with the cyclone wall at the inlet velocity.

To capture this contact area variation for micron-sized particles is not computationally feasible due to the incredibly small size of time scale needed to resolve such behaviour and the large number of particles to calculate this for. Instead, analytical expressions for the maximum contact area and contact time can be used. For two like spherical particles impacting at a relative speed V_{rel}, the maximum contact area is given by [137]

$$A_{c,max} = \pi r_p \left(\frac{15m_p}{64Y_c\sqrt{\frac{r_p}{2}}} \right)^{\frac{2}{5}} V_{rel}^{\frac{4}{5}}. \tag{2.35}$$

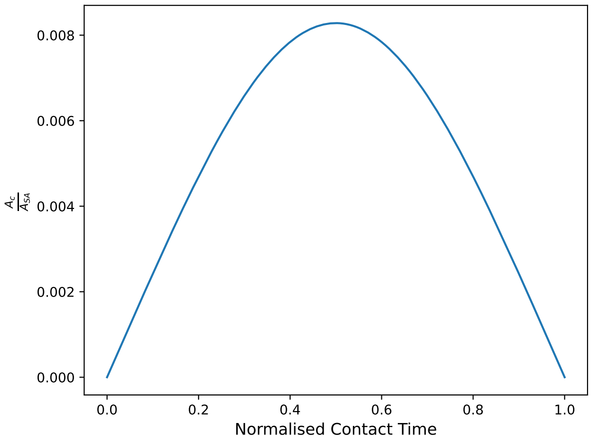

Figure 2.9: Non-dimensional contact area (contact area over particle surface area) as a function of contact time normalised with the total contact time ($\approx 1.32 \times 10^{-10}s$) from the developed code.

The contact time is given by [138]

$$t_c = I_{int} \left(\frac{5\sqrt{2}\pi\rho_p}{4} \frac{1-\chi^2}{Y} \right)^{\frac{2}{5}} \frac{d_p}{V_{rel}^{\frac{1}{5}}}, \tag{2.36}$$

where I_{int} is the value of the following integral which must be evaluated numerically

$$I_{int} = \int_0^1 \frac{dx}{\sqrt{1-x^{\frac{5}{2}}}} \approx 1.47. \tag{2.37}$$

For a sphere impacting an infinite plate, the maximum contact area and contact time are [139]

$$A_{c,max} = 1.36 Y_c^{\frac{2}{5}} \rho_p^{\frac{2}{5}} d_p^2 V_{rel}^{\frac{4}{5}}, \tag{2.38}$$

$$t_c = 2.54 Y_c^{\frac{2}{5}} \rho_p^{\frac{2}{5}} d_p V_{rel}^{-\frac{1}{5}}, \tag{2.39}$$

respectively.

Hertzian contact theory has been used extensively in the literature to model the collision conditions for use in a tribocharging model for experiments using pharmaceutical powders [140] and particles impacting a plate [12, 139]. For pharmaceutical powders, the individual micron-scale crystals did not have spherical shapes, however at the localised site of impact, Hertzian theory was found to still be valid as the situation resembled a sphere impacting a large plate under a scanning electron microscope [140]. This provides confidence that the Hertzian model can be applied to non-perfect spherical particles such as those expected to challenge a cyclone.

In applying Hertzian theory to sub-micron particles impacting a metal plate using an aerosol beam as in the experiments performed in Chapter 3, the particles will not be perfect spheres. This has been shown to not be a problem from the work on pharmaceutical powders in the literature. However, for particles smaller than the wavelength of light (and therefore invisible to the human eye), it may be difficult to verify whether these particles actually impact the plate, or whether they follow the fluid streamlines around the plate and avoiding impaction. When calculating the particles stop distance, Dahneke and Friedlander were able to observe the impact of sub-micron particles with a collection plate in their aerosol beam experiments [132] from Section 2.2.2 due to the large numbers of particles impacting and depositing on the plate visually. To ensure that impact is occurring in the experiments in Chapter 3, the plate must be examined post-test and checked for particle deposits.

2.2.4 Matsuyama's Plate Model

A range of particle charge models are present in the literature. These originally modelled charge exchange between large metal particles with small polymer particles [141] and have since been extended to insulating particles. In Matsuyama et al's work on single particle impacts in Section 2.2.1, they likened the particle-plate charging to a capacitor charging circuit (capacitor model - Figure 1.7). The contact potential difference V_0 is caused by the difference in work functions between the particle and plate [123] and this is equal to the voltage across the analogous capacitor (Eq. 1.42) at equilibrium to give

$$V_0 = \frac{\phi_m - \phi_p}{e} = \frac{Q_e}{C}. \tag{2.40}$$

Here ϕ_m and ϕ_p are the work functions of the metal plate and polymer respectively, e is the elementary charge, Q_e is the equilibrium charge and C is the capacitance of the capacitor circuit. From the equilibrium charge and the known work function of the metal plate, the effective work functions (from Davies' earlier work [119]) of different polymers can be calculated. The materials can be readily ordered by work function to produce a triboelectric series and therefore links observed charges to electron energy levels and the resultant polarity after contact. The equilibrium charges were also found to depend on the work function of the polymer only, with no dependence on the work function of the metal [142].

Matsuyama and Yamamoto then extended the model to include what they termed "charge relaxation" to form a more complete model of particle tribocharging [124]. The "relaxation" refers to electric gaseous discharge to the atmosphere and is an artefact of the separation process. For small distances ($d < 0.1mm$ [61]) electrical discharge can occur if the voltage between the plates exceeds $300V$. During charge separation between two particles, they physically separate and some of the charge on the particles is discharged to the surrounding air, leaving the observed post-impact charge [124]. This process was then determined to be the main mechanism responsible for determining the remaining charge post-impact [143].

Matsuyama *et al.* then extended the experiments from $d_p \approx 1mm$ to $d_p \approx 100\mu m$ [18]. They found their charge relaxation model to still be appropriate, however they claim there was greater scatter in their data from the uneven charge distribution across the surface of the particles at these smaller sizes.

The charge relaxation model gives key insight into the fundamental mechanisms at work which have been linked to the underlying physics of electron energy levels, work function and air breakdown. The model is very specific to the experimental set-up, however it is a stepping stone to more advanced models and therefore the underlying theory and methods will be considered for the proposed model. It should be noted that these sizes are still around 2-3 orders of magnitude larger than the particles considered in this work. The validity of this model with respect to this project would need to be proved and experimental results are given in Chapter 3.

2.2.5 Ireland's Model

Following on from Matsuyama's work on charge relaxation, Peter M. Ireland commented on their model, acknowledging that it provides a "good description" of their experiment [144]. Ireland then proceeded to focus less on the microscopic aspects of tribocharging and more on the macroscopic side of changing contact patterns between surfaces [145]. From this work he looked at the simplest case of particle charging between two materials using the well-established capacitor model [145] [146] (Figure 1.7). He related the charge transfer (current) to the overall potential difference between the two surfaces expressed as [147]

$$\frac{dQ}{dt} = \frac{V_0 - V_c}{R_0}, \tag{2.41}$$

where Q is the charge transferred, t is time, V_0 is the driving potential difference from the difference in work functions between the two materials, V_c is the potential difference associated with the charge already present on the surfaces and R_0 is the resistance of the circuit. The capacitance of the capacitor in Eq. 1.42 can be rewritten in terms of the contact area A_c and the surface charge density σ as [147]

$$C = \frac{\sigma A_c}{V_c}. \tag{2.42}$$

Combining Eqs. 2.41 and 2.42 results in

$$\frac{dQ}{dt} = \frac{A_c}{R_0 C}\left(\sigma_0 - \sigma\right) = \frac{1}{\tau}\left(A_c \sigma_0 - Q\right), \tag{2.43}$$

where σ_0 is the equilibrium charge density and $\tau = R_0 C$ is the charging time constant; the same as a capacitor circuit. This model was tested on particles travelling down a slide with their charges measured using a Faraday cage which is significantly different to the single particle impact experiments performed by Matsuyama.

Ireland attempted to include a simplified model of Matsuyama's charge relaxation model into his work [148], however as the premise of the model is too simplistic this will not be looked at. The model in Eq. 2.43 however, shows a dependence of a charging time constant like Matsuyama's model. This can be experimentally measured in a number of ways, both for single particles and powders, thus making this model a suitable candidate for modelling the charge transfer from particle collisions in a cyclone.

It should be noted that the model equation (Eq. 2.43) is valid for a single collision. If multiple collisions are occurring during the charging process then each collision may be modelled using Eq. 2.43 but not the process as a whole. If the model is applied to a situation like a beam of particles continuously charging a plate through impaction, then the charging time constant τ would take on a different definition and would be a function of the particle collision frequency. Care should therefore be applied when using the model in this way.

Ireland's capacitor model was validated using large millimetre-sized particles. This model has not been validated for particles 3-4 orders of magnitude smaller in size for this thesis from Figure 2.6. Novel experimental measurements are required to validate this simple charging model for small particles. Looking ahead to these experiments in Chapter 3, it is useful to estimate the amount of charge that is expected to be carried on the small aerosol particles which is to be measured. A rough estimate can be made from the surface charge density for air breakdown $\sigma_{max} \approx 2.5 \times 10^{-5} C/m^2$ [61] and the surface area of the insulating particles. The smallest particles of interest are $d_p = 100nm$ which gives the maximum charge on a single particle before air breakdown as $|Q_{max}| = \pi d_p^2 \sigma_{max} \approx 7.85 \times 10^{-19} C$ which is around 5 electrons per particle. Such low charge levels will not be easily measured; many particles will be needed for any charge measurement equipment to be used. This, along with the difficulty of controlling single $100nm$ particles means that single-particle experiments (such as those performed by Matsuyama *et al.*) are not possible for these small particles. Experiments will therefore involve many particles, with the single particle physics inferred from the results.

The experiments to be performed in Chapter 3 will produce the necessary model constants τ and σ_0 for Ireland's charge model for sub-micron particles. To check the orders of magnitude expected for these quantities, tribocharging data in the literature is applied to Ireland's model. This gives rough estimates for values of the equilibrium charge density and charging time constant for particles much larger than those considered in this work.

In the powder shaking experiments from Section 2.2.1 by Šupuk, Seiler and Ghadiri [126], a mean value for the saturated (equilibrium) intensive charge was found to be $q_{sat} = 4.54 \times 10^{-6} C/kg$ for the α-lactose monohydrate (α-LM) particles. To estimate the charge constants, all collisions are assumed to be particle-particle, which is a poor assumption given the presence of the walls. However, the results from their work used here are those where the shaking vessel was pre-coated in the powder; thus particle-particle collisions are expected to dominate. Assuming spherical particles with a mean diameter of $d_p = 275\mu m$ [126] and a density of $\rho_p = 1768 kg/m^3$ [149] gives $m_p = 1.93 \times 10^{-8} kg$ and a total saturation charge of $Q_{sat} = 2.70 \times 10^{-13} C$ per particle. As the equilibrium charge was found to be independent of shaking frequency (and therefore independent of the contact conditions) and the particles were charged by multiple chaotic impacts, the charge is assumed to be distributed uniformly over the entire surface area of the particle. Dividing the equilibrium charge by the surface area of the sphere gives an estimate of the equilibrium charge density on the particle surface as $\sigma_0 \approx 4.54 \times 10^{-6} C/m^2$. This surface charge density is approximately 5 times lower than the surface charge density for air breakdown for an isolated particle. This value of equilibrium charge density being the of the same order of magnitude as for the isolated air-breakdown appears reasonable.

A charging time constant for the powder shaking experiment is able to be very roughly estimated. A bulk charging time constant, which represents the speed of charging for the entire powder as a whole, can be estimated from the charging curves as $1333, 1000$ and $368.1s$ for shaking frequencies of $10, 20$ and $30Hz$ respectively. To estimate the charging scales for a single particle impact, the collision frequency is required. The total mass of the particles is $1g$ [126] giving the number of particles present as $N \approx 5.2 \times 10^4$. Each shaking cycle, it is assumed that particles experience two collisions to give a collision frequency as $C_{11} = 2f_c N \approx 1.04 \times 10^6$, 2.08×10^6 and 3.12×10^6 for $10, 20$ and $30Hz$ respectively. The bulk time constants are then normalised by the collision frequency to estimate the bulk charging time constant at a collision frequency of unity per second. An additional correction is needed as the impact during charging occurs over a small fraction of that one second which is given by the contact time from Eq. 2.36, where the impact velocity is assumed to be twice the length multiplied by the shaking frequency. The Young's modulus and Poisson ratio are given by $3.45 \times 10^9 Pa$ and 0.3 respectively [140] to give single particle charging time constants as $2.96 \times 10^{-9} s$, $9.65 \times 10^{-9} s$ and $2.19 \times 10^{-10} s$ for $10, 20$ and $30Hz$ respectively. These would be expected to be equal as τ is a constant, however increased shaking frequency results in faster impact velocities and greater deformations and impact times as predicted from the Hertzian model in Section 2.2.3.

2.2.6 Laurentie's Model

A more advanced triboelectric charging model was proposed by Laurentie *et al.* by considering the electric field surrounding the contact point between two particles [150]. This model was utilised in an Eulerian particle model (covered in Section 2.3) by Kolehmainen *et al.* as [137]

$$\frac{dQ}{dt} = H_e\left(\frac{dA_c}{dt}\right)\frac{dA_c}{dt}\epsilon_0\left(\frac{\phi_1-\phi_2}{\delta_c e} - \boldsymbol{E}\cdot\boldsymbol{k}\right), \tag{2.44}$$

where $H_e(.)$ is the Heaviside step function (equal to zero for negative inputs and equal to unity for all non-negative inputs), δ_c is a charge transfer cut-off distance and $\boldsymbol{k}$ is a unit vector pointing from particle "2" to "1". The rate of charge transfer is driven by the difference in work functions between the two colliding particles, the electric field strength $\boldsymbol{E}$ at the collision site and the rate of change of the contact area. In their work, Kolehmainen *et al.* considered a simplified model where contact area during the collision is independent of the charge transfer and initial charge to give [137]

$$\Delta Q = \frac{B_1}{B_2}\left(1 - e^{-B_2 A_{c,max}}\right), \tag{2.45}$$

$$B_1 = \epsilon_0\left(\boldsymbol{E} + \frac{Q_2 - Q_1}{\pi\epsilon_0 d_p^2}\boldsymbol{k}\right)\cdot\boldsymbol{k}, \tag{2.46}$$

$$B_2 = \frac{2}{\pi d_p}, \tag{2.47}$$

with the charge transfer from a single collision approximated by a truncated Taylor series expansion to provide

$$\Delta Q = \frac{B_1}{B_2}\left(1 - 1 + B_2 A_{c,max} + ...\right) \approx B_1 A_{c,max}. \tag{2.48}$$

The maximum contact area $A_{c,max}$ is estimated using a Hertzian model. The B_1 term is proportional to the difference in charge between the two particles and the electric field at the contact site. Calculating the electric field at the point of collision is computationally involved, requiring additional PDEs to be solved for. This extra level of detail makes the charge model inappropriate to use in a computationally "cheap" Eulerian model suggested in Section 2.3. The methodology used by Kolehmainen *et al.* however, can be applied to Ireland's model to provide a computationally inexpensive method to estimate the charge transfer during a collision.

By making the same assumptions that Kolehmainen *et al.* made about contact area and additionally assuming τ is constant, we find the solution of Ireland's model (Eq. 2.43) to be

$$Q(t) = A_{c,max}\sigma_0\left(1 - e^{-\frac{t}{\tau}}\right), \tag{2.49}$$

subject to the initial condition $Q(t=0) = 0$. Performing a truncated Taylor Series expansion yields

$$\Delta Q = A_{c,max}\sigma_0\left(1 - 1 + \frac{t}{\tau} + ...\right) \approx A_{c,max}\sigma_0\frac{t}{\tau}. \tag{2.50}$$

We may now directly compare the linearised result of Ireland's model to Kolehmainen *et al.* Both models are proportional to the maximum contact area. The other comparison is showing how B_1 matches with $\sigma_0\frac{t}{\tau}$. By taking Kolehmainen *et al.*'s B_1 and assuming the electric field represents the electric field between the two plates of a capacitor, we can relate Ireland's capacitor model to Kolehmainen *et al.*'s general model. The electric field from a capacitor is completely determined by the difference in charge between the plates Q and we may write B_1 as

$$B_1 = \frac{Q}{\pi d_p^2}. \tag{2.51}$$

This represents the charge per surface area on the particle and has the same dimensions as $\sigma_0\frac{t}{\tau}$ from Ireland's model. Ireland's model features a time ratio which is not present in Kolehmainen *et al.*'s model. This is due to the two differing approaches from the models. Ireland's model is built upon a capacitor model where the charge builds up to an equilibrium charge. Conversely, Kolehmainen *et al.*'s model is not built on capacitor-like relations and instead the physics of charge saturation is built-in by involving the effects of electrical fields. After applying similar assumptions, both models describe the same physics but from different approaches.

2.2.7 Tribocharging Conclusion

Tribocharging has been shown to be a complex process involving the material properties, duration and area of contact, humidity and initial charge present on the surfaces. Literature on the subject can be inconsistent, which therefore necessitates further experimentation to validate the claims.

The majority of authors agree that electron transfer is the main mechanism for charge separation. This has strong ties to the surface properties of materials, for which electrons form the outermost layer. The energy needed to remove an electron from a metal surface is known as the work function and this has been shown to be able to be extended from metals to insulating materials. Ordering materials by work function provides a list which matches the triboelectric series and therefore provides strong evidence that the physics of tribocharging is governed by the electrons on the surface of the material.

For two contacting particles tribocharging, a variety of models are present in the literature. Many of these models liken the contact as two plates of a capacitor in an electrical circuit. These models successfully reproduce the general behaviour observed experimentally and follow on from the assumption that electrons are the charge carriers. In modelling the charge transfer from sub-micron particles in a cyclone, a capacitor model has been chosen which consists of parameters which can be experimentally verified and contains an appropriate level of detail.

Along with a charge model, the mechanics of the particles impacting requires modelling. A popular method which has been coupled to charging models is Hertzian analysis. This model provides the contact area and time which can be fed directly into a tribocharging model. For the particles which challenge a small, high-speed cyclone, the contact times would require a such a small time step to model the entire collision process which would make modelling this computationally unfeasible. It is therefore suggested to use the maximum contact area during the charging collision process which allows the charge transfer to be accurately captured in a larger CFD time step.

Data for sub-micron particles charging is scarce and the capacitor models have only been validated for much larger particle sizes, predominantly by Matsuyama. This experimental validation is performed in Chapter 3 which will allow Ireland's model to be used to model the charge transfer for the Eulerian particle model in Chapter 4.

2.3 Eulerian Particle Modelling

The equations governing the fluid in Section 2.1 are expressed in an Eulerian framework whereby the fluid is considered a continuum and all of its properties are expressed as continuous fields. The continuity and momentum equations for the fluid can be derived by considering the Lagrangian system of the fluid molecules interacting and averaging over small control volumes [47]. These control volumes must be large enough to capture enough molecules for representative statistics, but small enough such that the macroscopic changes in the fluid properties are retained [37].

The same arguments can be applied to the particulate phase. This allows us to speak of an Eulerian particle velocity field $\boldsymbol{v}(\boldsymbol{x}, t)$, which is in some sense an average of the Lagrangian velocities of individual particles $\boldsymbol{V}(t)$. Information is lost concerning individual particle trajectories which may, at first, seem unacceptable. However the aim of this work is to predict cyclone separation efficiency which does not require the exact chaotic motion of every individual particle to be captured; only a way of tracking the local density of the particulate phase throughout the cyclone. An Eulerian description of the particulate phase allows a computationally efficient treatment of particle collisions relative to the expensive Lagrangian formulation. The particle concentration field is convected by the Eulerian particle velocity field $\boldsymbol{v}$ to model the flow of the dust through the cyclone.

One common tool to help us transition towards the Eulerian set of particle equations is the concept of phase space. This is a six dimensional space where the first three components are the usual components of space $\boldsymbol{x} = (x, y, z)$ and the other three are the velocity components $\boldsymbol{V} = (v_x, v_y, v_z)$ of a single particle all given at an instant of time, t. These variables are assumed to be independent. If the phase space is specified for every particle, then the state of this phase is completely defined [47]. The normalised phase space distribution function f is denoted as $f(\boldsymbol{x}, \boldsymbol{V}; t)$ which provides the number of particles at positions between $\boldsymbol{x}$ and $\boldsymbol{x} + d\boldsymbol{x}$, with velocities between $\boldsymbol{V}$ and $\boldsymbol{V} + d\boldsymbol{V}$ at time t, normalised by the number density. The normalised phase space distribution function is a probability density and therefore has the property [47]

$$\int_{-\infty}^{\infty}\int_{-\infty}^{\infty}\int_{-\infty}^{\infty}\int_{-\infty}^{\infty}\int_{-\infty}^{\infty}\int_{-\infty}^{\infty} f(\boldsymbol{x}, \boldsymbol{V}; t)\, dx dy dz dV_X dV_y dV_z = 1. \tag{2.52}$$

In deriving Eulerian equations from Lagrangian equations, moments are taken about the phase space f. The n^{th} central moment about a mean μ is defined for a 1D phase space in x as [30]

$$M_n = \int_{-\infty}^{\infty} (x - \mu)^n f(x) dx. \tag{2.53}$$

The governing equation for the normalised phase space distribution function is given by the Williams equation (Eq. 2.54). This equation describes the change in the distribution function due to the particle velocity field $\boldsymbol{v}$, external forces $\boldsymbol{F}$ and collisions Γ [151]

$$\frac{\partial f}{\partial t} = -\nabla_x \cdot (\boldsymbol{v} f) - \nabla_V \cdot (\boldsymbol{F} f) + \Gamma. \tag{2.54}$$

The ∇_x symbol explicitly refers to the usual spatial gradient operator. In 3D Cartesian this is expressed as

$$\nabla_x = \nabla = \frac{\partial}{\partial x}\boldsymbol{i} + \frac{\partial}{\partial y}\boldsymbol{j} + \frac{\partial}{\partial z}\boldsymbol{k}, \tag{2.55}$$

with ∇_V an analogous shorthand for the gradient operator acting on the velocity components

$$\nabla_V = \frac{\partial}{\partial V_x}\boldsymbol{i} + \frac{\partial}{\partial V_y}\boldsymbol{j} + \frac{\partial}{\partial V_z}\boldsymbol{k}. \tag{2.56}$$

The Eulerian particle velocity field $\boldsymbol{v}$, is the expected value of the particle velocity $\boldsymbol{v} = \langle \boldsymbol{V} \rangle$. More formally, the expected value of some quantity ψ is [47]

$$\langle \psi(\boldsymbol{x}, t) \rangle = \int_{-\infty}^{\infty}\int_{-\infty}^{\infty}\int_{-\infty}^{\infty} \psi f(\boldsymbol{x}, \boldsymbol{V}; t)\, dV_X dV_y dV_z. \tag{2.57}$$

This has been extended for particles with electric charge in a fluid flow by Kolehmainen *et al.* [137]. In their work, they studied a monodisperse particulate phase with a single work function (defined in Section 2.2). Their normalised phase space distribution function had an additional dimension of intensive charge q and therefore the distribution function $f(\boldsymbol{x}, \boldsymbol{V}, q; t)$ has extra complexity associated with it compared to the Williams equation.

From integrating the Williams equation over the particle property space, Kolehmainen *et al.* derive Enskog's general equation for the change in some function ψ as [137]

$$\frac{\partial\left(\alpha_p\rho_p\langle\psi\rangle\right)}{\partial t}+\frac{\partial\left(\alpha_p\rho_p\langle V_i\psi\rangle\right)}{\partial x_i}=\mathcal{C}(m_p\psi)+\alpha_p\rho_p\langle\frac{dV_i}{dt}\frac{\partial\psi}{\partial V_i}\rangle, \tag{2.58}$$

with the collision operator denoted by $\mathcal{C}$ and the particle volume fraction represented by α. Similar to deriving the Navier-Stokes equations from the Boltzmann equation, the governing equations for the particulate phase can be constructed from Eq. 2.58. By setting ψ to 1, v_i and $\frac{Q}{m}$ the continuity, momentum and charge conservation for the particulate phase may be formulated respectively as [137]

$$\frac{\partial\left(\alpha\rho_p\right)}{\partial t}+\frac{\partial\left(\alpha\rho_p v_i\right)}{\partial x_i}=0, \tag{2.59}$$

$$\alpha\rho_p\left[\frac{\partial v_i}{\partial t}+v_j\frac{\partial v_i}{\partial x_j}\right]=\mathcal{C}(m_p v_i^{'})-\frac{\partial\left(\alpha\rho_p\langle v_i^{'}v_j^{'}\rangle\right)}{\partial x_j}-\alpha\frac{\partial P_f}{\partial x_i}-\frac{\alpha\rho_p}{\tau_p}\left(v_i-u_i\right)+\frac{\alpha\rho_p}{m_p}\langle q\rangle E_i+\alpha\rho_p g_i, \tag{2.60}$$

$$\frac{\partial\left(\frac{\alpha\rho_p\langle q\rangle}{m_p}\right)}{\partial t}+\frac{\partial\left(\frac{\alpha\rho_p}{m_p}\langle q\rangle v_i\right)}{\partial x_i}=\mathcal{C}(q)-\frac{\partial\left[\frac{\alpha\rho_p}{m_p}\langle v_i^{'}q^{'}\rangle\right]}{\partial x_i}. \tag{2.61}$$

Here primed quantities represent fluctuations from the mean. The first two terms on the right-hand side (RHS) of the momentum equation can be combined into a stress tensor and closed assuming a Maxwellian velocity distribution. The charge unknowns are closed by using a Hertzian contact model and assuming an uncorrelated Maxwellian distribution for both velocity and charge.

For a particulate phase and a carrier fluid phase, Eqs. 2.59 and 2.60 (excluding the charge term) represent what is known as the standard two-fluid model where the two phases are coupled by the interfacial terms [152] (which are built-in to the equations above). Deutsch and Simonin have studied such models (although derived through Favre averaging the Navier-Stokes equations and therefore not directly through the Boltzmann equation) and in particular closures associated with applying LES to the model [153]. This introduces a spatial average to the already Favre averaged equations, therefore requiring the filtered small-scales of both phases to be modelled.

Druzhinin and Elghobashi performed studies using the two-fluid model on bubble-laden turbulent flows [154]. They simulated two flows: the first was a decaying 2D Taylor-Green flow field with one-way coupling and the second was a DNS of decaying isotropic turbulence. The Taylor-Green flow was discretised on a fully periodic uniform mesh with 96^3 computational nodes (the flow was 2D, however the solver used was 3D) at $Re = 5000$. To analyse the capture of preferential accumulation, the bubbles had a Stokes number of $Stk = 0.25$ and the volume fraction was initialised uniformly across the domain, with the initial bubble velocity set to zero. Numerical issues were observed in these simulations as the volume fraction gradients continuously increased over time, which suggests that the two-fluid model would be unable to produce a steady-state solution for this flow. For the decaying turbulence, they found the increasing bubble volume fraction along with lack of diffusive sources can cause solver instability; again due to large particle concentration gradients. The model was able to capture preferential accumulation in both cases. The instability over time, especially for the simple Taylor-Green flow, is a major drawback of the two-fluid model.

The Eulerian model incorporating charge from Kolehmainen *et al.* were validated only numerically against DEM simulations. The charge transfer model was validated using a fully periodic 3D box, with drag and electrostatic forces neglected in a periodic channel with conducting walls. Although they could not compare to experiment, they found that the model predicted higher charge build-up by the walls in agreement with the literature [137]. The charge results at very large volume fractions of $\alpha = 0.35$ matched the DEM simulations well. At a lower volume fraction of $\alpha = 0.15$, the two results diverged. Both of these volume fractions are in the dense limit and not representative, at least of the inlet conditions of the cyclone, where $\alpha_0 \approx 5 \times 10^{-7}$. With decreasing accuracy with decreasing volume fraction, it is therefore not reasonable to expect that this advanced model would provide accurate results well within the dilute regime in the cyclone.

Another "advanced" family of Eulerian models are the method of moments. These are applied to polydisperse particulate systems and track the moments (Eq. 2.53) of the number density (Eq. 2.54). These are efficient for tracking multiple particulate phases, however they are known to have many drawbacks [155]. These problems revolve around the lack of diffusion in the mathematical model, however the numerical diffusion in a finite volume scheme radically changes the model predictions [156]. This is very unwelcome behaviour, especially in a challenging highly-swirling flow and these methods will not be explored further.

The particulate phase continuity equation from the work of Kolehmainen *et al.* (Eq. 2.59) is a conservation equation for the volume fraction of the particulate phase. Many authors express this mass conservation in terms of the scalar number density n in the general transport equation given by

$$\frac{\partial \rho_p n}{\partial t} + \frac{\partial}{\partial x_i}\left(\rho_p n v_i - \rho_p D_n \frac{\partial n}{\partial x_i}\right) = \rho_p S_n, \tag{2.62}$$

where D_n is a suitable diffusion coefficient and S_n is a source term for the number density. The volume fraction analogous version of Eq. 2.62 used by Kolehmainen *et al.* can be shown to be equivalent to this equation by assuming no creation or destruction of mass from sources and negligible particle diffusion. This leaves only the temporal and convective terms in Eq. 2.62. The number density can be related to the volume fraction by

$$n = \frac{N}{V}, \tag{2.63}$$

$$\alpha = \frac{\sum V_p}{V} = \frac{N V_p}{V}, \tag{2.64}$$

$$n = \frac{\alpha}{V_p}. \tag{2.65}$$

The general conservation of mass for the particulate phase for the Eulerian model presented here will be expressed in terms of the volume fraction. For a particulate phase with constant density, the mass conservation equation with source term S_α is

$$\frac{\partial \alpha}{\partial t} + \frac{\partial}{\partial x_i}\left(\alpha v_i - D_\alpha \frac{\partial \alpha}{\partial x_i}\right) = S_\alpha. \tag{2.66}$$

In dense flows, where the volume fraction is expected to be large (from Section 1.3.3), the dynamics of the particulate flow are driven by particle-particle collisions. This bears similarities to the kinetic theory of dilute gases. In this theory, gas molecules are assumed to be monodisperse hard spheres undergoing perfectly elastic collisions [157]. As the gas phase is dilute, only binary collisions need to be included. These collisions transport information quickly to their neighbours due to the large numbers of collisions and give rise to the macroscopic fluid variables such as pressure and density. From kinetic theory, the mean free path between collisions of fluid molecules with diameter d_p is given by [157]

$$\lambda_f = \frac{\sqrt{2}}{12}\frac{d_p}{\alpha}. \tag{2.67}$$

The results obtained using kinetic theory require correction by a close-packing function as the gas becomes more dense [157]. Gidaspow has taken the results from kinetic theory and applied them to a particulate phase [158]. Ding and Gidaspow have also included the effects of dense packing of particles by defining a correction function $g_0(\alpha)$ as [159]

$$g_0 = \left[1 - \left(\frac{\alpha}{\alpha_{\max}}\right)^{\frac{1}{3}}\right]^{-1}, \tag{2.68}$$

where $\alpha_{\max}$ is the maximum permissible volume fraction which physically represents the close-packed limit. This is incorporated into the mean free path to give the particle mean free path with dense correction [158]

$$\lambda_p = \frac{\sqrt{2}}{12}\frac{d_p}{\alpha g_0}. \tag{2.69}$$

A mean free path allows determination of a diffusion coefficient due to particle-particle collisions. From dimensional analysis, the diffusion coefficient is expected to be the product of the particle mean free path and an average particle velocity (relative to a stationary carrier fluid) [158]

$$D_{coll} = \lambda_p \left\langle |\boldsymbol{V}| \right\rangle. \tag{2.70}$$

Gidaspow determines this average velocity by assuming a Maxwellian velocity distribution which results in an analogous result to the average speed of a gas molecule from kinetic theory, but as a function of the granular temperature. The granular temperature is related to the mean square of the particle velocity fluctuations as $\frac{1}{3} < \boldsymbol{V}^2 >$ [158]. This granular temperature can be determined by solving a corresponding transport equation for it and requiring a myriad of additional assumptions. These results deriving from kinetic theory assume that collisions are driving the physics of the particulate phase. Collisions are only expected to be relevant near to the walls in the cyclone flow and for the majority of the flow collisions are expected to be negligible from Section 1.3.3. Models of granular flow are therefore not suitable for this dilute cyclone flow, however collisions at the walls causing charge transfer necessitate the need to predict a collision frequency in these small regions. These collisions are expected to be due to velocity gradients in the shear flow, with a collision frequency function (in 1D) given by Eq. 1.35.

A suitable momentum equation for the particulate phase is required to provide the Eulerian particle velocity for the volume fraction transport equation. Solving another coupled set of PDEs for the particle momentum across the domain becomes computationally expensive, with any closures used required to be accurate. The momentum equation used by Kolehmainen *et al.* is too complex and expensive to evaluate and simpler closures for the particulate velocity are needed. Fortunately the particles in a cyclone are small, with low Stokes number, low Re_p and a large density ratio $\frac{\rho_p}{\rho_f} >> 1$. These allow selection of algebraic models for the particulate velocity field to replace the set of PDEs resulting in a simpler, computationally inexpensive method of solving for the transport of the particulate phase.

The simplest method of calculating the velocity of the particulate phase is to simply set $v_i = u_i$ in the "dusty gas" model. This is acceptable for $Stk \to 0$ when particles act as fluid tracers and has been used to model the transport of bacteria in operating theatres [160, 161]. The particulate phase in a cyclone is expected to have Stokes numbers of less than unity, however the particles have enough inertia that they can accumulate into banded structures from experimental evidence which would not be captured with this dusty gas model. This simple model is therefore not appropriate for a cyclone.

2.3.1 Mixture Model

The mixture model by Manninen and Taivassalo represents a slightly more advanced model than the passive scalar approach. The multiphase system (the fluid and particle phase) is represented by a homogeneous single-phase system known as the mixture [162]. The continuity and momentum equations are then solved for the mixture only and the velocities of each phase are calculated by a simple slip velocity formulation. A transport equation for the volume fraction of the particulate phase is then solved. The simplest specification of the (non-zero) relative velocity is given by

$$v_i = u_i + \tau_p g_i. \tag{2.71}$$

In this formulation, the particle velocity field is expected to reach terminal velocity, $\tau_p g_i$, in a time period much smaller than any characteristic time scale of the flow [162]. This essentially is a restriction on the maximum Stokes number of the flow; requiring that $Stk << 1$. In flows where gravity is negligible, this is equivalent to the dusty gas expression and results in both phases moving at the same velocity. In the original full derivation, a more complex expression is provided and this is the form of the mixture model which will be presented here following Manninen and Taivassalo [162] for an incompressible carrier fluid.

The main definitions in the model are that of the mixture density

$$\rho_m = \sum_{k=1}^{N} \alpha_k \rho_k, \tag{2.72}$$

where the k subscript runs over all N phases considered, the mixture dynamic viscosity

$$\mu_m = \sum_{k=1}^{N} \alpha_k \mu_k, \tag{2.73}$$

and the mixture (mass-weighted) velocity

$$\boldsymbol{v}_m = \frac{\sum_{k=1}^{N} \alpha_k \rho_k \boldsymbol{v}_k}{\rho_m}. \tag{2.74}$$

The continuity equation for the mixture is analogous to that of the usual fluid continuity equation

$$\frac{\partial \rho_m}{\partial t} + \nabla \cdot (\rho_m \boldsymbol{v}_m) = 0. \tag{2.75}$$

The momentum equation also corresponds to its single phase fluid counterpart, with an additional term on the RHS

$$\frac{\partial \rho_m \boldsymbol{v}_m}{\partial t} + \nabla \cdot (\rho_m \boldsymbol{v}_m \boldsymbol{v}_m) = -\nabla P + \nabla \cdot \left(\mu_m \left(\nabla \boldsymbol{v}_m + \nabla \boldsymbol{v}_m^T \right) \right) + \rho_m \boldsymbol{g} + \nabla \cdot \left(\sum_{k=1}^{N} \alpha_k \rho_k \boldsymbol{v}_{dr,k} \boldsymbol{v}_{dr,k} \right). \tag{2.76}$$

In this model, the phase pressures are assumed to be equal and thus there is only a single relevant pressure. The additional term on the RHS arises from the splitting of the non-linear convective term when the phases are summed together. This term is written in terms of a drift velocity, which is the velocity of phase k relative to the mixture velocity. Referring to a two-phase system of a fluid and particulate phase, the drift velocity of the particulate phase can be expressed in terms of the relative velocities between the phases and the particle mass fraction as

$$\boldsymbol{v}_{dr,p} = (1-c)\,\boldsymbol{w}. \tag{2.77}$$

The above set of equations are derived with no major additional assumptions to the full two-fluid model. An algebraic formulation for the relative velocity is required, for which Eq. 2.71 provides a very simple prescription. A more complex formulation, assuming Stokes drag is valid and spherical particles, specifies the relative velocity as

$$\boldsymbol{w} = \frac{\rho_p - \rho_m}{\rho_p}\tau_p \left(\boldsymbol{g} - (\boldsymbol{v}_m \cdot \nabla)\,\boldsymbol{v}_m - \frac{\partial \boldsymbol{v}_m}{\partial t} \right) = \frac{\rho_p - \rho_m}{\rho_p}\tau_p \left(\boldsymbol{g} - \frac{D\boldsymbol{v}_m}{Dt} \right). \tag{2.78}$$

It is this algebraic specification of the relative velocity which means that the model is only valid for $Stk << 1$ for Stokes drag. A local equilibrium is assumed in this formulation, with only first-order terms from the transfer of momentum between phases retained and local particle velocity derivatives approximated as the mixture counterpart ($(\boldsymbol{v}\cdot\nabla)\,\boldsymbol{v} \approx (\boldsymbol{v}_m \cdot \nabla)\,\boldsymbol{v}_m$). A transport equation for the volume fraction of the particulate phase (Eq. 2.66) is then solved for. The mixture model involves the solution of no additional PDEs compared to the dusty gas approach and is able to capture two-way coupling between a fluid and particulate phase. The mixture model also allows a slip velocity to exist between the two phases depending on the prescription for the relative velocity. Both models are limited to low Stokes numbers and assume that the particle Reynolds number is low and the density ratio between the particles and the fluid is large for Stokes drag to be the only significant force.

The mixture model, with the addition of a lift force in the relative velocity specification, has been used in a dense flow within a cyclone with height $12H$ relative to the cyclone of interest described in Table 1.1 by Aketi *et al.* [163]. This was performed with an RSM turbulence model on a grid size of 2×10^5 cells and inlet particle volume fractions of $\alpha = 0.35, 0.45$ and 0.6 were examined; around 6 orders of magnitude larger than those of interest here. They did not state their wall boundary condition for the volume fraction transport equations and it assumed that they used a reflect boundary condition as they discuss values of volume fraction on the wall. The cyclone had an inlet velocity of $0.04u_0$, therefore the cyclone is expected to be much slower than the cyclone of interest in Chapter 1. They validated their work by comparing the diameter of the vortex core to experiment, which is not sufficient validation for the fluid. There was no comparison of pressure drop, flow velocities or separation efficiencies to experiment, however they did validate the mean mixture density at the wall with experiment which closely matched. Given that there is no special wall treatment with the model, this gives a useful indication that the near-wall region is accurate and requires no additional numerical attention.

Grady *et al.* used RSM with a mixture model in a hydrocyclone of a similar size to the cyclone of interest at a smaller inlet velocity $0.54u_0$ [164]. The inlet Reynolds number was ≈ 10000 and $Sw_g = 8.4$, both closely matching the cyclone of interest. They performed no validation of their fluid results, apart from comparison of the tangential velocity profiles with a Rankine vortex (discussed in Appendix B). They found the mixture model to under predict the separation efficiency by up to $\approx 20\%$ compared to experiment, with particle diameters ranging from $d_p = 0.49\mu m$ to $d_p = 48.3\mu m$ (the lower limit within the range of interest).

The simulations of the mixture model in the literature have been performed in hydrocylones where the carrier fluid is water. In these flows the density ratio between the particle and fluid is near unity and additional forces in the Maxey-Riley equation should have been considered. Despite this, predicted separation efficiencies for a similar geometry, Re_0 and Sw_g to the cyclone of interest have been reasonable. Particle concentrations in the near-wall region using this model have also matched well to experiment.

2.3.2 Equilibrium Eulerian Model

The Equilibrium Euler (EE) method by Ferry and Balachandar proposes an algebraic formulation for the particle velocity field based on the velocity gradients of the fluid and particle response time for low Stokes numbers $Stk < 1$ [20]. For small enough τ_p, the Eulerian particle velocity field is expected to reach a unique equilibrium field which is independent of the initial conditions of the particle. This method, like the slip velocity of the mixture model, avoids solving additional PDEs for the particle momenta. However, the inclusion of the fluid velocity gradients in the model allows particles to accumulate in areas of local strain [165].

The derivation of the EE method builds upon the result by Maxey for the dimensionless Lagrangian equation of motion for small particles at low $Re_p << 1$ with a large density ratio ($\frac{\rho_p}{\rho_f} >> 1$) in isotropic turbulence [44], for which the dimensional equation reads

$$\frac{d\boldsymbol{V}}{dt} = \frac{1}{\tau_p}\big(\boldsymbol{u}(\boldsymbol{X}(t), t)) - \boldsymbol{V}(t)\big) + \boldsymbol{g}. \tag{2.79}$$

In the original work by Maxey, the dimensionless Eulerian particle velocity field is reduced to a first-order approximation in Stokes number

$$\boldsymbol{v}^*(\boldsymbol{x}^*, t^*) = \boldsymbol{u}^*(\boldsymbol{x}^*, t^*) + \boldsymbol{W}^* - Stk\left(\frac{\partial \boldsymbol{u}^*}{\partial t^*} + \boldsymbol{u}^* \cdot \nabla \boldsymbol{u} + \boldsymbol{W} \cdot \nabla \boldsymbol{u}^*\right) + \mathcal{O}(Stk^2), \tag{2.80}$$

with $\boldsymbol{W} = \tau_p \boldsymbol{g}$ and quantities non-dimensionalised by fluid turbulent scales denoted with *. Ferry and Balachandar take the dimensional form of Eq. 2.80 and impose a further restriction with the removal of all terms of $\mathcal{O}(\tau_p^2)$ and above [20]

$$\boldsymbol{v} = \boldsymbol{u} - \tau_p\left(\frac{D\boldsymbol{u}}{Dt} - \boldsymbol{g}\right) + \mathcal{O}(\tau_p^2). \tag{2.81}$$

Eq. 2.81 provides the unknown Eulerian particle velocity field from the known fluid velocity field and its derivatives (excluding the gravity term). For a steady, uniform flow ($\frac{Du_i}{Dt} = 0$), $v_i = u_i + \tau_p g_i$ and the method reduces to the simple mixture model velocity formulation. As $\tau_p \to 0$, $v_i = u_i$ and the passive scalar model limit is reached. Eq. 2.81 and the low Stokes number relative velocity formulation in the mixture model in Eq. 2.78 are analogous, with the mixture model formulation expressing this relative velocity in terms of the mixture velocity with a density correction. The main difference between these two methods is that in the mixture model, the mixture itself is solved for whereas in this approach the fluid is solved for and the particle velocity field is provided by this algebraic relation. The derivation of the EE method is based on the Lagrangian particle equation of motion and reduced to first order in Stk and τ_p, whereas the mixture model relative velocity derivation was more ad-hoc and was derived from the Eulerian mixture momentum equation. The EE method would appear to have better physical grounding and is preferable to the mixture model.

The EE method assumes that the particle velocity field reaches a unique equilibrium velocity field. Ferry and Balachandar show that the equilibrium velocity is unique if all the eigenvalues of the particle velocity field strain rate tensor S_{ij}^v are greater than $-\frac{1}{\tau_p}$ [20]. This uniqueness condition can be expressed mathematically as the most negative eigenvalue λ_s, found by the solution to the characteristic equation

$$\det\left(S_{ij}^v - \lambda_s \delta_{ij}\right) = 0, \tag{2.82}$$

satisfies

$$\lambda_s > -\frac{1}{\tau_p}. \tag{2.83}$$

Ferry *et al.* later modified the EE method in an attempt to extend the method to larger particles in what is termed the Modified Equilibrium Eulerian (MEE) method [166]. They praised the original method's ability to faithfully capture the turbophoresis of particles in wall-bounded flows, however the stream-wise particle velocity component predictions for larger particles is less successful. Instead of retaining all terms of $\mathcal{O}\left(\tau_p^2\right)$, a heuristic "correction" is employed as [166]

$$\boldsymbol{v} = \boldsymbol{u} - \tau_p\left(\boldsymbol{I} + \tau_p\left(\nabla \boldsymbol{u}\right)^T\right)^{-1}\left(\frac{D\boldsymbol{u}}{Dt} - \boldsymbol{g}\right). \tag{2.84}$$

This MEE velocity retains the turbophoretic migration and preferential accumulation from the original EE method and the error is still $\mathcal{O}\left(\tau_p^2\right)$. This heuristic modification comes at a computational price; a matrix inverse is now required at each point in the domain. Furthermore, the matrix to invert can be close to singular, which produces unphysical velocities and occurs in regions of intense compressive strain [166]. It is therefore expected that use of this heuristic addition in a highly-swirling, high speed flow will cause many numerical issues. Ferry *et al.* describe a numerical procedure in the appendix to their paper which produces a smooth velocity field which they describe as numerically stable (guaranteeing that $\det\left(\boldsymbol{I} + \tau_p\left(\nabla \boldsymbol{u}\right)^T\right) > 0.207$) by interpolating between the EE and MEE methods [167]. However, from brute-forcing with random numbers, it has shown that this claim is false with evidence provided in Appendix C.

The governing transport equation for the volume fraction of the particulate phase (Eq. 2.66) combined with the Equilibrium Euler method (Eq. 2.81) for calculating the particle velocity provides

$$\frac{\partial \alpha}{\partial t} + \frac{\partial}{\partial x_i}\left(\alpha\left(u_i - \tau_p u_j \frac{\partial u_i}{\partial x_j}\right) - D_\alpha \frac{\partial \alpha}{\partial x_i}\right) = 0. \tag{2.85}$$

By moving the τ_p term to the RHS as a source term, the LHS becomes the familiar transport equation for a passive scalar convected by the carrier fluid.

$$\frac{\partial \alpha}{\partial t} + \frac{\partial}{\partial x_i}\left(\alpha u_i - D_\alpha \frac{\partial \alpha}{\partial x_i}\right) = \tau_p \frac{\partial}{\partial x_i}\left(u_j \frac{\partial u_i}{\partial x_j}\alpha\right) \tag{2.86}$$

This form of the particle volume fraction transport equation is valid for unsteady, incompressible flows where the particulate phase is monodisperse and constant density. The governing physics of Eq. 2.86 becomes clear when it is non-dimensionalised using the Kolmogorov scales as follows: $\alpha = \alpha_0 \alpha^*$, $u_i = u_\eta u_i^*$, $x = l_\eta x^*$, $t = \tau_\eta t^* = \frac{l_\eta}{u_\eta} t^*$, $D_\alpha = D_0 D_\alpha^*$ and $\tau_p = \tau_{p,0}\tau_p^*$ to yield

$$\frac{\partial \alpha^*}{\partial t^*} + \frac{\partial}{\partial x_i^*}\left(\alpha^* u_i^* - \frac{1}{Pe_\eta} D_\alpha^* \frac{\partial \alpha^*}{\partial x_i^*}\right) = Stk \tau_p^* \frac{\partial}{\partial x_i^*}\left(u_j^* \frac{\partial u_i^*}{\partial x_j^*}\alpha^*\right), \tag{2.87}$$

where $Pe_\eta = \frac{u_\eta l_\eta}{D_0}$ and $Stk = \frac{\tau_{p,0}}{\tau\eta}$ are Péclet and Stokes numbers based on the smallest turbulent scales respectively. The Péclet number characterises the strength of convection to diffusion for the particulate phase; for no diffusion $Pe_0 \to \infty$. The strength of the source term on the RHS of Eq. 2.87 is governed by the Stokes number and the strength of both velocity and volume fraction gradients. This source term becomes large as the inertia of the particles increases, however for low Stokes numbers the source term is expected to be small. Treating this inertial term as a source allows finer control in a finite volume solver over this term and may help prevent instabilities which occur as the validity of the EE method is challenged.

Shotorban and Balachandar have applied the EE model in an LES of statistically isotropic turbulence [168]. In this work, they proposed a model for the effect of the unresolved SGS scales on the particulate phase. Starting with filtering (Eq. 1.12) the EE velocity field (Eq. 2.81) to provide

$$\hat{v}_i = \hat{u}_i - \tau_p\left(\widehat{\frac{\partial u_i}{\partial t}} + \widehat{u_j \frac{\partial u_i}{\partial x_j}} - \hat{g}_i\right) \tag{2.88}$$

$$= \hat{u}_i - \tau_p\left(\frac{\partial \hat{u}_i}{\partial t} + \widehat{u_j \frac{\partial u_i}{\partial x_j}} - \hat{g}_i\right). \tag{2.89}$$

The non-linear term here is rewritten in terms of a subgrid-scale stress tensor

$$\tau_{ij} = \widehat{u_i u_j} - \hat{u}_i \hat{u}_j, \tag{2.90}$$

to provide

$$\hat{v}_i = \hat{u}_i - \tau_p\left(\frac{\partial \hat{u}_i}{\partial t} + \hat{u}_j \frac{\partial \hat{u}_i}{\partial x_j} - \hat{g}_i + \frac{\partial \tau_{ij}}{\partial x_j}\right). \tag{2.91}$$

Only τ_{ij} requires modelling. As both the energy contained in the SGS and τ_p is small, Shotorban and Balachandar argued the subgrid-scale term is negligible [168]. The final filtered equation for the particle velocity field is

$$\hat{v}_i = \hat{u}_i - \tau_p\left(\frac{\partial \hat{u}_i}{\partial t} + \hat{u}_j \frac{\partial \hat{u}_i}{\partial x_j} - \hat{g}_i\right). \tag{2.92}$$

Performing the same filtering operation on the transport equation for the volume fraction (Eq. 2.66) with Brownian diffusion and no source terms yields

$$\frac{\partial \hat{\alpha}}{\partial t} + \frac{\partial}{\partial x_i}\left(\widehat{\alpha v_i} - D_{lam}\frac{\partial \hat{\alpha}}{\partial x_i}\right) = 0. \tag{2.93}$$

The non-linear filtered term is written in terms of a new vector h_i, analogous to the subgrid-scale stress tensor

$$\widehat{\alpha v_i} = h_i + \hat{\alpha}\hat{v}_i. \tag{2.94}$$

Substitution yields

$$\frac{\partial \hat{\alpha}}{\partial t} + \frac{\partial}{\partial x_i}\left(\hat{\alpha}\hat{v}_i - D_{lam}\frac{\partial \hat{\alpha}}{\partial x_i} + h_i\right) = 0. \tag{2.95}$$

Replacing the filtered Eulerian particle velocity field with the EE model and moving the τ_p term to the RHS yields

$$\frac{\partial \hat{\alpha}}{\partial t} + \frac{\partial}{\partial x_i}\left(\hat{\alpha}\hat{u}_i - D_{lam}\frac{\partial \hat{\alpha}}{\partial x_i} + h_i\right) = \tau_p \frac{\partial}{\partial x_i}\left(\hat{u}_j \frac{\partial \hat{u}_i}{\partial x_j}\hat{\alpha}\right). \tag{2.96}$$

Everything is in terms of filtered quantities apart from h_i which requires modelling. Shotorban and Balachandar model this term in an analogous way to the deviatoric part of the SGS stress tensor in the dynamic Smagorinsky model as [168]

$$\tau_{ij}^d = -2\left(C_s \Delta\right)^2 \hat{S}^u_{mag} \hat{S}^u_{ij}, \tag{2.97}$$

where Δ is the filter width, C_s is determined dynamically and a u superscript indicates that this involves the fluid velocity spatial derivatives. The SGS stress tensor can be approximated as the deviatoric part from the same assumption about the small energy contained in the SGS. Shotorban and Balachandar model q_i as

$$h_i = -\frac{\left(C_s \Delta\right)^2 \hat{S}^v_{mag}}{Sc_t}\frac{\partial \hat{\alpha}}{\partial x_i}, \tag{2.98}$$

where a v superscript indicates that this involves the Eulerian particle velocity spatial derivatives and the turbulent Schmidt number Sc_t and C_s are determined dynamically [168]. An important feature of the form of Eq. 2.98 is that it resembles a diffusive flux in the volume fraction transport equation. This will have the effect of spreading out the volume fraction where this term is large, which are regions of large strain and volume fraction gradients. The turbulent diffusion coefficient arising from the unresolved SGS scales is

$$D_t = \frac{\left(C_s \Delta\right)^2 \hat{S}^v_{mag}}{Sc_t}. \tag{2.99}$$

The EE method has been used to specify the slip velocity by Icardi *et al.* to track the particle number density in an LES fluid flow field. In their work, they used a Direct Quadrature Method of Moments (DQMOM) to track the particle size distribution. This was performed for a simple channel flow at Stokes numbers from 0.2 to 5, with the larger Stokes numbers appearing to invalidate the EE model. They reason that the model is still acceptable at these larger Stokes numbers as the Kolmogorov scales are not directly computed and so the flow field contains larger eddies of longer time scales than these Kolmogorov scales which allows them to relax the $Stk < 1$ condition [155]. They included the effects of the SGS using an approximate deconvolutional method (ADM). This method attempts to reconstruct the unresolved scales from the filtering function [169]. The results were compared to Lagrangian particle DNS data. They found that the slip velocity between the particles and the fluid was negligible in the mean stream-wise profile. The ADM was found to provide accurate wall-normal velocity fluctuation and if the effects of the SGS were ignored these fluctuations were not in agreement with the DNS data. They reported numerical instabilities at $Stk = 5$ and were unable to obtain a numerical solution with the ADM. For $Stk < 1$, good agreement with Lagrangian DNS data was observed. Fine wall resolution was also found to be important to approximate the high concentration gradients near the wall, which enabled to model to capture the physical phenomenon of turbophoresis from Section 2.1.2.

The ADM used in the work by Icardi *et al.* requires repeated use of the filter function to estimate the effects of the unresolved scales. If an LES has an implicit filtering operation (performed by the mesh), ADM is unable to be used in this scenario. ADM also requires specifying the “order” of the approximation, for which the optimal value is unknown.

2.3.3 Eulerian Particle Modelling Conclusion

There exist a variety of families of Eulerian methods to model the particulate phase. When used in a LES of a complex geometry, the more advanced models such as the full two-fluid Eulerian model are too computationally expensive. Method of moments is a better compromise and can handle polydisperse flow efficiently, however the interactions between different particulate sizes is a big unknown and cannot safely be employed here. Solving a transport equation for the volume fraction is computationally cheap if an algebraic relation is used to determine the particulate velocity field. This then allows that for a given CFD flow field, only one additional transport equation needs to be solved to track the particulate phase. Additional transport equations will be required for both charge and electric potential.

A range of simple algebraic models to determine the particle velocity field were explored. Setting $v_i = u_i$ neglects much of the rich physics of preferential accumulation and particle inertia effects which are expected to be important in a turbulent, highly-swirling flow. The EE method captures the local accumulation of particles in the flow and has been shown to provide good agreement with Lagrangian DNS in both isotropic turbulence and a channel flow. This model is therefore most appropriate to use to calculate the Eulerian particle velocity field which is used to transport the particle volume fraction.

Going from these basic flows to a cyclone is a large jump in complexity. The model has been shown to fail even in a channel flow if Stk becomes large and the model has not been tested against swirl or other flow features which may present numerical issues. This Eulerian model is implemented and tested in an analytical flow in Chapter 4, which features strong streamline curvature and large velocity gradients. These novel tests are performed at scales matching those of the expected Kolmogorov scales in the cyclone which are provided from the single-phase CFD results in Chapter 5.

2.4 Conclusion

The multidisciplinary nature of this work has required three distinct literature reviews for cyclones, particle tribocharging and Eulerian particulate modelling. From these surveys, the current state of knowledge relevant to the thesis has been determined and gaps in the understanding identified. These gaps and unknowns are to be investigated in the following chapters which aim to bring new understanding and further the field of research for particles in high-speed cyclones with charge transfer.

From the cyclone literature review in Section 2.1, LES has been identified as the most suitable method of accurately modelling the cyclone flow field computationally. This resolves many of the larger turbulent scales directly which the small Stokes number particles are expected to readily respond to. High near-wall resolution and in-depth particle trajectory integration studies are lacking in the literature for cyclones and therefore this is investigated in Chapter 5.

Section 2.2 identified the lack of information and validation of charging models for sub-micron particles, with high-quality single-particle charging experiments having only been performed on particles 4-5 orders of magnitude larger. The main difficulty in extending these experiments to smaller particles sizes arises from controlling individual sub-micron particles. An aerosol beam has been identified as an appropriate method of focusing these small particles to perform analogous experiments to the single particle impacts from literature. These results, along with a Hertzian contact model for impact conditions will permit the use of a simple capacitor-like tribocharging model which can be validated from the experiments in Chapter 3.

To model charge transfer from individual particle collisions for representative number densities is not computationally feasible and thus an Eulerian framework for the particle phase is more appropriate than the common Lagrangian approach. Section 2.3 detailed computationally efficient algebraic models for solving the particle momenta without resorting to PDEs. These models assumed low Stokes number as particles are expected to quickly reach an equilibrium with the carrier fluid such as the EE model. It is unknown whether this model can be used accurately in a complex, highly-swirling cyclone flow as only simple validation such as isotropic turbulence and a channel flow have been performed. An additional validation study using a flow field with strong streamline curvature which has been used to stress-test other Eulerian models is performed in Chapter 4.

Chapter 3

Particle Charging Experiments

From Section 2.2, experiments are needed in order to validate the charging characteristics of small, sub-micron sized particles. This is information which is missing in the literature. Additionally, the experiments provide the necessary adjustable model constants for Ireland's tribocharging model (Section 2.2.5) used in CFD. To accurately control these small particles an aerosol beam is created, which is made to impact a metal plate.

This chapter begins with introducing the experimental set-up of the aerosol beam along with the equipment used to both control the rig and collect the required measurements. Two set-ups are provided: one for characterising the aerosol and the other for capturing the required tribocharging data to validate Ireland's model. Aerosol characterisation is performed to ensure both the size distribution and charge state of the aerosol is constant during testing. This also yields the characteristic size of the particulate phase in the main experiments.

After characterisation, the main experiments are performed by impacting the beam with a metal plate and measuring the voltage build-up on the plate. This is compared to the analytical solution to Ireland's charge model to assess validity. From these results, estimates for the model constants σ_0 and τ are made which are to be used in the charge model implemented in a computer code in Section 4.7.

3.1 Experimental Set-Up

Aerosol beams, introduced in Section 2.2.2, allows particles to be focused aerodynamically into a well-defined beam. The controlled beam of particles is used to force small particles to impact a metal plate to measure charge transfer, in an analogous set-up to the experiments performed by Matsuyama *et al.* for single particles. A simplified sketch of an aerosol beam is shown in Figure 3.1. The particle-laden fluid is accelerated through a choked converging nozzle and collides with a metal plate.

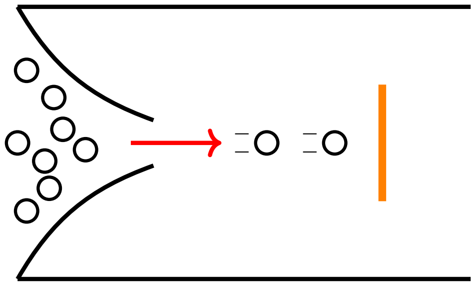

Figure 3.1: Aerosol beam of particles impacting a metal plate. The red arrow indicates the direction of the flow of particles, with the thin orange rectangle representing the metal plate.

The amount of charge transferred by impact with the plate is not known, however it is expected to be dependent on the collision rate, initial charge on the particles, impact velocity and the difference in work functions between the plate and the particles. The charging characteristics of small aerosol particles can be validated against their larger counterparts, with the experimental results be used to provide the unknown constants in Ireland's tribocharging model (Eq. 2.43). This equation predicts a charge saturation curve which can be seen by monitoring the build-up of charge on the metal plate. For a single particle charging, the charge saturation curve provides τ as the time taken to reach $1 - \frac{1}{e}$ of the saturation value and σ_0 by the saturation charge ($A_c\sigma_0$). For a beam of particles colliding, the saturation charge is unchanged, however the time constant from the charge-saturation curve is now also a function of both collision frequency and the impact time. By correcting for these, the particle charging time constant can be estimated.

3.1.1 Materials and Measuring Equipment

The air used in the experiments originates either from atmosphere, or from an $\approx$ 8bar airline. From whichever source the air originates, the fluid is passed through some form of filtration. This is to, for the atmosphere as an example, remove the ever-present particulates suspended in the room. All filters from atmosphere are HEPA filters from TSI. Filtration when using airlines is provided by an array of Festo filters and regulators.

TSI flow meters are used to measure mass flow rates. These have a range between $0 - 300l/min$ with an accuracy of $\pm2\%$ or 0.05slpm, whichever is greater (slpm represents standard litres per minute which is the volumetric flow rate for a fluid at the manufacturer's defined standard conditions). They measure pressures between $0.50 - 1.99$bar to an accuracy of $\pm1kPa$; due to the vacuum downstream of the nozzle, these flow meters cannot be used accurately there unless air is bled in through atmosphere.

For measuring the pressure drop across the nozzle, a Druck digital pressure indicator (DPI) is used with a measurement range of $0 - 100kPa$ and an accuracy of 0.1% (full-scale). Airline pressures were measured using a Druck DPI with a range of 7bar and an accuracy of 0.05% (full-scale).

For drawing air through the system, two pieces of equipment are used. The first is a Norgren vacuum pump which uses the airline to create vacuums up to $87kPa$ below atmosphere. The second is housed within the particle counting equipment to create choked flow across the equipment's internal aerosol beam.

The aerosol for experimental testing was created by atomising a solution containing the desired aerosol and then removing moisture from the result. The atomisation was performed using a TSI constant output atomiser which is able to atomise aerosols up to a diameter of $d_p = 2\mu m$. The pressurised air used for atomisation was filtered through a Festo regulator array. The atomised aerosol containing both the particles of interest and water droplets is then passed through a TSI diffusion dryer. This consists of a central mesh surrounded by silica desiccant which absorbs the water droplets. The desiccant was freshly prepared before testing by heating in an oven. The desiccant had indicating solution present which enabled its freshness to be examined visually.

The aerosol used was analytical reagent grade Sodium Chloride (salt) from Fischer Chemical, which has a purity of $> 99.5\%$. Salt was used instead of silica-based test dust due to its chemical purity, with dust being

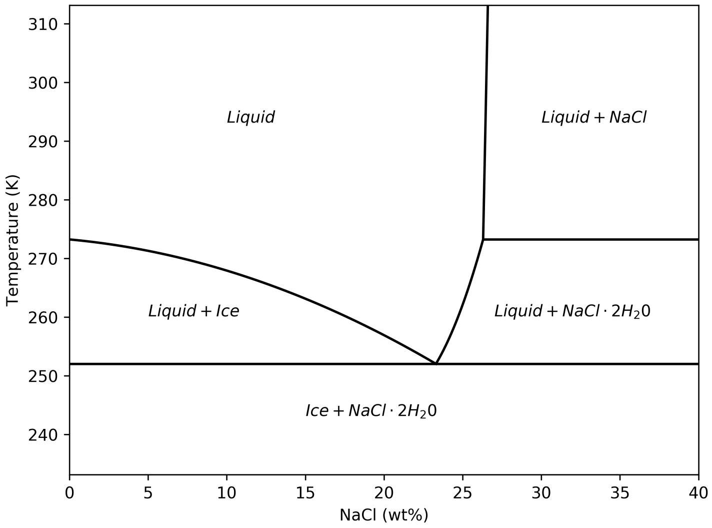

Figure 3.2: Typical phase diagram of Sodium Chloride and water adapted from Badawy [170].

composed of many different substances. This means that the results using salt will be more repeatable than the dust comprising of a mixture of substances. This was created by mixing a solution of salt with distilled water from The Distilled Water Company using a magnetic stirrer for 2 hours. The composition of the salt solution was 26.6% salt by weight which is at the eutectic point (at standard temperature) as shown in Figure 3.2 for standard atmospheric temperature. The salt solution is therefore saturated and expected to produce the maximum number of salt particles when atomised.

The size distribution of the dried salt aerosol was measured using a scanning mobility particle sizer (SMPS) from TSI. This consists of three pieces of equipment: a classifier, a differential mobility analyser (DMA) and a condensation particle counter (CPC). The classifier samples the aerosol by passing the flow through an impactor, which removes particles above a certain diameter via inertial impaction with the impactor plate. The sample is then passed through a radioactive Krypton-85 source to neutralise the aerosol, with the neutralised aerosol then ionised to produce a known charge state. The DMA consists of a long vertical pipe where the aerosol enters from the top. A uniform electric field is set-up which causes the charged particles to migrate across the DMA. The balance of the electrical force on the particle versus the drag of the flow moving down the DMA causes particles to follow different trajectories based on their electrical mobility. A small exit slit at the bottom of the DMA therefore allows only a small band of electrical mobilities to pass through it. The electrical mobility required to leave the DMA (and therefore the particle diameter) can be adjusted through altering the potential difference across the DMA. This allows the SMPS to sweep through a range of voltages and therefore particle diameters to pass to the particle counting equipment.

The CPC allows the concentration of the aerosol to be measured. If connected as part of the SMPS it can be used to determine the concentration of a specific size of particle. If connected as a stand-alone unit, it can be used to measure the concentration of an aerosol sample. The aerosol enters the CPC and is passed into a supersaturated butanol chamber. The sample then passes to a cooler chamber which causes the butan-1-ol to condense onto the particles which act as nucleation sites. This causes the particles to grow in size, such that they are able to measured optically. The sample is then passed through an aerosol beam and across a laser pointed at a photodetector. When a single particle passes through the laser, a drop in current is observed at the photodetector and a particle is counted. A maximum particle concentration of $5 \times 10^4 p/cc$ can be measured this way. For increased particle concentration, particle coincidence becomes prevalent and this single-particle count breaks down. To counter this, the equipment shifts operation to measure the scattering of the laser light by additional photodetectors situated perpendicular to both the flow and the laser. Particle concentration measurements become less accurate during this mode, however the maximum concentration able to be measured is increased to $1 \times 10^7 p/cc$. More detail on the theory of operation for the SMPS is provided in Appendix D.

The charge state of the salt aerosol was controlled by using a TOPAS neutraliser. This passed the aerosol into mixing chambers where a large potential difference causes a stream of ions to impact the particles. This can be used to neutralise the particles or to control the charge levels on the particles by adjusting the ionisation voltage. The ionisation chambers require an input pressure of $>$ 0.5bar to aid in mixing the particles. This pressure is adjusted manually, with high pressures used post-experiment to clean the ionisation heads of any particle deposits. This gives rise to a source of human error in returning the pressure back to 0.5bar for every experiment. The effect of this varying ionisation chamber pressure is discussed in Section 3.3.1.

To measure the charge carried by the aerosol, a PALAS Charme electrometer was used. This equipment uses a filter in a Faraday cage which charge particle collect on. The particles are discharged through high $1G\Omega$ resistance and this drop in voltage provides the discharging current. The electrometer can measure up to $22500fA$ with an accuracy of $0.1fA$.

To measure the voltage build-up on the metal plate, a JCI Static Monitor was used. This can measure up to $2kV$ with an accuracy of $\pm 1V$. This is then placed in a JCI Electrostatic Voltmeter which is a shielded enclosure which allows the static monitor to provide the measured voltage from the plate when directly connected. For larger voltages, the range can be extended to $20kV$ with the accuracy changing to $\pm 10V$.

3.2 Methodology

The particle charging experiments are built up gradually by performing smaller experiments. These smaller experiments perform necessary checks that the equipment is working as expected and what is being measured is real. Common to all these experiments is the production of the salt aerosol (aerosol generation) shown as a block diagram in Figure 3.3.

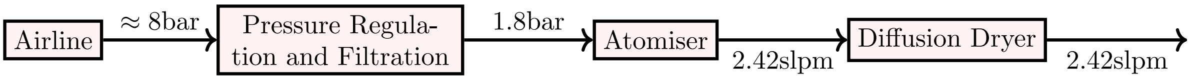

Figure 3.3: Block diagram of the aerosol generation section of the experimental rig. The 1.8bar static pressure used to operate the atomiser is measured using a DRUCK DPI.

The black connecting arrows represent conductive tubing connecting each piece of equipment. Metal tubing adaptors on the equipment have been connected to a common ground; preventing the build-up of charge on the pipe walls or connectors. The entire rig shown in Figure 3.3 is hereafter referred to as the aerosol generation section of the rig.

3.2.1 Characterisation

The aerosol itself is first characterised. The shape of the size distribution for the salt is unknown and so is the charge state. To measure the size distribution, the aerosol is atomised, dried by the diffusion dryer, diluted as to not over-range the CPC and then simultaneously measured using the SMPS and electrometer. A block diagram is shown in Figure 3.4.

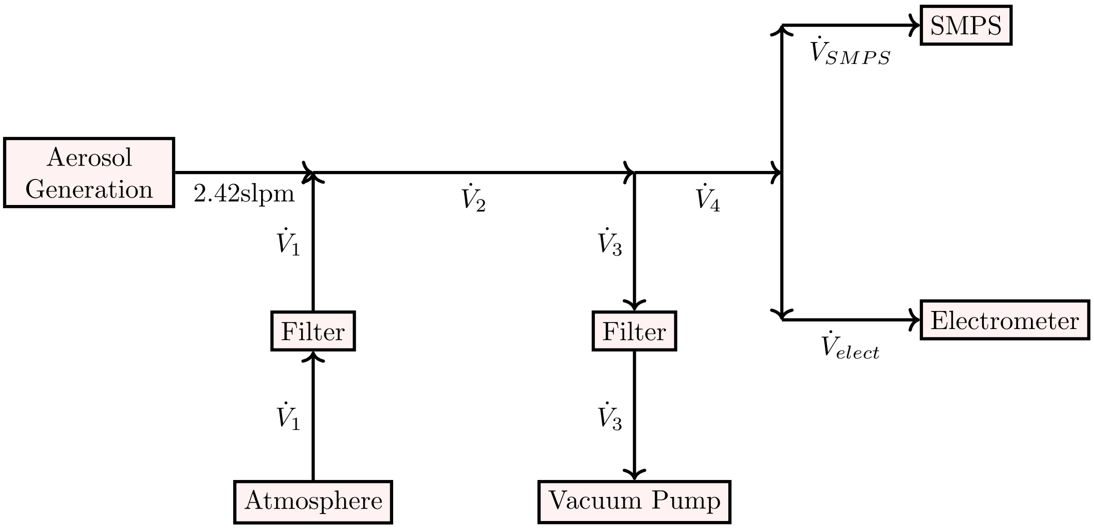

Figure 3.4: Block diagram of the experimental rig set-up used to measure the size distribution and net charge of the aerosol.

The SMPS and electrometer have different sampling flow rates. The concentrations measured by the CPC as part of the SMPS will be the same as the concentration seen by the electrometer, however the number of particles reaching the electrometer will differ from the SMPS due to the difference in flow rates. The ratio of flow rates between the electrometer and SMPS, R_f, is

$$R_f = \frac{\dot{V}_{elect}}{\dot{V}_{SMPS}}. \tag{3.1}$$

This flow rate ratio allows the charge and concentration measurements made by the different pieces of equipment to be combined to determine the state of the aerosol upstream. The flow rates used for the initial characterisation is provided in Table 3.1.

The SMPS takes time to scan through different voltages and therefore different particle sizes. The longer the scan time, the more particles are sampled and therefore the distribution calculated becomes more representative.

$\dot{V}_1$	$\dot{V}_2$	$\dot{V}_3$	$\dot{V}_4$	$\dot{V}_{SMPS}$	$\dot{V}_{elect}$
5.8slpm	8.42slpm	5.12slpm	3.3slpm	0.3slpm	3slpm

Table 3.1: Flow rates used in Figure 3.4 for characterising the size distribution and net charge of the aerosol.

However, the pressure drop across the impactor in the classifier increased over time as the salt clogged the impactor. Although longer scan times would collect better statistics, the concentrations for the last scans will be reduced as the impactor clogs. The effect of the scan time on the distribution was investigated to find the smallest scan time which would provide an accurate representation of the size distribution, before the clogging becomes significant. This scan time was found to be $90s$, with a $30s$ purge to remove remaining particles in the system.

The shape and concentrations of the size distribution remained repeatable throughout testing. The SMPS provided a constant monitor during the experiments that the aerosol output was constant.

3.2.2 Beam Measurements

The design of the aerosol beam was influenced by the beam created by Israel and Friedlander [130]. An engineering drawing of the beam used in these experiments is provided in Appendix E. The inclusion of a skimmer was not found to improve the vacuum downstream of the beam and was repurposed as a pressure tapping for all experimental results shown here. The flow rate was observed to choke at the critical pressure ratio of $\frac{\Delta P}{P_0} = 0.528$. The theoretical choked flow rate from the isentropic flow relations (Eq. 2.7) gives $3.00 \times 10^{-5} kg/s$, the choked mass flow rate from experiment was $2.94 \times 10^{-5} kg/s$, yielding a 2% difference. The experimentally observed choked mass flow rate is lower than the theoretical prediction due to the presence of a thin boundary layer in the nozzle which has the effect of slightly reducing the apparent nozzle diameter. This reduced nozzle diameter reduced the choked mass flow rate from Eq. 2.23.

The aerosol beam was inserted into the experimental rig after both the electrometer and SMPS to allow both the size distribution and charge state to be known before the beam impacts the metal plate. The JCI Static Monitor was electrically connected to the metal plate inside the beam.

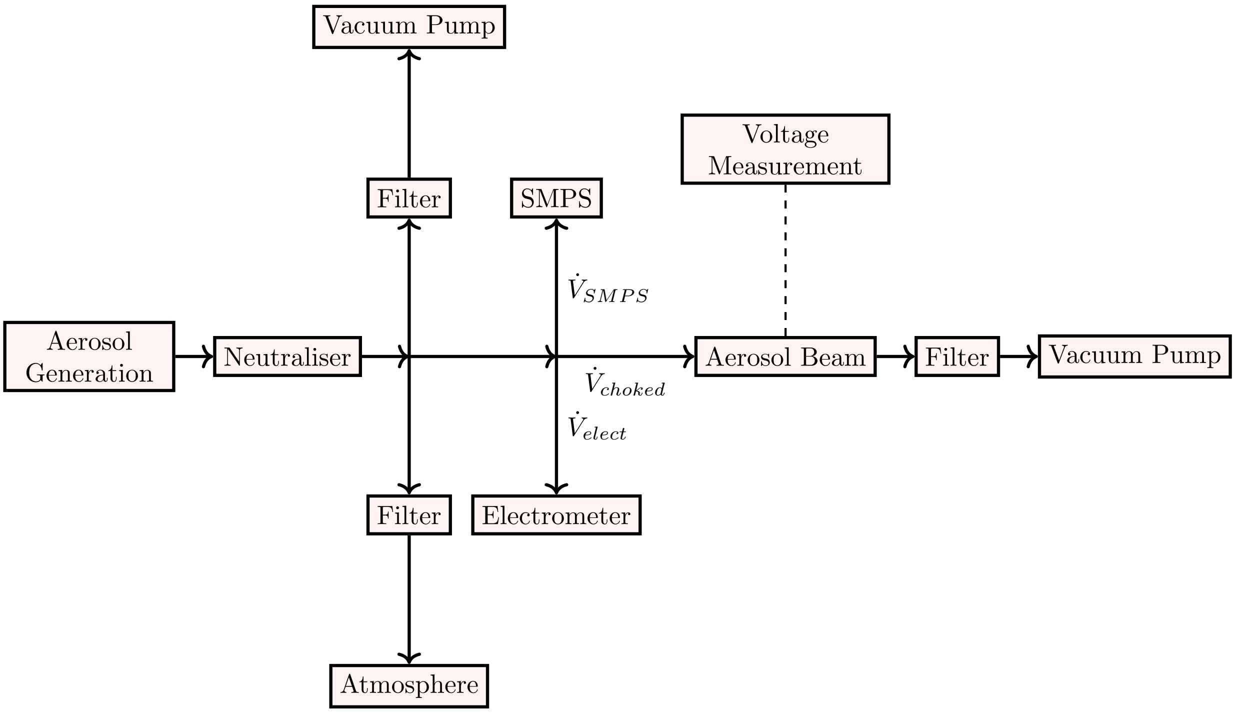

Figure 3.5: Block diagram of the experimental rig set-up used for the aerosol beam. The dashed line represents an electrical connection between the plate and the JCI Static Monitor.

3.3 Aerosol Characterisation

The results of the initial aerosol characterisation experiments and the monitoring of the size distribution during the plate experiments are given here.

3.3.1 Size Distribution

The size distribution of the salt aerosol showed a good qualitative fit with a log-normal distribution, whose probability density function is given by [171]

$$f(d_p) = \frac{1}{d_p\sqrt{2\pi}\ln\sigma_g} e^{-\frac{\left(\ln d_p - \ln d_{p,g}\right)^2}{2\left(\ln\sigma_g\right)^2}}, \tag{3.2}$$

where $d_{p,g}$ is the geometric mean diameter and σ_g is the geometric standard deviation (GSD) defined respectively as

$$\ln d_{p,g} = \int_0^\infty \ln d_p f(d_p) dd_p, \tag{3.3}$$

$$\ln\sigma_g = \sqrt{\int_0^\infty \left(\ln d_p - \ln d_{p,g}\right)^2 f(d_p) dd_p}. \tag{3.4}$$

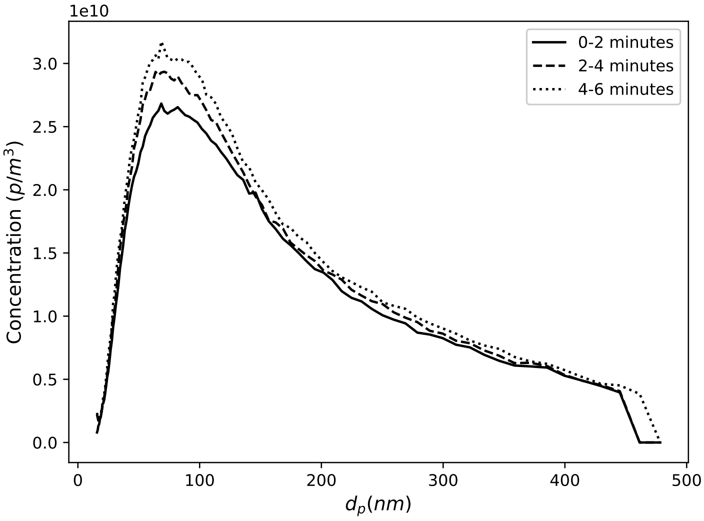

Figure 3.6: Aerosol size distribution recorded over two minute intervals during an experiment. These results were taken from an experiment using a $-6kV$ ionisation voltage with a brass plate at an angle of $\frac{\pi}{12}$. The mean total concentration was $1.5 \times 10^{12} p/m^3$.

Figure 3.6 shows the size distribution during testing as measured by the SMPS. The distribution is seen to remain fairly steady during testing with the modal diameter remaining approximately constant. This allows a representative particle diameter to be defined to represent the distribution. The area under the graph provides the concentration of the aerosol sampled by the SMPS. The concentration varied between tests due to the difficulty in repeating the same pressure at the ionisation chamber for the neutraliser. This allowed the effects of concentration on the plate saturation voltage and aerosol charge state to be quantified. The mean $d_{p,g}$ from all aerosol beam tests was $d_{p,g} = 107.5nm$ which will be used to estimate the contact area with the metal plate using the Hertzian contact model.

Background counts were taken with the aerosol generation section removed and replaced with a HEPA filter. Up to a maximum of 4 particles were measured in a 90 second window after 3 repeats. The aerosol generation section was replaced and only the distilled water was atomised; no salt was added to the solution. The size distribution was noisy and repeated 5 times. The mean total concentration from impurities in the water and diffusion dryer was $\approx 2.4 \times 10^7 p/m^3$. This is 5 orders of magnitude smaller than nominal mean total concentration measurements from the aerosol beam tests (such as Figure 3.6) and any background noise is insignificant.

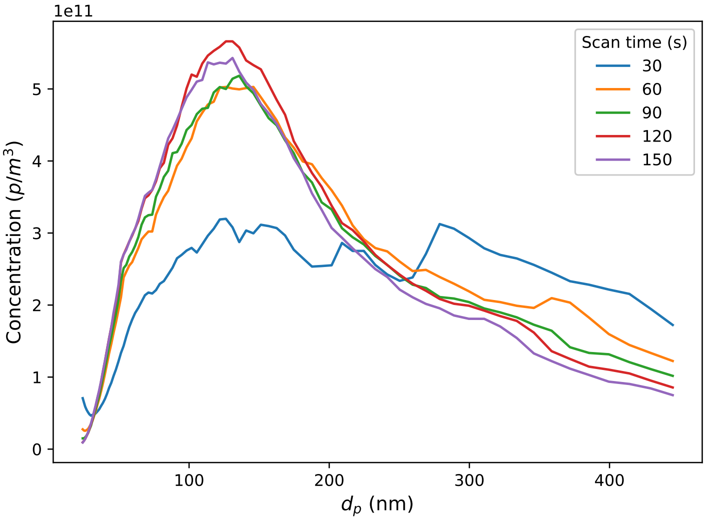

Figure 3.7: Mean aerosol size distribution recorded over various scan times; each with a 30 second purge.

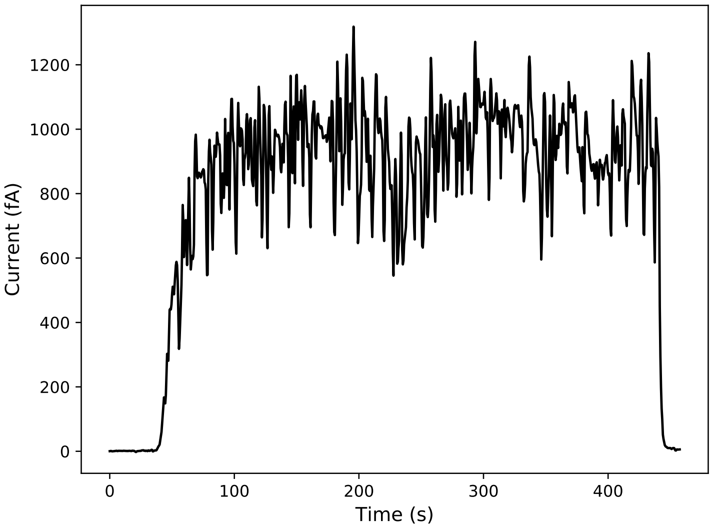

Figure 3.8: Aerosol current measured by the electrometer during an experiment. These results were taken from an test using a $+6kV$ ionisation voltage with a copper plate at an angle of 0.

The effect of scan time on the resulting shape of the distribution was investigated. The SMPS was directly connected to the aerosol generation section of the rig which ran with scan times from 30 seconds up to 180 seconds. Each scan time was repeated three times and averaged. The results are shown in Figure 3.7. It is clear that a 30s scan time does not recover the shape of the distribution and that at least a one minute scan time must be used. A scan time of 120 seconds (with a 30s purge) was used for all aerosol beam tests as it accurately recovers the shape of the distribution and the low scan time enables multiple scans to be made during the experiments.

3.3.2 Charge State

The charge carried by the salt particles after the neutraliser is measured by the electrometer from Figure 3.4. A typical current measurement during an aerosol beam experiment is shown in Figure 3.8. The background noise measured from the electrometer when no salt was atomised was $< 1fA$. The start and end times of the aerosol atomisation are clear from the current readings. When the distilled water was atomised with no salt, the current reading was indistinguishable from the natural background noise. These checks give confidence that the salt particles both dominate the size and charge distribution by several orders of magnitude and effects of contamination are negligible.

As the both the net aerosol current and concentration are measured simultaneously, they can be combined to provide the mean charge per particle using the flow rate ratio in Eq. 3.1. The number of particles per second (collision rate) entering the SMPS is given by

$$\dot{N}_{SMPS} = n\dot{V}_{SMPS}, \tag{3.5}$$

where n is the number density (concentration) measured by the SMPS. The number of particles per second entering the electrometer can be calculated by

$$\dot{N}_{elect} = \dot{N}_{SMPS}R_f. \tag{3.6}$$

The mean charge per particle is given by

$$\bar{Q}_p = \frac{I_{elect}}{\dot{N}_{elect}}, \tag{3.7}$$

with I_{elect} representing the current measured by the electrometer. This can be normalised by the charge of an electron, e, to provide the mean number of electrons per particle

$$\bar{N}_e = \frac{\bar{Q}_p}{e}. \tag{3.8}$$

3.4 Experimental Results

With the salt aerosol shown to have a steady net charge and size distribution, the aerosol beam can be created and made to impact a metal plate as shown in Figure 3.5. The size distribution is continually monitored immediately upstream of the beam along with the charge state before impact with the plate. Assuming all particles impact the plate, the collision frequency and mean charge per particle which exchange charge with the plate are known.

The charge build-up on the metal plate is measured by a build-up of voltage on the plate. Figure 3.9 shows a typical voltage saturation curve from the experiments. The form of the voltage saturation is an excellent match to Ireland's capacitor model (Eq. 2.43), with the charge Q replaced with CV_c (Eq. 1.42) to produce the governing differential equation as

$$\frac{dV_c}{dt} = \frac{1}{\tau_{tot}} \left(\frac{A_c \sigma_0}{C} - V_c \right) . \tag{3.9}$$

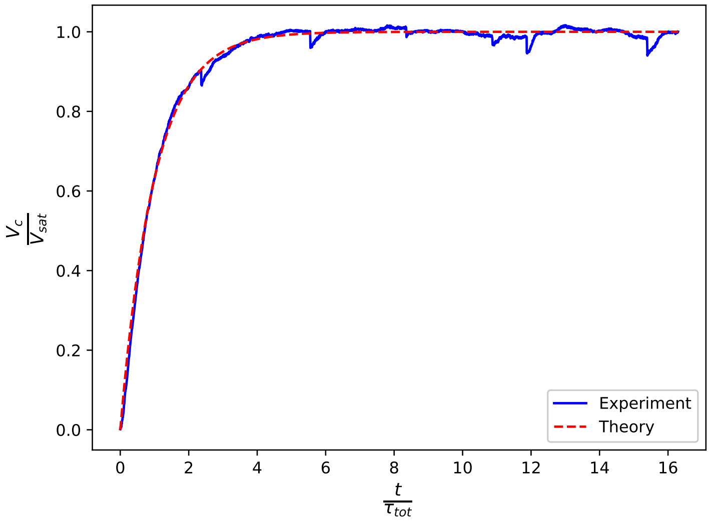

Figure 3.9: Plate voltage saturation curve normalised by the saturation voltage and total charging time constant. The dashed theory line indicates the result expected using Ireland's model and the solid line shows the experimental result. This was taken from one repeat of an experiment using a $-6kV$ ionisation voltage with a brass plate at an angle of $\frac{\pi}{4}$. The R^2 value of the experimental fit to theory is 0.997 (to 3 significant figures).

The sudden troughs present in the experimental data in Figure 3.9 are likely from salt which has adhered to the plate breaking away and removing some charge with it. This would be more likely to occur over time as more salt is allowed to build up on the metal plate. This reasoning is supported by Figure 3.9, which shows no sudden drops in normalised voltage until after $t = 2\tau_{\text{tot}}$.

In Eq. 3.9, the charging time constant is τ_{tot} which does not represent the time constant associated with a single particle impact. This is due to the many collision events occurring at the plate, for which this bulk result is measured. Extraction of a representative single particle charging time constant is explored in Section 3.4.1.

3.4.1 Charging Time Constant

When the aerosol source is removed at the end of the experiments, the voltage on the plate decays back to zero. This is due to the charge leaving the plate through leakage paths. These have been minimised by using insulating materials, however these precautions were not enough to prevent charge leakage from the plate surface. The leakage voltage had the form of an exponential decay. This is shown in Figure 3.10.

Including the effects of the leakage current provides the actual governing equation for the charge on the plate as

$$\frac{dV_c}{dt} = \underbrace{\frac{1}{\tau_{\text{bulk}}} (V_{\text{sat}} - V_c)}_{\text{Charging}} + \underbrace{\frac{1}{\tau_l} V_c}_{\text{Leakage}} , \tag{3.10}$$

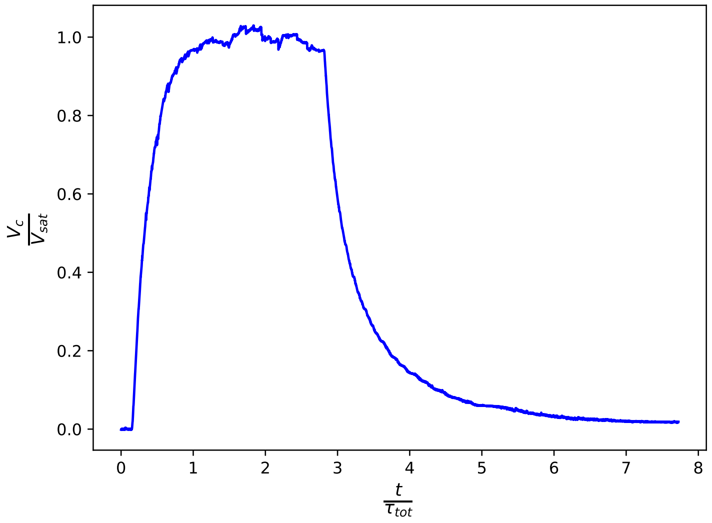

Figure 3.10: Plate voltage saturation curve normalised by the saturation voltage and total charging time constant over an entire test. The decay of voltage on the plate when the aerosol source is removed begins at $\approx 3\tau_{tot}$. This was taken from one repeat of an experiment using a $+6kV$ ionisation voltage with a brass plate at an angle of 0.

where τ_l is the leakage time constant. Here there is a competition between the plate tribocharging due to the aerosol beam acting to increase the plate voltage and leakage paths reducing the voltage on the plate surface. This results in a reduced measured voltage saturation on the metal plate, seen as the point where the two opposing mechanisms balance each other. The solution for the plate voltage charge curve, given the initial condition $V_c(t=0)=0$ yields

$$V_c(t) = \frac{A_c\sigma_0}{C\left(1-\frac{\tau_{\text{bulk}}}{\tau_l}\right)}\left(1-e^{-\left(\frac{1}{\tau_{\text{bulk}}}-\frac{1}{\tau_l}\right)t}\right). \tag{3.11}$$

The effects of the leakage voltage can be removed by estimating τ_l from the voltage decay curve at the end of each experiment. The actual "charging" bulk time constant τ_{bulk} is related to the measured (total) voltage charging time constant τ_{tot} and the leaking time constant τ_l by

$$\tau_{\text{bulk}} = \frac{\tau_l\tau_{\text{tot}}}{\tau_l+\tau_{\text{tot}}}. \tag{3.12}$$

This bulk charging constant varied between tests as shown in Figure 3.11.

This bulk time constant is expected to be a function of collision frequency, contact time and the true, single-particle collision time constant τ. The collision frequency from each experiment is calculated from

$$\dot{N} = n\dot{V}_{\text{choked}}. \tag{3.13}$$

The functional dependence of the bulk particle time constant and collision frequency is hypothesised to be a power law. A curve fit to the experimental results are shown in Figure 3.12.

The single particle collision time constant τ can be calculated from this power law when the collision frequency is equal to unity. This gives the estimated single particle collision charging time constant as $\tau = 1091s$, however this assumes constant particle contact with the plate. In reality, contact occurs for a fraction of a second and can be estimated using Hertzian contact theory from Section 2.2.3. This requires the particle impact velocity with the plate. Solving Eq. 2.27 with $f_s = 0.4$ as found from Dahneke and Friedlander gives a theoretical upper bound for the particle speed, assuming that particles remained in the beam. A lower bound can also be determined by assuming that the particles were able to sufficiently decelerate due to drag and only impacted the plate with the mean convectional velocity in the vacuum chamber, given by the volumetric flow rate divided by the cross sectional area. The contact time calculated from both of these limits is shown in Figure 3.13.

In a worst-case scenario, the contact time differs by a factor of around 4. Around the predicted beam velocity, the curve in Figure 3.13 is almost flat and small discrepancies between the theoretical impact velocity and reality are not expected to greatly affect the contact time. In order to provide some reassurance that the beam was impacting the plate at appreciable velocity, photographs were taken of the plate after a test and the

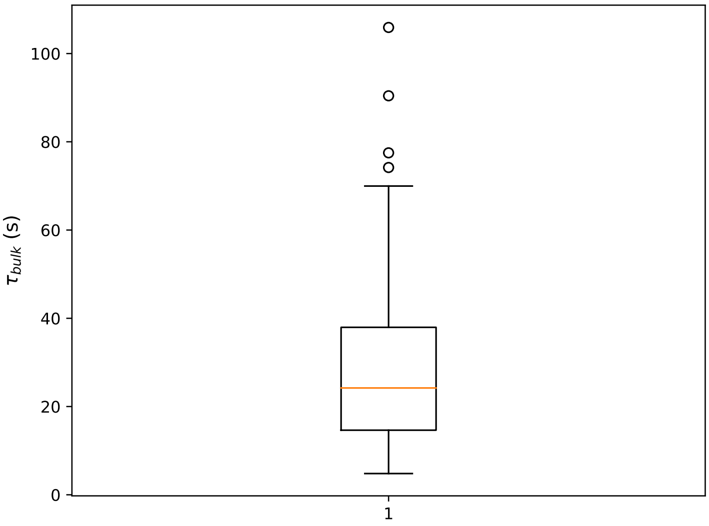

Figure 3.11: Bulk charging time constant after leakage correction for all 128 tests.

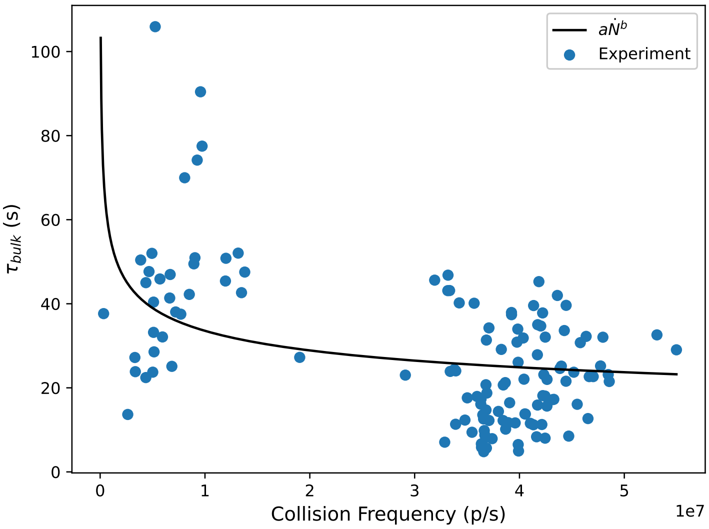

Figure 3.12: Bulk charging time constant as a function of collision frequency. The constants were determined by least-squares using the Levenberg-Marquardt algorithm. The fitted constants are $a = 1091$ and $b = -0.2160$ to 4 significant figures.

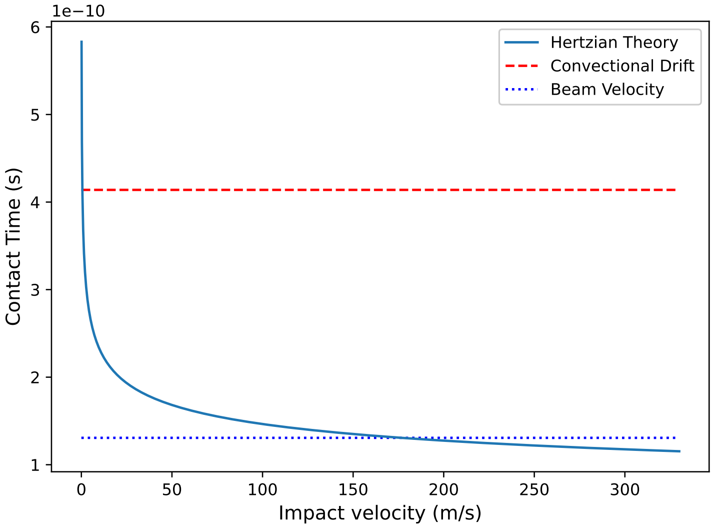

Figure 3.13: Contact time between a particle and a plate as a function of impact velocity predicted using Hertzian theory.

deposits of salt along the edges of the plate are clearly visible in Figure 3.14, suggesting that particles impacted the plate at high velocity along the centreline of the beam.

The true single particle charging time constant can therefore be calculated as $\tau = 1091 \cdot \frac{t_c}{1} \approx 1.426 \times 10^{-7} s$. Compared to the time constants estimated from the powder shaking experiments in Section 2.2.5, the salt particles charged 2-3 orders of magnitude slower than the α-LM particles, which were 2-3 orders of magnitude greater in size than the salt. Thus the estimates made here appear reasonable.

3.4.2 Equilibrium Charge Density

With the time constant known from Section 3.4.1 and the contact area able to be calculated from the Hertzian contact model in Chapter 2, only one unknown remains in Ireland's charge model; the equilibrium charge density σ_0. This is the charge per unit area on the surface of the particle when it has reached saturation. This can be calculated knowing the charge state of the particles pre-impact (Eq. 3.7) with the plate and the saturation voltage of the plate.

The charge state of the aerosol was altered in the ionisation chambers of the neutraliser and was measured by the electrometer. The effect of the neutraliser ionisation voltage on the mean charge particle normalised by the charge of an electron (Eq. 3.8) is shown in Figure 3.15. Ionisation voltage did not effectively charge the salt particles until the ionisation voltage reached $\pm 4kV$, with positive voltages charging the particles positively and vice versa. The number of elementary charges on particles from exposure to the $8kV$ ionisation heads showed a large spread, with large negative ionisation voltages causing the particles to lose their additional surface charge. It is not known what caused these phenomena and possible suggestions are lack of adequate mixing in the ionisation chamber for the positive cases and corona discharge for the negative cases.

No dependence of initial aerosol charge per particle was found with the plate saturation voltage as shown in Figure 3.16. This result suggests that the double layer formed during the collision of small particles was dominated by the difference in work functions, not of the contribution to the electric field from the initial charge on the particle. From Laurentie's model used by Kolehmainen *et al.* in Eq. 2.44, this would be equivalent to ignoring the $\boldsymbol{E} \cdot \boldsymbol{k}$ term; reducing the model to a similar form to that of Matsuyama *et al.* (Eq. 2.40). The insignificance of the contribution of the electric field from excess charge on the particle may be due to the very low levels of charge present on the particle (a few electrons).

In addition, the angle of the plate also showed no relationship to the saturation voltage from Figure 3.17. The plate angle effectively controls the normal velocity component of the particle impact with the plate, which is expected to decrease the contact area with increasing plate angle from Hertzian theory. This effect was not observed. This is likely due again to the very low charge levels on the particles. Charge is discrete and not continuous at these small scales and each particle has a very limited number of charges which is can exchange with the plate. The clumps of results with similar V_{sat} values at the same plate angle are results with similar collision frequencies.

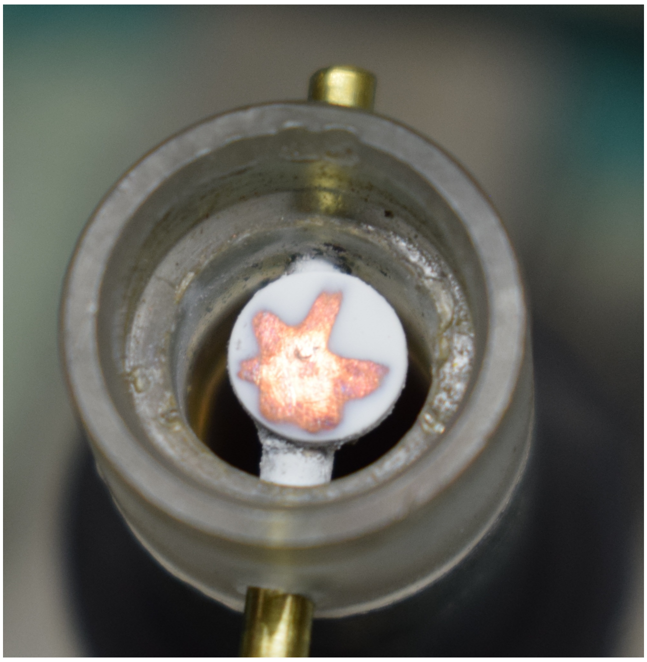

Figure 3.14: Salt build-up on the edges of the plate after testing.

It was found that the collision frequency (Figure 3.18) showed a correlation to the saturation voltage of the plate, with the magnitude of the plate voltage increasing with collision rate. The reason for this is that at higher collision frequencies, more charge is being exchanged with the plate to counteract the leakage current (discussed in Section 3.4.1), thereby allowing a greater amount of charge to be held on the plate at equilibrium.

The material of the plate did not affect the saturation voltage. This was unexpected as the two different materials used (copper and brass) have different work functions and should reach different surface equilibrium charges. This may be caused by the very small amount of charge on the particles and the small currents to the plates (when the salt is not ionised, the mean net number of electrons per particle is ≈ 0.1 which must mean that only around 1 in 10 particles have an additional electron on the surface). Electron transfer becomes probabilistic at these scales, with the observed currents and voltages due to the large ($\approx 10^7$) collisions occurring per second. When dealing with these small particles and charge levels, a simpler approach seems more appropriate whereby each particle will exchange, at most, one electron with the plate. This net gain/loss of one electron divided by the surface area of the particle can provide an estimate of the equilibrium charge density of the small salt particles as $\sigma_0 \approx 4.413 \times 10^{-6} C/m^2$. This estimate is ≈ 5.6 times smaller than the limiting value given for air breakdown in Section 2.2.5 and is therefore physical. This experimental value obtained is very similar to the equilibrium charge density estimated from the α-LM ($\sigma_0 \approx 4.54 \times 10^{-6} C/m^2$) from Section 2.2.5 and provides confidence in the results obtained here.

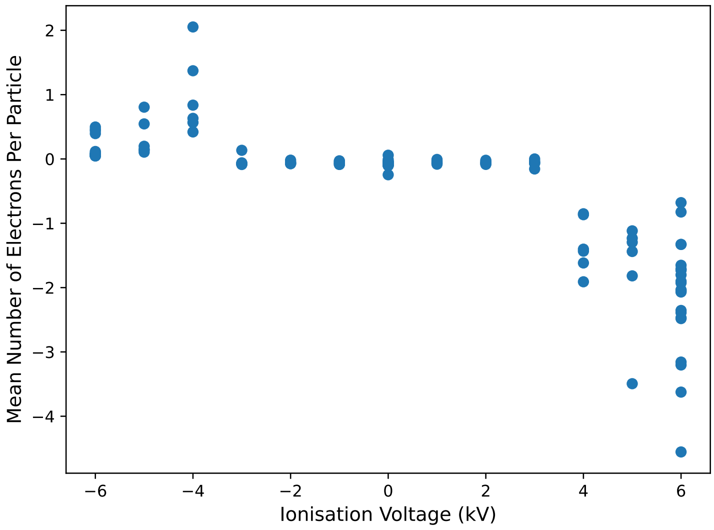

Figure 3.15: Mean number of additional electrons on the particle surface for a range of ionisation voltages over all 128 tests.

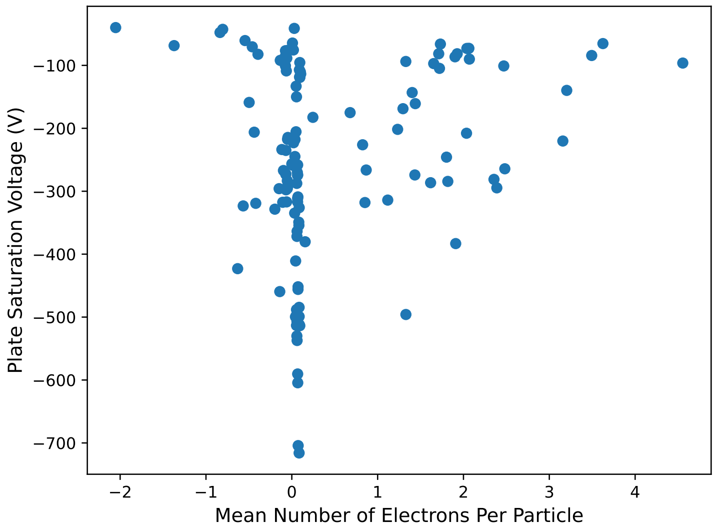

Figure 3.16: Mean number of additional electrons per particle against plate saturation voltage over all 128 tests.

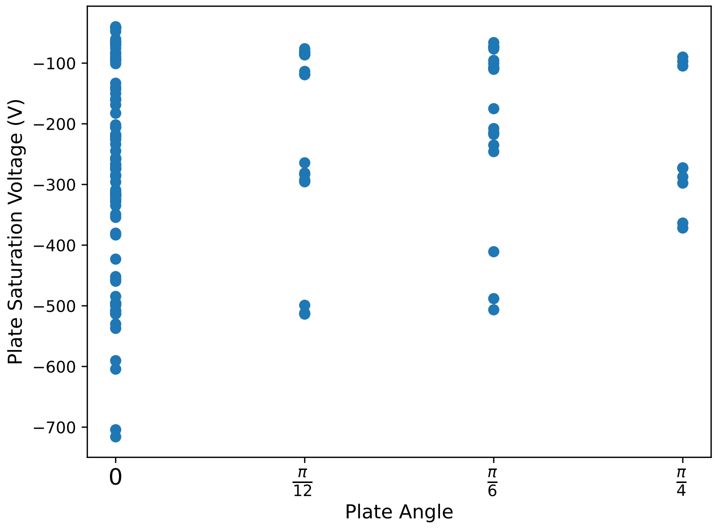

Figure 3.17: Plate saturation voltage against plate angle (radians) over all 128 tests.

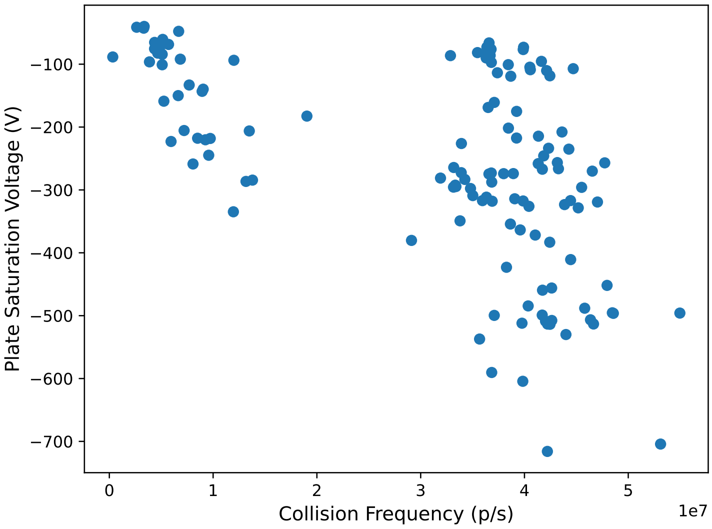

Figure 3.18: Plate saturation voltage vs Collision Frequency over all 128 tests.

3.5 Conclusion

An aerosol beam has been used to provide a stable, controllable stream of salt particles to impact a metal plate. These experiments were performed using a range of particle concentrations, charge states, plate angles and two different plate materials. These have been performed using particles sizes far smaller than those used to do similar charge experiments in the literature and represent novel work. The macroscopic variables such as the voltage build-up on the metal plate have matched models and measurements in the literature for particles with sizes orders of magnitude larger than those studied here. Due to the probabilistic nature at low charge levels, conditions at impact including the charge state, surface material and impaction angle had no measurable effect on either the speed or total amount of charge transfer.

These measurements and conclusions have allowed the determination of the remaining two unknowns from Ireland's charge model, the charging time constant τ and the equilibrium charge density σ_0. The effect of collision frequency on the macroscopic charging time constant has also been modelled which will aid in applying the model in an Eulerian framework for a cyclone in Chapter 5 from the model's original Lagrangian formulation.

Chapter 4

Particle Eulerian Model Validation

The Equilibrium Eulerian (EE) model introduced in Section 2.3 is to be used to convect an Eulerian particle phase through a cyclone. This model assumes that $Stk < 1$ and provides a computationally efficient way of computing the particle velocity field without the need to solve additional PDEs. The EE model has been validated for use with low Stokes number particles in statistically isotropic turbulence, however not for a complex flow field such as a cyclone.

To bridge the gap in the model validation, a challenging analytical flow field is presented which contains the prominent physics present in the cyclone fluid flow from Section 2.1. The fluid and particle scales are matched to the results from the cyclone CFD and Lagrangian particle tracking in Chapter 5. The analytical flow field is representative of the cyclone and allows a deeper understanding and validation of the model to be performed before applying it to the complex, 3D cyclone.

This chapter begins with introducing the analytical fluid flow field, with an analysis performed of the EE particle velocity field as a function of Stokes number. A finite volume Eulerian particle model implementation is discussed in Section 4.2.1 with a fully hand-coded model presented. The Eulerian model behaviour in this flow is discussed for different discretisations and Stk and in particular how the model can be broken or invalidated. Lagrangian particle tracking is performed as a benchmark for comparison with the Eulerian results, which allows both the accuracy to be assessed and any numerical issues to be characterised. This new thorough understanding of the model behaviour informs the implementation for the cyclone flow in the final body of work.

4.1 Taylor-Green Vortex

Before the EE method is used to convect a particulate phase in the cyclone, the model is validated on a simpler test flow not seen from literature. The test flow is analytical and ensures the model is implemented correctly. It also provides numerical insight including behaviour at singularities and testing the range of validity. The steady Taylor-Green vortex is an analytical solution of the Navier-Stokes equations [172], describing a periodic, incompressible flow consisting of counter-rotating vortices. Owing to the analytical nature, this flow field has been used in the validation and accuracy of CFD codes [173]. In 2D, the steady fluid velocity field can be expressed as

$$u_i = u_{mag} \begin{pmatrix} \cos(ax)\sin(ay) \\ -\sin(ax)\cos(ay) \end{pmatrix}, \tag{4.1}$$

where u_{mag} is the maximum flow velocity (the amplitude) in the domain and a is a constant which determines the frequency of the vortices. The flow has a period of $\frac{2\pi}{a}$, with the diameter of an eddy given as half the period

$$l = \frac{\pi}{a}. \tag{4.2}$$

A vector plot of the flow field is provided in Figure 4.1, centred at $\boldsymbol{x} = \begin{pmatrix} 0 \\ 0 \end{pmatrix}$. The Taylor-Green vortex features fluid gradients and strong streamline curvature, which provide a useful benchmark for validation for the cyclone CFD in Chapter 5. This is the same flow field used by Druzhinin and Elghobashi in their two-fluid model from Section 2.3 which posed numerical issues. The Taylor-Green flow field therefore presents a difficult challenge numerically for this Eulerian model.

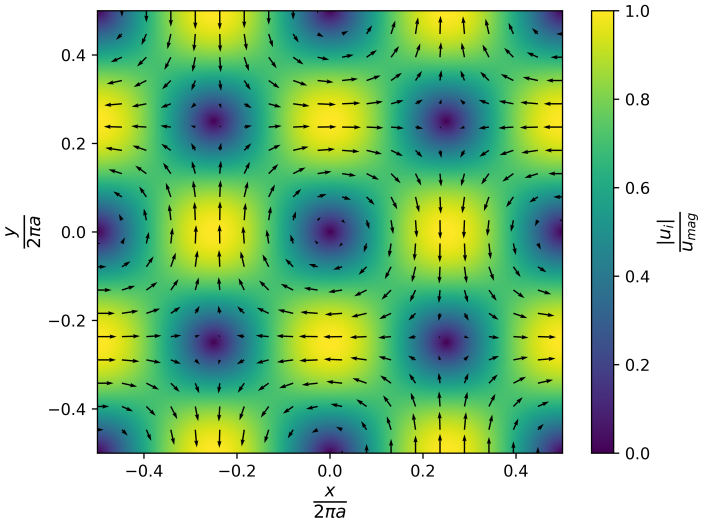

Figure 4.1: Taylor-Green Vortex flow. Black arrows represent the direction of the local fluid velocity vector, with the background colour representing the local flow speed. The fluid velocity is normalised by u_{mag} and the domain is normalised by the period to provide a unit square domain.

An eddy time scale can be defined as

$$\tau_f = \frac{l}{u_{mag}} = \frac{\pi}{u_{mag} a}. \tag{4.3}$$

The fluid time scale enables a particle Stokes number (Eq. 1.22) to be defined using the particle relaxation time (Eq. 1.24). As the fluid flow field is analytical and differentiable everywhere, the particle EE velocity field is also analytical. The EE particle velocity field for the steady Taylor-Green vortex with no gravity can be derived from substituting Eq. 4.1 and its spatial derivatives into Eq. 2.81 to produce

$$v_i = u_{mag} \begin{pmatrix} \cos(ax)\sin(ay) + \frac{1}{2}\tau_p u_{mag} a \sin(2ax) \\ -\sin(ax)\cos(ay) + \frac{1}{2}\tau_p u_{mag} a \sin(2ay) \end{pmatrix}. \tag{4.4}$$

The EE particle velocity field approaches the fluid velocity as $\tau_p \to 0$. In the limit of large τ_p, the particle velocity field is dominated by the doubled frequency terms. The two limiting cases balance when $\tau_{p,bal} = \frac{2}{u_{mag} a}$,

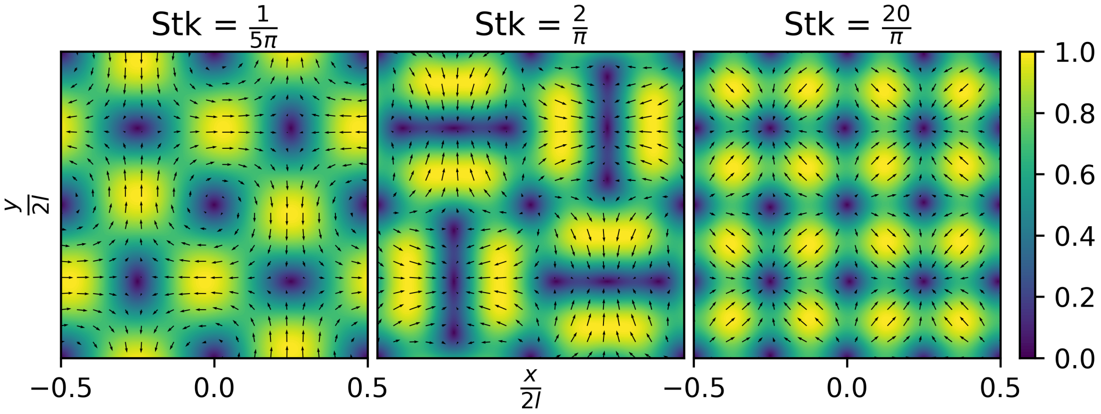

Figure 4.2: EE Taylor-Green flow field for Stokes numbers of $0.1Stk_{bal}$, Stk_{bal} and $10Stk_{bal}$. Black arrows represent the direction of the local particle velocity vector, with the background colour representing the local particle speed normalised by the maximum particle speed in the domain.

giving a Stokes number of $Stk_{bal} = \frac{2}{\pi}$. Around this balanced Stokes number, the particle velocity field changes shape as shown in Figure 4.2. As Stokes number increases, the velocity vector rotates and produces a flow field which no longer consists of counter-rotating vortices. The centre of the fluid eddy at $(x, y) = (0, 0)$ now is a source with velocity vectors diverging away from the centre. Where fluid vortices cancelled each other out at $(x, y) = \left(\frac{\pi(2n-1)}{2a}, \frac{\pi(2m-1)}{2a}\right)$ where n and m are integers, these become sinks with the velocity vectors pointed directly at the centres.

The double frequency dominated particle flow field in Figure 4.2 is unphysical and occurs when τ_p becomes too large. The upper limit for τ_p, which provides a unique EE solution, is found from Eqs. 2.82 and 2.83. For the Taylor-Green flow, the particle velocity field strain rate tensor is

$$S^v_{ij} = \begin{pmatrix} -u_{mag} a \sin(ax)\sin(ay) + \tau_p u_{mag}^2 a^2 \cos(2ax) & 0 \\ 0 & u_{mag} a \sin(ax)\sin(ay) + \tau_p u_{mag}^2 a^2 \cos(2ay) \end{pmatrix}. \tag{4.5}$$

The upper limit for τ_p where the flow field has a unique Equilibrium Euler method particle velocity can be determined for this Taylor-Green vortex by solving the characteristic equation

$$\lambda_s^2 - \tau_p u_{mag}^2 a^2 \left(\cos(2ax) + \cos(2ay)\right) \lambda_s - u_{mag}^2 a^2 \sin^2(ax)\sin^2(ay) + \\ \tau_p u_{mag}^3 a^3 \sin(ax)\sin(ay)\left(\cos(2ax) - \cos(2ay)\right) + \tau_p^2 u_{mag}^4 a^4 \cos(2ax)\cos(2ay) = 0. \tag{4.6}$$

The regions of greatest compressive strain for the Taylor-Green flow field occur periodically at $(x, y) = \left(\frac{\pi(2n-1)}{2a}, \frac{\pi(2m-1)}{2a}\right)$ where n and m are integers as before. From the symmetry of the flow field we can focus on just one region which will be $(x, y) = \left(\frac{\pi}{2a}, \frac{\pi}{2a}\right)$ for which $n = m = 1$. The characteristic equation simplifies to a quadratic equation for λ_s

$$\lambda_s^2 + 2\tau_p u_{mag}^2 a^2 \lambda_s - u_{mag}^2 a^2 + \tau_p^2 u_{mag}^4 a^4 = 0. \tag{4.7}$$

The characteristic equation has solution

$$\lambda_s = -\tau_p u_{mag}^2 a^2 \pm u_{mag} a, \tag{4.8}$$

for which the most negative eigenvalue is $\lambda_s = -\tau_p u_{mag}^2 a^2 - u_{mag} a$. From Eq. 2.83, a unique EE flow field must satisfy

$$\tau_p^2 + \frac{1}{u_{mag} a}\tau_p - \frac{1}{u_{mag}^2 a^2} < 0. \tag{4.9}$$

This equation has roots

$$\tau_p < \frac{-1 \pm \sqrt{5}}{2 u_{mag} a}. \tag{4.10}$$

The particle relaxation time is strictly positive, therefore we take the positive solution to provide the uniqueness criterion for the flow field as

$$\tau_{p,max} < \frac{\sqrt{5}-1}{2u_{mag}a}. \tag{4.11}$$

If $u_{mag}a = 1$, the uniqueness criterion yields the negative reciprocal of the golden ratio $\frac{\sqrt{5}-1}{2}$. Eq. 4.11 provides a validity limit for τ_p for a Taylor-Green flow field with specific u_{mag} and a. The validity limit for Stokes number is

$$Stk_{max} = \frac{\tau_{p,max}}{\tau_f} = \frac{\sqrt{5}-1}{2\pi}. \tag{4.12}$$

This uniqueness criterion informs us that of the particle flow fields presented in Figure 4.2, only the lowest Stokes number flow field is a valid solution. As $Stk_{max} < Stk_{bal}$, EE particle velocity fields which introduce new flow structures seen in Figure 4.2 will not be considered as they formally do not meet the uniqueness criterion.

For comparison, the MEE particle velocity in Eq. 2.84 can be calculated in the Taylor-Green flow. From Section 2.3.2 this velocity field specification is expected to produce anomalously large values of velocity due to the large compressive strain as Stk increases. The MEE velocity in a 2D Taylor-Green flow is

$$\begin{aligned} v_i = {} & u_{mag}\begin{pmatrix}\cos(ax)\sin(ay)\\ -\sin(ax)\cos(ay)\end{pmatrix} \\ & + \begin{pmatrix}1-\tau_p u_{mag}a\sin(ax)\sin(ay) & -\tau_p u_{mag}a\cos(ax)\cos(ay)\\ \tau_p u_{mag}a\cos(ax)\cos(ay) & 1+\tau_p u_{mag}a\sin(ax)\sin(ay)\end{pmatrix}^{-1}\begin{pmatrix}\frac{1}{2}\tau_p u_{mag}^2 a\sin(2ax)\\ \frac{1}{2}\tau_p u_{mag}^2 a\sin(2ay)\end{pmatrix}. \end{aligned} \tag{4.13}$$

The MEE particle velocity fields are plotted in Figure 4.3 for the same choice of Stk as shown in Figure 4.2. For the low Stokes number case of $Stk = 0.1Stk_{bal}$, the flow field appears physical. However for the two larger Stokes numbers, the particle velocity blows up in specific regions where the matrix to be inverted is expected to be close to singular. The absolute value of the determinant of $\boldsymbol{I} + \tau_p\left(\nabla\boldsymbol{u}\right)^T$ is provided in Figure 4.4 which shows that the matrix is close to singular along the almost diagonal lines for $Stk = \frac{20}{\pi}$. The large velocities observed in Figure 4.3 can be seen to lie on these diagonal lines in Figure 4.4 at the same Stokes number. At the intermediate Stokes number of $Stk = \frac{2}{\pi}$, the points of anomalously large velocity are situated closer to the regions of maximum compressive strain.

To further investigate the cause of the vanishing determinants along the diagonal lines in the Taylor-Green flow, the inverse in Eq. 4.13 is evaluated analytically from the determinant and adjugate matrix to provide the MEE particle velocity field in the Taylor-Green flow as

$$\begin{aligned} v_i = {} & u_{mag}\begin{pmatrix}\cos(ax)\sin(ay)\\ -\sin(ax)\cos(ay)\end{pmatrix} \\ & + \Psi\begin{pmatrix}\sin(2ax) + \tau_p u_{mag}a\left(\sin(ax)\sin(ay)\sin(2ax) + \cos(ax)\cos(ay)\sin(2ay)\right)\\ \sin(2ay) - \tau_p u_{mag}a\left(\cos(ax)\cos(ay)\sin(2ax) + \sin(ax)\sin(ay)\sin(2ay)\right)\end{pmatrix}, \end{aligned} \tag{4.14}$$

$$\Psi = \frac{\tau_p u_{mag}^2 a}{2 + \tau_p^2 u_{mag}^2 a^2\left(\cos(2ax) + \cos(2ay)\right)}. \tag{4.15}$$

Numerical issues in the MEE method occur in the Taylor-Green flow when the denominator of Ψ approaches zero. Setting the denominator equal to zero gives

$$\cos(2ax) + \cos(2ay) = -\frac{2}{\tau_p^2 u_{mag}^2 a^2}. \tag{4.16}$$

The RHS of Eq. 4.16 is always negative and the most negative value able to be reached by the LHS is -2. These minima first occur at the regions of greatest compressive strain as Stokes number is increased. To prevent division by zero in these regions, we require

$$\tau_p < \frac{1}{u_{mag}a}. \tag{4.17}$$

Using the definition of the fluid time scale from Eq. 4.3 provides the Stokes number limit for the MEE method in the Taylor-Green flow as

$$Stk < \frac{1}{\pi}. \tag{4.18}$$

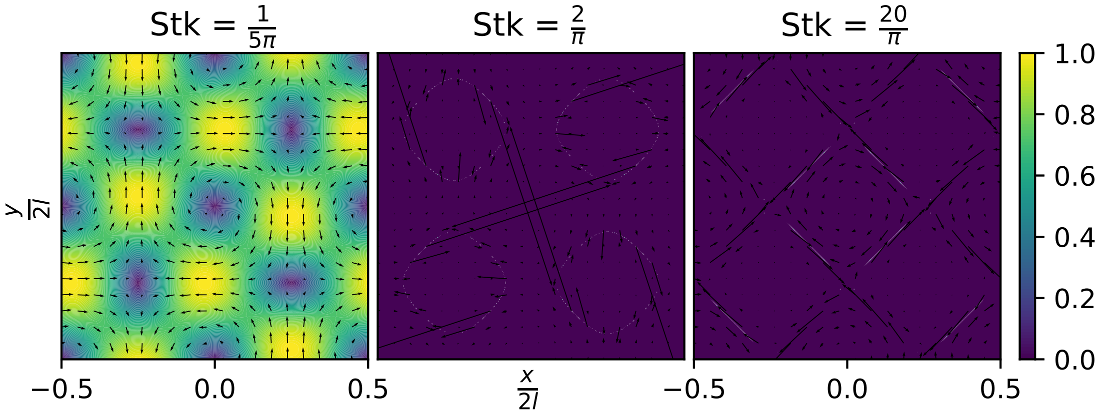

Figure 4.3: MEE Taylor-Green flow field for Stokes numbers of $0.1Stk_{bal}$, Stk_{bal} and $10Stk_{bal}$. Black arrows represent the direction of the local particle velocity vector, with the background colour representing the local particle speed normalised by the maximum particle speed in the domain.

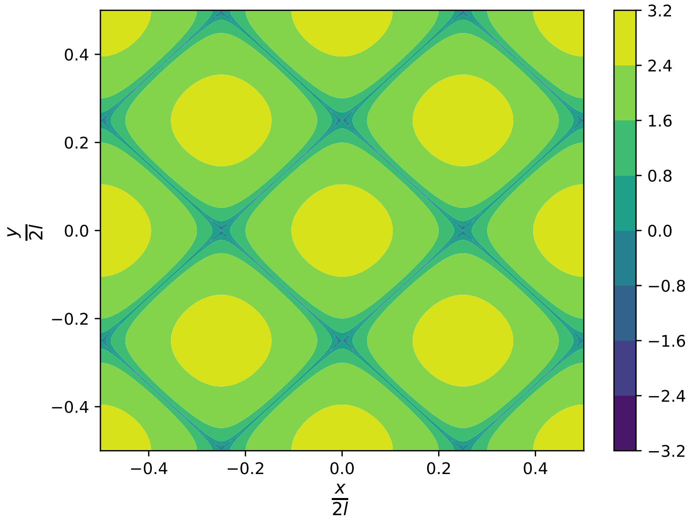

Figure 4.4: $\log_{10}(|\det(\boldsymbol{I} + \tau_p (\nabla \boldsymbol{u})^T)|)$ for the Taylor-Green flow field at a Stokes number of $10Stk_{bal}$.

This value is exactly half of the balanced Stokes number for the EE method and agrees with the anomalously large velocity values observed for Stokes numbers larger than this in Figure 4.3. This value is larger than the validity limit for the EE method, however at $Stk = \frac{1}{\pi}$, the EE method still provides a “reasonable” velocity field as it is less than the balanced Stokes number. However the MEE velocity is undefined at problem spots at this Stokes number. The denominator of Ψ may also lie close to zero at regions surrounding these spots and also produce spuriously large values for the Eulerian particle velocity. As Stk is increased above $\frac{1}{\pi}$, the regions where the denominator of Ψ equals zero moves away from the areas of maximum compressive strain. This explains the movement of the large values of velocity observed in Figure 4.3 as the Stokes number is increased. In more complicated flows from CFD, the matrix inverse will have to be attained numerically and the procedure is likely to fail at these moderate Stokes numbers. The MEE method is therefore limited to very small Stokes number and is not suitable for flows such as the cyclone presented in this work which may have Stokes numbers approaching unity.

4.2 Eulerian Model Implementation

The Eulerian particle model for the Taylor-Green flow is now implemented into a computer code. The Eulerian model is also later implemented into the CFD software ANSYS FLUENT for use in the cyclone in Chapter 5. A hand-coded implementation allows greater flexibility in checking for errors as all program variables are able to be accessed, unlike when using the proprietary, closed-source software.

The governing equations of the Eulerian model are presented and discretised using the finite-volume method to produce a linear system of equations to be solved for the volume fraction of the particulate phase in Section 4.2.1. This is applied to the Taylor-Green flow, with the determination and implementation of diffusion coefficients for the volume fraction discussed in Section 4.2.2.

4.2.1 Finite Volume Discretisation

We begin discussing the motivation behind the choice of discretisation and solution method for the Eulerian model, before listing off the discretisation equations. The unsteady transport equation for the volume fraction of a particulate phase convected by the EE particle velocity with diffusion is given by Eq. 2.86, which is a PDE. There is no analytical solution to this, so an approximate numerical solution is sought instead. A common numerical method for solving such a transport equation is the finite volume method (FVM). In the FVM, the solution domain is discretised into a mesh of non-overlapping control volumes called cells and the conservative form of the equation is solved on each computational cell [32]. A key advantage to this method is that it exhibits global conservative properties, no matter how coarse the mesh is [174].

The FVM requires that the PDE be cast into a linear system of equations of the form $a\alpha = b$, where a is the matrix of coefficients, α is an array holding the volume fraction at each cell centroid and b is an array containing the explicit source term for each cell. Each individual linear equation arises from the discretisation and linearisation of the governing equation for each computational cell.

In discretising the domain into cells, the solution variables are stored at the cell centroids. These cell centroid values are an approximation of the mean value over the cell to second-order spatial accuracy [32]. The convection/diffusion volume integral is cast into a surface integral across the cell from the divergence theorem. These volume and surface integrals in the PDE require approximation to obtain algebraic equations for each cell.

The surface integrals can be expressed as a sum of integrals over each planar face of the cell. In evaluating the integral on a face, the distribution of the integrand along the face is unknown. The distribution is replaced with a mean value across the face and the integral remains exact. The face centroid value is used as a second-order accurate approximation to the mean value on the face, in an analogous fashion to the cell centroid values. The value of the solution at the face centroid is unknown as the solution variables are stored at the cell centroids. Interpolation formulae are used to estimate the face centroid values from the neighbouring cell centroid values.

A simple, first-order accurate method of interpolating the face centroid values is by using upwind differencing. This approximates the value of the variable at the face as the cell centroid value of the cell upwind of the face [174]. A major drawback of this method is that it exhibits false-diffusion where flow is oblique to the face. This results in gradients becoming smeared-out and can require fine grids to reduce the relative strength of this. A second-order method for interpolating the face value is by central differencing (linear interpolation) between the two neighbouring cells. This method does not suffer from false-diffusion like the upwind scheme, however it can produce unbounded oscillatory solutions. This instability arises when the local Péclet number of the cell is greater than 2 [174]. For convection-dominated problems, central differencing cannot be used and the upwind scheme is preferred as it provides bounded, realistic results independent of Péclet number.

Additional cell neighbours can be included in the interpolation formulae. This increases the size of the computational molecule but requires more computational effort. One such method is the second-order upwind scheme, which can be used to provide a more accurate prescription for the face value than first-order upwind. This involves a Taylor-series expansion about the cell centroid, in which calculating the gradient involves neighbouring cells. Another scheme known as QUICK provides a weighted average of the second-order upwind and central differencing schemes [175]. Both of these higher-order methods can produce unbounded solutions and are unlikely to work in this set-up due to the lack of diffusion (large Péclet numbers) without some form of limiter.

For the volume integrals, the integration is evaluated as the product of the mean value of the integrand with the cell volume [32]. The mean value of the integrand is approximated with the cell centroid value which is second-order accurate.

For unsteady problems, the time derivatives must be discretised. This can be done explicitly in terms of the current solution values or implicitly using future solution values. Explicit time stepping schemes require small time steps for stability. This is determined in a 1D situation by the Courant number defined as [32]

$$C_{\text{num}} = \frac{u\Delta t}{\Delta x}. \tag{4.19}$$

Temporal stability is determined by the Courant-Friedrichs-Lewy (CFL) condition which for stability states $C_{\text{num}} < 1$. This strict requirement is not required for implicit time stepping which allows larger time steps to be taken whilst remaining stable. To avoid having to satisfy the CFL condition, implicit time stepping will be used. First and second-order time schemes can be used, with the second-order scheme requiring the solution values at the previous 2 time steps be kept in computer memory.

Finally, the source terms require discretisation. This requires linearisation of the source term S and the volume fraction α is placed into the form $S = S_c + S_p\alpha$, where S_c and S_p are the explicit and implicit parts of the source term respectively. The explicit term is placed directly into the b source term array in the discretisation equation whereas the implicit term is moved onto the main diagonal of the matrix of coefficients; thus increasing the number of terms on the diagonal and increasing the stability of the system.

Having discussed the method of discretisation, the equations are now presented. The unsteady transport equation for the volume fraction of a particulate phase convected by the EE particle velocity is given by Eq. 2.86, which expressed in conservative form with no diffusive sources reads

$$\int \frac{\partial \alpha}{\partial t} dV + \int \frac{\partial}{\partial x_i}(\alpha u_i)\, dV = \int \frac{\partial}{\partial x_i}\left(\tau_p\left(\frac{Du_i}{Dt} - g_i\right)\alpha\right) dV. \tag{4.20}$$

Here the transport equation is integrated over a volume V. The dimensions of each term are volumetric flow rate multiplied by the dimensionless scalar particle volume fraction, which from Section 2.3 is a conservation equation for particle mass within the volume. The convection volume integral can be recast into a surface integral by using the divergence theorem [176]

$$\int (\nabla \cdot \boldsymbol{u})\, dV = \int (\boldsymbol{u} \cdot \boldsymbol{n})\, dA. \tag{4.21}$$

In Eq. 4.21, A is the area of the surface and $\boldsymbol{n}$ represents the normal to the area pointing out of the volume. It is also convenient to combine the area and unit normal into a single vector $A_i = An_i$. Applying the divergence theorem to the convection term yields

$$\int \frac{\partial \alpha}{\partial t} dV + \int \alpha u_i dA_i = \int \frac{\partial}{\partial x_i}\left(\tau_p\left(\frac{Du_i}{Dt} - g_i\right)\alpha\right) dV. \tag{4.22}$$

From the discretisation process, the matrix of coefficients is sparse, with the non-zero entries lying on and around the main diagonal. It is memory inefficient to store the entire sparse matrix, therefore only the main diagonals are stored as individual arrays in computer memory. The discretisation equation can be written as [174]

$$a_P\alpha_P = \sum_{nb} a_{nb}\alpha_{nb} + b_\alpha, \tag{4.23}$$

where the P subscript indicates the current cell for which the equation is for (the main diagonal), nb represents the neighbours to cell P and b_α are any explicit sources. The dimensions of Eqs. 4.23 and 4.22 must match. The a coefficients must have dimensions of the fluid volumetric flow rate; thus Eq. 4.23 is a discretised conservation equation.

We now discretise Eq. 4.22 for each cell, such that it can be placed into the form of Eq. 4.23. Starting with the convection term, the surface integral over the computational cell becomes a discrete sum over the cell faces F

$$\int \alpha u_i dA_i = \sum_F \int_A (\alpha u_i dA_i)_F\,. \tag{4.24}$$

The surface integral is approximated using the second-order accurate midpoint rule as [32]

$$\sum_F \int_A (\alpha u_i dA_i)_F \approx \sum_F (\alpha u_i A_i)_F\,, \tag{4.25}$$

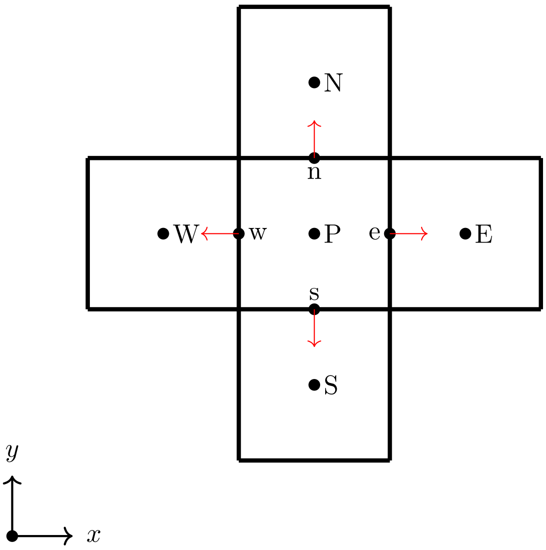

Figure 4.5: Compass notation of a computational cell in 2D centred at P with indices (i, j) with its four neighbouring cells. Cell centred values are denoted in uppercase, with face-centred values denoted with lowercase letters. Red arrows indicate the direction of the unit normal on each face.

where the face centroid values are used to approximate the mean value across the face. The convective term can be rewritten as

$$\sum_F (\alpha u_i A_i)_F = \sum_F \dot{V}_F \alpha_F, \tag{4.26}$$

with the volumetric flow rate and volume fraction matching the dimensions to the discretisation equation. Consider a 2D, uniform mesh aligned to the Cartesian coordinate system. The stencil surrounding the computational cell P is shown in Figure 4.5.

The volumetric flow rate at the face can be provided analytically in the Taylor-Green flow. In non-analytical flows, the volumetric flow rate at the face can be estimated by linearly interpolating between the adjacent cell centroids (central differencing). For face e, this can be written as [32]

$$\dot{V}_e \approx \dot{V}_E I_e + \dot{V}_P (1 - I_e) = \left((\boldsymbol{u})_E I_e + (\boldsymbol{u})_P (1 - I_e)\right) \cdot \boldsymbol{A}_e, \tag{4.27}$$

with the interpolation factor defined as

$$I_e = \frac{|\boldsymbol{x}_e - \boldsymbol{x}_P|}{|\boldsymbol{x}_E - \boldsymbol{x}_P|}. \tag{4.28}$$

The volume fraction can be upwinded on face e to give

$$\alpha_e = \begin{cases} \alpha_P, & \text{if } \dot{V}_e > 0 \\ \alpha_E, & \text{otherwise.} \end{cases} \tag{4.29}$$

The discretisation equation coefficients for convection, using first-order upwinding for the volume fraction and central differencing for the volumetric flux for a cell P, located at grid points (i, j) is

$$a_E^{i,j} = \max(-\dot{V}_e), \tag{4.30}$$

$$a_W^{i+1,j} = \max(\dot{V}_e), \tag{4.31}$$

$$a_N^{i,j} = \max(-\dot{V}_n), \tag{4.32}$$

$$a_S^{i,j+1} = \max(\dot{V}_n), \tag{4.33}$$

where the superscripts indicate the grid point which the coefficient applies to. The i and j indices reference the cell index along the positive x and y directions respectively. For the east face of cell P, the mass flow through the face provides a_E for cell P and a_W for the cell east of P. Similarly for the north face, the volumetric flow through the face provides a_N for cell P and a_S for the cell south of P. After looping over all the cells, the central coefficient for each cell is given by

$$a_P^{i,j} = a_E^{i,j} + a_W^{i,j} + a_N^{i,j} + a_S^{i,j}. \tag{4.34}$$

As mentioned at the start of this section, first-order upwind is overly diffusive and will smear-out sharp gradients in the volume fraction. A higher-order face interpolation method such as central differencing will fail with this model due to the Péclet number tending towards infinity from the lack of diffusion. Use of higher-order face interpolation schemes, such as second-order upwind, may be possible to use in this work from the addition of flux-limiters to ensure the scheme is total variation diminishing (TVD) [177]. A second-order upwind scheme can be written as [178]

$$\alpha_e = \alpha_P + (\nabla \alpha)_P \cdot (\boldsymbol{x}_f - \boldsymbol{x}_P), \tag{4.35}$$

where the discretisation of the gradient operator is discussed later in this section. The consequences of using these schemes is discussed in Section 4.3.

The source term is linearised and placed into the form $S_\alpha = S_c + S_p\alpha$, with the implicit term moved onto a_P if and only if $S_p < 0$. The explicit term remains on the RHS to provide

$$\left(\sum_{nb} a_{nb} - S_p\right)\alpha_P = \sum_{nb} a_{nb}\alpha_{nb} + S_c. \tag{4.36}$$

To linearise the source term and place it into the above form, the source term volume integral is approximated by the cell centroid values multiplied by the cell volume

$$S_\alpha \approx \frac{\partial}{\partial x_i}\left(\tau_p\left(\frac{Du_i}{Dt} - g_i\right)\alpha\right)_P \Delta V_P. \tag{4.37}$$

The term inside the divergence operator can be simplified. From the definition of the EE velocity (Eq. 2.81) we have

$$\tau_p\left(\frac{Du_i}{Dt} - g_i\right) = u_i - v_i = -w_i, \tag{4.38}$$

where w_i is the relative velocity vector between the EE particle velocity and the fluid velocity. Substitution into Eq. 4.37 yields

$$S_\alpha = -\frac{\partial}{\partial x_i}(w_i\alpha)_P \Delta V_P. \tag{4.39}$$

We now present an explicit formulation for the source term. The terms inside the derivative of the source term are saved as separate variables for each coordinate direction.

$$S_x = -w_x\alpha, \tag{4.40}$$
$$S_y = -w_y\alpha, \tag{4.41}$$
$$S_z = -w_z\alpha \tag{4.42}$$

to provide the complete source term

$$S_\alpha = \left(\frac{\partial S_x}{\partial x} + \frac{\partial S_y}{\partial y} + \frac{\partial S_z}{\partial z}\right)_P \Delta V_P. \tag{4.43}$$

The gradients themselves require approximation. A common method for discretising the gradient operators is by a modified version of the divergence theorem, which for a scalar ψ reads

$$\int \nabla\psi dV = \int \psi \boldsymbol{n} dA. \tag{4.44}$$

The gradient of ψ at cell P is discretised by the weighted sum of the neighbouring cells

$$(\nabla\psi)_P = \frac{1}{\Delta V_P}\sum_f \psi_f \boldsymbol{A}_f, \tag{4.45}$$

with the face values requiring interpolation. These face values can be simply estimated by linear interpolation, giving rise to the Green-Gauss Cell-Based gradient scheme. The discretised gradients for a 2D mesh aligned with the coordinate system become

$$\begin{aligned}\left(\frac{\partial S_x}{\partial x}\right)_P &\approx \frac{1}{\Delta V_P}\left(S_{x_e} n_e A_e + S_{x_w} n_w A_w\right)\\ &\approx \frac{1}{\Delta V_P}\Big(S_{x_P}\big((1-I_e)\,n_e A_e + (1-I_w)\,n_w A_w\big) + S_{x_E} I_e n_e A_e + S_{x_W} I_w n_w A_w\Big),\end{aligned} \tag{4.46}$$

$$\begin{aligned}\left(\frac{\partial S_y}{\partial y}\right)_P &\approx \frac{1}{\Delta V_P}\left(S_{y_n} n_n A_n + S_{y_s} n_s A_s\right)\\ &\approx \frac{1}{\Delta V_P}\Big(S_{y_P}\big((1-I_n)\,n_n A_n + (1-I_s)\,n_s A_s\big) + S_{y_N} I_n n_n A_n + S_{y_S} I_s n_s A_s\Big),\end{aligned} \tag{4.47}$$

$$\begin{aligned}\left(\frac{\partial S_z}{\partial z}\right)_P &\approx \frac{1}{\Delta V_P}\left(S_{z_t} n_t A_t + S_{z_b} n_b A_v\right)\\ &\approx \frac{1}{\Delta V_P}\Big(S_{z_P}\big((1-I_t)\,n_t A_t + (1-I_b)\,n_b A_b\big) + S_{z_T} I_t n_t A_t + S_{z_B} I_b n_b A_b\Big).\end{aligned} \tag{4.48}$$

This provides the complete source term as

$$\begin{aligned}S_\alpha = S_{x_P}&\big((1-I_e)\,n_e A_e + (1-I_w)\,n_w A_w\big) + S_{x_E} I_e n_e A_e + S_{x_W} I_w n_w A_w\\ &+ S_{y_P}\big((1-I_n)\,n_n A_n + (1-I_s)\,n_s A_s\big) + S_{y_N} I_n n_n A_n + S_{y_S} I_s n_s A_s\\ &\qquad + S_{z_P}\big((1-I_t)\,n_t A_t + (1-I_b)\,n_b A_b\big) + S_{z_T} I_t n_t A_t + S_{z_B} I_b n_b A_b.\end{aligned} \tag{4.49}$$

The linearised source term now needs to be put into the form $S = S_c + S_p\alpha$. The discretised version of the explicit source term (Eq. 4.49) for the Taylor-Green flow on the uniform mesh becomes

$$S_\alpha = S_c = \frac{A}{2}\left(S_{x_E} - S_{x_W} + S_{y_N} - S_{y_S}\right) = \frac{A}{2}\Big((w_x\alpha)_W - (w_x\alpha)_E + (w_y\alpha)_S - (w_y\alpha)_N\Big), \tag{4.50}$$

with $S_p = 0$.

For an implicit treatment of the source term, we use the product rule for differentiation on Eq. 4.39 to provide

$$S_\alpha = -\left(w_i\frac{\partial\alpha}{\partial x_i} + \alpha\frac{\partial w_i}{\partial x_i}\right)_P \Delta V_P. \tag{4.51}$$

The second term on the RHS is a linear function of volume fraction, making an implicit source term treatment possible. The implicit and explicit parts of the source term become

$$S_p = \min\left(-\left(\frac{\partial w_i}{\partial x_i}\right)_P, 0\right)\Delta V_P \tag{4.52}$$

$$S_c = -w_i\frac{\partial\alpha}{\partial x_i}\Delta V_P + \max\left(-\frac{\partial w_i}{\partial x_i}, 0\right)\Delta V_P\alpha_P, \tag{4.53}$$

with the gradients discretised using the Green-Gauss Cell-Based scheme. The implicit implementation of the source term for the Taylor-Green flow on the uniform mesh becomes

$$S_p = \min\left(-\frac{A}{2}\left(w_{x_E} - w_{x_W} + w_{y_N} - w_{y_S}\right), 0\right), \tag{4.54}$$

$$S_c = -\frac{A}{2}\left(w_x\left(\alpha_E - \alpha_W\right) + w_y\left(\alpha_N - \alpha_S\right)\right) + \max\left(-\frac{A}{2}\left(w_{x_E} - w_{x_W} + w_{y_N} - w_{y_S}\right), 0\right)\alpha_P. \tag{4.55}$$

Finally for the implicit temporal discretisation, the volume fraction is evaluated at the future time step [32]. For a backward Euler scheme

$$\int\frac{\partial\alpha}{\partial t}dV \approx \left(\frac{\Delta V}{\Delta t}\right)_P\left(\alpha_P^{n+1} - \alpha_P^n\right), \tag{4.56}$$

where Δt is the time step and the superscripts n and $n+1$ represent the value evaluated at the current and future time step respectively. The full discretisation equation for the unsteady volume fraction transport equation becomes

$$\left(\sum_{nb} a_{nb} + \left(\frac{\Delta V}{\Delta t}\right)_P - S_p\right)\alpha_P^{n+1} = \sum_{nb} a_{nb}\alpha_{nb}^{n+1} + \left(\frac{\Delta V}{\Delta t}\right)_P\alpha_P^n + S_c, \tag{4.57}$$

which provides

$$a_P = \left(\sum_{nb} a_{nb} + \left(\frac{\Delta V}{\Delta t} \right)_P - S_p \right), \tag{4.58}$$

$$b_\alpha = \left(\frac{\Delta V}{\Delta t} \right)_P \alpha_P^n + S_c, \tag{4.59}$$

with the neighbour coefficients specified from Eqs. 4.74 to 4.77 for a 2D flow. For 3D flow, the top T and bottom B cell neighbours are also considered for cell P as

$$a_T^{i,j,k} = \max(-\dot{V}_t, 0), \tag{4.60}$$

$$a_B^{i,j,k+1} = \max(\dot{V}_t, 0). \tag{4.61}$$

The linear system is solved in Python code using the point by point Gauss-Seidel method. In the point by point Gauss-Seidel method, each cell is visited in order and the solution variable is calculated by [174]

$$\alpha_{P,new}^{i,j} = \frac{\sum_{nb} a_{nb}^{i,j} \alpha_{nb}^{i,j} + b^{i,j}}{a_P^{i,j}}, \tag{4.62}$$

with α_{nb} continuously updated to hold the most up-to-date information. Numerical difficulties may arise from the explicit source term and the solution may require relaxing. A relaxation factor ξ_{relax} with $0 < \xi_{relax} \leq 1$ to limit the change in the solution at P from the previous solution $\alpha_{P,old}$ as

$$\alpha_P^{i,j} = \xi_{relax} \alpha_{P,new}^{i,j} + (1 - \xi_{relax}) \, \alpha_{P,old}^{i,j}. \tag{4.63}$$

Convergence is judged using the scaled residual defined as

$$R_{scaled} = \frac{\sum_{cells} \left| \sum_{nb} a_{nb} \alpha_{nb} + b - a_P \alpha_P \right|}{\sum_{cells} \left| a_P \alpha_P \right|}, \tag{4.64}$$

where the numerator is the absolute residual [174] which is then normalised.

4.2.2 Computational Set-up

The scales of the Taylor-Green simulation are chosen to be representative of the Kolmogorov scales seen by particles in the swirling cyclone flow in Chapter 5. The eddy length l and velocity u_{mag} scales are based on the cell volume weighted average of the Kolmogorov scales from the cyclone CFD in Chapter 5. From these, the flow parameter a can be calculated using Eq. 4.2. The particle density is set to $\rho_p = 2650 kg/m^3$ in line with Section 1.3.3 and τ_p is determined by the choice of Stk. Finally, τ_p provides the particle diameter from Eq. 1.21, where μ_f is given by the dynamic viscosity of air at standard conditions. The particle diameters are checked, such that the worst-case maximum Re_p seen by a particle is < 0.1 to ensure Stokes drag is valid and to ensure $d_p << l$ for the point-particle approximation. The simulation conditions are described in Table 4.1.

Quantity	**Value**
a	$\approx 35521 m^{-1}$
u_{mag}	$\approx 0.29283 ms^{-1}$
α_0	5×10^{-7}
T_f	$300K$
μ_f	$1.7894 \times 10^{-5} kgm^{-1}s^{-1}$
$\frac{\sqrt{5}-1}{2u_{mag}a}$	$\approx 5.94 \times 10^{-5} s$

Table 4.1: Simulation conditions for the 2D Taylor-Green flow. The final row represents the RHS of the uniqueness criterion (Eq. 4.11).

The Stokes numbers tested are those representative along Lagrangian particle trajectories, calculated *a posteriori* from Chapter 5. Values of $Stk = 1 \times 10^{-3}$ and $Stk = 1 \times 10^{-2}$ are used to represent the ensemble-averaged Stokes number for the $0.1 \mu m$ and $1 \mu m$ particles respectively. A stress-test of $Stk = 0.1$ is used to analyse how the model may break as the small Stokes number assumption becomes invalidated. This stress-test also allows methods of stabilising the volume fraction solution to be assessed. The parameters used for each

Stk	d_p (m)	τ_p (s)	$Re_{p,max}$
1×10^{-3}	$\approx 1.92 \times 10^{-7}$	$\approx 3.0 \times 10^{-7}$	≈ 0.0047
1×10^{-2}	$\approx 6.06 \times 10^{-7}$	$\approx 3.0 \times 10^{-6}$	≈ 0.015
1×10^{-1}	$\approx 1.92 \times 10^{-6}$	$\approx 3.0 \times 10^{-5}$	≈ 0.047

Table 4.2: Particulate phase parameters for the 2D Taylor-Green flow.

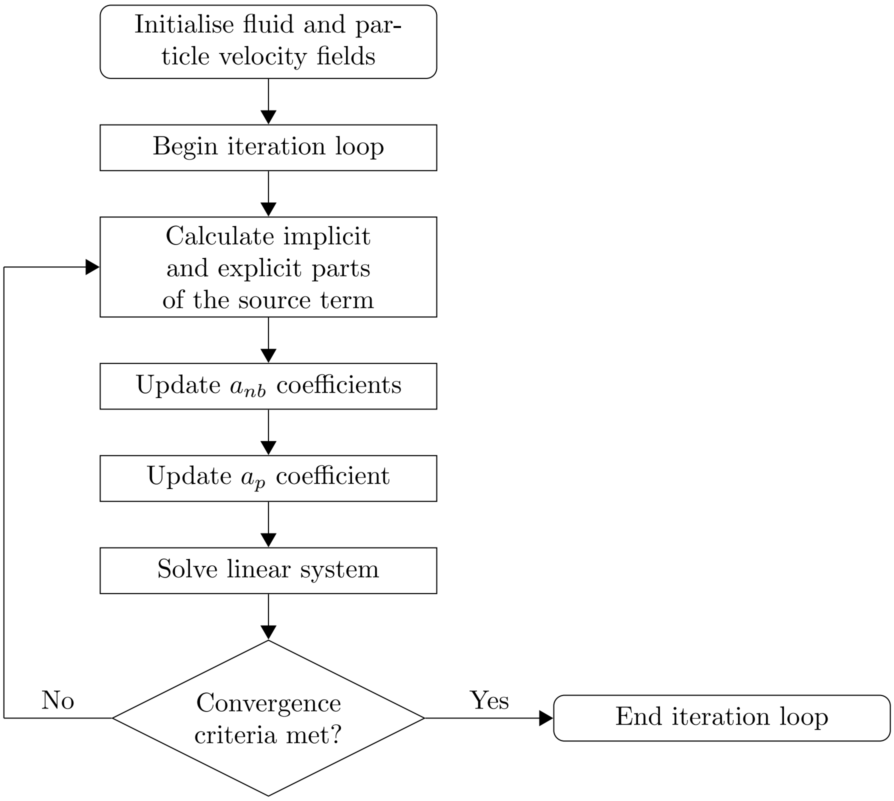

Figure 4.6: Solution process diagram for the steady particle volume fraction for a frozen fluid flow field.

particle phase are shown in Table 4.2. From τ_p, it is clear that only the Stokes numbers of 1×10^{-3} and 1×10^{-2} will give a valid EE velocity field from the criterion in Table 4.1, with the $Stk = 0.1$ having a larger time scale than the validity limit which is expected to present numerical difficulties.

A set of uniform square meshes were employed, with the coarsest and finest consisting of 4^2 and 1024^2 cells respectively. The domain is fully periodic from $(x, y) = (-l, -l)$ to $(x, y) = (l, l)$ and no special treatment at the boundaries is necessary. The particle volume fraction was initialised with a uniform distribution of α_0 everywhere to mimic the uniform random initial conditions for the Lagrangian particles to be tracked in Section 4.4. The fluid volumetric flow rates at the cell face centroids is exact for the Taylor-Green flow from Eq. 4.1 and no interpolation is required.

We now look to find the steady-state solution for the volume fraction given an initial uniform distribution using first-order upwinding for the convective term. The order for the solver process is shown in Figure 4.6. Both the analytical fluid and EE velocity are calculated at the cell centroids in the domain (which also provides $\boldsymbol{w}$ at every cell). As these values are constant, the discretisation coefficients a_E, a_W, a_N, a_S and a_P are constant when using the explicit source term; whereas S_p and S_c vary between iterations for the implicit treatment.

4.3 Eulerian Model Numerical Tests

The transport equation for volume fraction is solved numerically in the 2D Taylor-Green flow using the FVM discretisation from Section 4.2 for a variety of mesh sizes and Stokes numbers. In this section, a mesh independence study is performed by monitoring the shape of the volume fraction distribution. Eulerian particle velocity and volume fraction plots will be provided later for the comparison with Lagrangian results in Section 4.5.

The volume fraction distribution is two dimensional, therefore to aid in quantifying the shape of the distribution, information relating to the first four moments (Eq. 2.53) of the radial distribution of the volume fraction are presented. These are the mean radial position, standard deviation, skewness and kurtosis. The radial component r is given by the polar transformation $r = \sqrt{x^2 + y^2}$ and therefore the centre coincides with the Cartesian origin at $(x, y) = (0, 0)$ which is the centre of Figure 4.1. The mean radial position is expressed in terms of the first raw moment and discretised by

$$\langle r \rangle = \frac{\int_{-\infty}^{\infty} r\alpha(r)dr}{\int_{-\infty}^{\infty} \alpha(r)dr} \approx \frac{\sum_{i=1}^{N}\sum_{j=1}^{N} r^{i,j}\alpha^{i,j}}{\sum_{i=1}^{N}\sum_{j=1}^{N} \alpha^{i,j}}, \tag{4.65}$$

where N is the number of grid points in each coordinate direction. The remaining central moments are discretised the same way. The standard deviation is the square root of the second central moment

$$\text{standard deviation} = \sqrt{M_2}. \tag{4.66}$$

This provides the average radial distance from the mean. The skewness and kurtosis represent the lack of symmetry and tail extremity [180] of the distribution respectively as [134]

$$\text{skewness} = \frac{M_3}{M_2^{\frac{3}{2}}}, \tag{4.67}$$

$$\text{kurtosis} = \frac{M_4}{M_2^4}. \tag{4.68}$$

A benchmark set-up with $Stk = 1 \times 10^{-3}$ on a 128^2 grid with no diffusion is used to check whether both the explicit and implicit implementations of the source term converge to the same solution. Both methods required a different number of iterations to reach convergence (5962 and 6076 for the explicit and implicit formulations respectively), which was judged to be when the normalised residual (Eq. 4.64) is less than 1×10^{-14}. Additionally, the moments of the radial volume fraction distribution were monitored over each iteration to check that stationary values were reached. Figure 4.7 shows these values for both source term implementations, which converged in an almost identical manner. Both source term implementations converge to the same solution and a convergence criterion of 1×10^{-7} indicates a converged solution. This will be selected as the convergence criterion in all subsequent results. As both implementations of the source term provide the same solution, only the implicit formulation results will be shown in the following studies due to its increased solver stability.

A mesh independence study is now performed. Grids ranging from 4^2 to 1024^2 were considered in this study, for the 3 Stokes numbers from Table 4.2. For $Stk = 0.1$, numerical instability and negative volume fractions necessitated the use of a relaxation factor for the Gauss-Seidel solver (Eq. 4.63). On all grids finer than 4^2, relaxation was not enough to prevent negative values of volume fraction from occurring in the domain. An explicit source term formulation also created negative volume fractions on fine grids for the middle-ground $Stk = 1 \times 10^{-2}$ which is not shown in Figure 4.8. The mean and central moments as a function of mesh size are shown in Figure 4.8, with the single $Stk = 0.1$ result not included. The skewness of the volume fraction radial distribution is the only statistic which reaches a mesh-independent value for either choice of Stokes number.

A mesh-independent result cannot be obtained as the finer the mesh, the greater the build-up of volume fraction in regions of greatest compressive strain, with no mechanism present to prevent this continuous build-up. As the mesh becomes finer, larger volume fraction gradients are present which increase the strength of the source term and decrease the numerical stability of the system. As Stk is increased, the numerical stability of the system decreases due to the increasing strength of the source term. Considering the changes in the EE flow field from Figure 4.2, the increase in Stk causes the regions of maximum compressive strain to become sinks in the particle velocity field. This enhances the entrainment of volume fraction to these regions and creates larger gradients at these problem spots. As Stk is increased, this accumulation of volume fraction at these sinks becomes ever-stronger.

The use of second-order upwind as a higher-order face interpolation scheme caused the solution to diverge over iteration, even for a low Stokes number of $Stk = 1 \times 10^{-3}$ and a relaxation factor of 0.1, as expected from Section 4.2.1. The use of a flux limiter in tandem with the higher-order scheme was proposed to keep the

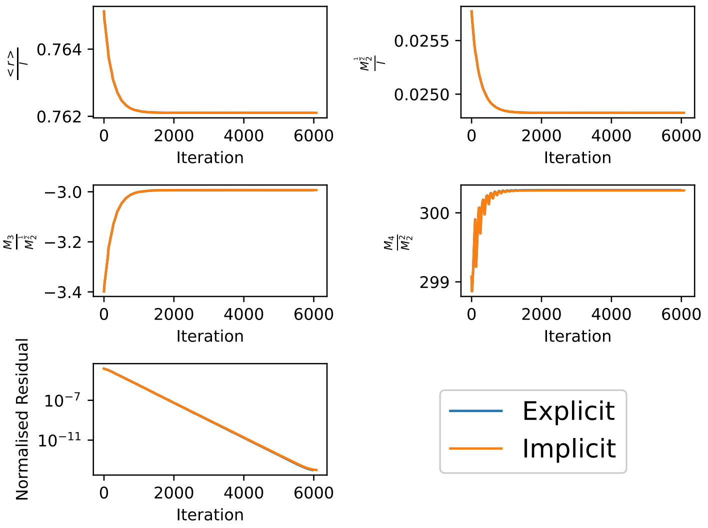

Figure 4.7: Normalised moments of the radial volume fraction distribution and residual for both source term implementations on a 128^2 uniform grid with no diffusion for $Stk = 1 \times 10^{-3}$.

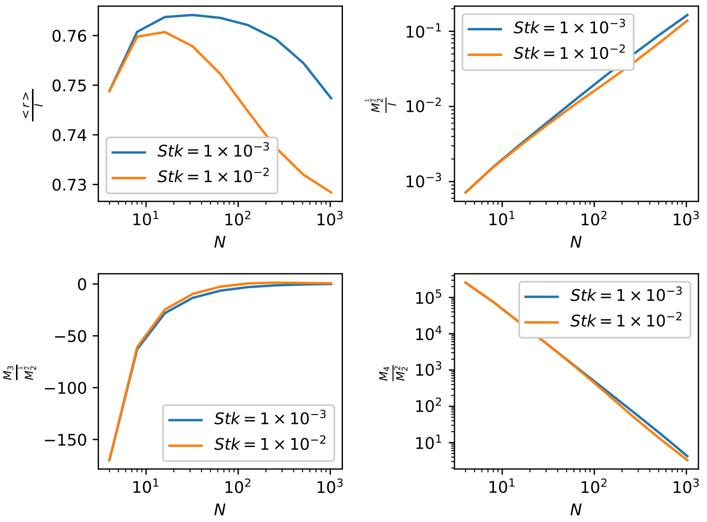

Figure 4.8: Normalised moments of the radial volume fraction distribution for both source term implementations on a variety of uniform grids with no diffusion for $Stk = 1 \times 10^{-3}$. The convergence criterion for the normalised residual was $< 1 \times 10^{-7}$.

solution bounded to decrease the likelihood of solver divergence whilst providing a higher-order estimate of the volume fraction at the cell faces. Two flux limiters were investigated in this work: MINMOD and SUPERBEE. The SUPERBEE flux limiter has good step resolution when faced with steep gradients however it tends to distort smooth solution profiles [177]. The MINMOD flux limiter is known to perform better in smooth profiles however it does so by being overly-diffusive [177].

The flux limiters were found to stabilise the solution and prevent the volume fraction from diverging to infinity. The unacceptable cost of this is the continuous reduction in total volume fraction in the domain over iteration. This results in convergence being obtained when there is zero particle volume fraction in the domain. This occurs because although the flux between two adjacent cells is limited (thereby reducing the amount of volume fraction convected), the source term is unaffected by this limiter which results in a net loss of volume fraction in cells where the flux is limited. The use of flux limiters to allow the use of higher-order face interpolation schemes will not converge to a physical solution and first-order upwind will have to be retained for the volume fraction transport equation in this work.

A steady-state solution for the volume fraction which is mesh independent could not be found for the examined Stokes numbers due to missing physics in the model. For every Stk, as the mesh is refined, the volume fraction increases without bound at the regions of greatest compressive strain. Lagrangian particles are now to be tracked in the same flow, mimicking the same Stk and Re_p as for this Eulerian study. The results using both the Eulerian and Lagrangian particle framework are then compared in Section 4.5, with the issues encountered with the Eulerian method discussed in terms of the Lagrangian steady-state results.

4.3.1 Diffusion Coefficients and Discretisation

The transport of particle volume fraction using the EE specification of the particle velocity field in the Taylor-Green flow failed at a Stokes number of 0.1. Physically, the diffusive behaviour of particle interactions such as from collisions, was neglected. Numerically, the absence of diffusion in the transport equation caused the source-dominated system to destabilise at this Stokes number. The effect of including some of the neglected physics relevant to the specific numerical scales tested via diffusion coefficients in the Taylor-Green flow is now explored.

For the diffusion coefficients for the volume fraction, the laminar (Brownian) diffusion coefficient (Eq. 1.32) is constant, as T_f is constant, throughout the domain in the Taylor-Green flow. The remaining diffusion coefficients can be normalised by this benchmark value to assess the relative strength of each source of particle diffusion.

When a turbulence model is employed for a computed flow field such as an LES, the diffusion of particles due to the unresolved scales can be modelled using a diffusion coefficient. A simpler prescription of the turbulent diffusion coefficient for LES (Eq. 2.99), which avoids dynamically determining C_s, can be obtained if the classical Smagorinsky model is used instead where both $Sc_t \approx 1$ and $C_s \approx 0.1$ are constant. In this 2D Taylor-Green flow, the turbulent diffusion can be tested by treating the flow field as a filtered LES flow field. There are no walls and $L = C_s \Delta x$ where Δx is the grid spacing and our assumed filter width. Like the Smagorinsky constant, the turbulent Schmidt number has no universal value; varying between 0.2 and 1.3 for RANS simulations of a wide range of flows [181]. In this model it will be assumed that $Sc_t \approx 1$. The particle velocity strain rate magnitude can be calculated analytically from the strain rate tensor of the particle velocity (Eq. 4.5). The square of the particle strain rate magnitude is given by

$$\left(S^v_{mag}\right)^2 = 4u^2_{mag}a^2\sin^2(ax)\sin^2(ay) + 2\tau_p^2 u^4_{mag}a^4\left(\cos^2(2ax)+\cos^2(2ay)\right) + 4\tau_p u^3_{mag}a^3\sin(ax)\sin(ay)\left(\cos(2ay)-\cos(2ax)\right). \quad (4.69)$$

As $\tau_p \to 0$, the particle strain rate magnitude approaches the fluid strain rate magnitude as expected ($S^u_{mag} = 2u_{mag}a\sin(ax)\sin(ay)$). The turbulent particle diffusion coefficient in Eq. 2.99 is proportional to the square of the filter width and the particle strain rate magnitude (Eq. 4.69 which is a complicated function of τ_p), whereas the Brownian diffusion coefficient in Eq. 1.32 is inversely proportional to the particle diameter. The turbulent diffusion coefficient is also a function of position, with the maximum and minimum values occurring in regions of greatest and smallest strain. The ratio of turbulent to laminar diffusion in the Taylor-Green flow provides the relative strengths of each type of particle diffusion caused by the carrier fluid. The distribution of this ratio for both the maximum and minimum regions against Stokes number is shown in Figure 4.9. This diffusion ratio is inversely proportional to the grid size squared; the effects of finer or coarser meshes can be found by applying this scaling law to the results in Figure 4.9. At points of least strain, the turbulent diffusion coefficient is directly proportional to Stokes number. This occurs as the only non-zero term of the strain rate magnitude, the second term in Eq. 4.69, yields $S^v_{mag} = 2\tau_p u^2_{mag}a^2$. For regions of greatest strain, only the first

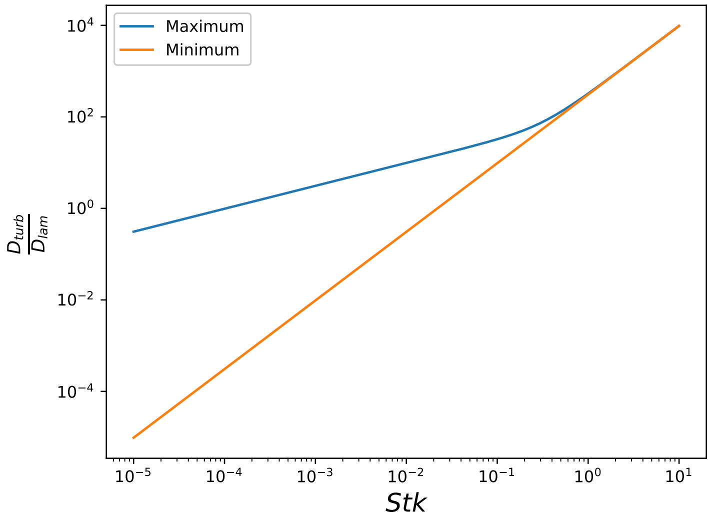

Figure 4.9: Particle diffusion coefficient ratio in the Taylor-Green flow as a function of Stokes number. The grid size is 128^2 and the fluid temperature is assumed to be $T_f = 300K$. The maximum values indicate the value of the diffusion coefficients evaluated at any of the regions of maximum compressive strain i.e. $(x, y) = \left(\frac{\pi}{2a}, \frac{\pi}{2a}\right)$ and the minimum values at regions of minimum compressive strain i.e. $(x, y) = (0, 0)$.

and third terms of Eq. 4.69 are non-zero, yielding $S^v_{mag} = 2\sqrt{u^2_{mag}a^2 + \tau_p^2 u^4_{mag} a^4}$. At regions of maximum strain at small Stk, the strain rate magnitude is dominated by the first term yielding $S^v_{mag} \approx 2u_{mag}a$. As $Stk > 0.1$, the strength of the second term begins to rival the first term, eventually overpowering it causing for large Stk, the strain rate magnitude to approach the same value as for regions of minimum strain.

From the diffusion ratio, it is clear that the strength of Brownian diffusion is weak compared to that of unresolved turbulent scales for large Stokes numbers except in regions with negligible velocity gradients at very low Stk. Looking ahead to the cyclone CFD in Chapter 5, the turbulent diffusion coefficient will be stronger in regions where the mesh is coarse such as the bin, helping to stabilise the solution in this region by increasing the size of the terms on a_P. In regions of very high strain such as the cone tip, the turbulent diffusion will be very large compared to Brownian diffusion alone. This extra stability may be necessary as the source term will become large in these regions and the constraint on Stk for the EE model may be invalidated.

The final source of particle diffusion considered is due to particle-particle collisions. From both the experimental evidence in Figure 1.2 and knowledge of the vortex core, this diffusion coefficient is expected to only be significant near to walls and by the cone tip of a cyclone due to the accumulation of particles and large velocity gradients in these regions. From Eq. 2.70, the collisional diffusion coefficient is expected to be proportional to the particle mean free path (provided by Eq. 2.69) and a representative velocity difference. This particle velocity difference across the cell can be estimated as the cell centroid value of the particle velocity strain rate magnitude multiplied by the cube root of the cell volume to provide

$$D_{\text{coll}} = \lambda_p < |\boldsymbol{V}| > = \frac{\sqrt{2}}{12} \frac{\Delta^{\frac{1}{3}} d_p}{\alpha g_0} S^v_{mag}. \tag{4.70}$$

One caveat to this diffusion coefficient is that the volume fraction cannot be zero in the domain. This is not expected to be a problem in the Taylor-Green flow, however this will be a problem in the cyclone. The relative strength of this diffusion coefficient compared to the turbulent diffusion is shown for a range of Stk in Figure 4.10. The expression in Eq. 4.70 yields an over-powering diffusion coefficient which is many orders of magnitude stronger than turbulent diffusion. In this dilute flow, this is not expected to be true.

The break-down of the collisional diffusion coefficient at zero volume fraction also highlights that as the particulate phase becomes more dilute, the collisional diffusion coefficient becomes larger. This is due to the increase of the particle mean free path with decreasing volume fraction (Eq. 2.69). Gidaspow presented arguments that the highest mean free path that a particle can achieve is equal to the diameter of its containing vessel [158]. For this work in determining the collisional length scale in a computational cell, the upper limit should be the cube root of the cell volume to provide the particle mean free path as

$$\lambda_p = \min\left(\frac{\sqrt{2}}{12} \frac{d_p}{\alpha g_0}, \Delta^{\frac{1}{3}}\right). \tag{4.71}$$

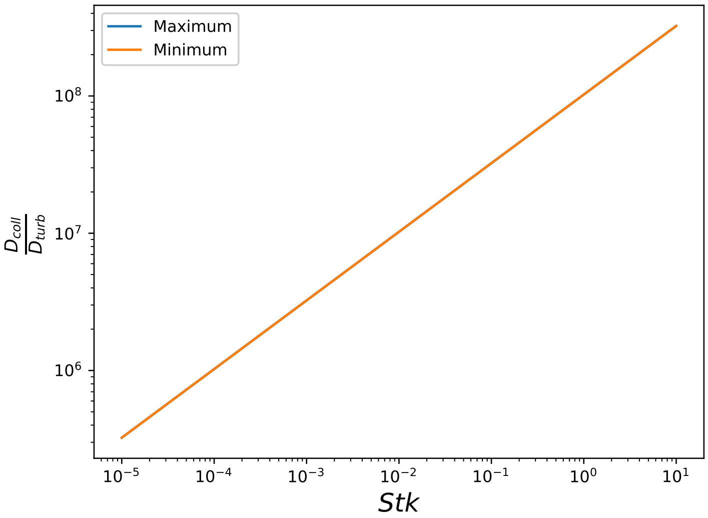

Figure 4.10: Particle diffusion coefficient ratio in the Taylor-Green flow as a function of Stokes number. The grid size is 128^2 and $\alpha = \alpha_0 = 5 \times 10^{-7}$ everywhere. The maximum values indicate the value of the diffusion coefficients evaluated at any of the regions of maximum compressive strain i.e. $(x, y) = \left(\frac{\pi}{2a}, \frac{\pi}{2a}\right)$ and the minimum values at regions of minimum compressive strain i.e. $(x, y) = (0, 0)$.

If the particle mean free path estimated from kinetic theory is greater than the grid-spacing, the collisional diffusion coefficient becomes proportional to the turbulent diffusion coefficient (differing by a factor of C_s^2). Despite this, they are representing two very different sets of physics. The turbulent diffusion coefficient is modelling the effects of the unresolved scales from an LES on the particle volume fraction, whereas the collisional diffusion coefficient is modelling the effects of particle-particle collisions due to the presence of shear.

The lack of a mesh-independent solution and the failure of a solution at larger Stokes numbers due to numerical instability in Section 4.3 presents a problem with the Eulerian method. So far the effects of diffusion, which are known to increase the stability of the solution, have been ignored. For the diffusion term, the discretisation equation for the uniform 2D stencil is

$$\sum_f \left(D_\alpha \frac{\partial \alpha}{\partial x_i} A_i \right)_f = A \left(\left(D_\alpha \frac{\partial \alpha}{\partial x} \right)_e - \left(D_\alpha \frac{\partial \alpha}{\partial x} \right)_w + \left(D_\alpha \frac{\partial \alpha}{\partial y} \right)_n - \left(D_\alpha \frac{\partial \alpha}{\partial y} \right)_s \right). \tag{4.72}$$

The diffusion coefficient D_α represents any diffusional contributions to the particle volume fraction. To calculate the volume fraction spatial derivatives, central differencing is employed using the cell centroid values on each side of the face. For face e

$$A \left(D_\alpha \frac{\partial \alpha}{\partial x} \right)_e \approx \frac{A}{\Delta x} D_e \left(\alpha_E - \alpha_P \right) = \Delta x D_e \left(\alpha_E - \alpha_P \right), \tag{4.73}$$

with the diffusion coefficient on the face able to be estimated using linear interpolation between the neighbouring cell centroids if it is not constant (for both the turbulent and collisional diffusion coefficients). For these two diffusion coefficients in the Taylor-Green flow, only the volume fraction at the cell face requires estimation using linear interpolation as the particle strain rate magnitude is given analytically from Eq. 4.69. The terms multiplying the α terms in Eq. 4.73 have dimensions of fluid volumetric flow rate and therefore provide the coefficients for the discretisation matrix due to diffusion. Combining upwind convection and central differencing for diffusion leads to the discretisation coefficients

$$a_E^{i,j} = \max(-\dot{V}_e, 0) + \Delta x D_e, \tag{4.74}$$

$$a_W^{i+1,j} = \max(\dot{V}_e, 0) + \Delta x D_e, \tag{4.75}$$

$$a_N^{i,j} = \max(-\dot{V}_n, 0) + \Delta x D_n, \tag{4.76}$$

$$a_S^{i,j+1} = \max(\dot{V}_s, 0) + \Delta x D_n. \tag{4.77}$$

The central coefficient a_P is again the sum of the neighbouring coefficients.

The mesh independence study is repeated with the inclusion of diffusion. Brownian diffusion alone, which was expected to be weak from Figure 4.9, has a negligible influence on the results. By pretending the flow is

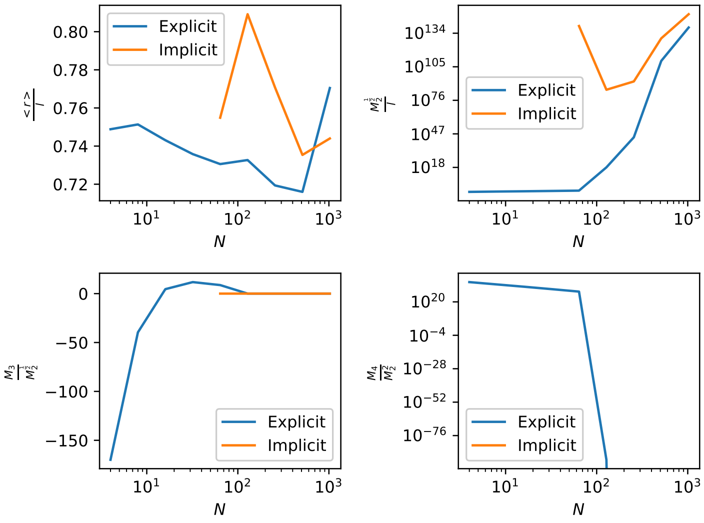

Figure 4.11: Normalised moments of the radial volume fraction distribution for both source term implementations on a variety of uniform grids with turbulent diffusion for $Stk = 1 \times 10^{-1}$. The convergence criterion for the normalised residual was $< 1 \times 10^{-7}$.

an LES and including the effects of an SGS diffusion (Eq. 2.99), the transport equation becomes solvable at a larger Stokes number of $Stk = 0.1$. For the 512^2 grid and finer, the volume fraction becomes so small in many cells that floating point underflow occurs and negative volume fractions are produced. This occurred for both source term implementations and small relaxation factors could not prevent this. To prevent this non-physical behaviour, the source term is set to zero in cell P if $\alpha_P < \frac{\alpha_0}{5 \times 10^{13}}$ (a value incredibly small). This allowed a solution to be found on the 512^2 grid, however numerical difficulties were still encountered for the finest 1024^2 grid, with the moments shown in Figure 4.11.

The turbulent diffusion is included in the original $Stk = 1 \times 10^{-3}$ set-up to check whether this aids in providing a mesh independent solution. No reduction in the relaxation factor was required and no limits on the volume fraction for the source term were imposed. The moments are shown in Figure 4.12, which follow the same trend as for the no-diffusion case, however the mean radial position shows a smaller range of values compared to the no-diffusion case due to the smearing effect of diffusion.

From Section 4.2.2, the effect of collisional diffusion in the Taylor-Green flow will be the same as turbulent diffusion. In every simulation performed in this section, the volume fraction was observed to accumulate in regions of maximum compressive strain. This echoes the phenomenon of the preferential accumulation of particles observed in isotropic turbulence introduced in Section 2.1.2, with Ferry and Balachandar observing an ever-increasing strength of the phenomenon with Stk using the EE method [166]. This provides extra insight into why the method encounters numerical difficulties at higher Stk.

Mass conservation was checked by calculating the ratio of the mean value of α in the domain and comparing that to α_0 in Figure 4.13. A ratio of unity indicates perfect conservation of volume fraction (and therefore of particle mass). For the lower Stokes numbers of 1×10^{-3}, particle mass was conserved well for all grids considered, with the worst mass conservation occurring on the finest grid (2.3% discrepancy for the no diffusion case). At larger Stokes numbers, mass conservation becomes considerably worse in the Taylor-Green flow. This loss of conservativeness is due to the source term. On the finest grids, the sharper volume fraction gradients present in the problem regions are able to produce more volume fraction, causing the total mass in the system to increase. The total mass in the system stabilised to the values shown in Figure 4.13 and were not continually increasing/decreasing with iteration, even for the larger Stokes numbers and lack of diffusion.

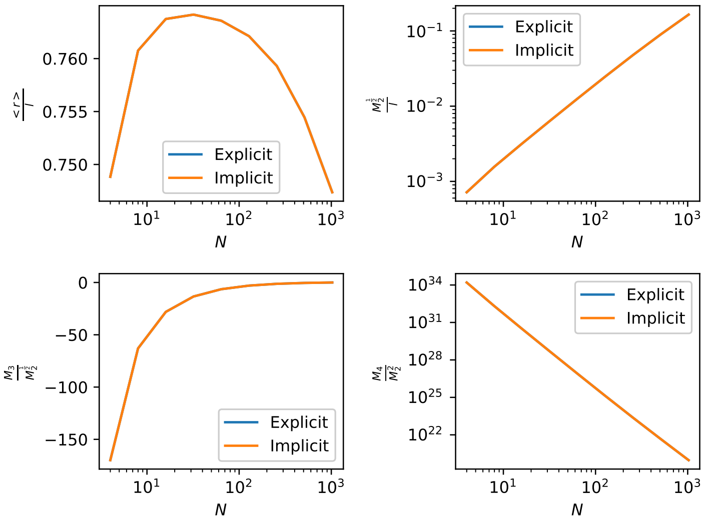

Figure 4.12: Normalised moments of the radial volume fraction distribution for both the explicit and implicit source term on a variety of uniform grids with turbulent diffusion for $Stk = 1 \times 10^{-3}$. The convergence criterion for the normalised residual was $< 1 \times 10^{-7}$.

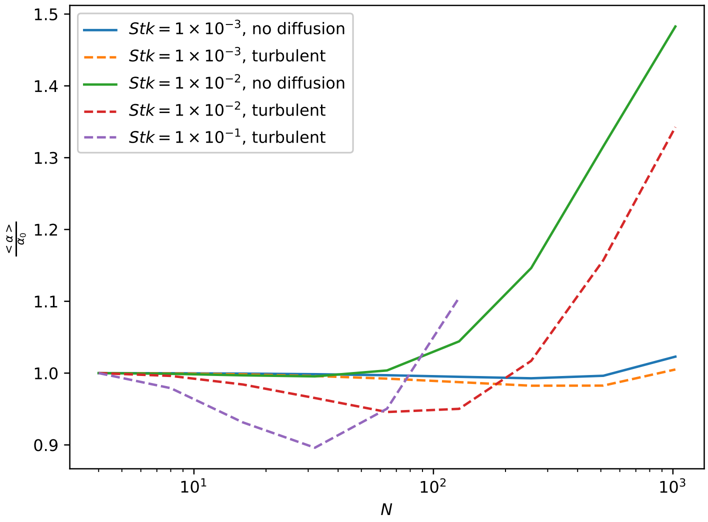

Figure 4.13: Ratio of the mean value of α in the domain to α_0 for various Stokes numbers and diffusion coefficients as a function of mesh size.

4.3.2 Eulerian Model Numerical Tests Conclusion

The Taylor-Green flow has been shown to be a challenging flow for the EE Eulerian model. Convergence of the steady-state solution has been judged from the scaled residuals and normalised central moments of the radial volume fraction distribution. A variety of discretisations have been investigated including the treatment of the source term (explicit vs implicit), the use of higher-order and TVD convection schemes along with the effects of diffusion coefficients representing different physical phenomena.

A mesh-independent solution is not able to be reached in this flow field as the finer the mesh, the greater amount of volume fraction at cells located at the regions of maximum compressive strain. The comparison with the Lagrangian particle result in Section 4.5 provides closure to this issue.

An implicit formulation for the source term has provided superior stability during iteration whilst converging at a comparable rate to the simple explicit formulation. This added stability by increasing the diagonal dominance of the linear system is especially welcome in the case of zero diffusive sources and is the chosen formulation to be used in the cyclone model in Chapter 5.

Higher-order convection schemes will fail for this model in this flow field. The use of flux limiters to provide a TVD scheme increase the stability of the solver as expected, however these continuously remove volume fraction from the domain and provide an unphysical solution. First-order upwind for the face interpolation is therefore used in the cyclone Eulerian model. The smearing out of large gradients due to this will be minimised if the mesh is sufficiently refined.

The inclusion of Brownian diffusion is negligible as expected. Tests of the turbulent diffusion coefficient by assuming the fluid velocity represents an LES filtered flow field extended the use of the model to higher Stokes numbers which is welcome behaviour for implementation into the cyclone LES model in Chapter 5, especially in cells near to the cyclone cone tip where the largest strain rates are expected.

The discretisation of the Eulerian model in a 2D Taylor-Green flow has been presented and the stability of the method for various grid sizes, Stokes numbers and choices of diffusion coefficient assessed. The accuracy of the model will be compared to the analogous results using Lagrangian particles in the same flow field.

4.4 Lagrangian Particle Tracking

Having completed the Eulerian particle model simulations in the Taylor-Green flow, Lagrangian particle reference data will now be obtained in order to further assess and validate the Eulerian model. This Lagrangian particle tracking will additionally be used to inform the particle cyclone work in Chapter 5. Both the scales of the particles and flow field, along with the initial conditions of the particles are such that a direct comparison between the Lagrangian and Eulerian results will be able to be made in Section 4.5.

4.4.1 Particle Numerical Study

Before the Lagrangian particles can be tracked in either the Taylor-Green or cyclone flow in Section 5.2, the time-step dependence and accuracy of the numerical integration scheme must first be known. These numerical studies can be performed by using the Taylor-Green flow field defined in Section 4.1 to mimic the motion of small particles in the turbulent eddies of the cyclone.

The particle acceleration is provided by Stokes drag only, without any additional stochastic forces. These have been removed in this numerical study as the stochastic nature of the force will create noisy results. This allows the effect of the choice of numerics on the drag force to be directly correlated, with the governing particle ODEs given by Eqs. 1.26 and 1.27. These are numerically integrated in time using an embedded Runge-Kutta scheme from Cash and Karp [182]. This embedded scheme provides a family of Runge-Kutta methods of order up to 5, involving 6 function evaluations. The formulae for the stages are given in Eqs. 4.78 to 4.83.

$$\boldsymbol{k}_1 = f\left(t_n, \boldsymbol{Z}_n\right) \tag{4.78}$$

$$\boldsymbol{k}_2 = f\left(t_n + \frac{1}{5}\Delta t, \boldsymbol{Z}_n + \Delta t\left(\frac{1}{5}\boldsymbol{k}_1\right)\right) \tag{4.79}$$

$$\boldsymbol{k}_3 = f\left(t_n + \frac{3}{10}\Delta t, \boldsymbol{Z}_n + \frac{\Delta t}{40}\left(3\boldsymbol{k}_1 + 9\boldsymbol{k}_2\right)\right) \tag{4.80}$$

$$\boldsymbol{k}_4 = f\left(t_n + \frac{3}{5}\Delta t, \boldsymbol{Z}_n + \Delta t\left(\frac{3}{10}\boldsymbol{k}_1 - \frac{9}{10}\boldsymbol{k}_2 + \frac{6}{5}\boldsymbol{k}_3\right)\right) \tag{4.81}$$

$$\boldsymbol{k}_5 = f\left(t_n + \Delta t, \boldsymbol{Z}_n + \Delta t\left(-\frac{11}{54}\boldsymbol{k}_1 + \frac{5}{2}\boldsymbol{k}_2 - \frac{70}{27}\boldsymbol{k}_3 + \frac{35}{27}\boldsymbol{k}_4\right)\right) \tag{4.82}$$

$$\boldsymbol{k}_6 = f\left(t_n + \frac{7}{8}\Delta t, \boldsymbol{Z}_n + \Delta t\left(\frac{1631}{55296}\boldsymbol{k}_1 + \frac{175}{512}\boldsymbol{k}_2 + \frac{575}{13824}\boldsymbol{k}_3 + \frac{44275}{110592}\boldsymbol{k}_4 + \frac{253}{4096}\boldsymbol{k}_5\right)\right) \tag{4.83}$$

The n subscript denotes the value at the current time step. The function, f, in the stages is given by

$$f\left(t, \boldsymbol{Z}\right) = \begin{pmatrix} \boldsymbol{Z}_2 \\ \frac{1}{m_p}\sum \boldsymbol{F}_{\text{fluid}}\left(t, \boldsymbol{Z}\right) \end{pmatrix}, \tag{4.84}$$

where $\boldsymbol{Z}$ is a state vector holding the particle position and velocity. The fifth-order scheme provides the particle position and velocity after a single time step as

$$\boldsymbol{Z}_n^{\left(5^{th}\text{order}\right)} = \begin{pmatrix} \boldsymbol{X}_{n+1} \\ \boldsymbol{V}_{n+1} \end{pmatrix}^{\left(5^{th}\text{order}\right)} = \begin{pmatrix} \boldsymbol{X}_n \\ \boldsymbol{V}_n \end{pmatrix} + \Delta t\left(\frac{37}{378}\boldsymbol{k}_1 + \frac{250}{621}\boldsymbol{k}_3 + \frac{125}{594}\boldsymbol{k}_4 + \frac{512}{1771}\boldsymbol{k}_6\right). \tag{4.85}$$

Due to the embedded nature of the scheme, a fourth-order solution can be obtained without performing additional function evaluations as

$$\boldsymbol{Z}_n^{\left(4^{th}\text{order}\right)} = \begin{pmatrix} \boldsymbol{X}_{n+1} \\ \boldsymbol{V}_{n+1} \end{pmatrix}^{\left(4^{th}\text{order}\right)} = \begin{pmatrix} \boldsymbol{X}_n \\ \boldsymbol{V}_n \end{pmatrix} + \Delta t\left(\frac{2825}{27648}\boldsymbol{k}_1 + \frac{18575}{48384}\boldsymbol{k}_3 + \frac{13525}{55296}\boldsymbol{k}_4 + \frac{277}{14336}\boldsymbol{k}_5 + \frac{1}{4}\boldsymbol{k}_6\right). \tag{4.86}$$

The implementation and order of these two integration schemes can be validated against the analytical solution of a particle, initially at rest, falling due to gravity through a still fluid. The equation of motion of the particle in 1D acted on by Stokes drag and gravity is $\frac{dV}{dt} = g - \frac{1}{\tau_p}V$ with initial conditions $V(t=0) = 0m/s$ and $X(t=0) = 0m$. The analytical solutions of the particle velocity and position are $V(t) = \tau_p g\left(1 - e^{-\frac{t}{\tau_p}}\right)$ and $X(t) = \tau_p g\left(t - \tau_p\left(1 - e^{-\frac{t}{\tau_p}}\right)\right)$ respectively. The terminal velocity of the particle in this case is given by

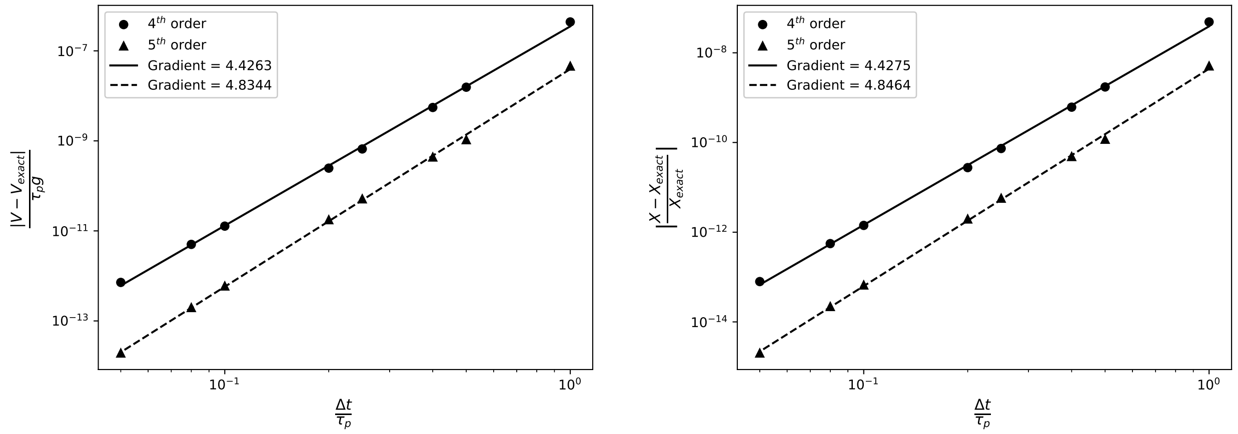

Figure 4.14: Normalised integration error from the embedded Runge-Kutta schemes plotted on a log-log graph for both velocity and position. The gradient of each scheme was calculated using ordinary least-squares regression.

$\lim_{t \to \infty} \big[V(t)\big] = \tau_p g$. Particles are integrated using time steps in the range $1 \geq \frac{\Delta t}{\tau_p} \geq 0.05$ up to $\frac{t}{\tau_p} = 10$. The error from numerically integrating the particle equation of motion using the two schemes for varying time steps is shown in Figure 4.14.

The error of each scheme is provided by the gradient on a log-log plot and is in rough agreement with the order of the scheme. In addition to this, the embedded Runge-Kutta scheme can be used with adaptive time-stepping. The estimated error of each integration step, computed as

$$\text{error} = \left\| \boldsymbol{Z}_n^{\left(5^{th}\text{order}\right)} - \boldsymbol{Z}_n^{\left(4^{th}\text{order}\right)} \right\|, \tag{4.87}$$

is compared to a pre-defined tolerance (tol). If the error exceeds the tolerance, the integration is repeated using a smaller time step until the error is below the tolerance. If the estimate of the error is greater than the tolerance, the time step is increased for the subsequent time step. This allows smaller time steps to be taken in regions where a particle is rapidly accelerating and smaller steps when particle accelerations are small. This adaptive time stepping may save on computational expense by factors of 10 or 100 [179] and will be used for the cyclone Lagrangian particle tracking in Chapter 5. The time step is recalculated whenever a particle enters a new computational cell as

$$\Delta t_p = \frac{\Delta V^{\frac{1}{3}}}{|\boldsymbol{u}| + |\boldsymbol{V}|}. \tag{4.88}$$

This provides an estimate for the time taken for a particle to traverse the cell. The time step is also adjusted to ensure that a particle is only travels a maximum of one cell per time step. As the Taylor-Green flow field is simple in comparison with the cyclone, the Runge-Kutta scheme of order 5 with a fixed time step will be used in this study. To find a suitable time step for the integration of the particle equations of motion, a single particle was tracked in a Taylor-Green eddy. The particle was initialised at the location $\boldsymbol{X} = (0, 0.45l)$ which places it close to the top of the central eddy. The particle was tracked for a single fluid timescale τ_f for a range of time steps with the final position recorded. The norm of the difference in the final position vector to the finest time step ($\Delta t_p = \frac{\tau_p}{1000}$) was used as an estimate of the error. The error normalised by the eddy diameter as a function of time step is shown in Figure 4.15.

Stokes numbers of 0.01 and 0.1 were used as these are representative of an average and worst-case scenario for the largest particles in the cyclone respectively, as is shown later in Section 5.2. The normalised error is proportional to the normalised time step size, with a smaller normalised error for the $Stk = 0.01$ particles due to the smaller time step used. A time step of $\Delta t_p = \frac{\tau_p}{10}$ is chosen to ensure accuracy for the integration ($< 1\%$ normalised error in position per fluid timescale) whilst balancing computational cost. It is also of note that using excessively small time steps may exacerbate the error from the numerical integration due to the large number of integration steps required. The chosen time step avoids this issue.

The particles are now to be injected into the Taylor-Green flow and tracked in time to provide a source of validation for the Eulerian model. Particles are initialised into the domain with their positions drawn from a uniform random distribution. For the positions $X \sim U(-l, l)$ and the velocities are set to zero. Particles are not initialised with the local fluid conditions to ensure the particles are initially uncorrelated with the fluid

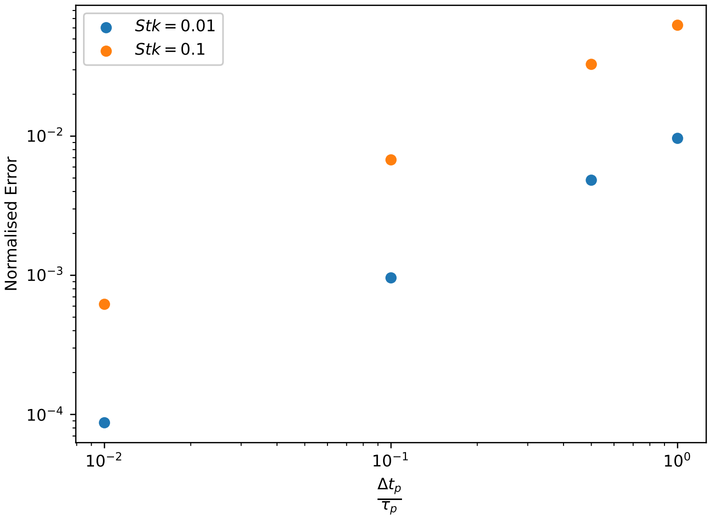

Figure 4.15: Position error normalised by the eddy diameter for a range of time steps with a Stokes numbers of $Stk = 1 \times 10^{-2}$ and $Stk = 1 \times 10^{-1}$.

(this is revisited later). The fluid domain is the same Taylor-Green flow from Section 4.1. To assess whether the particle distribution has reached a statistically stable state, quantities relating to the central moments (Eq. 2.53) of the radial distribution are calculated at each time step. The mean and central moments of the radial particle distribution are given by [134]

$$\langle r \rangle = \frac{\sum_{i=1}^{N} r^{(i)}}{N}, \tag{4.89}$$

$$M_n = \frac{\sum_{i=1}^{N} \left(r^{(i)} - \langle r \rangle \right)^n}{N}, \tag{4.90}$$

$$\tag{4.91}$$

respectively, where $r^{(i)}$ is the radial position of particle i, n is the order of the central moment and N is the total number of particles.

Figure 4.16 shows the statistics of the particle radial distribution over time for 10, 100 and 1000 particles with $Stk = 1 \times 10^{-2}$. Each central moment converges to the same value apart from the skewness, which has a value of ≈ -0.5 for 10 particles and a value of ≈ -1 for greater numbers of particles. The central moments level-off after $\approx 22000\tau_p$ and the line is flat. This is because at this time, all the particles have been centrifuged out of the eddies and have collected in the regions of greatest compressive strain (identified as $(x, y) = \left(\frac{n\pi}{2a}, \frac{m\pi}{2a}\right)$ from Section 4.1) and is in qualitative agreement with the Eulerian model prediction of particles collecting in these locations. With only 10 particles (which were introduced randomly), an uneven number of particles have collected in these spots; hence why the skewness differs for this low particle number.

The particle study in the Taylor-Green flow is repeated, however the particles are initialised with random velocities as $\boldsymbol{V} \sim U(-u_{mag}, u_{mag})$. This second, completely different initialisation is used to check that the final particle statistics are independent of this initial condition. The results are shown in Figure 4.17. The same statistically stationary results were achieved as the different initial velocity condition. The results are therefore independent of the initial particle conditions.

The study was repeated using particles with a larger Stokes number of $Stk = 0.1$ and random velocity initialisation shown in Figure 4.18. The moments of the radial distribution reached a stationary state at $\approx 300\tau_p$; almost 100 times quicker than the $Stk = 0.01$ particles. As these particles required fewer time steps to reach a converged result, a larger particle number of 10000 was also considered. The statistics of the radial distribution of the $Stk = 0.1$ particles matched the results for the $Stk = 0.01$ particles. A larger Stokes number resulted in the statistically stationary state being reached in less dimensionless time. The stationary state was approached in a smoother fashion for the $Stk = 0.01$ particles, which were slowly centrifuged out. The more inertial $Stk = 0.1$ particles featured more chaotic trajectories towards an equilibrium state.

As the particle number is increased, the statistical measures reached a converged value, independent of the initial conditions or Stokes number. In all cases, this state is reached once particles have collected in the regions of greatest compressive strain between the eddies. From the symmetry of the flow field it is expected that equal

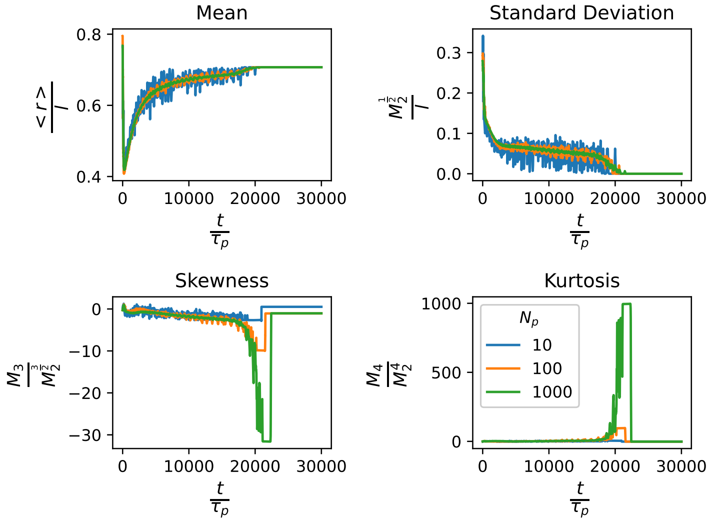

Figure 4.16: Statistics of the particle radial distribution in the Taylor-Green flow for various particle numbers with $Stk = 0.01$. The mean and standard deviation are normalised by the eddy diameter. Particles were initialised as stationary.

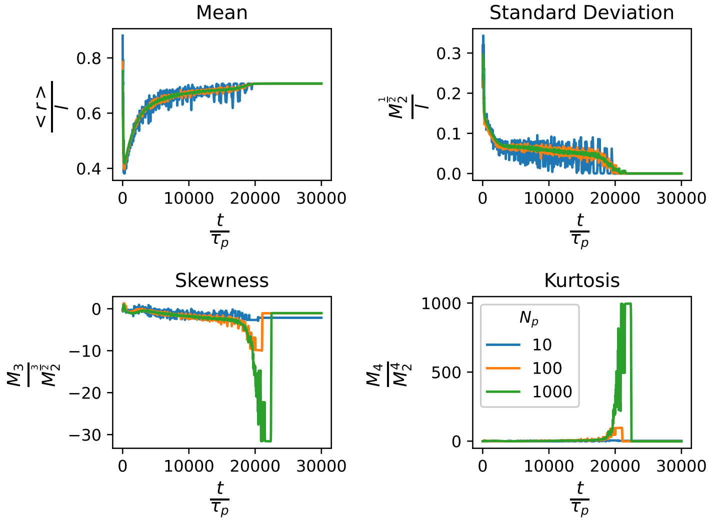

Figure 4.17: Statistics of the particle radial distribution in the Taylor-Green flow for various particle numbers with $Stk = 0.01$. The mean and standard deviation are normalised by the eddy diameter. Particles were initialised with random velocities.

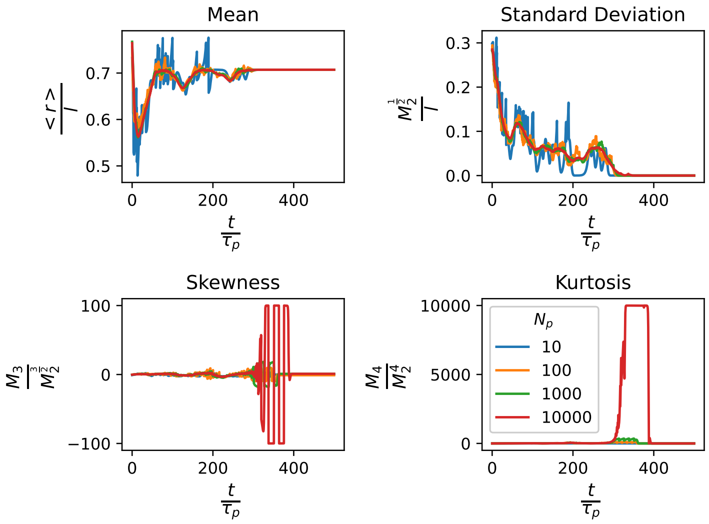

Figure 4.18: Statistics of the particle radial distribution in the Taylor-Green flow for various particle numbers with $Stk = 0.1$. The mean and standard deviation are normalised by the eddy diameter. Particle were initialised with random velocities.

Quantity	$\frac{<r>}{l}$	$\frac{M_2^{\frac{1}{2}}}{l}$	$\frac{M_3}{M_2^{\frac{3}{2}}}$	$\frac{M_4}{M_2^4}$
Value	$\frac{\sqrt{2}}{2}$	0	Undefined	Undefined
Limiting value as $N \to \infty$	$\frac{\sqrt{2}}{2}$	0	0	0

Table 4.3: Statistics of the particle radial distribution in the Taylor-Green flow for particles sat at the locations of maximum compressive strain. The values from both direct substitution and the limit as $N \to \infty$ are provided.

numbers of particles should accumulate in each of the 4 spots (each located at $\frac{r}{l} = \frac{\sqrt{2}}{2}$). This leads to an analytical solution for the particle statistics, which are expected to be reached as $N \to \infty$, including a standard deviation of zero (as there is no spread in the radial positions). This also leads to the normalised higher-order moments being undefined due to division by powers of the standard deviation. These statistics are tabulated in Table 4.3.

The Lagrangian particle statistics from Figures 4.16 and 4.17 are seen to converge towards the analytical solution from Table 4.3 (the normalised mean particle radial position, for example, tends towards $\frac{\sqrt{2}}{2} \approx 0.7$). The standard deviation tends towards zero (as the particles all lie at a constant radial position once they have collected at the spots). The normalised higher-order moments are therefore undefined, however they can be seen to approach the limiting value of zero. The error in the mean radial value for all particle numbers is vanishingly small $< 1.7 \times 10^{-14}$. The eventual collection of all particles into these well-defined spots explains the numerical difficulties encountered in the Eulerian model at these points; all the particles (and therefore volume fraction) is entrained towards these infinitesimal points. Further discussion of the similarities and differences of the Lagrangian with the Eulerian results is presented in the following section.

4.5 Eulerian Model Comparison with Lagrangian Results

The Eulerian particle model has been shown to be unable to produce a mesh-independent solution, even at a low Stokes number in Section 4.3. This was due to finer meshes allowing larger volume fractions to occur in regions of greatest compressive strain without bound. In the Lagrangian counterpart, particles were observed to accumulate in these same spots becoming trapped in Section 4.4. As more Lagrangian particles are introduced into the simulation, the larger number densities/volume fractions would build-up in these same spots without bound. This phenomena makes it clear why the Eulerian method failed in this regard; the scenario is unphysical in both senses as particle-particle collisions would prevent an infinite build-up in these spots with the maximum volume fraction given by the close-packed limit. Both the Eulerian and Lagrangian models omitted this set of physics and exhibited this same collection of particles in regions of greatest compressive strain. The effect of particle-particle collisions on the volume fraction is continued to be omitted from the model due to the dilute (low volume fraction) particle regime expected in the cyclone in Chapter 5, with this Taylor-Green flow providing a more difficult numerical challenge as there is no outlet for particles to escape to. This build-up in the problem regions is shown in Figure 4.19.

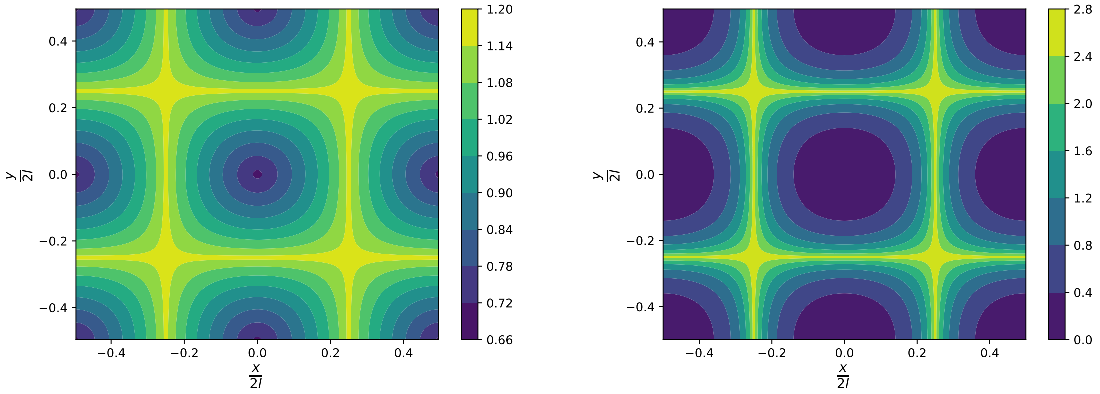

Figure 4.19: Volume fraction distribution normalised by α_0 in the Taylor-Green flow at $Stk = 1 \times 10^{-3}$ with no diffusion and an implicit source term for a mesh size of 128^2 on the left and 1024^2 on the right.

Another feature of the predicted Eulerian volume fraction distribution are both horizontal and vertical "lines" joining the problem spots which are visible in Figure 4.19. These lines lie on the edge of the central vortex. Lagrangian particles near the eddy centres are centrifuged out and their trajectories begin to resemble the line structure of the volume fraction distribution. One such particle trajectory is provided in Figure 4.20 showing the box-like path traced out with rounded vertices. These box trajectories continue until the particle becomes trapped in one of the corners forever. These box trajectories will occur around each eddy an therefore match up with the lines predicted in the Eulerian model.

From the Lagrangian results, it was reasoned that there exists analytical solutions to the mean, standard deviation, skewness and kurtosis of the radial particle distribution given by Table 4.3. The Eulerian results from Section 4.3 can be compared to these analytical solutions. The mean radial position predicted by the Eulerian model was around twice as large as the analytical solution, however as the mesh is refined the mean radial position decreases. The standard deviation becomes larger as the grid is refined for the Eulerian model, when it should be tending to zero. This is due to increasing volume fraction concentrations in the "lines" joining the problem spots. The skewness of the Eulerian model tended to zero, indicating that the volume fraction distribution is symmetric as expected. This moment, along with the kurtosis is undefined in the analytical solution as the standard deviation is zero. The raw third and fourth central moments would be zero in the analytical form and thus the Eulerian model is tending towards the correct Lagrangian solution. For the fourth moment in the Eulerian model, the values obtained were very large as this moment is sensitive to extreme values on the tails of the distribution. As the grid is refined, this moment reduces and is expected to tend towards the analytical solution.

The Eulerian model can additionally be compared to the Lagrangian model for an unsteady solution. The centrifuge of the particles (or volume fraction for the Eulerian case) away from vortex centres over time can be compared by studying the central moments of the radial volume fraction distribution as a function of time. The Lagrangian case from Section 4.4 requires no additional set-up as particles were already tracked through time and space. For the Eulerian counterpart, the backward Euler scheme results in the discretisation of the volume fraction transport equation in each cell to be given by Eqs. 4.57, 4.58 and 4.59. In-line with the Lagrangian results, the Stokes number is set to $Stk = 1 \times 10^{-2}$ and a grid-size of 128^2 cells is used for the Eulerian case.

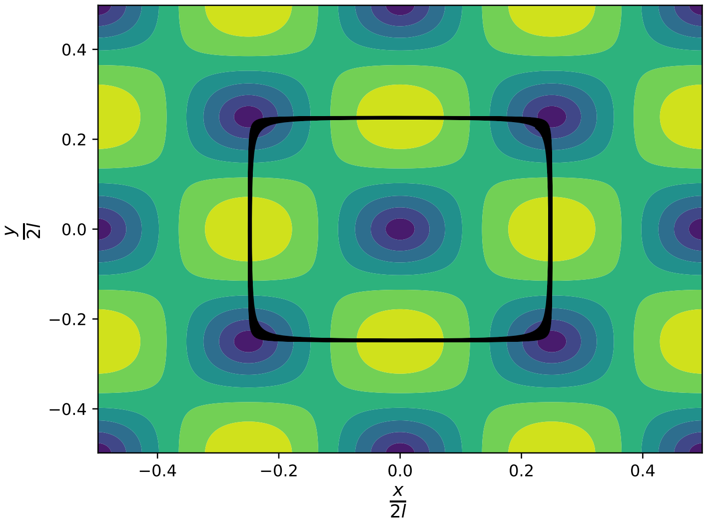

Figure 4.20: Trajectory of a $Stk = 1 \times 10^{-3}$ particle initialised stationary at $(x, y) = (0.45l, 0.45l)$ and tracked for $\frac{t}{\tau_p} = 1 \times 10^5$. The background is coloured by the fluid speed, identical to Figure 4.1.

The Lagrangian time step used was $\Delta t_P = \frac{\tau_p}{10}$ and for comparison the Eulerian model is run using the same time step. This results in a maximum Courant number (Eq. 4.19) in the domain as $C_{\text{num}} = \frac{u_{\text{mag}}\Delta t}{\Delta x} \approx 6.4 \times 10^{-2}$ which is expected to provide a stable solution during time stepping. No diffusion models are present and the Eulerian model is run for $t_{\max} = 30000\tau_p$ matching the Lagrangian case. The Eulerian results are compared against the moments obtained using the highest number of particles from Section 4.4 (1000).

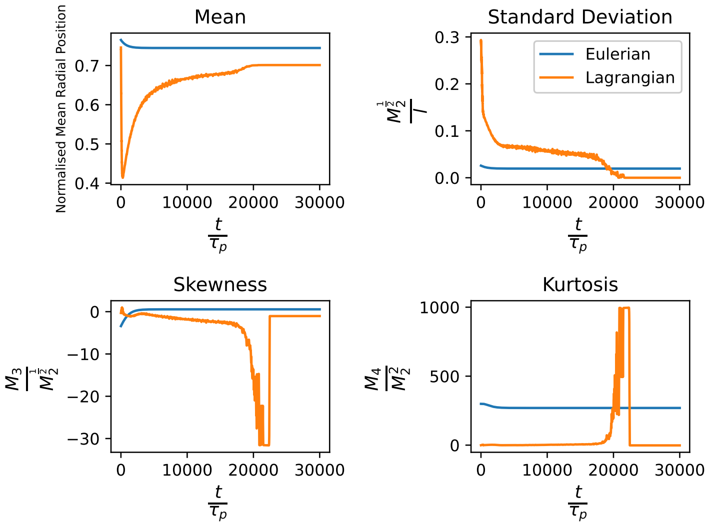

Figure 4.21: Statistics of the particle radial distribution in the Taylor-Green flow for both the unsteady Eulerian and Lagrangian particle models for $Stk = 1 \times 10^{-2}$ as a function of time. The mean and standard deviation are normalised by eddy diameter. Particles were initialised as stationary in the Lagrangian case.

Figure 4.21 shows the moments of the radial distribution for both the Lagrangian and unsteady Eulerian cases over time. The moments of the Eulerian model converge to the same values as for the steady-state solution. Reasonable agreement is observed for the first 3 moments, whereas the kurtosis has a large discrepancy due to the strong influence of extreme values on this statistic. The percentage error of the Eulerian model compared to the Lagrangian particles is approximately 6% for the normalised mean, with the percentage errors of the higher-order moments being undefined due to division by zero. This is a small discrepancy considering the simplicity of the EE model which is being applied in challenging strong streamline curvature.

Both models approach statistically stationary values over time, with the Eulerian model reaching a statistically stationary state around 10 times faster than for the Lagrangian model. This is expected, as the Eulerian model assumes that the particle velocity field has reached an equilibrium (the EE model). Having fewer time steps to reach the final state compared to Lagrangian particle tracking is a beneficial characteristic of the Eulerian model, especially when utilised in an unsteady flow field as this will result in a computationally cheaper model to run. The moments displayed in Figure 4.21 also converge to a statistically stationary state in a much smoother fashion in the Eulerian case compared to the Lagrangian set-up.

The Eulerian model predicted the same regions of volume fraction build-up as with the Lagrangian particles. The volume fraction distribution was more smeared-out. Part of this was due to the choice of discretisation of the convective term using first-order upwinding producing false diffusion. This false diffusion is so called as the leading order error term in the Taylor series expansion of the scalar volume fraction about the cell centroid resembles a diffusive flux [32]. Calculating the Taylor series expansion for the east face from Figure 4.5 gives

$$\alpha_e = \alpha_P + \frac{\Delta x}{2}\left(\frac{\partial \alpha}{\partial x}\right)_P + \mathcal{O}\left((\Delta x^2)\right), \tag{4.92}$$

where Δx is the grid spacing in the x-direction. If the local flow is going east, the first term on the RHS represents the upwind scheme, with leading order error term $\frac{\Delta x}{2}\left(\frac{\partial \alpha}{\partial x}\right)_P$. This false diffusion error can be reduced by further refining the mesh however, from the earlier discussion, the volume fraction will tend towards infinity at the singularities. Reduction in false-diffusion from finer meshes also aided in reducing the kurtosis of the radial volume fraction distribution for the Eulerian model.

The particle velocity is known at each location along the Lagrangian particle trajectory. The accuracy of the EE velocity, evaluated at each position along the trajectory can be quantified. Two measures for the accuracy will be considered: the first is the difference in speeds between the methods normalised by u_{mag} given by

$$\text{Normalised speed error} = \frac{\left|\boldsymbol{V}\left(\boldsymbol{X},t\right) - \boldsymbol{v}_{ee}\left(\boldsymbol{X}\right)\right|}{u_{mag}}. \tag{4.93}$$

The second is the angle between the two velocity vectors which can be calculated by the well-known dot product formula

$$\text{Normalised angle error} = \arccos\left(\frac{\boldsymbol{V}\left(\boldsymbol{X},t\right)\cdot\boldsymbol{v}_{ee}\left(\boldsymbol{X}\right)}{\left|\boldsymbol{V}\left(\boldsymbol{X},t\right)\right|\left|\boldsymbol{v}_{ee}\left(\boldsymbol{X}\right)\right|}\right). \tag{4.94}$$

The particle trajectories considered in this study are initialised stationary at $(x, y) = (0.45l, 0.45l)$ as in Figure 4.20, however they are tracked for a single "orbit" of the fluid eddy. Stokes numbers of $Stk = 1\times10^{-3}$, $Stk = 1\times10^{-2}$ and $Stk = 1\times10^{-1}$ are tested to quantify the effect of Stokes number on the different specifications of the velocity error.

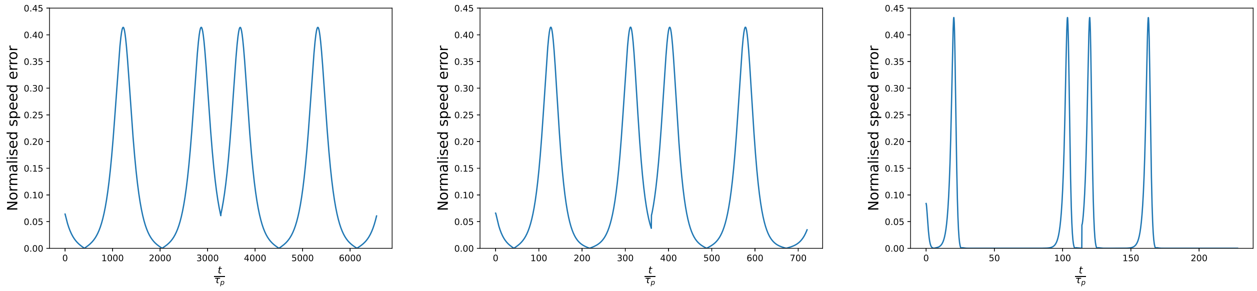

Figure 4.22: Particle speed error along a single orbit trajectory for $Stk = 1\times10^{-3}$, $Stk = 1\times10^{-2}$ and $Stk = 1\times10^{-1}$ from left to right respectively.

The normalised particle speed error is shown in Figure 4.22. All errors show 4 distinct peaks for all Stokes numbers, with the peaks becoming more defined with increasing Stokes numbers. The graphs of the speed error are symmetrical about half of the orbit. The speed error for $Stk = 1\times10^{-3}$ and $Stk = 1\times10^{-2}$ show very little difference in terms of shape and peak error values. The $Stk = 1\times10^{-1}$ speed error, along with the spikier peaks, exhibits larger peak error values as expected. The speed error for the $Stk = 1\times10^{-1}$ particle lies close to zero for most of the trajectory and is smaller on average than the two lower Stokes numbers. This result goes against what we would expect for a larger Stokes number. To explain both this result and the structure of the 4 peaks in the speed error, we look at the orbital trajectories of each Stokes number.

The trajectories in Figure 4.23 each show the particle centrifuged away from the centre of the eddy, with the strength of this centrifuge increasing with Stokes number. The rounded corners of the "box" trajectory

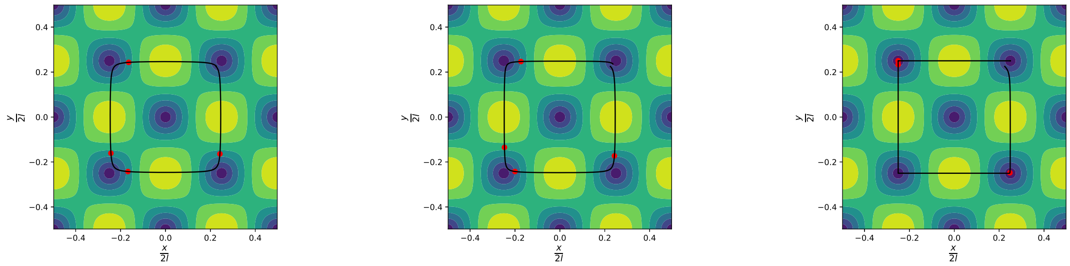

Figure 4.23: Particle trajectory along a single orbit for $Stk = 1 \times 10^{-3}$, $Stk = 1 \times 10^{-2}$ and $Stk = 1 \times 10^{-1}$ from left to right respectively. Red dots indicate the spatial locations where the peak speed errors occur. The background is coloured by the fluid speed, identical to Figure 4.1.

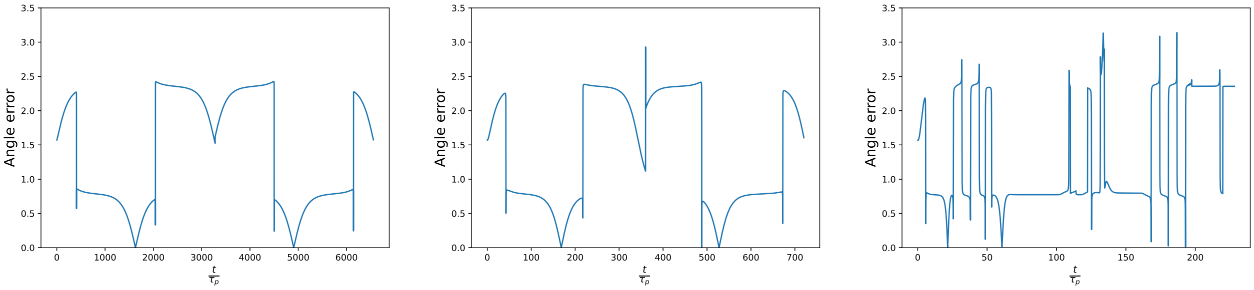

Figure 4.24: Particle velocity angle error along a single orbit trajectory for $Stk = 1 \times 10^{-3}$, $Stk = 1 \times 10^{-2}$ and $Stk = 1 \times 10^{-1}$ from left to right respectively.

becomes less round and sharper with increasing Stk. The peaks in the speed error are shown by the red dots on the figure, which lie near the regions of maximum compressive strain. At $Stk = 0.1$, the locations of maximum speed error lie very close to these regions, with 3 of the 4 peaks occurring at the top left problem region. This is because the particle slightly overshoots the central eddy and enters a neighbouring eddy, it is then flung out that eddy and returns to the central starting vortex.

The particle velocity angle error is shown in Figure 4.24. The angle error along the trajectory has a completely different form to the speed error, with peaks and troughs in the two varieties of errors not occurring at the same points. This error is particularly more chaotic for the larger Stokes number trajectory due to the less-smooth path taken around the eddy. The angle error is large for all Stokes numbers as the EE method assumes the particle velocity field is independent of the particle history; a Lagrangian particle may reach a particular location in the flow from a variety of different paths and therefore angles of approach. This is a deficit in the EE method for the particle velocity, especially in strong streamline curvature. The end result of the particle centrifuged out of the eddy into regions of high compressive strain is captured in the Eulerian model, however the statistics of the EE velocity along the particle trajectory are not representative of the Lagrangian results, especially the angle of the velocity vector. This error grows for increasing Stokes number.

4.6 Comparison with The Mixture Model

The EE method has been compared to Lagrangian particle results in the Taylor-Green flow and found to capture the accumulation of particles on the edges of the vortices. The other computationally-cheap candidate Eulerian method is the mixture model from Section 2.3.1. The specification of the relative velocity has a similar form between the EE method (Eq. 2.81) and the mixture model (Eq. 2.78), however the governing transport equations are now in terms of the mixture. This comparison is performed to assess the advantages and disadvantages of these two Eulerian particle methods in a flow with strong streamline curvature.

For the mixture model, the mixture velocity is specified as the steady Taylor-Green velocity. The mixture momentum and particle volume fraction equations (Eqs. 2.76 and 2.66 respectively) are expressed in steady conservative form and solved in a coupled manner using the FVM on the same grid and flow field as for the EE tests. These PDEs are solved separately, with the SIMPLE method (briefly described below) used for the velocity-pressure coupling, for the same range of Stokes numbers tested from Table 4.2. Gradients are again discretised using the Green-Gauss cell-based method in Eq. 4.45 and first-order upwinding (Eq. 4.29) is used for convective terms. The discretisations used for the mixture model match those used for the EE method in this flow.

The Semi-Implicit Method for Pressure-Linked Equations (SIMPLE) allows a pressure field to be determined which guarantees that the mixture velocity field will satisfy the continuity equation [174]. Although the mixture velocity field is specified in this 2D Taylor-Green flow, using this method allows a pressure field to be obtained as well. This "solving" of the mixture velocity field is a necessary work-around to apply this method in ANSYS FLUENT, with the Taylor-Green flow field imposed as the mixture velocity solution after every iteration.

The mixture model is now applied in the Taylor-Green flow. A grid refinement study for $Stk = 1 \times 10^{-3}$ for the central moments of the radial volume fraction distribution is provided in Figure 4.25. Poor convergence of the model was observed, with relaxation factors of 0.1 required for all transport equations for the finer grid sizes. The normalised residual for continuity levelled-out at $\mathcal{O}\left(10^{-4}\right)$ for grid sizes greater than 128^2 and all simulations were required to achieve a normalised residual for the volume fraction less than 1×10^{-6}. This is compared to the EE result using an implicit source term and no diffusion, representing a like-for-like comparison for the physics. Both methods yield almost identical results for mesh sizes smaller than 64^2 with the standard deviation, skewness and kurtosis both following the same trends for all mesh sizes considered. As the mesh is refined, the normalised mean radial location of the particle volume fraction appears to converge to ≈ 0.765 for the mixture model. The true value obtained from the Lagrangian particle tracking in Section 4.4.1 was $\frac{\sqrt{2}}{2} \approx 0.707$; a percentage error of 8.2%. The percentage error from the EE method on the finest mesh is 5.7%. The expected value for the normalised standard deviation is zero from Table 4.3, with the EE method yielding standard deviations lower (and therefore closer to the expected result) than the mixture model for all mesh sizes. This suggests that the EE method is more accurate than the mixture model in a flow with strong streamline curvature at low Stokes number.

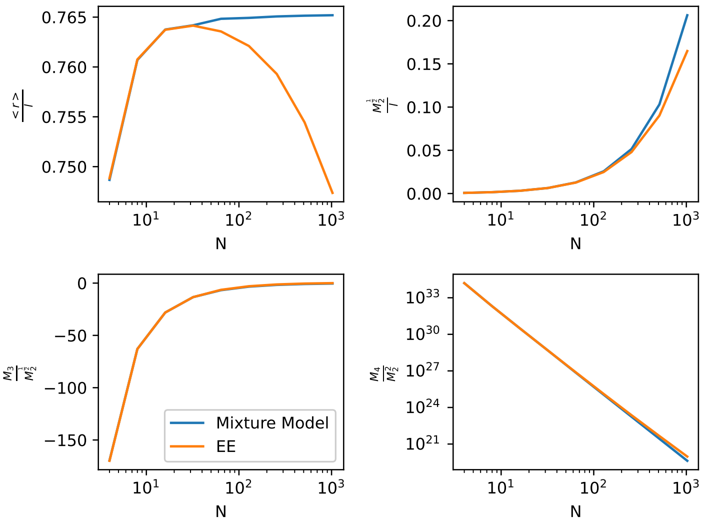

Figure 4.25: Normalised moments of the radial volume fraction distribution for the mixture model and EE method on a variety of uniform grids with no diffusion for $Stk = 1 \times 10^{-3}$.

At the larger Stokes number of $Stk = 1 \times 10^{-2}$, almost identical trends in the moments of the radial volume

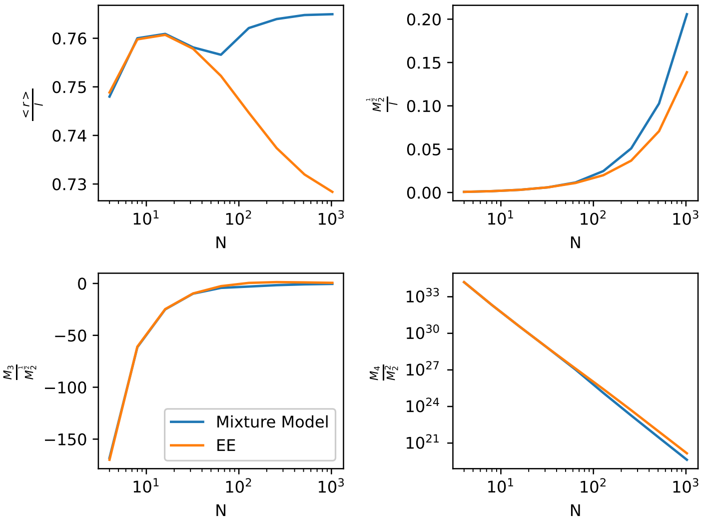

Figure 4.26: Normalised moments of the radial volume fraction distribution for the mixture model and EE method on a variety of uniform grids with no diffusion for $Stk = 1 \times 10^{-2}$.

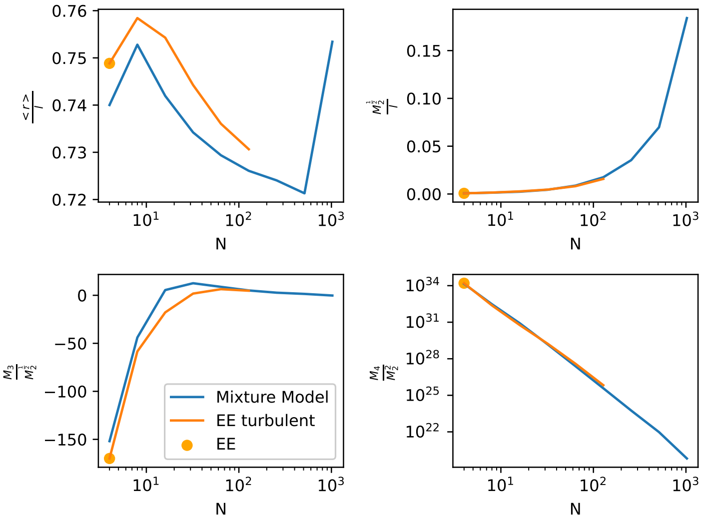

Figure 4.27: Normalised moments of the radial volume fraction distribution for the mixture model and EE method on a variety of uniform grids with no diffusion for $Stk = 1 \times 10^{-1}$.

fraction distribution in Figure 4.26. The only notable difference is in the normalised mean radial location, which at this higher Stk decreases in accordance with the EE method between grid sizes of 16^2 and 64^2. The two methods begin to diverge at a grid size of 64^2, with the mixture model converging again to $\frac{<r>}{l} \approx 0.765$ whilst the EE method decreases. On finer grids at the two presented Stokes numbers, the EE method has provided the best match to the Lagrangian particles.

Finally the normalised moments for the mixture model are shown for the $Stk = 1 \times 10^{-1}$ case against the single result attainable with the EE method and the available results for the turbulent diffusion cases in Figure 4.27. The finest mesh size for the mixture model (1024^2) did not reach the convergence criterion for the volume fraction and the last point on the graphs are most likely incorrect. At this larger Stokes number, the mixture model was able to converge to a solution for all but the finest mesh size, with the turbulent diffusion EE set-up breaking on a coarser mesh. The normalised mean radial position now matches the form of the EE model prediction at lower Stokes numbers and resembles the same form predicted by the turbulent diffusion case of the EE method. These results suggest that the mixture model performs better than the EE method at larger Stokes numbers.

This section of work has found that at low Stokes number ($Stk < 0.1$), the EE method with no diffusion provides a more accurate match to Lagrangian particles for the volume fraction distribution than the mixture model. At a larger Stokes number of $Stk = 0.1$, the EE method fails to converge without diffusion whereas the mixture model is able to converge, except on a very fine grid. The EE method also features a very useful advantage over the mixture model; given a solved fluid velocity field, the EE method can be run directly using this flow field by the solution of only the volume fraction transport equation. If a mixture model is to be used, the mixture velocity is required to be solved for, which is not the fluid velocity. Due to the coupling between the transport equations in the mixture model, they should be solved simultaneously. This greatly increases the memory requirements and along with the need to solve for the mixture, makes the mixture model more computationally expensive than the EE method. The capture of preferential accumulation and turbophoresis, along with the relatively small computational cost makes the EE method the most suitable Eulerian model for a dilute low Stokes number particulate phase in a small, high-speed cyclone.

4.7 Charge Model Implementation

With the discretisation of the volume fraction transport equation shown using the EE velocity, the transport of charge by the particulate phase is now of focus. This is to be computed after a converged solution is reached for the particle volume fraction. Although there is no validation data to compare against, reasonable checks can be made on the model such as identifying if a steady state solution for charge can be reached and if the method is stable.

In the Eulerian model of Kolehmainen *et al.* from Section 2.3, they presented a transport equation for the charge in Eq. 2.61. The LHS are the usual temporal and convection terms in a standard transport equation. The first term on the RHS represents the change in charge due to collisions and the second term represents the correlation between charge and velocity fluctuations. In their work, Kolehmainen *et al.* limited their attention to systems where these fluctuations were essentially uncorrelated [137]. Following their work and using the specific charge $q \equiv \frac{<Q>}{m_p}$, the unsteady transport equation simplifies to

$$\frac{\partial\left(\alpha\rho_p q\right)}{\partial t}+\frac{\partial\left(\alpha\rho_p q v_i\right)}{\partial x_i}=\mathcal{C}(q). \tag{4.95}$$

As the particulate phase has a constant particle density, this can be cancelled everywhere

$$\frac{\partial\left(\alpha q\right)}{\partial t}+\frac{\partial\left(\alpha q v_i\right)}{\partial x_i}=\frac{1}{\rho_p}\mathcal{C}(q). \tag{4.96}$$

The change in charge due to collisions is equal to the charge transferred from a single collision, multiplied by the collision frequency

$$\mathcal{C}(q)=\Delta Q C_{11}. \tag{4.97}$$

The collision frequency can be estimated from the extension of the laminar shear formulation in Eq. 1.35 to 3D (by using the particle strain rate magnitude instead of a 1D flow velocity gradient) as

$$C_{11}=\frac{4n^2d_p^3}{3}S^v_{mag}. \tag{4.98}$$

The number density can be calculated using the volume fraction and particle diameter from Eq. 1.30. Using Ireland's charge model, the charge transferred from a single collision is given by Eq. 2.49. Together, these yield the charge contribution due to collisions as

$$\mathcal{C}(q)=\frac{4n^2d_p^3A_{\text{c, max}}\sigma_0}{3}\left(1-e^{-\frac{t_c}{\tau}}\right)S^v_{mag}. \tag{4.99}$$

The transport equation becomes

$$\frac{\partial\left(\alpha q\right)}{\partial t}+\frac{\partial\left(\alpha q v_i\right)}{\partial x_i}=\frac{4n^2d_p^3A_{\text{c, max}}\sigma_0}{3\rho_p}\left(1-e^{-\frac{t_c}{\tau}}\right)S^v_{mag}. \tag{4.100}$$

If the particle velocity field is given by the EE velocity (Eq. 2.81), the same splitting of the convective term as for the volume fraction transport equation can be made to yield

$$\frac{\partial\left(\alpha q\right)}{\partial t}+\frac{\partial\left(\alpha q u_i\right)}{\partial x_i}=\frac{4n^2d_p^3A_{\text{c, max}}\sigma_0}{3\rho_p}\left(1-e^{-\frac{t_c}{\tau}}\right)S^v_{mag}-\frac{\partial}{\partial x_i}\left(\alpha w_i q\right), \tag{4.101}$$

where w_i is the relative velocity between the particles and the fluid. This form of the charge transport equation is valid for unsteady, incompressible fluid flow. We are only interested in the steady state solution, which expressed in conservative integral form would be

$$\int \alpha q u_i dA_i=\int \frac{4n^2d_p^3A_{\text{c, max}}\sigma_0}{3\rho_p}\left(1-e^{-\frac{t_c}{\tau}}\right)S^v_{mag}dV-\int \frac{\partial}{\partial x_i}\left(\alpha w_i q\right)dV. \tag{4.102}$$

For the FVM discretisation, the convective term surface integral is approximated using the second-order accurate midpoint rule as [32]

$$\int \alpha q u_i dA_i=\sum_F\int_A\left(\alpha q u_i dA_i\right)_F\approx\sum_F\left(\alpha q u_i A_i\right)_F=\sum_F\left(u_iA_i\right)_F\alpha_F q_F. \tag{4.103}$$

The bracket $(u_i A_i)_F$ is given analytically on the face from the EE velocity, the volume fraction on the face α_F is estimated using linear interpolation (Eq. 4.27) and the specific charge on the face q_F is calculated using first-order upwinding 4.29. The neighbour coefficients for a 2D uniform mesh are therefore

$$\begin{aligned} a_E^{i,j} &= \max(-\frac{\alpha_P + \alpha_E}{2}\dot{V}_e), & (4.104)\\ a_W^{i+1,j} &= \max(\frac{\alpha_P + \alpha_E}{2}\dot{V}_e), & (4.105)\\ a_N^{i,j} &= \max(-\frac{\alpha_P + \alpha_N}{2}\dot{V}_n), & (4.106)\\ a_S^{i,j+1} &= \max(\frac{\alpha_P + \alpha_N}{2}\dot{V}_n). & (4.107) \end{aligned}$$

The volume integrals for the source term are discretised for cell P as

$$\begin{aligned} &\int \frac{4n^2 d_p^3 A_{\text{c, max}}\sigma_0}{3\rho_p}\left(1 - e^{-\frac{t_c}{\tau}}\right) S_{mag}^v dV - \int \frac{\partial}{\partial x_i}\left(\alpha w_i q\right) dV \\ &\qquad \approx \left(\frac{4n^2 d_p^3 A_{\text{c, max}}\sigma_0}{3\rho_p}\left(1 - e^{-\frac{t_c}{\tau}}\right) S_{mag}^v - \frac{\partial}{\partial x_i}\left(\alpha w_i q\right)\right)_P \Delta V. \qquad (4.108) \end{aligned}$$

The first term (collisions) is always positive and will be treated as an explicit source in the FVM. The product rule can be used on the second term on the RHS to give both an explicit and implicit source term component as with the volume fraction transport equation yielding

$$S_p = \min\left(-\frac{\partial}{\partial x_i}\left(\alpha w_i\right)_P, 0\right)\Delta V \qquad (4.109)$$

$$S_c = -\left(\alpha w_i \frac{\partial q}{\partial x_i}\right)_P \Delta V + \max\left(-\frac{\partial}{\partial x_i}\left(\alpha w_i\right)_P, 0\right) q_P \Delta V + \left(\frac{4n^2 d_p^3 A_{\text{c, max}}\sigma_0}{3\rho_p}\left(1 - e^{-\frac{t_c}{\tau}}\right) S_{mag}^v\right)_P \Delta V. \qquad (4.110)$$

The source term due to collisions is not a non-linear source term (unlike the splitting from the EE velocity) and should be better-behaved. In the collisional source term, values are needed for the average contact area $\bar{A}_c$, the equilibrium charge density σ_0, the charging time constant τ and the contact time t_c. Both A_c and t_c can be calculated from Hertzian contact theory (Eqs. 2.35 and 2.36 respectively), with σ_0 and τ provided from the results from the aerosol beam experiments in Chapter 3.

From the charge distribution, the electric potential ϕ_e can be determined from Eq. 1.41. The charge density is found by multiplying the specific charge by the total mass of particles in the cell and then dividing by the cell volume

$$\rho_e = \frac{qNm_p}{\Delta V} = \frac{qn\Delta V m_p}{\Delta V} = qn\rho_p V_p = \frac{\rho_p \alpha V_p q}{V_p} = \rho_p \alpha q. \qquad (4.111)$$

This is a steady diffusion-source equation which can expressed in conservative form in a Cartesian coordinate system as

$$\int \frac{\partial \phi_e}{\partial x_i} dA_i = -\int \frac{\rho_p \alpha}{\epsilon_m} q dV. \qquad (4.112)$$

The source term is always-negative and constant in each cell to give a fully explicit FVM discretised source for cell P as

$$\begin{aligned} S_p &= 0, & (4.113)\\ S_c &= -\left(\frac{\rho_p \alpha q \Delta V}{\epsilon_m}\right)_P. & (4.114) \end{aligned}$$

The neighbour coefficients due to diffusion in a 2D, uniform mesh are simply

$$\begin{aligned} a_E^{i,j} &= \Delta x, & (4.115)\\ a_W^{i+1,j} &= \Delta x, & (4.116)\\ a_N^{i,j} &= \Delta x, & (4.117)\\ a_S^{i,j+1} &= \Delta x. & (4.118) \end{aligned}$$

When the electric potential has been solved for using the FVM, the electric field can be calculated using Eq. 1.38. This can be estimated using second-order central differencing for the gradients on a uniform mesh as

$$\boldsymbol{E}^{i,j} \approx \frac{1}{2\Delta x}\begin{pmatrix}\phi_e^{i+1,j}-\phi_e^{i-1,j}\\ \phi_e^{i,j+1}-\phi_e^{i,j-1}\end{pmatrix}. \tag{4.119}$$

4.7.1 Charge Model Results

A brief examination of the charge model applied to the Taylor-Green flow is made. Mesh independent results could not be obtained for the volume fraction, apart from the skewness of the radial volume fraction distribution. This reached an effectively stationary state for all Stokes numbers considered on a 128^2 grid and will be the only grid size employed here. The initial condition for charge is $q = 0$ everywhere, representing an initially uncharged aerosol. The effect of Stokes number on the charge distribution, the electric potential and the electric field strength will be examined. The volume fraction results are taken from the diffusion-free cases, with an implicit source term.

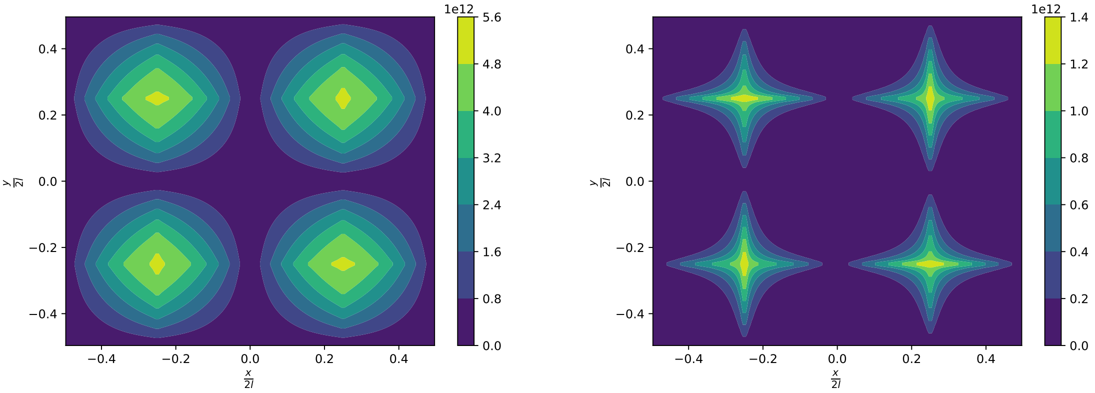

Figure 4.28: Particle binary collision frequency (s^{-1}) in the Taylor-Green flow for $Stk = 1 \times 10^{-3}$ and $Stk = 1 \times 10^{-2}$ on the left and right respectively.

The collision frequency for both $Stk = 1 \times 10^{-3}$ and $Stk = 1 \times 10^{-2}$ in Figure 4.28 show that the binary particle collisions are most significant in the particle collection spots, due to the large accumulation of both volume fraction and large strain rates in these regions. The source term in the charge transport Eq. 4.101 is proportional to this collision frequency and predicts that these are the sites of largest charge creation. At first, it may seem incorrect that the collision frequency is lower for a higher Stokes number as the relative velocities would be larger at $Stk = 1 \times 10^{-2}$ compared to $Stk = 1 \times 10^{-3}$. However, as the particle diameter of the $Stk = 1 \times 10^{-2}$ particles is ≈ 3.16 times larger than the $Stk = 1 \times 10^{-3}$ particles, this means that the number densities in the domain are lower for the same volume fraction. Expressing the collision frequency (Eq. 4.98) in terms of α yields

$$C_{11} = \frac{4n^2 d_p^3}{3} S_{mag}^v = \frac{48\alpha^2}{\pi^2 d_p^3} S_{mag}^v. \tag{4.120}$$

The dependence of the collision frequency on the inverse of the particle diameter cubed is the cause of the decrease in collision frequency. From the collision frequency with increasing Stokes number, we expect greater levels of particle tribocharging for the lower Stokes number case in the Eulerian model for these same initial conditions. The distribution of the collision frequency around the areas of maximum compressive strain also differs between the two considered Stokes numbers. The shape of the distribution of collision frequency for $Stk = 1 \times 10^{-3}$ is dominated by the particle strain rate magnitude (square root of Eq. 4.69), which for low τ_p tends towards the fluid strain rate magnitude of $S_{mag} = 2u_{mag}a\sin(ax)\sin(ay)$. For the larger Stokes number case, the “sharpness” of the volume fraction distribution which has been centrifuged away from eddy centres has an appreciable effect on the shape of the collision frequency distribution, with the fluid eddy positions seen in this distribution.

The particle specific charge distribution in Figure 4.29 has the same form as the volume fraction distribution from Figure 4.19. The specific charge levels are low, with the largest value in the domain providing a single particle charge of $\approx 1.21 \times 10^{-26} C$ for $Stk = 1 \times 10^{-3}$; around 8 orders of magnitude smaller than an electron. These values assume the particles share the same tribocharging constants as the salt found from experiment in

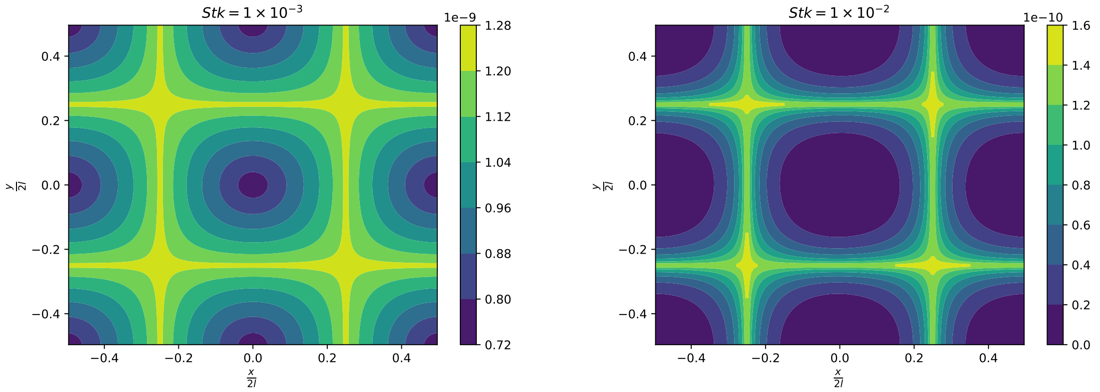
$Stk = 1 \times 10^{-3}$ $Stk = 1 \times 10^{-2}$

Figure 4.29: Particle specific charge (C/kg) in the Taylor-Green flow for $Stk = 1 \times 10^{-3}$ and $Stk = 1 \times 10^{-2}$ on the left and right respectively.

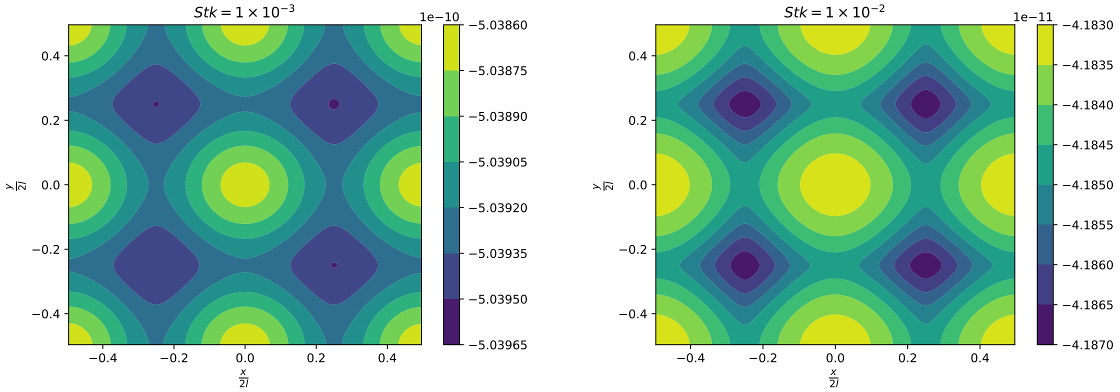
$Stk = 1 \times 10^{-3}$ $Stk = 1 \times 10^{-2}$

Figure 4.30: Electric potential normalised by the breakdown voltage for air in the Taylor-Green flow for $Stk = 1 \times 10^{-3}$ and $Stk = 1 \times 10^{-2}$ on the left and right respectively.

Chapter 3, which exchanged very little charge with the metal plate in those experiments. This is reflected here, with a dilute suspension of particles colliding at low impact velocities producing very little charge.

The resulting electric potential from this charge (Figure 4.30) is also very small compared to the breakdown voltage for air. The shape of the distribution for both Stokes number are similar, with the particle collection zones acting as low electric potential wells. As the electric field strength is the negative gradient of this electric potential, the electric field strength is expected to point away from these low potential wells towards areas of high electric potential.

The electric field strength from the scalar electric potential is provided in Figure 4.31. The electric field as expected points away from the areas of high charge towards the regions of lowest charge and provides the electrostatic force acting on particles per unit positive charge. As expected, the shape of the electrical field strength in the domain has a similar form for both Stokes numbers, with maxima occurring along diagonal lines relative to the coordinate system. These maxima lie closer to the particle collection spots with increasing Stokes number, due to the sharper gradients in these regions. The distribution of the collision frequency, specific charge, electric potential and electric field strength all make physical sense and provide confidence that the model is implemented correctly.

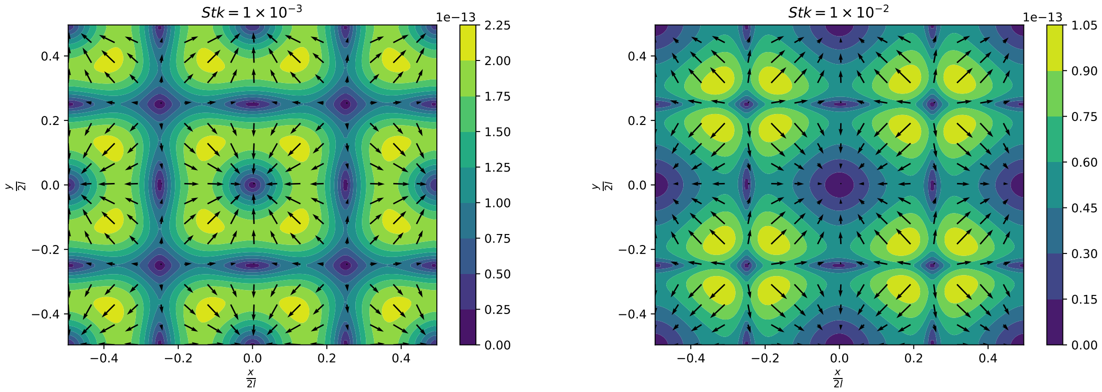

Figure 4.31: Electric field strength normalised by the breakdown field strength for air in the Taylor-Green flow for $Stk = 1 \times 10^{-3}$ and $Stk = 1 \times 10^{-2}$ on the left and right respectively. The local electric field strength vector is shown by the arrows with the colour indicating the magnitude of the normalised field strength at that location.

4.8 Conclusion

A 2D Taylor-Green fluid flow has been used to challenge and test the Eulerian particle model using the EE velocity specification. This flow features strong streamline curvature and large gradients and the eddy scales have been set to be characteristic of the Kolmogorov scales present in the cyclone. A validity criterion for τ_p and Stk were identified, with the change in the particle velocity field noted for increasing Stk. The FVM discretisation was presented, with results from a bespoke code and an implementation into a proprietary software matching. A choice of discretisation options for the source term, along with various diffusion coefficients were presented.

As volume fraction was found to accumulate in problem spots indefinitely with increasing mesh resolution, a mesh-independent solution could not be obtained for the Eulerian model. This is due to unrealistic physics of the set-up here, where particle collisions would prevent an ever-increasing concentration. The accuracy of the integration of Lagrangian particle trajectories were assessed which also provided a source of validation for the Eulerian model. Lagrangian particles were also found to accumulate in the same problem regions as the Eulerian model predicted.

Despite the difficulties regarding the singularities, convecting the volume fraction using the EE velocity produces a solution which captures the accumulation of particles in regions of large strain and the dispersion of particles from regions of high vorticity. This statistics of the particle volume fraction using the EE method better match the Lagrangian particle results than the mixture model for $Stk < 0.1$. The fluid can be directly solved for in the EE method, whereas in the mixture model the fluid velocity is determined by algebraic relations from the mixture velocity. Additionally, given a converged fluid flow field, the EE method is computationally cheaper than the mixture model. If singularities arise in a flow field, limits can be imposed to prevent the source term causing unphysical solutions and an implicit source term formulation can be used to increase solver stability, along with upwinding the volume fraction at the faces of the computational cells. These difficulties experienced in the model have not been assessed in this way in the literature and solutions have been obtained to both identify and deal with numerical issues. In addition to this, both the charge distribution and electric potential in the domain can be solved for. This can then yield the electrical field strength which can be used to predict where air breakdown is expected to occur in the domain. This work provides a solid foundation with which to apply this model to the cyclone flow in Chapter 5.

Chapter 5

Cyclone CFD Study

In this chapter, a LES cyclone CFD model is presented with the resolution quantified. This is compared to other cyclone work in the literature and provides the carrier flow field for the particulate phase. The near-wall regions are examined closely for evidence of secondary structures which may influence particle trajectories.

Lagrangian particles are tracked through this cyclone flow field. The statistics of the particles along their trajectories are analysed and a separation efficiency is estimated and compared to experimental evidence. The number of particles and integration settings needed for accurate results are explored. These statistics, such as Re_p and Stk both along trajectories and across the CFD domain, are used to inform the conditions of the flow seen by the particles for the Eulerian model.

Finally, the Eulerian model using the EE method is applied to the cyclone. The effect of the boundary conditions and diffusion coefficients on the volume fraction distribution and separation efficiency are discussed. The predicted separation efficiency is compared to the Lagrangian particle result to assess the accuracy and suitability of this model in a complex, highly-swirling flow. This section of work concludes with predictions of the transport of charge through the cyclone and the resulting electric fields from these charged particles.

5.1 Single-Phase Cyclone CFD

The CFD is performed using ANSYS Fluent which is a finite volume solver (the basics of which are provided in Section 4.2.1). In the FVM, the solution domain must be discretised into a mesh of non-overlapping cells which each provide an equation in the form of Eq. 4.23. This cyclone mesh is block-structured, such that the matrix of coefficients has a regular structure and is easier to solve [32]. The mesh is also refined in areas where large velocity gradients are expected for increased resolution of these regions.

An unsteady LES is performed using the mesh, with the experimental pressure drop of the cyclone used as a boundary condition. The resolution of the simulation is discussed, with the form of the tangential velocity profile compared to other cyclones as commonly performed in the literature from Section 2.1.1. Evidence for vortical structures near to the walls is explored to explain the banding seen in the experimental evidence from Figure 1.2.

5.1.1 Mesh Sizing

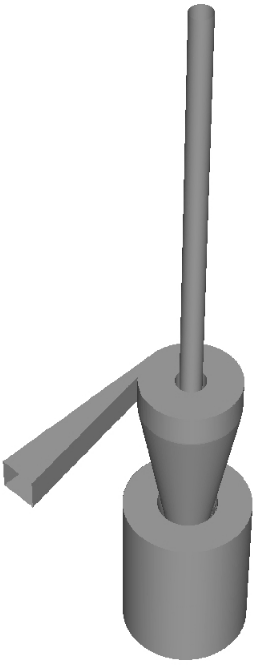

Figure 5.1: Outer surface of the entire cyclone mesh used for CFD. The inlet is aligned along the z-axis, with the outlet pipe aligned along the y-axis.

Figure 5.1 shows the mesh outline of the entire geometry. The model features a long inlet pipe which joins the cyclone tangentially at the top. This is to ensure the flow at the entry to the cyclone is not constrained by an inlet boundary condition and allows the flow to naturally develop into a swirling motion in the cyclone. At the base of the cyclone is a cylindrical bin, made large as to not disturb the flow from the cone tip. Finally the geometry features a long, straight outlet pipe extending $1.5H$ above the cyclone. This length was informed following the results by Schmidt *et al.* [94] from Section 2.1.1, who found that the swirl velocities in the cyclone were undisturbed by outlets of length $\approx 1.5H$. This also enables a fixed pressure outlet boundary condition to be used without affecting the flow within the cyclone itself [29].

In sizing the mesh for LES, the state of the inlet flow is used to estimate the number of cells needed to adequately resolve the boundary layer. This will be defined in terms of viscous wall scales in the inlet pipe, which from Section 2.1, are a function of Reynolds number. For the Reynolds number for the inlet flow, a characteristic length is required. For a rectangular duct, a hydraulic diameter can be defined as [183]

$$d_H = \frac{2a_h b}{a_h + b}. \tag{5.1}$$

At the cyclone inlet, $d_H = 3.96mm$. The Reynolds number of the inlet pipe flow using the hydraulic diameter is $Re_{in} \approx 9770$, indicating that the flow in the inlet pipe is turbulent. Following Pope [30], by assuming a smooth

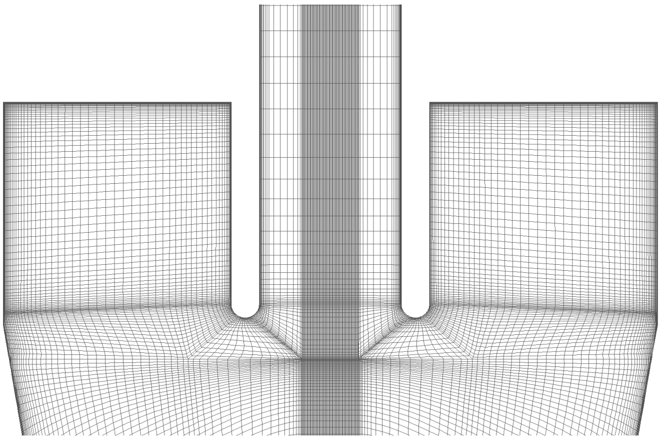

Figure 5.2: 2D slice of the mesh at the top of the cyclone on the x-y plane.

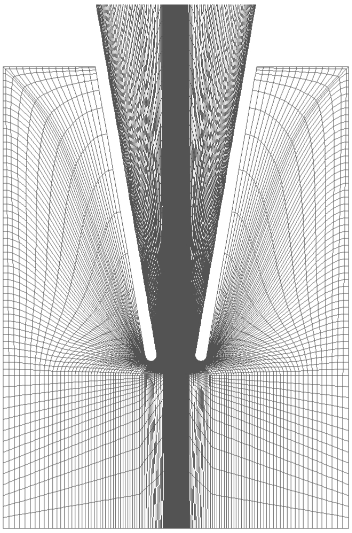

Figure 5.3: 2D slice of the mesh at the bottom of the cyclone with the bin.

pipe wall, Prandtl's friction law is defined as

$$\frac{1}{\sqrt{f_f}} = 2.0 \log_{10}(\sqrt{f_f} Re_{in}) - 0.8. \tag{5.2}$$

Solving this implicit equation for the friction factor f_f yields $f_f \approx 0.0031$. The friction velocity at the wall u_τ can be calculated using this and the bulk mean flow as $u_\tau = u_0\sqrt{\frac{f_f}{8}} \approx 2.32m/s$. The viscous wall length scale $\delta_\tau \approx 6.5 \times 10^{-6}m$ provides the distance y of the first cell by the wall required to have a dimensionless wall distance of $y^+ = \frac{y}{\delta_\tau} = \frac{u_\tau y}{\nu_f} = 1$ [45]. We therefore expect to be resolving down to the viscous sublayer of the boundary layer.

This then provided a useful estimate for which to size the cells starting from the wall, with an expansion ratio of 1.2. The mesh consists of ≈ 9 million computational cells, which is higher than those from previous cyclone studies [7, 184], including the DNS by Zhu *et al.* of a hydrocyclone at $Re_D < 2000$. A 2D section of the mesh at the top of the cyclone is shown in Figure 5.2. There is a highly refined region along the central spine of the cyclone to ensure the strong fluid velocity gradients in this region are resolved [29] and to capture the vortex breakdown instability predicted from Section 1.3.2. The mesh is also refined by the walls to capture the boundary layer structures predicted seen by Zhu *et al.* in Section 2.1.1.

The mesh at the base of the cyclone including the bin is shown in Figure 5.3. The mesh in the bin is coarse with a high detail region extending from the vortex core to capture any swirling flow spilling over the cone tip into the bin.

5.1.2 Solver Numerics

The equations of motion for the fluid are solved using the finite-volume method introduced in Chapter 4. The full set of equations for the LES are supplied in Appendix F. In this section the differences in discretisation compared to the Taylor-Green flow are highlighted.

Gradients in flow variables are calculated similarly to the method used for the Taylor-Green flow (Eq. 4.45) by using the modified divergence theorem (Eq. 4.44). Instead of estimating the face centroid values using linear interpolation between cell centroids, the average of the nodal values on the face are used. The nodal values are computed by a weighted average of the cell centroid values surrounding the nodes to give the Green-Gauss Node based gradient method, which is second-order accurate in space.

A bounded central differencing discretisation for convective-diffusive fluxes was used which ensures stability when using LES. This is based on the normalised variable diagram [185] to blend between pure central differencing (Eq. 4.27) which is only stable if the local Péclet number is less than 2 [174] and a second-order upwind scheme given by Eq. 4.35. The gradient operator is discretised using the Green-Gauss Node-Based method. Both pure central differencing and second-order upwinding can result in unphysical oscillations in the solution. In the bounded central differencing method, if the solution attained is not bounded, the face value is computed using first-order upwinding (Eq. 4.29). The diffusion terms are central differenced.

Temporal derivatives were discretised using a bounded second order implicit method which, analogous to the bounded central differencing scheme, blends between a second order and a first order implicit scheme. The fluid time step had to be small enough in order to capture the PVC behaviour of the cyclone and the resolved turbulent scales. An estimate of the Kolmogorov time scale (Eq. 1.7) at the inlet pipe was used to inform the selection of the time step. Following Pope [30], the largest turbulent scales can be estimated as $l_0 \approx \frac{1}{6}d_H$, with the dissipation rate scaling as $\epsilon_f \approx \frac{u_0^3}{l_0}$ to provide a time scale of the smallest eddies as $\tau_\eta \approx 4.4 \times 10^{-7}s$. As these scales are not expected to be resolved by the LES, the time step can be slightly above this estimate and was set to $\Delta t = 5 \times 10^{-7}s$.

The LES was run with pressure-velocity coupling, where the momentum and pressure equations are solved together. This fully implicit approach increases the stability of the system and enables faster convergence. Pressure was calculated using the pressure staggering option (PRESTO!), where the pressure is solved on a staggered grid which provides the face centroid pressures without interpolation. This also provides a more accurate prescription for the wall pressure gradient in the presence of curvature than the standard Rhie and Chow scheme [186], which can result in velocity vectors pointing into or out of walls.

The system of equations are solved using an algebraic multigrid method. This involves solving the linear system on coarser meshes to increase the rate of convergence. This reduction in computational effort is achieved as the solution information propagates through the domain one cell at a time. For large meshes this makes the solution of the linear system prohibitively expensive. By solving on a coarser mesh, information from the boundaries is able to propagate through the domain faster; thus requiring less computational expense to solve the linear system. For solving the scalar volume fraction and charge equations in Section 5.3, the point-by-point Gauss-Seidel method (Eq. 4.62) is used. For the coupled LES fluid equations, an incomplete lower-upper (ILU) method is used [187].

At the inlet, the total gauge pressure is set to $0kPa$. The walls are stationary, apply the no slip condition and have zero heat flux across them. For the fluid, $C_p = 1006.43Jkg^{-1}K^{-1}$, the thermal conductivity $= 0.0242Wm^{-1}K^{-1}$, the molecular weight $= 28.966kg/kmol$ and $\mu_f = 1.7894 \times 10^{-5}kgm^{-1}s^{-1}$. The operating pressure was set to $101325Pa$. A fluctuating velocity algorithm was used on the inlet face to provide a more realistic turbulent flow state entering the domain after an initial run without this fluctuating velocity algorithm. A spectral synthesizer is used which produces a divergence free velocity field [188], given the turbulent intensity and hydraulic diameter.

The area-averaged fluid quantities on the inlet face of the CFD model are used to calculate the Reynolds number in order to estimate the turbulent intensity. The inlet Reynolds number, based on the hydraulic diameter is $Re_{\text{face}} \approx 3328$. It should be noted that this is not the Reynolds number of the flow entering the cyclone from Section 2.1.1. This is the Reynolds number of the fluid on the inlet face of the domain at the start of the inlet pipe. The turbulent intensity was estimated by using two empirical correlations for fully-developed turbulent pipe flow. The first is given by [189]

$$I_1 = 0.16Re_{\text{face}}^{-\frac{1}{8}}. \tag{5.3}$$

The second empirical correlation is [189]

$$I_2 = 0.227Re_{\text{face}}^{-0.1}, \tag{5.4}$$

which provides $I_1 = 5.8\%$ and $I_2 = 10\%$. A middle-ground of $I = 7\%$ was used for the turbulent intensity with a hydraulic diameter of approximately $8.1mm$.

The outlet total gauge pressure is $-5kPa$, in line with the experimentally validated pressure drop of $\Delta P = 5kPa$. An average-pressure specification, which would promote solver convergence, was not used as this would over-constrain the swirling flow at the outlet. The current boundary condition allowed reversed flow at the outlet face which is to be expected with highly-swirling flow at the boundary and is therefore a more realistic boundary condition. This reversed flow phenomenon was also seen in the work by Schmidt *et al.* who concluded that this would not affect the swirl velocities in the cyclone given a sufficiently long outlet pipe [94]. The inlet and outlet temperatures were specified as $300K$.

The convergence criteria for the mass and velocity component scaled residuals (Eq. 4.64) was set to 1×10^{-5} with energy set to 1×10^{-6} for every time step (where mass was the last variable to reach this criteria and the velocity components residual reached in the order of 1×10^{-9}). The static pressure in the outlet pipe, the mass flow rate at the inlet and the mass flow rate at the outlet were continually monitored during the numerical time stepping of the solution to aid in determining when a statistically stationary state had been reached for the flow field.

5.1.3 Fluid Results

To assess the spatial resolution of the LES, the local grid scale can be compared to the smallest eddies in the flow given by Eq. 1.6. The ratio of the Kolmogorov length scale, η, to the local grid scale, Δ, for the different cyclone sections (defined in Figure 1.3) is provided in Figure 5.4. Due to the volume of each computational cell varying, the count on each histogram in this thesis has been weighted with the cell volume to make the results independent of the mesh. As most of the eddies are within an order of magnitude of the local grid scale, the LES is modelling only the very smallest eddies in the flow and therefore has high spatial resolution. Starting from the top of the cyclone, the majority of the Kolmogorov length scales decrease in size as we move vertically down the cyclone, with an increase near the cone tip. This is due to the majority of the cells capturing the "eye" of the vortex core by the cone tip, where the fluid velocity is small. On the edges of the vortex core, the flow is travelling at the fastest speed in the domain. This is seen as the peak around $\frac{l_\eta}{\Delta} \approx 0.1$ for the middle two sections.

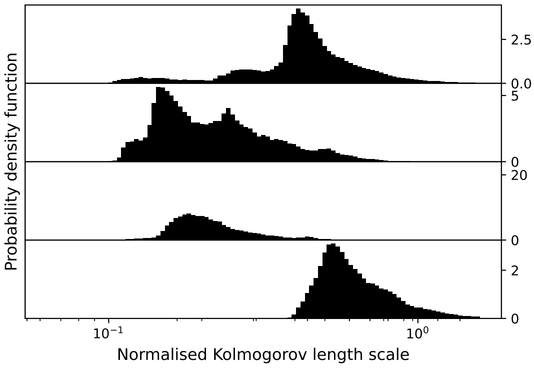

Figure 5.4: Histogram of the Kolmogorov length scale divided by the local grid scale Δ. Most of the cells in the domain are within an order of magnitude of the size of the dissipative eddies in the flow. The histograms represent the sections 1 to 4, defined in Figure 1.3, from top to bottom respectively.

The Kolmogorov timescale, τ_η, normalised with the fluid time step, Δt, for each of the 4 sections of the cyclone is shown in Figure 5.5. From this figure, the time step for the CFD is smaller than any of the Kolmogorov eddy timescales and the inlet scaling performed in Section 5.1.2 provided an underestimate for the smallest turbulent time scales. The temporal resolution of the simulation is therefore comparable to a resolved DNS.

Also evident from Figure 5.5 is a structure to the distribution in each section. At the top of the cyclone, there is a large spread in the τ_η distribution. This wide range of time scales are due to the influence of multiple flows in this region including the inlet flow, the outer vortex flow, a permanent vortical structure where the inlet pipe joins the cyclone and the core within the vortex finder. Moving vertically down the cyclone to section 2, the distribution begins to become unimodal. The peak at around $\frac{\tau_\eta}{\Delta t} \approx 10^2$ becomes more prominent in the

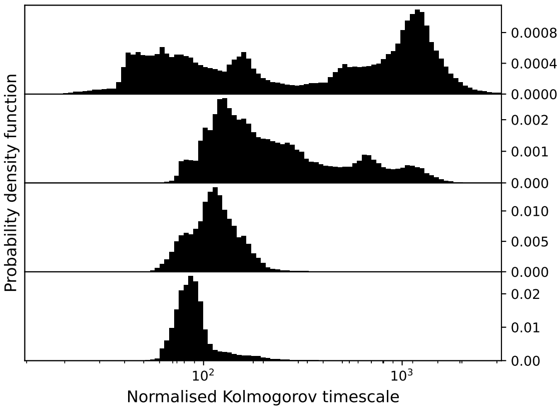

Figure 5.5: Kolmogorov timescale distribution normalised with the time step for each of the four sections of the cyclone. The histograms represent the sections 1 to 4 from top to bottom respectively.

Section	1	2	3	4
$\frac{\bar{k}}{\bar{k}+\bar{k}_{SGS}}$	86.8%	89.3%	97.6%	99.4%

Table 5.1: Cell volume weighted average of the turbulent kinetic energy ratio for each cyclone section.

unimodal distribution in section 3. These dominant turbulent time scales are related to the high-speed vortex core. Finally by the cone tip, the distribution is unimodal, with a well-defined peak at a smaller time scale than the rest of the cyclone. This where the outer swirling flow reverses direction, forming the vortex core. This suggests that the cone tip features the strongest turbulence in the cyclone as both the turbulent time scales are smallest and the length scales are larger in the cyclone at this region.

A common method of determining the resolution of an LES is by looking at the ratio of the resolved to the total turbulent kinetic energy; with a well-resolved LES having 80% of the turbulent kinetic energy resolved. The resolved turbulent kinetic energy is given by the resolved fluctuations as [30]

$$\bar{k} = \frac{1}{2}\overline{u_i' u_i'}. \tag{5.5}$$

An estimate of the unresolved turbulent kinetic energy can be obtained assuming a sharp spectral filter as [30]

$$\bar{k}_{SGS} \approx 2.25 \left(\frac{\bar{\epsilon}_f L_s}{\pi}\right)^{\frac{2}{3}}, \tag{5.6}$$

where the mean turbulent dissipation rate $\bar{\epsilon}$ is estimated from the time average of Eq. 1.14 and the mixing length L_s from Eq. F.10. The filtering is implicit in this LES and does not have a sharp cut-off in wavenumber space as with a sharp spectral filter, however it provides a useful estimate for the unresolved energy. The cell volume weighted average of the turbulent kinetic energy ratio in the cyclone is 89.2%, indicating that the LES is well-resolved. The energy ratio PDF for each cyclone section is presented in Figure 5.6, with the average energy ratios for the sections given in Table 5.1. The cone tip is very well resolved, with over 99% of the turbulent kinetic energy directly computed. This is in agreement with the resolution of the length and time scales in this region and means that the flow field seen by particles in Section 5.2 is accurate and will produce realistic trajectories. The turbulent kinetic energy ratio decreases moving vertically up the cyclone as the mesh becomes less dense, with the worst resolution observed on the edges of the vortex core by the vortex finder in Figure 5.7. The energy ratio by the walls indicates high wall resolution as expected from the mesh scaling using the inlet scales in Section 5.1.2.

The normalised tangential velocity profile of the main cyclone flow compared to data in the literature is shown in Figure 5.8. Though the cyclone dimensions vary an order of magnitude between cases ($D = 0.0223m$ for the present cyclone and $D = 0.4m$ for Shalaby's cyclone), the general shape of the tangential velocity slice across the cyclone share a common form. Sharp velocity gradients are seen by the walls as the fluid reaches the outer vortex velocity and then increases until it reaches its peak at the edges of the vortex core. Within the eye of the vortex core the velocity drops off steeply to zero at the centre of the vortex.

Due to the wildly varying geometries (the results in Figure 5.8 are not similar cyclones scaled), swirl numbers and operating Reynolds numbers, the velocity profiles would never be expected to match perfectly. Due to the

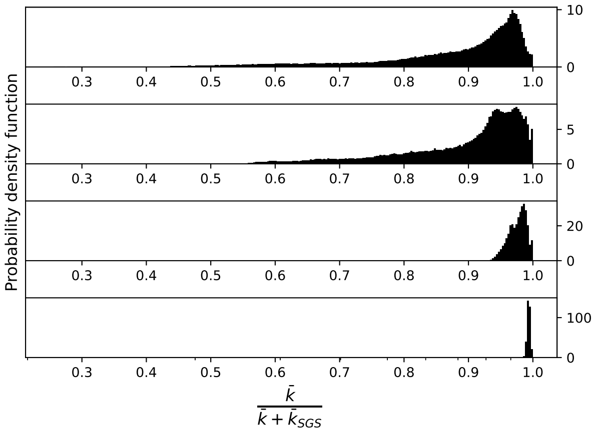

Figure 5.6: SGS energy ratio distribution for each of the four sections of the cyclone. The histograms represent the sections 1 to 4 from top to bottom respectively.

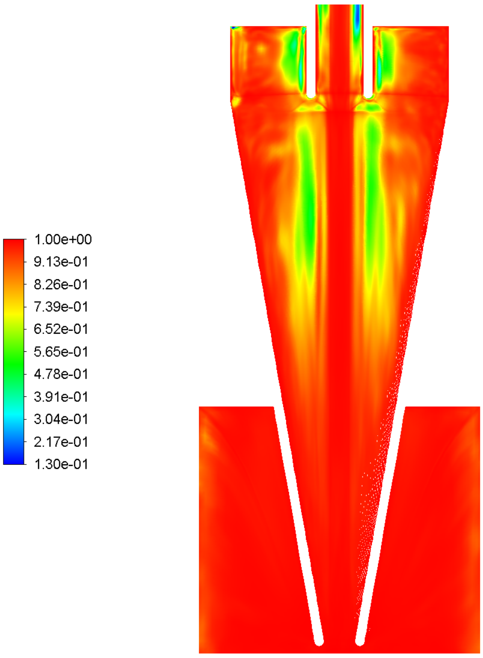

Figure 5.7: SGS energy ratio distribution along the centre of the cyclone on the x-z plane.

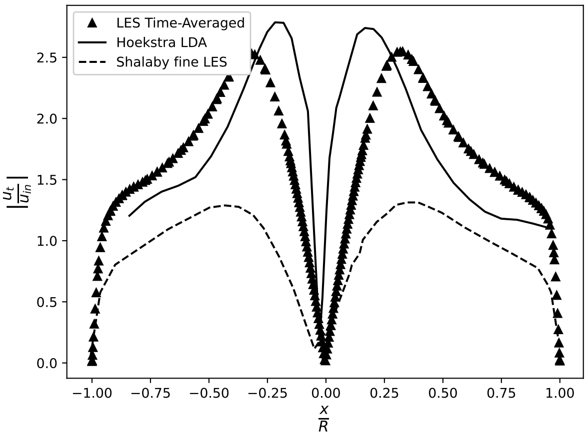

Figure 5.8: Cyclone tangential fluid velocity normalised by the bulk inlet velocity against local cyclone radius. The results of this study are shown compared to the laser doppler anemometry results from Hoekstra for the Stairmand high efficiency cyclone [22] and the "fine" LES model from Shalaby *et al.* [86]. The geometry of each cyclone varies greatly, with Reynolds numbers and swirl numbers of $Re \approx 34000, 27000$ and 700000 and $Sw_g \approx 4.6, 6.0$ and 3.1 for the current work, Hoekstra's data and Shalaby's data respectively.

lack of like-for-like geometry in the literature and caveats to measuring the flow field experimentally (Section 2.1), validation of the flow field is difficult. The experimentally-measured mass flow rate (provided by Dyson) at this pressure drop matched the CFD result to $\leq 1\%$ providing confidence in the results. The tangential flow field also has the expected form compared to other geometries in the literature and flow variables were monitored to assess when a statistically-stationary state was reached, after which the model was run further to collect time-averaged data. The level of validation performed here is also consistent with that performed in many cyclone CFD studies in the literature as discussed in Section 2.1.1. The separation efficiencies predicted in Section 5.2.1 are also used as an additional form of validation as an accurate flow field is required to match experimental separation efficiencies.

The current cyclone model shows high dimensionless tangential velocities like the Stairmand high efficiency cyclone and the mean velocity profile shows a symmetrical shape as expected. Large numbers of data points in Figure 5.8 are observed for the current study, especially by the walls (for which LDA data is limited as discussed in Section 2.1) and the vortex core, showing the excellent resolution of the current study.

Figure 5.8 shows that the peaks of the tangential velocity distribution is a strong function of the geometric swirl number. Larger values of Sw_g results in higher dimensionless tangential velocities. The normalised velocity distribution appears to be independent of the cyclone Reynolds number for the high Re turbulent cases considered and the boundary layer by the walls is thin which is also expected from the high Reynolds numbers.

From the experimental evidence in Figure 1.2, particles were seen accumulating in long-lived structures in the boundary layer of a cyclone. The CFD performed allows an in-depth look at the structure of these boundary layers. The resolution of the near-wall region can be assessed by looking at the y^+ distribution at the first cell from the wall. From Figure 5.9, the boundary layer is well resolved in the wall-normal direction with $y^+ < 1$ for most of the walls. The maximum y^+ value of the first cell from the wall in the cyclone is $y^+ = 4.00$.

The velocity distribution of the boundary layer can give an indication as to its structure. The mean velocity can be normalised with the skin friction velocity $u_\tau = \sqrt{\frac{\tau_w}{\rho_f}}$ [45]. This can then be plotted against y^+ for the 4 sections of the cyclone and the inlet pipe. The mean velocity is normalised with the skin friction velocity to give u^+ [45]. It can also be compared to a flat plate covering the viscous sublayer ($u^+ = y^+$ for $y^+ < 5$ [30]) and the log-law region given by [30]

$$u^+ = \frac{1}{\kappa}\ln(y^+) + B_B, \tag{5.7}$$

where κ is the Von Karman constant and $B_B = 5.2$ from experiment [30]. The normalised inlet pipe boundary layer velocity profile in Figure 5.10 closely resembles that of a flat plate as expected, thus providing evidence that the LES is providing accurate results at the walls.

The normalised boundary layer velocity profile in each of the cyclone sections differs from the inlet pipe. The first 2 sections closely match their velocity profiles until far from the wall with the flow speeding up as we move vertically down the cyclone. The concave geometry of the cyclone walls is seen to cause the boundary layer to grow slower than the flat plate result and reduces the extent of the log-law region in agreement with

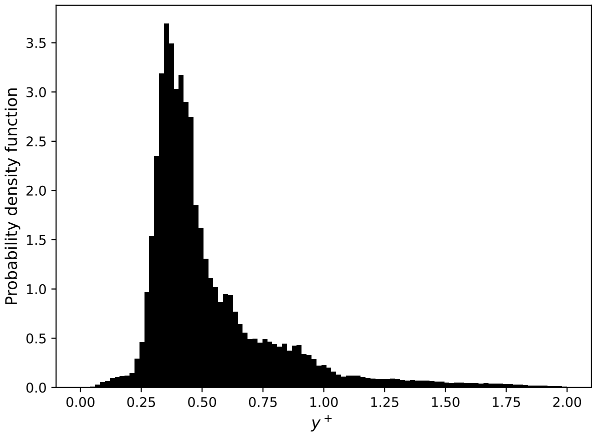

Figure 5.9: Wall y^+ distribution of the cyclone.

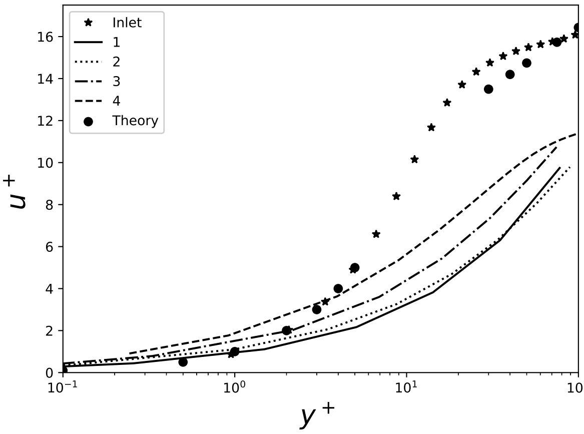

Figure 5.10: Time-averaged u^+ distribution against normalised local wall distance. This is shown for the inlet pipe and the 4 cyclone sections. Also shown is a flat plate solution for comparison.

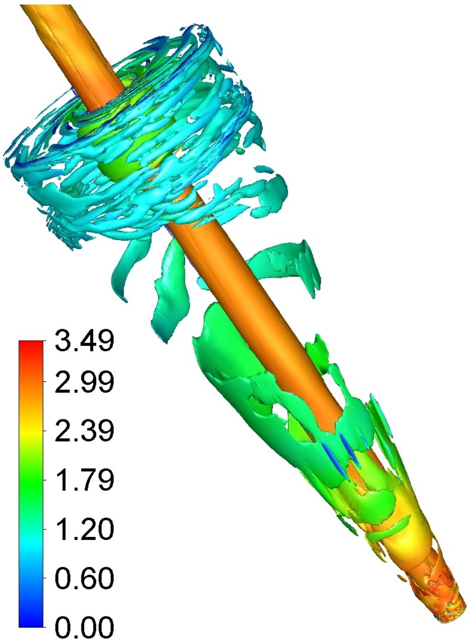

Figure 5.11: Iso-contour of the Q-criterion with $Q_c = 1 \times 10^7 s^{-2}$, coloured by the mean local fluid speed normalised with the mean cyclone inlet velocity. The vortex core is clearly identified by the long solid structure through the centre of the cyclone. Smaller streaky structures are observed predominantly at the top section of the cyclone, with longer banded structures appearing along the conical section.

previous work [190]. A thinner boundary layer may decrease the likelihood of particles becoming trapped by the wall as only particles with trajectories taking them very close to the wall will be able to enter the boundary layer.

Possible boundary layer structures are visualised by iso-contours of the Q-criterion [191]. The Q-criterion allows a method of finding vortical fluid structures where the vorticity magnitude exceeds the strain rate magnitude of the filtered flow field [192]

$$Q_c = \frac{1}{2}\left(\hat{\Omega}^2_{mag} - \hat{S}^2_{mag}\right) > 0. \tag{5.8}$$

An iso-contour of Q-criterion is provided in Figure 5.11 and shows many vortical structures situated close to the walls, most notably at the top of the cyclone. A band of these vortical structures can also be seen spiralling down the conical section of the cyclone which qualitatively match the bands of particles seen in the experimental evidence in Figure 1.2. Also visible from the iso-contour are vortical structures at the very top of the cyclone by the wall which spiral in towards the vortex finder. The vortices are situated where the lip-leakage phenomena occurs, providing evidence that these vortical structures may contribute to this particle-escape mechanism.

The distribution of the dimensionless distance from the wall of the small structures are shown in Figure 5.12. The y^+ values indicate that these structures lie mainly within the boundary layers of the cyclone and these structures are likely to be partially-resolved Görtler vortices. As discussed in Section 2.1.1, definitively identifying these structures as Görtler vortices is not possible, however the velocity profile in Figure 5.10 shows a similar reduction in u^+ for $y^+ > 8$ as seen by Wang *et al.* compared to the flat plate result. The resolution is described as partial as the wall-normal direction of the boundary layer is well-resolved as evidenced by Figure 5.9, however the inflation-layer boundary cells are elongated parallel to the wall. This causes the cell volume to be large compared to the wall-normal distance and therefore the LES filter width increases. The full structure of these vortices are not able to be directly computed in this LES, but indicative structures are present from the high wall-normal resolution. Lagrangian particles will see these partially-resolved boundary layer structures, however they will not see any of the unresolved scales.

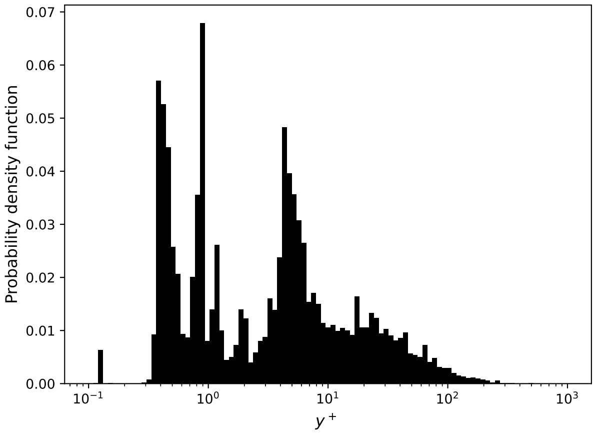

Figure 5.12: Normalised wall distance distribution of the vortical wall structures in Figure 5.11, excluding the vortex core.

5.2 Lagrangian Particle Tracking

With the resolution and structure of fluid flow field analysed, Lagrangian particles are now tracked in this frozen flow field in Fluent. The numerical schemes used to integrate the equations of motion of the particles are the same that were used for the Taylor-Green flow in Chapter 4. The integration tolerance and the number of particles necessary to track in the cyclone are first explored in Section 5.2.1. With no analytical solution for a particle trajectory to compare to, the estimated separation efficiency is instead used to validate the particle study by comparison with experimental results. This is performed for a variety of forces acting on the particle from Section 2.1.2, with the effects of the inclusion of the forces on separation efficiency explored.

With the computational separation efficiency in agreement with experiment, statistics such as Stk and Re_p along particle trajectories are presented. This allows the validity of Stokes drag and the EE model to be assessed as a function of particle diameter in a cyclone. The particle trajectories show how particles translate through the boundary layers, in particular whether they enter and are able to leave or become trapped by the wall. This interaction between the particles and the boundary layer is linked to the Stokes and Reynolds numbers and the impact on separation efficiency is assessed.

Finally, the Lagrangian particle tracking study in the cyclone provides a comparison for the results of the EE model. Through careful choice of ensemble and volume averaging, "Eulerian" statistics can be created for this Lagrangian phase to provide a direct comparison to the results of the Eulerian model used in the following section.

5.2.1 Computational Set-Up and Separation Efficiency

The Lagrangian particles are initialised on the inlet face of the domain with the same velocity as the carrier fluid. The particles are evenly spaced in the x and y directions on the inlet plane with no two particles occupying the same position. As the inlet (which sits on the plane $z = -0.045m$) is rectangular, more particles are placed along the x-direction N_x than the y-direction N_y as the inlet is wider than it is tall. Figure 5.13 shows a typical arrangement of particles on the inlet plane with $N = 40$. If the horizontal particle spacing between particles is denoted by Δx_p, the spacing between particles adjacent to the wall and the wall itself is $\frac{\Delta x_p}{2}$ and likewise for the y-direction.

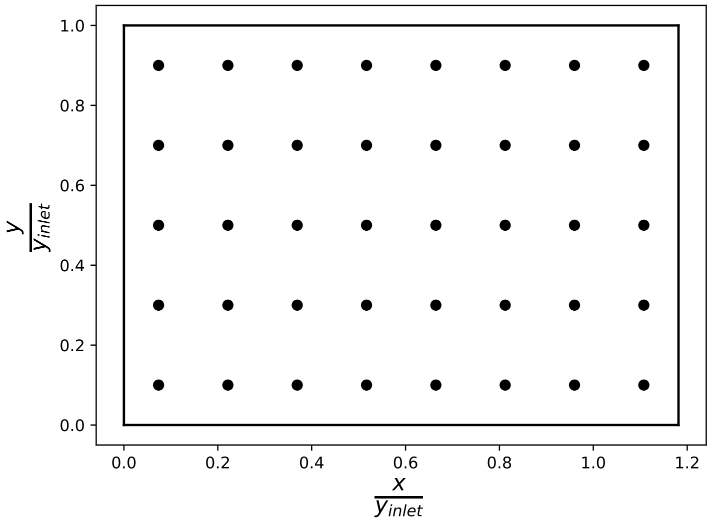

Figure 5.13: Typical particle injection arrangement on the inlet plane. Here 8 particles are uniformly spaced in the horizontal x-direction and 5 in the vertical y-direction.

The particle equations of motion (Eqs. 1.26 and 1.27) are integrated in time using the Runge-Kutta scheme outlined in section 4.4.1. The number of particles tracked and the tolerance of the Runge-Kutta scheme needed for statistically stationary results are unknown. The smallest particles ($0.1\mu m$) will require the most computational effort as they have the smallest τ_p, requiring smaller time steps than the larger particles to resolve their motion to the same tolerance. If the $0.1\mu m$ particle statistics are stationary, the statistics of the larger particle sizes are also expected to be stationary.

Due to the highly chaotic flow pattern in the cyclone, particle positions and velocities are not suitable

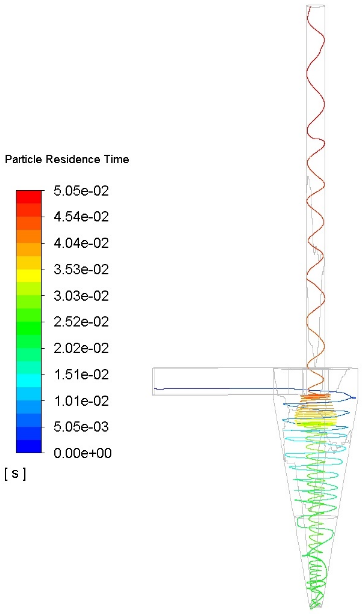

Figure 5.14: Particle trajectory of a $0.1 \mu m$ particle integrated using the Runge-Kutta scheme with a tolerance of 1×10^{-16} coloured by residence time. The particle is acted on by Stokes drag only.

candidates for judging a statistically stationary state. The bulk particle statistic of separation efficiency is a more suitable measure, with the overall picture of whether particles are separated used, instead of the fates of individual particle tracks. The separation efficiency is measured for a range of integration tolerances and particle numbers. To ensure repeatable results which are not affected by stochastic forces, these numerical studies are performed with only Stokes drag with Cunningham slip assumed to act on the particles.

An additional problem with calculating particle trajectories in the cyclone arises from particles becoming trapped; either by slowly crawling through the boundary layers or by rotating around the cyclone endlessly (a key phenomenon which is not considered in the simple time-of-flight model in Section 2.1). These particles may never leave the cyclone and require excessive computational resources to continue tracking. Particles will be assumed to be trapped when they collide with the cyclone walls which physically represents them adhering to the cyclone walls. These particles are assumed to be separated as they will not leave through the vortex finder, a big assumption which is analysed later. For the particles stuck in endless loops, the integration should be stopped after some elapsed time with any remaining particles assumed to separated (as they are not leaving the cyclone). This assumption will overestimate the separation efficiency as there is no guarantee of separation from this, the same applies to the trap boundary condition at the wall. To determine this cut-off time, a range of trajectories were studied where a particle escaped through the vortex finder. One such trajectory, which performed many core rotations is shown in Figure 5.14.

The escape trajectory shown in Figure 5.14 took a greater amount of time to leave than most escape trajectories, most of which entered the cyclone and immediately left through the vortex finder. This trajectory is representative of a worst-case scenario for the duration of time needed to separate a particle and the cut-off time selection is based on this result. The cut-off time is set to $t_{max} = 5.055 \times 10^{-2} s$. Particles still in the domain after this time are assumed to be separated. For comparison, the time taken for a particle to impact a wall based on the time-of-flight model (Eq. 2.5) is $t_{wall} = 9.2 \times 10^{-2} s$, almost twice as long as the cut-off time considered here. This cut-off time is revisited to check that the results are independent of this choice.

The separation efficiency of the cyclone is given by

$$\eta = 1 - \frac{N_{esc}}{N}, \tag{5.9}$$

where N_{esc} is the number of particles escaping out of the vortex finder. For stationary separation efficiency statistics, a certain tolerance and number of particles are required. It is not known from any of the literature in Section 2.1 whether these two factors are independent. An initial estimate for the tolerance used is 1×10^{-8} and the number of particles varied. When a suitable number of particles are found, the tolerance will then be varied to find a suitable value. These suitable values will be ones which recover the separation efficiency result for higher particle numbers (or lower tolerances) with less computational effort. For the initial estimate for tolerance, the separation efficiency as a function of number of particles is shown in Figure 5.15.

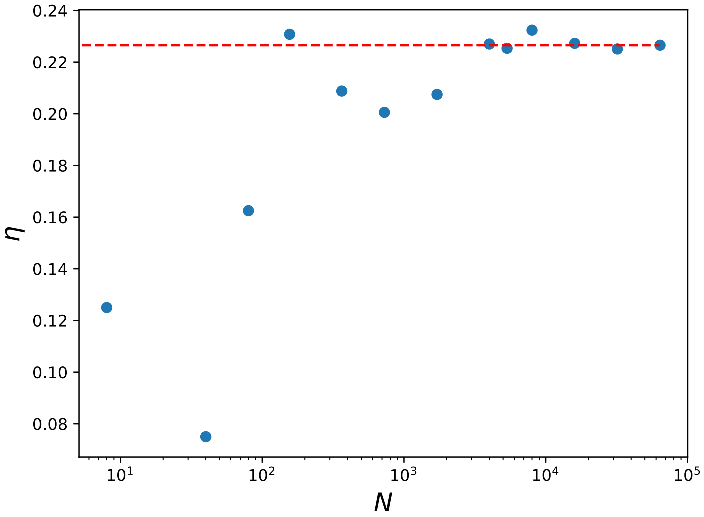

Figure 5.15: Separation efficiency as a function of number of particles tracked for a tolerance of 1×10^{-8}. The dashed red line represents the value of separation efficiency obtained using the largest number of particles in this study (64000).

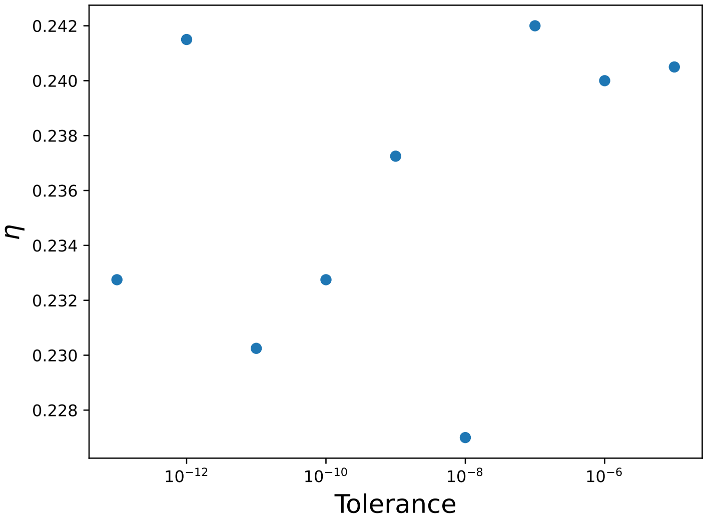

Figure 5.16: Separation efficiency as a function of integrator tolerance for 4000 particles.

A suitable number of particles, for which the separation efficiency varies by less than 1% from estimates using greater numbers of particles, is $N = 4000$. We now keep this value of N and adjust the tolerance to check if the initial estimate was satisfactory. Figure 5.16 shows no statically stationary solution for the separation efficiency for the tolerances examined, where the range of the data is 0.015. As the results were within 2% of each other, the separation efficiency is independent of the tolerance for the range of values examined. The largest tolerance tested of 1×10^{-5} is used along with $N = 4000$ for all future particle tracking.

A separation efficiency graph may now be created and compared to experimental evidence provided by Dyson. The separation efficiency is calculated using a range of additional forces on the particles to quantify the effects of the individual force contributions to the accuracy of the separation efficiency. These forces, introduced in Section 5.2.1, include the Brownian force (Eq. 2.21), Saffman Lift and the DRW model to capture the effects of the unresolved turbulent scales on the particles. For the DRW model, both methods presented of estimating the eddy lifetime from Section 5.2.1 are examined, with the constant τ_e given by Eq. 2.19 and the random prescription given by Eq. 2.20. For these force combinations, Cunningham slip has been incorporated into the particle relaxation time (Eq. 1.24), a separate case of just Stokes drag with no Cunningham slip correction of τ_p (Eq. 1.21) is also examined. The separation efficiencies from different combinations of these forces are shown in Figure 5.17.

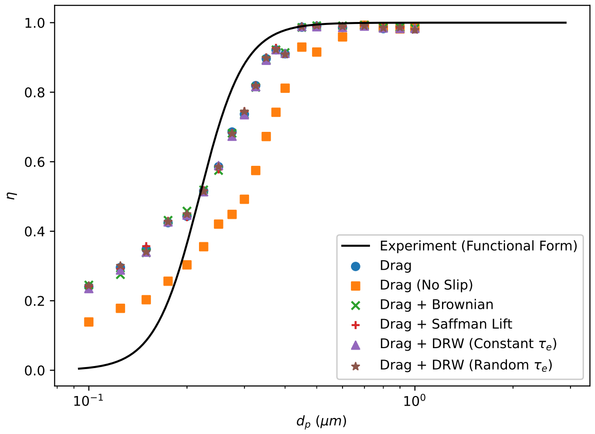

Figure 5.17: Separation efficiencies for a range of forces compared to experiment. Every force combination is inclusive of Cunningham slip except for the "No Slip" results.

The experimental results have been fitted to the functional form given by Eq. 2.7 in Section 2.1. The results show that the $0.1\mu m$ particles are unlikely to be separated at all, with perfect separation predicted for the larger $1\mu m$ particles. The separation efficiency increases with particle diameter as expected and provides an excellent reference to compare the computational results to.

The different force combinations all provide similar results, with the effects of additional forces on separation efficiency becoming more prominent with decreasing particle size. The only exception is the exclusion of Cunningham slip, which shifts the separation efficiency curve to the right and grossly under-predicts the separation efficiency of the majority of particle diameters considered. The inclusion of a Cunningham slip correction factor for the particle motion is therefore needed for sub-micron particles in this highly-swirling flow, henceforth only results including Cunningham slip are discussed.

The separation efficiencies for particles $d_p \geq 0.4\mu m$ match the experimental result of approximately perfect separation. Particles smaller than this follow the correct experimental trend, however the sharpness of the experimental drop-off of η is not faithfully captured. The beginning of the dip in the separation efficiency is well-matched and the cut-off diameter predicted from CFD closely matches experiment. This is the most important aspect to capture as d_{p50} effectively characterises the separation performance of a cyclone at a given pressure drop from Section 2.1. The Lagrangian particle tracking over-predicts the separation efficiency of the smallest $0.1\mu m$ particles. These particles are expected to have the lowest Stokes numbers and readily respond to the smallest scales of turbulence in the flow which are not directly resolved in the LES. Modelling the effects of the unresolved scales with the DRW model produced a negligible effect on the separation efficiency, as did including the effects of both Brownian motion and the Saffman Lift force. Discrepancies between the CFD results and experiment also arise due to the missing physics in the computational model. These include particle collisions and electrostatic interactions which may cause small colliding particles to agglomerate into larger structures which are able to be separated.

The Lagrangian particle tracking has assumed a monodisperse particulate phase, whereas the experimental results were obtained by using a polydisperse particulate phase. The polydisperse case will feature collisions between different particle sizes and therefore particles of dissimilar diameters may affect each other. Particles of similar diameter (and therefore alike in Stokes number) will follow closely-matching trajectories. The biggest deviations in particle trajectories compared to monodisperse modelling is expected to be due to the interaction of large particles with much smaller particles. As will be shown in Section 5.2.2, the largest particles are trapped in the boundary layers of the cyclone and do not reside in the main flow. The smallest particles are overall not caught in the boundary layer, with the ones that are being separated. The collisional interactions between the large and small particles are expected to only be significant in the boundary layer and these interactions would not be expected to influence the separation efficiency of either size class as both are being separated.

The discrepancy between the computational and experimental results for the $0.1\mu m$ particles has been argued to be from missing physics in the model. This is the particle size for which the particle number independence tests were performed. In light of these results, this numerical validation is repeated for a particle size which is expected to be governed by the covered physics from the computational model, however shows a deviance from the experimental result. The particle number independence study is therefore repeated using $0.3\mu m$ particles, with the results shown in Figure 5.18.

As for the $0.1\mu m$ particles, using $N = 4000$ for the $0.3\mu m$ particles differs from the $N = 64000$ result

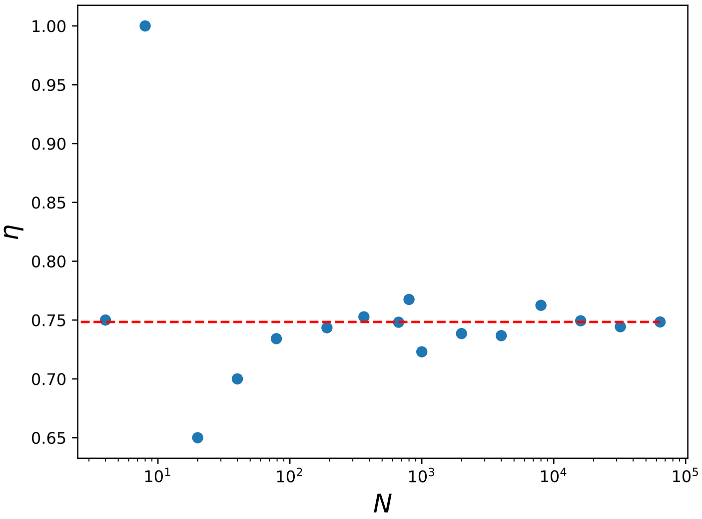

Figure 5.18: Separation efficiency of $0.3\mu m$ as a function of number of particles tracked for a tolerance of 1×10^{-5}. The dashed red line represents the value of separation efficiency obtained using the largest number of particles in this study (64000).

by $\approx$ 1% and the use of $N = 4000$ is justified. Although the separation efficiency is independent of the number of particles, it does not converge to the experimental value of $\eta_{300nm} \approx 0.89$. This could be due to the inclusion of the trapped wall boundary condition, which was included due to physical reasoning and the save in computational effort. The impact of this boundary condition on the separation efficiency of $0.3\mu m$ is investigated. In tandem with this, the effect of the particle initialisation position on the inlet face on separation efficiency is investigated. The inlet injection face in Figure 5.13 is split into halves: a top, bottom, left and right half. For each of these 4 halves, 4000 particles are injected evenly spaced as before, with the separation efficiency calculated and compared to the result using the entire face.

The results using both the trapped and the perfectly elastic wall reflection boundary condition for different inlet injection locations are shown in Figure 5.19. These separation efficiencies are relative to the result obtained by using the entire inlet plane. Particles injected from the bottom half of the inlet plane are have $> 6\%$ higher separation efficiencies than the full inlet face reference. Particles injected from the top half of the inlet plane resulted in the lowest estimation of the separation efficiency. This may be due, in part, to the particles being closer to the top wall of the cyclone where there exists a lip-leakage flow. Particles closer to the top wall are more likely to be entrained by this flow feature which results in them bypassing the main vortex flow and exiting out of the vortex finder. The differences in separation efficiency from injecting particles in the left or right half of the inlet plane is less pronounced, with both results deviating from the reference by $\approx 1.8\%$. This further evidences the lip-leakage hypothesis. The same trends are evident for the reflect as for the trapped boundary condition, with particles injected from the bottom half of the plane more likely to be separated than particles at the top. The separation efficiency predicted using the reflect boundary condition is $\approx 20\%$ lower than the trapped boundary condition. The trapped boundary condition provides a better fit to the experimental result ($\eta = 0.89$) which evidences the physical reasoning of particles adhering to the walls on impact. These results provide useful information for the choice of wall boundary condition for the particulate phase in the Eulerian model in Section 5.3.

The final numerical independence check to be made is determining the cut-off time and this is checked for the $0.3\mu m$ particles. The characteristic wall-impact time from the time-of-flight model (Eq. 2.5) for these $0.3\mu m$ particles $t_{wall} \approx 0.02s$ is used to normalise the cut-off time in Figure 5.20. The cut-off time includes the time taken for a particle to traverse the long inlet pipe which is not considered in the time-of-flight model. This time to traverse the inlet pipe is $\approx t_{wall}$, which explains why very low separation efficiencies are predicted for t_{max} values below this. The results show that the time-of-flight estimate for the time taken for a particle to hit the wall from entering the cyclone is a good estimate for the cut-off time, however it is a slight underestimate. The initial estimate for the cut-off time provided results which were independent of t_{wall} and this aspect had no issues.

The Lagrangian particles have been tracked in a “frozen” instantaneous fluid flow field. At a different moment in time, the resolved unsteady motions may be vastly different and provide a different result for the separation efficiency. The $0.3\mu m$ particles are tracked in the same result-independent set-up using the instantaneous fluid

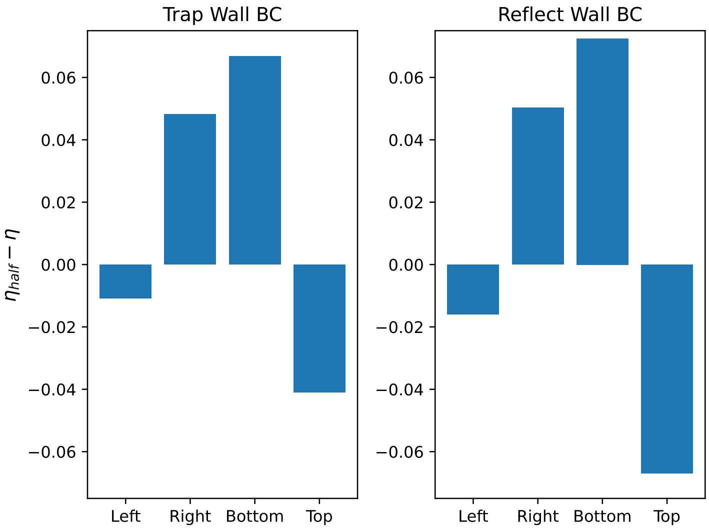

Figure 5.19: Separation efficiency of $0.3\mu m$ particles at different injection locations relative to the full inlet plane result. For each injection 4000 particles with a tolerance of 1×10^{-5} were tracked for both a trap and reflect wall boundary condition. The separation efficiency using the full inlet plane to inject particles was approximately 0.74 and 0.5 for the trap and reflect boundary conditions respectively.

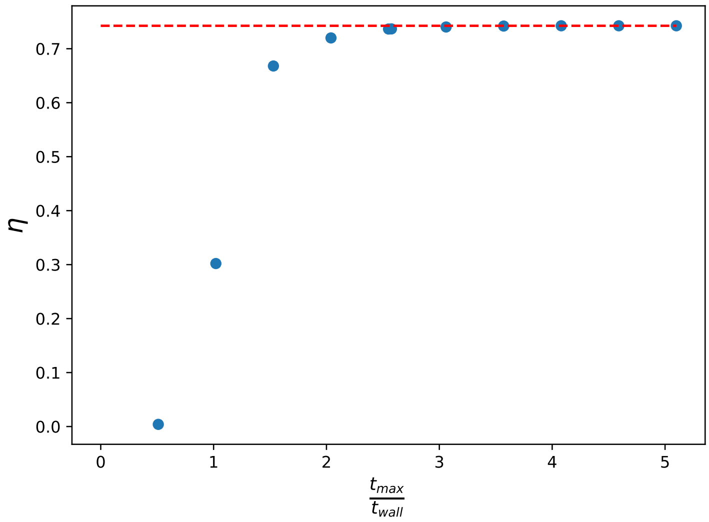

Figure 5.20: Separation efficiency of $0.3\mu m$ as a function of t_{max} using 4000 particles with a tolerance of 1×10^{-5} with a trap wall boundary condition. The dashed red line represents the value of separation efficiency obtained using the largest value of cut-off time considered in this study.

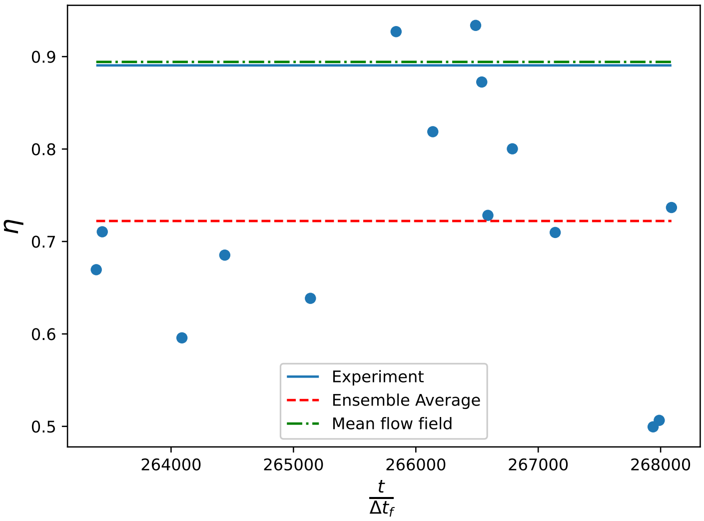

Figure 5.21: Separation efficiency of $0.3\mu m$ for different flow realisations in time. Also shown is the experimental value, an ensemble average of the different realisations and the result using the time-averaged flow field as horizontal lines.

flow field from earlier periods in time. Figure 5.21 shows a large variance in the estimated separation efficiency for different realisations of the flow field, with a spread of almost 50% for this particle diameter. This indicates that these particles readily respond to the resolved unsteady structures in the turbulent flow and that these structures affect the separation efficiency. An ensemble average of these realisations also shows a large deviation from the experimental value. The turbulent structures can be averaged out if instead the particles are tracked in the time-averaged flow field. This is a flow field which would never in reality be seen by the particles and is expected to provide a less accurate result. The separation efficiency estimated using the mean flow field is $< 0.5\%$ from the experimental value, which contradicts the reasoning above.

A range of particle diameters were tracked using the time-averaged flow field to see if the separation efficiency provided a better fit to experiment than the instantaneous flow field. Figure 5.22 shows this comparison and it is immediately clear that the $0.3\mu m$ result using the mean flow field was a chance occurrence as the rest of the results diverged from the experimental result. The slope of the separation efficiency graph using the mean flow is flatter than the instantaneous result, with the separation efficiency of small $0.1\mu m$ particles grossly over-predicted and the separation efficiency of large particles dropping-off near $1\mu m$. This occurred due to larger of numbers of particles exceeding t_{max} instead of impacting the wall in the time-averaged flow field which resulted in them being counted as not separated. This suggests unsteady structures contribute to the wall-deposition of particles and aid in increasing the separation efficiency.

Finally, the ensemble-averaged results are examined for all considered particle sizes in Figure 5.23. The form of the ensemble-averaged separation efficiency follows the general experimental form, however the graph is much flatter than the experimental result as has been seen with all other results. Around $d_{p,50}$, the spread in separation efficiency results is greatest, with both the largest and smallest particles showing smaller absolute spread over different fluid realisations. The diameters of greatest spread in η occurring around $d_{p,50}$, where centrifugal and drag forces are expected to match from Bath's model, suggests that this force balance is continuously changing during cyclone operation. The PVC behaviour of the cyclone is likely the cause for the spread in this region as the position of the vortex core from the instantaneous flow field is in a different position for each fluid realisation.

A final check was made to ensure that the ensemble-averaged results had reached a statistically stationary value. Figure 5.24 shows the rolling ensemble-averaged separation efficiency over each realisation for every particle diameter. The separation efficiencies after 10 realisations show converged statistics, providing a measure of reliability to the results shown in Figure 5.23.

As has been shown, estimating the cyclone separation efficiency is difficult. Simple separation models such as the time-of-flight model from Section 2.1 are far removed from reality and raise questions as to how a single value for the number of spirals, N_s, can be reliable. The force-balance approach by Barth can be used to estimate $d_{p,50}$ for this cyclone as the velocities in the vortex core are known. From the CFD results, the mean tangential and radial speed on the edge of the vortex core are $|\bar{\boldsymbol{u}}_t| \approx 55.44 m/s$ and $|\bar{\boldsymbol{u}}_r| \approx 1.41 m/s$ respectively, which from Eq. 2.3 provide an estimate of the cut-off diameter as $0.375\mu m$ without Cunningham slip and $2.99\mu m$ with

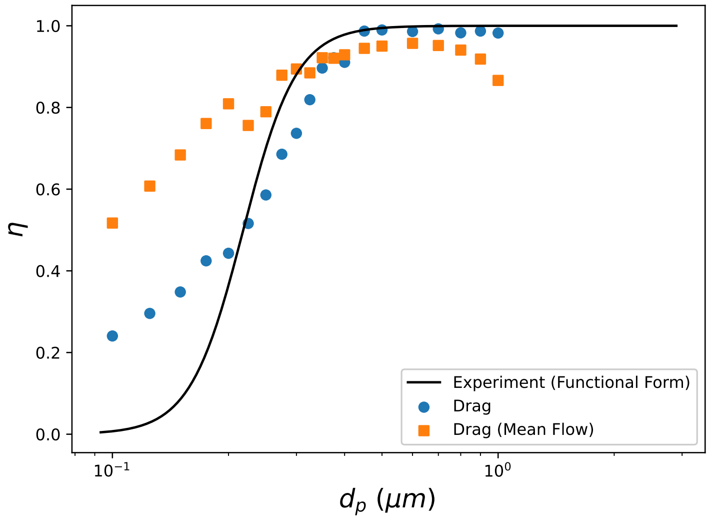

Figure 5.22: Separation efficiency using the instantaneous and time-averaged flow field compared to the experimental fit.

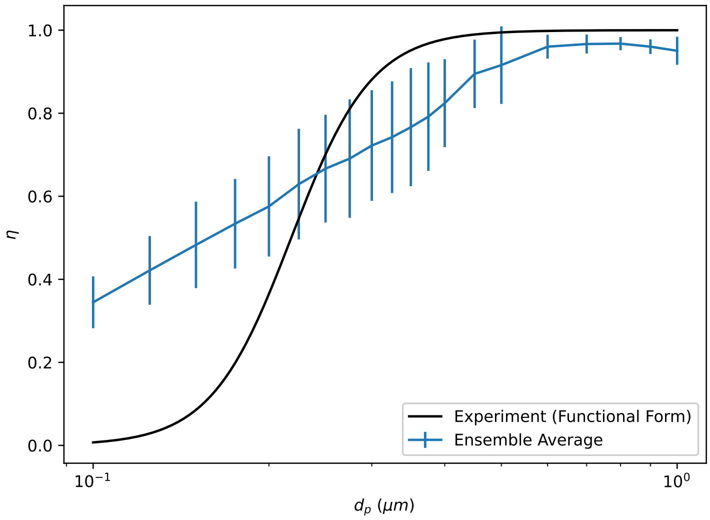

Figure 5.23: Separation efficiency ensemble-average compared to the experimental fit, with error bars indicating results one standard deviation from the ensemble-average.

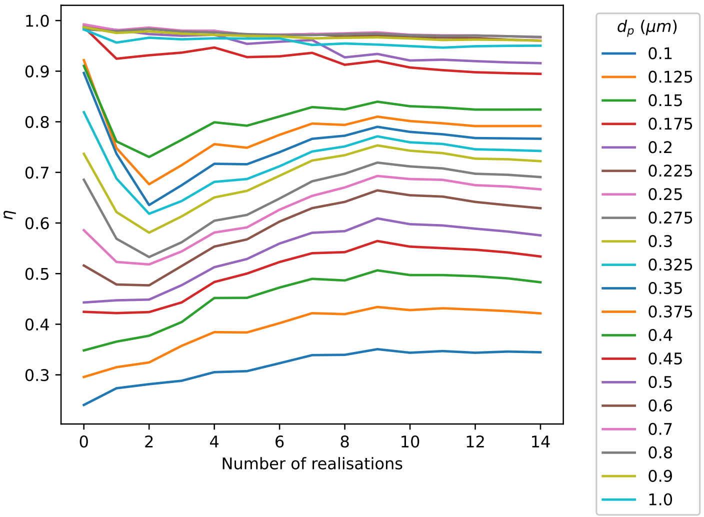

Figure 5.24: Separation efficiency ensemble-averages for each particle diameter as a function of number of fluid realisations.

Cunningham slip. Comparing this to the experimental cut-off diameter of $2.18\mu m$ shows reasonable agreement with the inclusion of Cunningham slip (as is expected from the separation efficiency results). This suggests that the balance of centrifugal forces to drag is an important factor in determining $d_{p,50}$, which has been well-captured from the CFD results. However, the simple separation models offer no method of determining the exponent m in the functional form of the separation efficiency, which determines the gradient. Lagrangian particle tracking has closely matched the experimental $d_{p,50}$, however the matching the steepness of the η curve to experiment is much more difficult.

5.2.2 Particle Statistics

In using the Stokes drag law, we have assumed that the particle Reynolds number is much smaller than unity. This can now be verified post-assumption. The particle Reynolds number, along with the Stokes number in the cyclone, will change as a function of both time and position. The local strain rate seen by the particles also provides useful information for the diffusion coefficients for the Eulerian model from Chapter 4. To determine these, we track these quantities along particle trajectories through the cyclone. All analysis in this section is performed using the separation efficiency independent parameters obtained in Section 5.2.1, for particles acted on by Stokes drag with Cunningham slip correction.

We can now check *a posteriori* the assumption of $Re_p << 1$ for the valid use of Stokes drag on the particles. This can be monitored along every point of the trajectory. As these trajectories differ wildly, the statistics along each trajectory also vary greatly. Key statistics over the entire trajectory for both the largest and smallest particles are provided in Table 5.2. For Re_p, the maximum value obtained over all particles at any point in the trajectory is pushing validity of Stokes drag, however from the ensemble average and minimum value, this is an extreme value and thus Stokes drag is valid. This validates its use as the force considered in the Equilibrium Eulerian model from Section 2.3 for the cyclone. The Stokes numbers of larger particles are generally higher than the smaller particles as expected, with $Stk < 1$ satisfied along each point of the trajectory. This important result, along with the evidence that $Re_p << 1$, validates the use of the EE model in the cyclone.

d_p	$Re_{p,max}$	$Re_{p,min}$	$< Re_p >$	Stk_{max}	Stk_{min}	$< Stk >$
$1\mu m$	1.62	4.20×10^{-7}	2.48×10^{-2}	9.48×10^{-1}	1.08×10^{-6}	1.05×10^{-2}
$0.1\mu m$	1.24×10^{-1}	1.02×10^{-8}	5.57×10^{-4}	2.29×10^{-2}	1.40×10^{-7}	1.36×10^{-3}

Table 5.2: Key statistics gathered along particle trajectories.

From the experimental evidence from Figure 1.2, particles are expected to be translating through the boundary layers of the cyclone close to the walls. Examining the ensemble averaged particle trajectory for each diameter does not provide useful information, again due to the wildly differing trajectories. Instead the focus is on a single trajectory for a given diameter, with useful information extracted from these individual tracks. The trajectory of focus is initialised in the centre of the inlet pipe, away from the influence of the inlet walls. This is examined for both the largest and smallest particle diameters considered in this work. The trajectories of these particles, plotted on each coordinate plate is provided in Figure 5.25. Both particle sizes traverse the inlet pipe in the same manner, with the trajectories diverging as soon as the particles reach the entrance to the cyclone. The larger $1\mu m$ particle is thrown out towards the wall centrifugally due to its inertia and translates around the cyclone close to the wall before impacting the wall towards the cone tip. The smaller $0.1\mu m$ particle has a much more chaotic journey, making many more rotations in the outer vortex flow and reaching the cone tip where it reverses direction and travels up the vortex core. The particle then travels up the vortex core near to the vortex finder where it continues to make many core rotations for a long period of time. This residence time of the particle then exceeds t_{max} and its trajectory is ended.

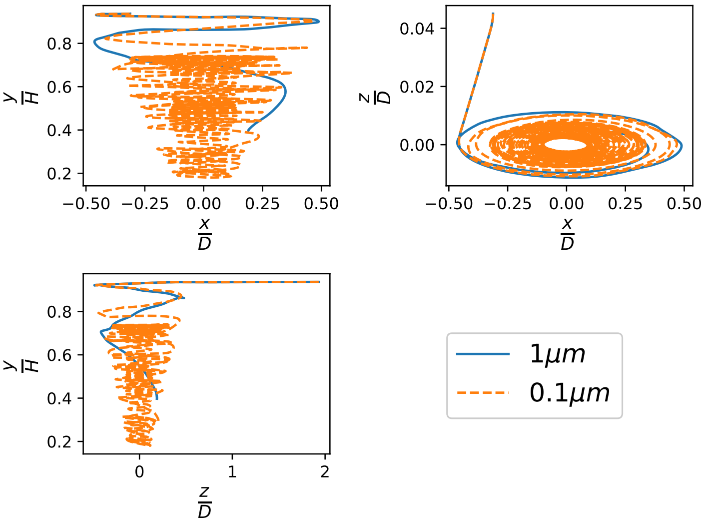

Figure 5.25: Particle trajectories of a $1\mu m$ and a $0.1\mu m$ particle initialised in the centre of the inlet plane.

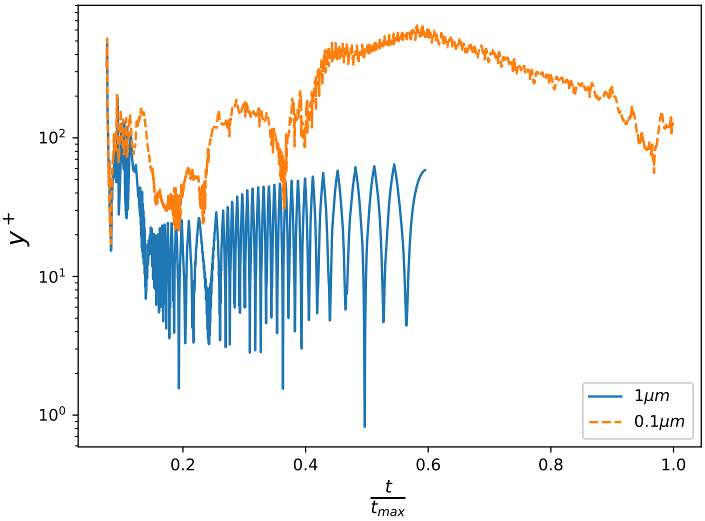

Figure 5.26: Particle y^+ along trajectories of a $1\mu m$ and a $0.1\mu m$ particle initialised in the centre of the inlet plane.

From the experimental evidence and the trajectory plots, it appears that the particles and in particular the large particles, are moving through the boundary layer. From the individual trajectories, the particle position in the boundary layer as it moves through the cyclone can be seen in Figure 5.26. The $1\mu m$ particle enters the boundary layer almost immediately after entering the cyclone and then dips into and out of the boundary layer a few times. After this, the particle becomes trapped in the boundary layer for the remainder of its trajectory. Once trapped inside the boundary layer, a cyclical pattern is observed with y^+ quickly increasing towards the log-law region of the boundary layer ($30 \leq y^+ \leq 70$) and then swiftly dropping down the viscous sublayer ($y^+ \approx 5$). This suggests that small scale motions present in the boundary layer outside the viscous sublayer are transporting these large particles both away and towards the wall, with the final boundary layer structure encountered causing a wall impact. For the trajectory of the small $0.1\mu m$ particle, the particle is considered to only enter the boundary layer on entry to the cyclone where $y^+ = 17$. The small particle then translates through the log-law region as it travels down the cyclone until it reaches the cone tip at $\frac{t}{t_{max}} \approx 0.4$, where it is forced out of the boundary layer and spends the remainder of its time in the vortex core.

The results for the y^+ values along the particle trajectory provide strong evidence that particles are moving by the cyclone walls in different layers of the boundary layer dependent on their inertia, with larger particles occupying the regions of the boundary layer closest to the wall. These different size classes of particles therefore see differing local fluid conditions, with large particles bouncing between the laminar viscous sublayer and the inertial log-law region away from the wall and small particles only able to see outer log-law structures. The high boundary layer resolution of the flow field in Section 5.1 is justified in this highly-swirling flow as particles both see and respond to these structures as a function of diameter.

Looking ahead to the Eulerian particle model, the relative strength of diffusion due to turbulence versus Brownian motion can be calculated along the particle trajectory. The diffusion coefficient due to turbulence used by Balachandar is given by Eq. 2.99, with the particle strain rate magnitude approximated by the fluid strain rate magnitude at the particle location. The turbulent Schmidt number is assumed to be unity and the fluid static temperature is also evaluated along the trajectory. The ratio $\frac{D_{turb}}{D_{brown}}$ along the two trajectories is shown in Figure 5.27. The diffusion coefficient due to the unresolved turbulent scales is predicted to $5-8$ orders of magnitude stronger than Brownian motion, with the diffusion ratio an order of magnitude stronger for the larger $1\mu m$ particles than the $0.1\mu m$ particles.

The diffusion coefficient ratio can also be calculated at each cell centroid to examine the strength of diffusion across the domain. Figure 5.28 shows contour plots of this ratio for $0.1\mu m$ and $1\mu m$ particles. The diffusion is large by the cyclone walls due to high strain rates and in the bin due to a coarser mesh which increases the subgrid length scale L_s. This is welcome behaviour for the Eulerian model in the bin as skewed cells here will introduce instabilities into the resulting set of linear equations and a larger diffusion coefficient increases the size of a_P and helps to counteract this effect.

As the Stokes number for a given particle is completely dependent on the local fluid turbulent time scales, an Eulerian Stokes number field can be estimated from the CFD flow field by dividing τ_p by the local Kolmogorov time scale. Contour plots of the Stokes number field are shown in Figure 5.29. These contour plots give an

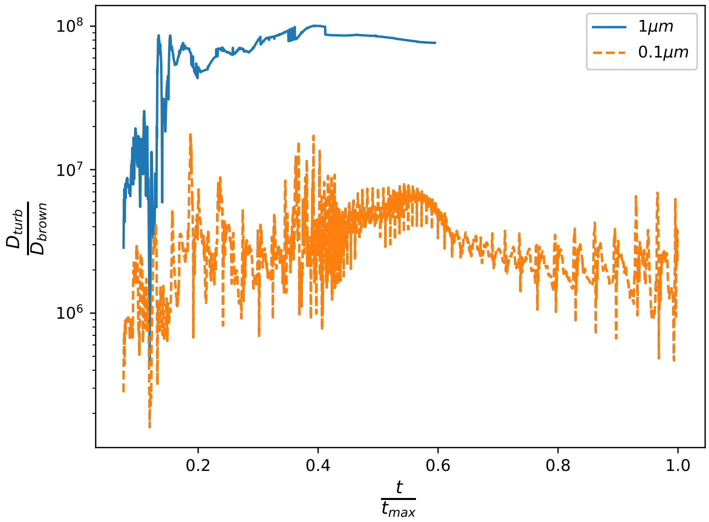

Figure 5.27: $\frac{D_{turb}}{D_{brown}}$ along trajectories of a $1\mu m$ and a $0.1\mu m$ particle initialised in the centre of the inlet plane.

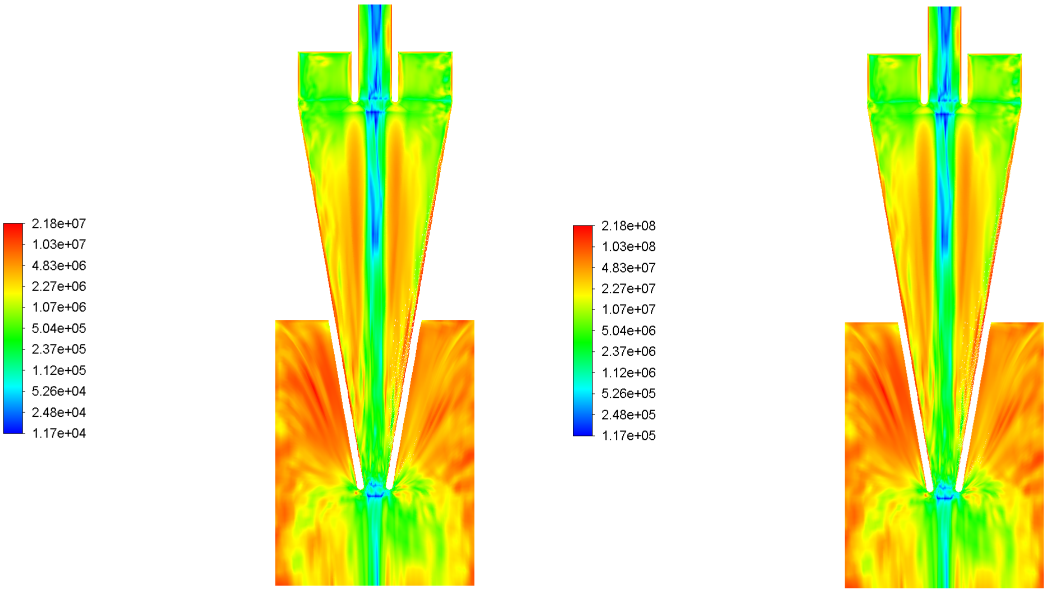

Figure 5.28: Diffusion ratio across the central x-y plane of the cyclone for $d_p = 0.1\mu m$ on the left and $d_p = 1\mu m$ on the right.

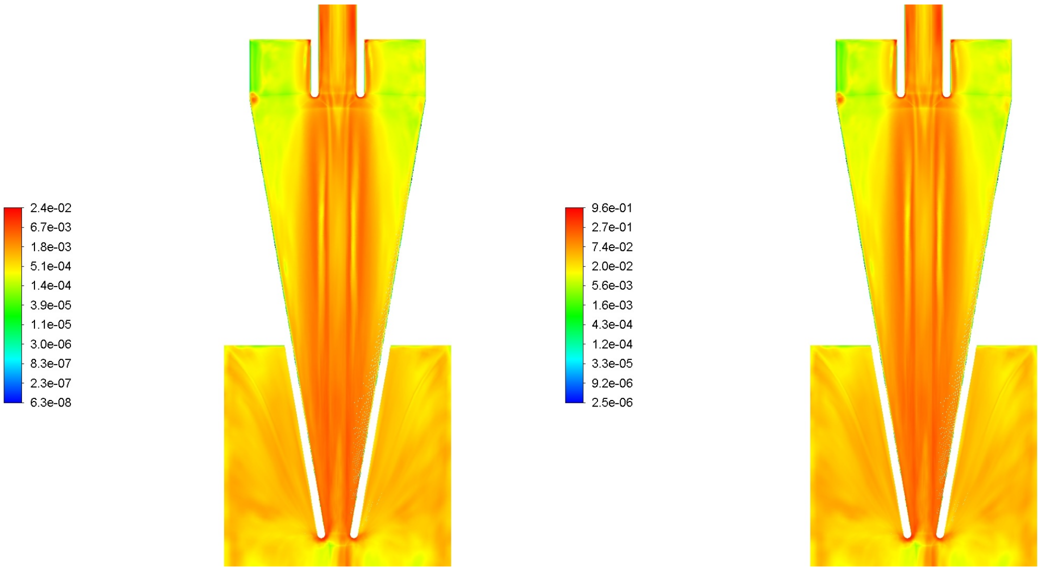

Figure 5.29: Eulerian Stokes number field across the central x-y plane of the cyclone for $d_p = 0.1\mu m$ on the left and $d_p = 1\mu m$ on the right.

indication as to where the most difficulty will be faced for the EE model, as a larger Stokes number results in a larger source term. For the $0.1\mu m$ particles, the maximum Stokes number is 2.4×10^{-2} which is expected to not pose a challenge numerically. However for the $1\mu m$ particles, the maximum Stokes number in the contour plot is 0.96 which does not satisfy $Stk << 1$. These large values occur in the vortex core and by the cone tip, where the flow velocities and velocity gradients are largest. Looking ahead to the Eulerian model, these problematic regions may limit the maximum valid particle diameters which can be used with the EE model in the cyclone, unless special numerical treatment is employed at these locations. The large diffusion coefficients from the unresolved turbulent scales at these regions may be able to stabilise the Eulerian model at these locations.

5.3 Eulerian Particle Cyclone Model

The particulate phase is now tracked in the cyclone in an Eulerian framework. This allows representative particle volume fractions to be tracked in the cyclone with reasonable estimates of collision frequency and therefore charge transfer is able to be calculated. The model consists of the transport equation for particle volume fraction, the charge density and the electric potential. The Eulerian particle velocity field, which is required for the convection term in both the volume fraction and charge density transport equations, is provided by the Equilibrium Eulerian velocity.

The computational set-up, which builds upon the model set-up in the Taylor-Green flow from Chapter 4, is provided in Section 5.3.1. The primary differences between the cyclone set-up and the Taylor-Green flow is that the cyclone is a 3D, compressible LES flow field on a non-uniform mesh with walls. The boundary conditions for the volume fraction, charge density and electric potential are discussed, along with sub-models for the diffusion coefficient for the particle volume fraction.

The results of both the particle velocity field and volume fraction are presented in Section 5.3.2. These are compared to the Lagrangian particle tracking from Section 5.2 and additionally to experimental evidence for the volume fraction. A separation efficiency graph can be produced from the Eulerian model and the build-up of particles by the cyclone walls can be quantitatively analysed, with an assessment made of the accuracy of the Eulerian model in small, high-speed cyclones.

Having convected the particle volume fraction through the cyclone, both the charge density and the resulting electric potential and field strength due to the particles predicted from the Eulerian model, are shown. This provides details as to where particle charge is expected to build-up in the cyclone, data which is completely missing in the literature. Due to the lack of validation data for this, checks are performed to ensure that the results are physically reasonable.

Finally concluding remarks are made in Section 5.4. These include design suggestions for cyclones which can utilise the areas of particle and charge build-up to further increase the separation efficiency of the system.

5.3.1 Discretisation and Computational Set-Up

The transport equation for the volume fraction with EE velocity (Eq. 2.66) must be filtered in the LES model which yields Eq. 2.96. Only the steady-state solution is sought and the temporal derivative can be removed. As the model is applied to a compressible carrier fluid, the fluid density is included in each term otherwise the model would not be conservative. The dimensions of each element in the matrix of coefficients (Eq. 4.23) therefore have dimensions of mass flow rate. The governing steady transport equation for the particle volume fraction for the compressible cyclone LES using the EE model becomes

$$\int \left(\tilde{\rho}_f \hat{u}_i \hat{\alpha} - \tilde{\rho}_f D_\alpha \frac{\partial \hat{\alpha}}{\partial x_i} \right) dA_i = \int \frac{\partial}{\partial x_i} \left(\tilde{\rho}_f \tau_p \hat{u}_j \frac{\partial \hat{u}_i}{\partial x_j} \hat{\alpha} \right) dV, \tag{5.10}$$

where the diffusion coefficient D represents the combination of all forms of diffusion presented in Chapter 4. From the LES filtering process, this diffusion coefficient at the very least should include the effects of the unresolved LES scales from Eq. 2.99. The effect of excluding this source of diffusion on the volume fraction will also be analysed. As with the Taylor-Green flow, the diffusion term is central differenced.

The source term is can be discretised as both an explicit and implicit formulation outlined in Section 4.2.1. The source term in this compressible flow for cell P is now

$$S_\alpha = -\frac{\partial}{\partial x_i} \left(\tilde{\rho}_f \hat{w}_i \hat{\alpha} \right)_P \Delta V_P. \tag{5.11}$$

For the explicit formulation, the terms inside the derivative of the source term are saved as separate variables as

$$S_x = -\tilde{\rho}_f \hat{w}_x \hat{\alpha}, \tag{5.12}$$

$$S_y = -\tilde{\rho}_f \hat{w}_y \hat{\alpha}, \tag{5.13}$$

$$S_z = -\tilde{\rho}_f \hat{w}_z \hat{\alpha}, \tag{5.14}$$

to provide the complete explicit source term

$$S_\alpha = S_c = \left(\frac{\partial S_x}{\partial x} + \frac{\partial S_y}{\partial y} + \frac{\partial S_z}{\partial z} \right)_P \Delta V_P, \tag{5.15}$$

$$S_p = 0. \tag{5.16}$$

The derivatives are evaluated again using a modified version of the divergence theorem, however the nodal values are used instead of the face values for higher accuracy. These nodal values are constructed from linear interpolation between neighbouring cell centroids. For the implicit formulation, the product rule for differentiation is applied to the source term yielding

$$S_p = \min\left(-\left(\frac{\partial \tilde{\rho}_f \hat{w}_i}{\partial x_i}\right)_P, 0\right)\Delta V_P, \tag{5.17}$$

$$S_c = -\tilde{\rho}_f \hat{w}_i \frac{\partial \hat{\alpha}}{\partial x_i}\Delta V_P + \max\left(-\frac{\partial \tilde{\rho}_f \hat{w}_i}{\partial x_i}, 0\right)\Delta V_P \hat{\alpha}_P. \tag{5.18}$$

For the convection term, the flux on the faces is not analytical as in the Taylor-Green flow and linear interpolation is used from the neighbouring cell centroids. The value of the volume fraction on the face is first-order upwinded for stability. As was seen with the Taylor-Green flow in Section 4.5, this is expected to smear-out sharp volume fraction gradients in the solution, however it will aid in preventing unphysical oscillations and negative values in the volume fraction.

For convecting an Eulerian particle phase representing the larger $1\mu m$ particles, the Stokes number is expected to be ≈ 1 in many places in the domain from Figure 5.29. This is pushing the validity of the EE model and may result in a non-physical particle velocity field, as observed in the Taylor-Green flow in Section 4.1. This source term strength is governed by the Stokes number in Eq. 2.87 and both fluid and volume fraction gradients which may cause instabilities in the solution. Relaxation factors will be used as required to prevent the source term from destabilising the solution.

Boundary conditions are required for α at the domain inlet, outlet and cyclone walls. From the experimental inlet mass flow rate of the particles from Section 1.3.3, the inlet volume fraction is $\alpha_0 \approx 5 \times 10^{-7}$ which is used as a Dirichlet boundary condition. As the outlet pipe is long, the volume fraction distribution is expected to be fully-developed and a Neumann boundary condition of zero gradient normal to the outlet face is specified. From the separation efficiency results in Section 5.2.1, it was found that a wall-trap boundary condition yielded the most accurate results for the Lagrangian particles. This is equivalent to an absorbing wall which translates to a Dirichlet boundary condition of $\alpha = 0$. Both the trap and reflect wall boundary condition for the volume fraction will be examined.

For computational cells in the cyclone bin, the source term can be removed. This is done for a number of reasons: the first is that when Lagrangian particles entered in the bin in Section 5.2.1, they were removed from the simulation. The second is that it saves computational effort in computing source terms in a region which is not of interest and is not expected to affect the distribution in the cyclone. The third is that large skewed cells may promote solver divergence in this region and switching off the source term here avoids that. This switching-off of the source term is preferable to simply setting $\alpha = 0$ in the bin as the latter may introduce a very sharp α gradient near the cone tip. This would cause the source term to become even larger in this region which is anticipated to be numerically challenging and is therefore avoided.

Convergence of the solution can be monitored using both the normalised residual and the area-averaged value of α on the outlet face. The area-averaged value of the volume fraction on the outlet face (α_{out}) allows monitoring for when a stationary separation efficiency is reached, which can be calculated as

$$\eta = 1 - \frac{\alpha_{out}}{\alpha_0}. \tag{5.19}$$

A range of particle diameters matching those used in the Lagrangian particle tracking are used. The diameter then provides the particle relaxation time (with Cunningham slip correction) using Eq. 1.24. The simulations are performed using the current instantaneous filtered flow field in the cyclone.

When a converged solution is obtained for the volume fraction, the charge transport equation may be solved in the domain. The charge transport equation (Eq. 4.101), when applied to a compressible flow in conservative, steady form is

$$\int \rho_f \alpha q v_i dA_i = \int \frac{48\rho_f \alpha^2 A_{\mathrm{c,\ max}}\sigma_0}{\rho_p \pi^2 d_p^3}\left(1 - e^{-\frac{t_c}{\tau}}\right) S^v_{mag} dV. \tag{5.20}$$

The dimensions of each term are now $[Q]\,[T]^{-1}$. This equation now requires filtering and Favre-averaging the fluid density (Eq. 1.13) to yield

$$\int \tilde{\rho}_f \widehat{\alpha q v_i} dA_i = \int \frac{48\tilde{\rho}_f A_{\mathrm{c,\ max}}\sigma_0}{\rho_p \pi^2 d_p^3}\left(1 - e^{-\frac{t_c}{\tau}}\right) \widehat{S^v_{mag}\alpha^2} dV. \tag{5.21}$$

Starting with the convection term, the same assumption that charge and velocity are independent from Chapter 4 can be made. Additionally, charge and volume fraction are assumed to be independent to provide

$$\int \tilde{\rho}_f \widehat{\alpha q v_i} dA_i = \int \tilde{\rho}_f \hat{q} \widehat{\alpha v_i} dA_i. \tag{5.22}$$

The non-linear filtered term is split and modelled in the same manner by Shotorban and Balachandar as in Section 2.3 to yield

$$\int \tilde{\rho}_f \hat{q} \widehat{\alpha v_i} dA_i = \int \tilde{\rho}_f \hat{q} \hat{\alpha} \hat{v}_i dA_i - \int \frac{\partial}{\partial x_i} \left(\tilde{\rho}_f \hat{q} \frac{(C_s \Delta)^2 \hat{S}^v_{mag}}{Sc_t} \frac{\partial \hat{\alpha}}{\partial x_i} \right) dV. \tag{5.23}$$

The filtered EE particle velocity can be split as done in Eq. 2.96 to give

$$\int \tilde{\rho}_f \hat{q} \widehat{\alpha v_i} dA_i = \int \tilde{\rho}_f \hat{q} \hat{\alpha} \hat{u}_i dA_i - \int \frac{\partial}{\partial x_i} \left(\tilde{\rho}_f \hat{q} \frac{(C_s \Delta)^2 \hat{S}^v_{mag}}{Sc_t} \frac{\partial \hat{\alpha}}{\partial x_i} \right) dV + \int \frac{\partial}{\partial x_i} \left(\tilde{\rho}_f \tau_p \hat{u}_j \frac{\partial \hat{u}_i}{\partial x_j} \hat{\alpha} \hat{q} \right) dV. \tag{5.24}$$

For the collisional source term in Eq. 5.21, the filtered term $\widehat{S^v_{mag}\alpha^2}$ can be written in terms of a subgrid-scale stress tensor $\tau^c_{ij} = \hat{S}^v_{mag}\hat{\alpha}^2 - \widehat{S^v_{mag}\alpha^2}$. The volume fraction is expected to be in the dilute regime and therefore it will be assumed that this SGS stress tensor is negligible to yield the full filtered transport for charge as

$$\begin{aligned} \int \tilde{\rho}_f \hat{q} \hat{\alpha} \hat{u}_i dA_i = \int \frac{\partial}{\partial x_i} \left(\tilde{\rho}_f \hat{q} \frac{(C_s \Delta)^2 \hat{S}^v_{mag}}{Sc_t} \frac{\partial \hat{\alpha}}{\partial x_i} \right) dV - \int \frac{\partial}{\partial x_i} \left(\tilde{\rho}_f \tau_p \hat{u}_j \frac{\partial \hat{u}_i}{\partial x_j} \hat{\alpha} \hat{q} \right) dV \\ + \int \frac{48 \tilde{\rho}_f A_{\text{c, max}} \sigma_0}{\rho_p \pi^2 d_p^3} \left(1 - e^{-\frac{t_c}{\tau}} \right) \hat{S}^v_{mag} \hat{\alpha}^2 dV. \end{aligned} \tag{5.25}$$

The first two source terms on the RHS are both non-linear and can be split using the product rule to provide an implicit source term formulation in the FVM. The final source term on the RHS is an always-positive, constant source term for a given cell and will be dealt with explicitly. The source term components for cell P are

$$S_p = \min \left(\frac{\partial}{\partial x_i} \left(\tilde{\rho}_f \frac{(C_s \Delta)^2 \hat{S}^v_{mag}}{Sc_t} \frac{\partial \hat{\alpha}}{\partial x_i} \right)_P, 0 \right) \Delta V_P + \min \left(-\frac{\partial}{\partial x_i} \left(\tilde{\rho}_f \hat{w}_i \hat{\alpha} \right)_P, 0 \right) \Delta V_P, \tag{5.26}$$

$$\begin{aligned} S_c = \max \left(\frac{\partial}{\partial x_i} \left(\tilde{\rho}_f \frac{(C_s \Delta)^2 \hat{S}^v_{mag}}{Sc_t} \frac{\partial \hat{\alpha}}{\partial x_i} \right)_P, 0 \right) \Delta V_P \hat{q}_P + \max \left(-\frac{\partial}{\partial x_i} \left(\tilde{\rho}_f \hat{w}_i \hat{\alpha} \right)_P, 0 \right) \Delta V_P \hat{q}_P \\ + \left(\frac{48 \tilde{\rho}_f A_{c,max} \sigma_0}{\rho_p \pi^2 d_p^3} \left(1 - e^{-\frac{t_c}{\tau}} \right) S^v_{mag} \hat{\alpha}^2 \right)_P \Delta V_P. \end{aligned} \tag{5.27}$$

The boundary condition at the inlet can be $\hat{q} = 0$, indicating uncharged aerosol entering the cyclone (or net neutral). At the outlet, it is assumed to be fully developed $\frac{\partial \hat{q}}{\partial x_i} = 0$. The walls can either be earthed $\hat{q}_{wall} = 0$ or perfectly insulating $\frac{\partial \hat{q}}{\partial x_i}_n = 0$ and both choices are to be investigated.

The electric potential Poisson equation (Eq. 1.41) is

$$\int \frac{\partial \phi_e}{\partial x_i} dA_i = -\int \frac{\rho_p \hat{\alpha}}{\epsilon_m} \hat{q} dV, \tag{5.28}$$

which provides the explicit source as

$$S_p = 0, \tag{5.29}$$

$$S_c = \left(\frac{\rho_p \hat{\alpha}}{\epsilon_m} \hat{q} \right)_P \Delta V_P, \tag{5.30}$$

from which the electric field can be obtained as the gradient of the potential from Eq. 1.38.

The equations implemented into Fluent for the Eulerian particle model are provided in Table 5.3 in the order in which they are solved.

Name	Equation Number
Particle Volume Fraction Transport	5.10
Particle Charge Transport	5.25
Electric Potential	5.28
Electric Field	1.38

Table 5.3: Eulerian particle partial differential equations implemented into Fluent.

5.3.2 Uncharged Results

In this section, the focus is on information regarding the Eulerian particle velocity and volume fraction fields, with electrostatic quantities covered in the following section. From the solution to the volume fraction transport equation, the separation efficiency can be calculated and compared to both the Lagrangian particle simulations and experimental evidence. This is examined for a variety of additional models of the physics, which are provided by the relevant diffusion coefficients. The steady EE particle velocity field is examined for the range of particle diameters pertinent to this work, with the relative velocity between the particulate phase and fluid examined. The volume fraction distribution as a function of wall distance is analysed, information which is difficult to obtain from Lagrangian particle tracking due to the limited numbers of particles. Evidence of the particle "streaky bands" seen experimentally from Chapter 1 is also presented.

The accuracy of the various choices for the diffusion coefficient and the wall boundary condition for the volume fraction is characterised by comparing the resulting separation efficiency to both experiment and the Lagrangian particles result as shown in Figure 5.30 for $d_p = 0.1\mu m$. This particle size, being the smallest of interest, is expected to be the most stable to solve due to the small τ_p, with the Eulerian particle velocities being the most accurate. Both types of wall boundary condition over-predict the experimental result by at least $\approx 10\%$ and the Lagrangian particle result by at least 4%. A completely non-physical result of $\eta \approx 1$ was observed for the turbulent diffusion coefficient with the trap wall boundary condition. This occurred as the particle volume fraction was readily diffused towards the walls where it was removed from the domain. This informs us that this combination of diffusion coefficient with the wall boundary condition is not appropriate to accurately determine the separation efficiency.

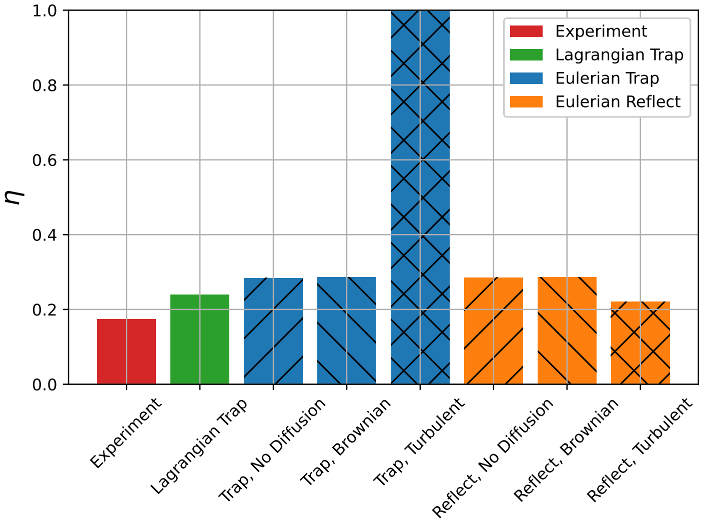

Figure 5.30: Separation efficiency of $d_p = 0.1\mu m$ from experiment, Lagrangian particle tracking and the various diffusion and wall boundary conditions. Hatching is only used for the Eulerian cases, indicating which diffusion model was present.

Also demonstrated from Figure 5.30 is the negligible effect of Brownian diffusion compared to the no diffusion cases. The separation efficiencies differed from the diffusion-free cases by 0.18% and 0.05% for the trap and reflect boundary condition respectively. This mirrors what was observed for the Lagrangian particles in Section 5.2.1 and provides some confidence that the physics for the Lagrangian particles is being replicated in the Eulerian model. Additionally, Brownian diffusion is expected to be at its strongest for these small particles. It is therefore safe to assume that the effects of Brownian diffusion will be negligible for all particle sizes considered in this project.

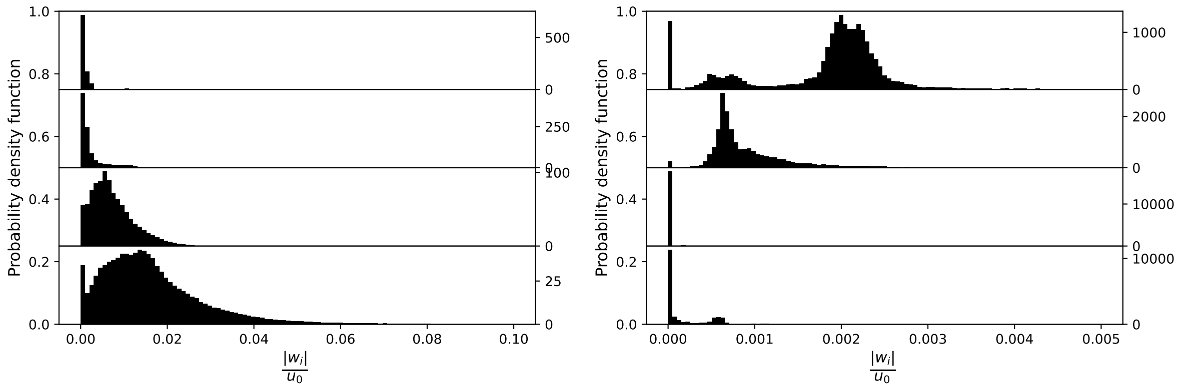

Figure 5.31: Relative velocity magnitude PDFs in the 4 cyclone sections from top to bottom normalised by the inlet speed for $d_p = 0.1\mu m$. The EE and Lagrangian particle results are shown on the left and right respectively.

The separation efficiencies predicted for the no diffusion cases are very similar, with the trap wall boundary condition separation efficiency 0.13% lower than the reflect case. For these small $0.1\mu m$ particles, which are expected to not be separated well by the cyclone, the choice of wall boundary condition has very little effect on the separation efficiency. As the particles become more inertial with increasing d_p and Stk, this choice may have a significant impact as larger particles are expected to travel closer to the cyclone walls from Section 5.2.2. Lastly, the reflect wall BC with turbulent diffusion provided an excellent match to the Lagrangian particle solution, with a difference of 2%. Whilst including the effects of the unresolved scales on the Lagrangian particles in Section 5.2.1 had a negligible effect on the separation efficiency, for the Eulerian model it has improved the accuracy as would be expected. An additional benefit to this turbulent diffusion is the increase of terms on the central coefficient a_P and therefore an increase in numerical stability, which may be required as the particle sizes increase and the EE model is pushed further.

The relative velocity probability density function in the cyclone is examined. This is presented for the $d_p = 0.1\mu m$ particle phase in Figure 5.31. The $|w_i|$ value in each cell is weighted by the volume fraction, weighted by the cell volume. This double weighting is performed by first multiplying the volume fraction by the volume in each cell, which provides the volume occupied by the particles in each cell (directly proportional to the number of particles in that cell). The $|w_i|$ values in each cell are then weighted by this total particle volume in the cell.

For these tiny particles, the relative speed between the particles and the fluid is small as expected. The distribution of relative speeds becomes wider travelling vertically down the cyclone towards the cone tip, where larger extreme values of relative velocity are expected. The maximum value of relative speed normalised by the inlet velocity in the entire cyclone is 0.26 and 10.2 for the $d_p = 0.1\mu m$ and $d_p = 1\mu m$ particles respectively. The extreme relative speeds for the largest particle sizes are unphysical, indicating that the EE model is invalidated in that region (in the cone tip). This is expected to destabilise the solution to the volume fraction transport equation for large particles as the source term is a function of the gradient of the relative velocity.

The relative velocity predicted by the EE method is compared to the Lagrangian particles result evaluated at their end positions. This is checked using the end locations from the time integration of the particles used in Section 5.2 to provide the Lagrangian statistics. It was found that the statistics were noisy using only $N = 4000$ particles and instead $N = 4 \times 10^5$ particles have been tracked using the same integration settings as from Section 5.2 to provide cleaner results.

The relative velocity magnitude for the $0.1\mu m$ particles in Figure 5.31 shows both the Eulerian and Lagrangian models predicted that the majority of particles have vanishing normalised relative velocities. This was to be expected due to the low Stokes numbers of these particles. The EE method predicts larger relative velocities than was seen for the Lagrangian particles at the end of their integration. This large discrepancy occurs as the Lagrangian particles of this size range are either trapped in the boundary layers (and moving slowly with the fluid) or are caught traversing endlessly in the vortex core. The particles in the vortex core are seen as the large peaks at higher relative speeds near to the top of the cyclone.

The relative velocity magnitude for the larger $1\mu m$ particles in Figure 5.31 shows both the Eulerian and Lagrangian models predicted that the majority of particles have vanishing normalised relative velocities as for the $0.1\mu m$ case. The results are noisy for the Lagrangian particles by the cone tip due to the very few numbers of particles able to reach this location. Both the Eulerian and Lagrangian models show a heavily

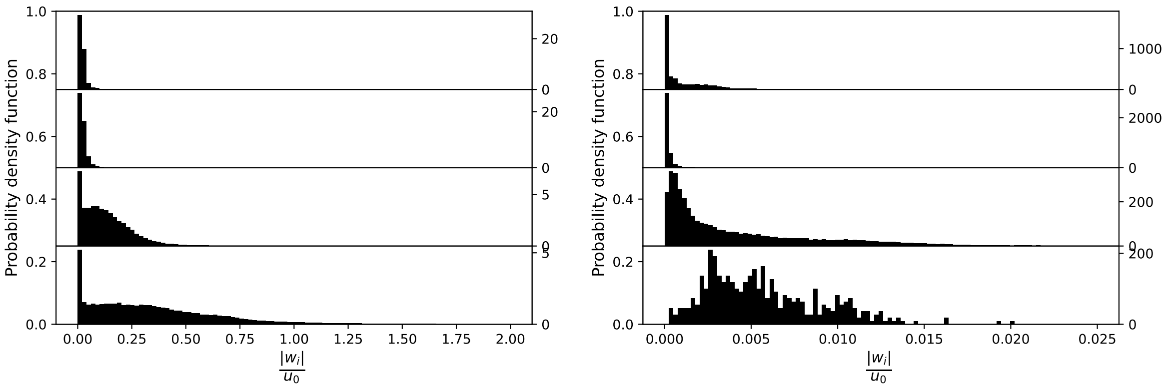

Figure 5.32: Relative velocity magnitude PDFs in the 4 cyclone sections from top to bottom normalised by the inlet speed for $d_p = 1\mu m$. The EE and Lagrangian particle results are shown on the left and right respectively.

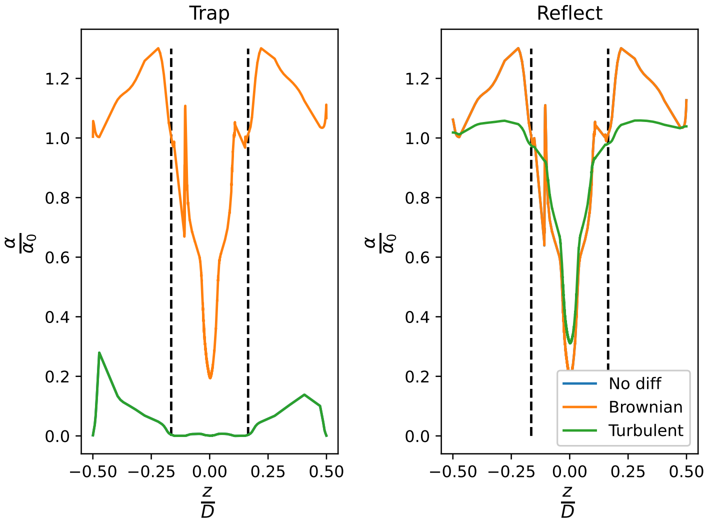

Figure 5.33: Volume fraction distribution of $d_p = 0.1\mu m$ from the various diffusion and wall boundary conditions along a horizontal line at the top of the cyclone. The line passes from $(x, y, z) = \left(0, H - \frac{h}{2}, -\frac{D}{2}\right)$ to $\left(0, H - \frac{h}{2}, \frac{D}{2}\right)$. The vertical dashed lines represent the location of the vortex finder walls.

right-skewed relative speed distribution, however as with the $0.1\mu m$ particles the EE method predicts much larger relative velocities. This is especially true close to the cone tip, where the relative velocity is comparable to the inlet velocity. This further evidences the scale of the numerical instabilities of the model in this region, which necessitates both relaxation factors in the solution and large diffusion coefficients for convergence.

From the $d_p = 0.1\mu m$ results, 1D slices of the volume fraction distribution across the cyclone can be examined. This allows predictions of the most probable particle locations to be compared for the various wall boundary conditions and diffusion coefficients. This distribution at the top of the cyclone parallel to the inlet flow is provided in Figure 5.33. From the turbulent diffusion result with a trap wall boundary condition, most of the volume fraction has already diffused towards the walls and been absorbed by this half-turn around the cyclone. Inside the vortex finder, it is evident that no particle volume fraction was able to leave the cyclone through the exit pipe which in accordance with the prediction for separation efficiency in Figure 5.30. This combination of the trap wall BC with turbulent diffusion is expected to continue to provide unphysical results and is therefore not explored further.

As with the separation efficiency in Figure 5.30, the Brownian diffusion provided a negligible difference to using no diffusion for the 1D volume fraction distribution. On Figure 5.33, both of these lines completely overlap. Brownian diffusion has been shown to provide a negligible effect on the particle volume fraction and will also be ignored in further studies. For cases with no diffusion, the wall boundary condition had a negligible effect

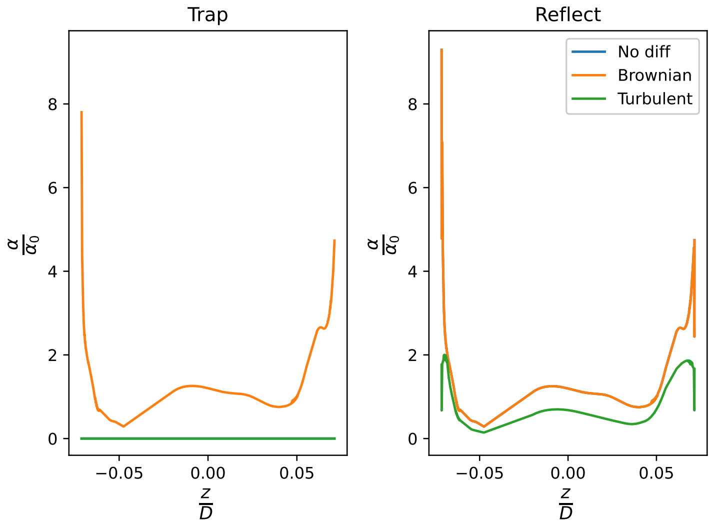

Figure 5.34: Volume fraction distribution of $d_p = 0.1\mu m$ from the various diffusion and wall boundary conditions along a horizontal line at the cone tip of the cyclone. The line passes from $(x, y, z) = \left(0, 0, -\frac{S}{2}\right)$ to $\left(0, 0, \frac{S}{2}\right)$.

on the particle volume fraction for these $0.1\mu m$ particles. The volume fraction peaks close to the walls (both of the outer cyclone walls and the inner and outer walls of the vortex finder), with peak values around 25% larger than the inlet volume fraction. In the centre of the vortex core, the volume fraction along this 1D slice reaches a minimum value of $\approx$ 20% of the inlet value. This provides evidence that the particles leaving the cyclone are travelling along the edge of the vortex core, where the velocities and velocity gradients are largest. This qualitatively matches the escape trajectory of a Lagrangian particle in Figure 5.14 and thus the Eulerian model is capturing the physics of Lagrangian particles even in the outlet pipe. This is also suggestive of numerical issues in these regions for larger particles using the EE model. The reflect wall BC with turbulent diffusion, which provided the most accurate separation efficiency in Figure 5.30, is a smoothed version of its no diffusion counterpart. Both the maximum and minimum values with this combination are less extreme, however it shares the same general form as for the no diffusion case. This additional diffusion, as was seen with the Taylor-Green flow in Chapter 4, smears out the volume fraction distribution and will provide increased numerical stability. This is expected to be important to provide a converged solution for the larger particle sizes.

The main location identified which is expected to present the greatest numerical difficulties is the cone tip of the cyclone. A 1D horizontal slice of the volume fraction along this region is shown in Figure 5.34. Again, the Brownian diffusion result and the no diffusion result overlap for the reflect wall BC, however for the trap wall BC, the Brownian diffusion result overlaps the turbulent diffusion. The trap wall boundary condition with both no and turbulent diffusion informs us that a negligible amount of volume fraction was able to reach the cone tip and must have been absorbed by the walls towards the top of the cyclone. For this wall BC, Brownian diffusion was able to diffuse volume fraction away from the walls which prevented it being absorbed and thus was able to convect to the bottom of the cyclone. Although of a similar form, the trap and reflect wall boundary condition for Brownian and no diffusion respectively provided different results in this region, unlike at the top of the cyclone. The reflect wall BC predicts a peak volume fraction 19% higher than the Brownian trap case, which is the expected trend as the trap wall BC would remove more volume fraction in the domain before reaching the cone tip. Turbulent diffusion for the reflect wall BC reduced the extremity of the peaks and smoothed the distribution as with the top of the cyclone. The volume fraction peak values by the cone tip walls are large compared to the inlet value. The large values, along with large gradients for volume fraction (and the fluid velocity in this region) creates a powerful source term by the cone tip as expected. The presence of turbulent diffusion, which smears out the gradients, can reduce the size of the source term in this region and increase the stability of the linear system, especially when larger-sized particles are used.

The Eulerian model is now run for the same range of particle diameters considered for the Lagrangian particle tracking. The separation efficiencies calculated from each of the runs is provided in Figure 5.35, where the experimental and Lagrangian particle tracking result with a trap wall boundary condition are additionally presented. A well-converged result is unable to be obtained for $d_p \geq 2.5\mu m$ and $d_p \geq 2.75\mu m$ with a trap and reflect boundary condition with no diffusion respectively, even with a relaxation factor of 0.1. This numerical issue occurs at a smaller particle diameter for the trap BC as this causes larger volume fraction gradients at the walls (where $\alpha = 0$) and creates very strong source terms in these regions. The reflect boundary condition

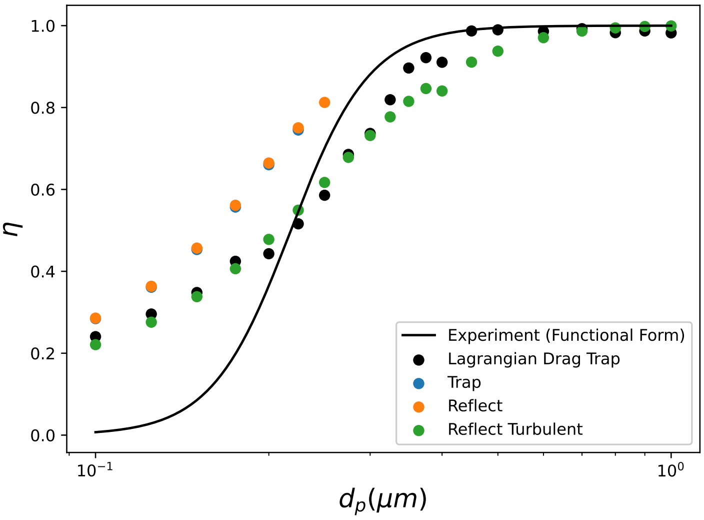

Figure 5.35: Separation efficiency plots for the Eulerian model runs compared with both the experimental functional form and Lagrangian particle tracking results.

provides some additional stability as the volume fraction gradient on the wall is smaller and thus the source term is also smaller. Both choices of wall boundary condition for the zero diffusion cases yielded similar results, with the maximum difference in separation efficiency being 0.5%.

The separation efficiencies predicted by the Eulerian model with a reflect wall BC and turbulent diffusion shown in Figure 5.35 are an excellent match to the Lagrangian particle result across all considered particle diameters. The effects of the unresolved turbulent scales on the particles, which was found to be negligible for the Lagrangian particles, reduced the predicted separation efficiency for the Eulerian model. As with the Lagrangian result, the steepness of the separation efficiency graph is flatter than the experimental result, however $d_{p,50}$ was able to be accurately obtained. This provides evidence that this Eulerian model is suitable for use in small, high-speed cyclones. The inclusion of the diffusion term increased the stability of the model at larger particle diameters as expected and allowed the entire range of particle diameters of interest to reach a converged solution.

The excellent match between the Lagrangian and Eulerian models provides strong evidence that the Eulerian model is capturing the same physics as the Lagrangian model. Both exhibit a discrepancy to the experimental result with the separation efficiency graph being less steep in the computational results compared to experiment. The experiments, as discussed in Section 5.2.1, were performed using a polydisperse particulate phase whereas both the Lagrangian and Eulerian models are assuming a monodisperse particulate phase. This was explained to only be of significance in the boundary layers. In reality, the presence of large particles traversing through the boundary layer may act to "mop-up" smaller particles and agglomerate into larger structures which are easily separated. This would cause a larger fraction of particles which are able to enter the boundary layer to be separated; thus providing a sharper gradient in the separation efficiency graph. Such phenomena is not easily captured numerically due to the complex coupling between particles sizes and would not be feasible in a computationally inexpensive model such as the one examined here. This missing physics provides a possible explanation to the separation efficiency curve flatness in the computational results compared to the experiment.

The reflect boundary condition for the volume fraction allows a non-zero value for the volume fraction on the walls itself. A contour plot of $\hat{\alpha}$ on the cyclone walls is shown in Figure 5.36 for the turbulent diffusion case for $d_p = 1\mu m$. A streaky pattern of volume fraction is observed along the walls similar to the experimental evidence in Figure 1.2. These streaks are not present for the $0.1\mu m$ results which suggests that the particle bands seen experimentally are of the larger particles.

As with the Lagrangian particles, we now check where in the boundary layer the Eulerian model predicts that the particle phase is travelling through. This comparison is provided in Figures 5.37 and 5.38, with the Lagrangian particle data provided by the end positions of 4×10^5 particles. For the both particle sizes, the Lagrangian results show particles situated closer to the wall compared to the Eulerian model. This is due to the lowest y^+ value permitted in the Eulerian method being determined by the y^+ value of the centroid of the first cell by the wall. Therefore the distribution at $y^+ < 1$ cannot be adequately compared between the models. The two models at both particle sizes predict the significant accumulation of particles in the boundary layer, especially close to the wall in the viscous sub-layer $y^+ < 5$.

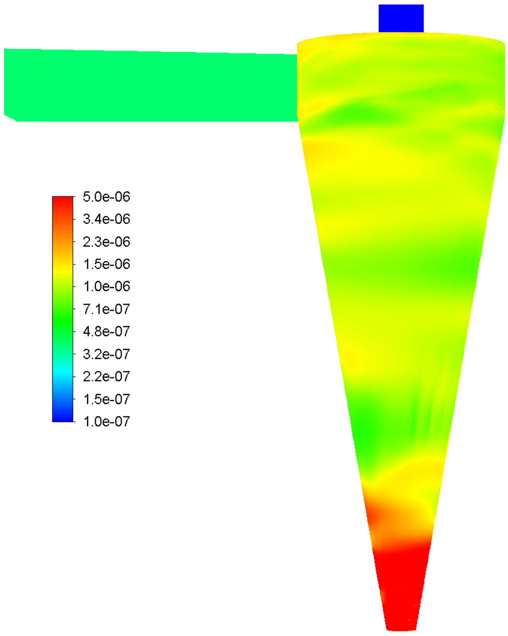

Figure 5.36: Volume fraction distribution along the cyclone walls for $d_p = 1\mu m$ with a reflect wall boundary condition and turbulent diffusion. The volume fraction is clipped to the provided range.

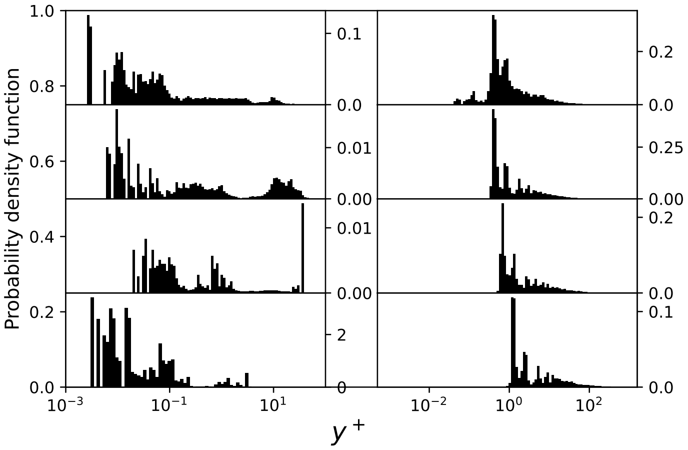

Figure 5.37: PDF of y^+ vs volume fraction of the $0.1\mu m$ particles for $N = 4 \times 10^5$ Lagrangian particles on the left with the Eulerian reflect wall BC and turbulent diffusion results on the right. Each row shows the PDF in a different cyclone section from the top travelling vertically down towards the cone tip.

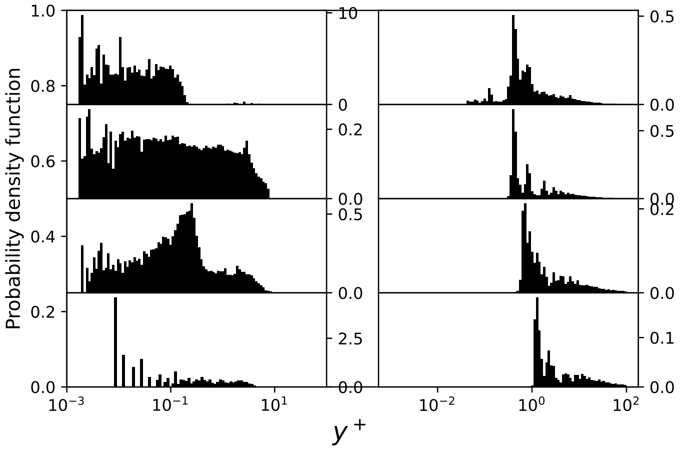

Figure 5.38: PDF of y^+ vs volume fraction of the $1\mu m$ particles for $N = 4 \times 10^5$ Lagrangian particles on the left with the Eulerian reflect wall BC and turbulent diffusion results on the right. Each row shows the PDF in a different cyclone section from the top travelling vertically down towards the cone tip.

The Eulerian model for the particle volume fraction, specifying the particle velocity field by the EE method, with a reflect boundary condition at the walls and turbulent diffusion has provided an excellent match to the Lagrangian particle result for predicting separation efficiency. The method is stable for all particle diameters of interest and is able to convect representative volume fractions through the domain. Key physics of the particles becoming trapped in the boundary layers is also captured. The collision frequency is thus able to be estimated in a computationally inexpensive manner and predictions for the transport of particle charge and the resulting electric field in the cyclone are able to made in the following section.

5.3.3 Charge Discussion

The transport of particle charge and the resulting electric field in the cyclone is now analysed. The charge distribution is assumed to be fully developed at the outlet, providing $\left(\frac{\partial \hat{q}}{\partial x_i}\right)_n = 0$. Finally the walls are assumed to be perfectly insulating, yielding $\left(\frac{\partial \hat{q}}{\partial x_i}\right)_n = 0$ at the walls. As with the volume fraction transport equation, the source terms are "switched-off" in the bin for numerical stability. In this section, only the charge results for both the smallest and largest particle sizes are investigated with turbulent diffusion, providing lower and upper bounds in the results for the intermediate particle diameters. A convergence criterion of $< 1 \times 10^{-7}$ is used for all transport equations as informed by the Taylor-Green results in Chapter 4, with the area-averaged value of the solution variables on the outlet monitored to ensure a stationary state is reached.

We begin with a net neutral aerosol entering the cyclone, giving the inlet boundary condition for charge as $\hat{q} = 0$. These neutrally charged particles exchanged very little charge from collisions for both particle diameters, with the distribution of the specific charge normalised by the maximum value in the domain shown in Figure 5.39. Both particle diameters exhibit increased levels of charge travelling vertically down the cyclone as expected. As the particles were initially uncharged, the levels of specific charge seen are completely due to particle-particle collisions in the model. The large increase of charge in the cone tip region evidences the increased likelihood of collisions in this region. The peak at zero charge for the $1\mu m$ distribution at the cone tip is due to the influence of cells in the centre of the vortex core, where no particles (volume fraction) entered and therefore no charge could be transported to this region.

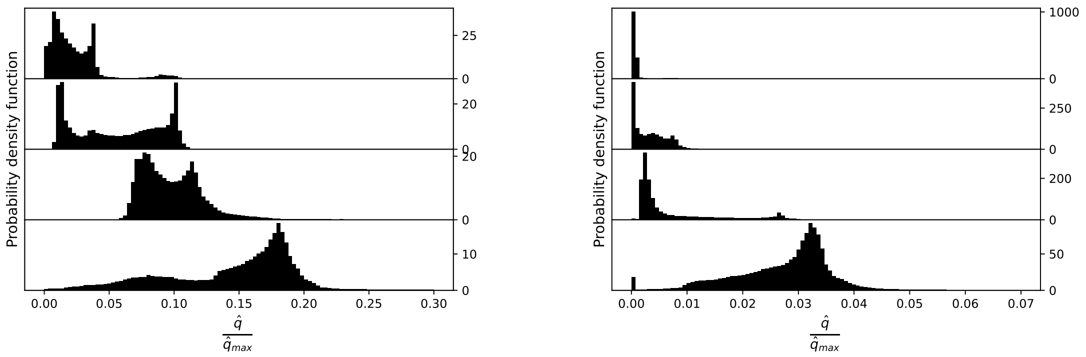

Figure 5.39: Specific charge distribution across the 4 cyclone section for $d_p = 0.1\mu m$ on the left and $d_p = 1\mu m$ on the right, normalised by the maximum specific charge in each respective domain. The inlet boundary condition for charge is $\hat{q} = 0$.

The charge distribution along the walls from a "birds-eye" view are shown for $d_p = 0.1\mu m$ in Figure 5.40. A stream of relatively highly-charged particles can be seen travelling along the top of the cyclone walls from the inlet, bypassing the outer vortex flow and moving towards the vortex finder. This is the well-known lip-leakage phenomena and the current study predicts that this creates relatively large levels of charge due to particle-particle collisions. This lip-leakage of charge was not observed for the larger $d_p = 1\mu m$ particles; further evidencing that this physics is only present for small particles which are not expected to be separated. Smaller lip-leakage "currents" are observed spiralling towards the vortex finder at the top of the cyclone bringing particles radially inwards and creating charge along the walls. Additionally, a stripy pattern of charge is observed travelling up the outlet pipe due to the helical particle bands centrifuging particles towards the wall, matching the pathline of the Lagrangian particle trajectory from Figure 5.14. The observed build-up of charge on the walls mirrors the results from the Eulerian model of Kolehmainen *et al.* in Section 2.3.

The resulting electric potential from the particle charge distribution is then solved for. The walls are assumed to be grounded, giving the wall boundary condition as $\phi_w = 0$. At the inlet, the electric potential is set to zero and at the outlet the electric potential is assumed to be fully-developed. Due to the low charge levels, the electric potential is also very small. The gradient of the electric potential gives the electric field strength, with the distribution in each section of the cyclone provided in Figure 5.41. The electric field of the $d_p = 1\mu m$ particles is around 2 orders of magnitude stronger than the $d_p = 0.1\mu m$ particles and the distribution of the electric field in the cyclone is different for both diameters. For the larger $1\mu m$ particles, the electric field strength is dominated by the cone tip region, where the distribution is skewed to the right. For the smaller $0.1\mu m$ particles, the electric field in the top section due to particle-particle collisions is weakest. In the top of the conical section of the cyclone, the electric field strength is greatest. This is due to the particles which have

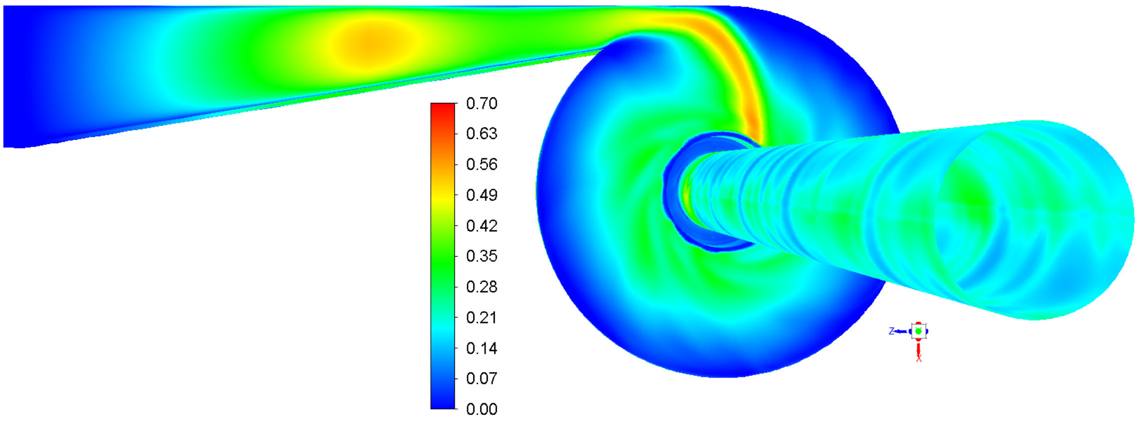

Figure 5.40: Specific charge distribution along the cyclone walls for $d_p = 0.1\mu m$ with a reflect wall boundary condition and turbulent diffusion normalised by the maximum value in the domain.

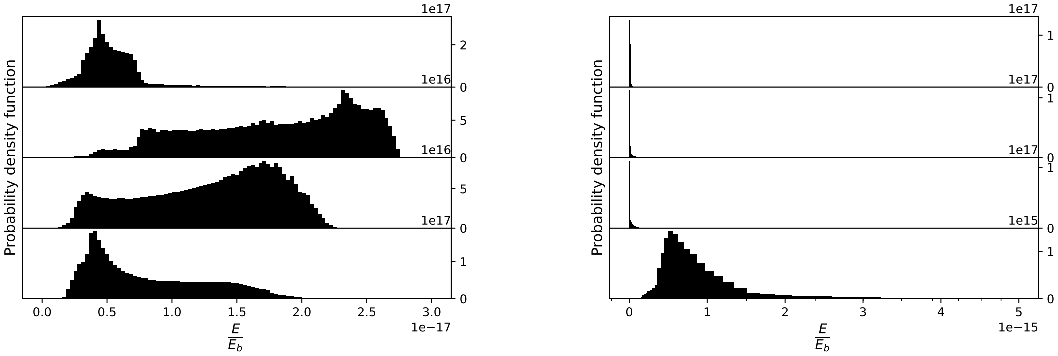

Figure 5.41: Electric field strength magnitude across the 4 cyclone section for $d_p = 0.1\mu m$ on the left and $d_p = 1\mu m$ on the right, normalised by the limit for electrical breakdown.

been charged in other sections of the cyclone traversing up through the vortex core to escape the cyclone. At the cone tip, a right-skewed distribution for the electric field strength is observed as for the larger particles.

The transport equations for both charge and electric potential in the cyclone are solved again for two different inlet boundary conditions for the specific charge. Instead of neutral, the particles entering the cyclone are assumed to already be charged, with one boundary condition assuming $Q_p = 1e$ and the other $Q_p = 2e$ matching the charge state of the aerosol after the neutraliser from the experiments performed in Chapter 3. The charge levels observed for these boundary conditions were many orders of magnitude greater than the uncharged inlet BC, with the results of both charged boundary conditions having identical forms and the magnitudes scaled up by a factor of 2 for the $Q_p = 2e$ BC relative to $Q_p = 1e$. Only the results for $Q_p = 2e$ will be presented.

Figure 5.42 shows the specific charge distributions in the cyclone at the high charge inlet BC. Both the small and larger particle diameters show an almost identical charge distribution, with the larger $d_p = 1\mu m$ particles exhibiting a peak around zero in the lower sections of the cyclone in the vortex core where these larger particles could not enter. In these highly charged inlet cases, particle collisions are seen to reduce the charge magnitudes of the particles for the given triboelectric constants obtained from experiment and is why in these cases the charge distribution in the cone tip region is the lowest. This exchange of charge to produce more neutral and stable particles is suggestive that agglomeration would physically be occurring in the cyclone cone tip.

The electric field strength distribution for the highly-charged inlet cases in Figure 5.43 shows that the electric field strength is 2-3 orders of magnitude from the air breakdown voltage $E_b \approx 3 \times 10^6 V/m$ [61]. For particles with charging properties of salt at this highly-charged inlet state, air breakdown is not expected to occur. This is suggestive that for higher-charging, larger volume fraction cases, the model would predict electrical breakdown in the cyclone. The electric field strengths for both particle diameters are scaled-up versions of the neutral inlet cases in Figure 5.41. It was also observed that the electric field strength vector is pointed directly towards the cyclone walls, therefore electrostatic forces acting on the particles act in the wall-normal direction and can both aid or inhibit the separation of charged particles.

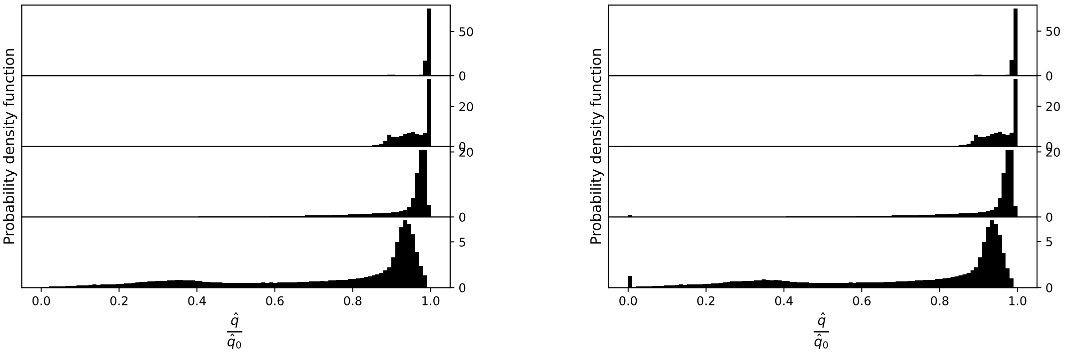

Figure 5.42: Specific charge distribution across the 4 cyclone section for $d_p = 0.1\mu m$ on the left and $d_p = 1\mu m$ on the right, normalised by the inlet specific charge boundary condition. The inlet boundary condition for specific charge is $\hat{q}_0 = 0.032974 C/kg$.

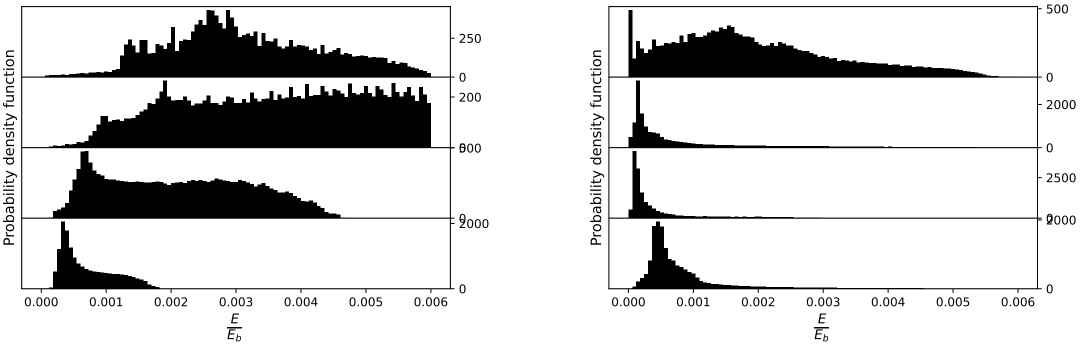

Figure 5.43: Electric field strength magnitude across the 4 cyclone section for $d_p = 0.1\mu m$ on the left and $d_p = 1\mu m$ on the right, normalised by the limit for electrical breakdown for the highly-charged inlet boundary condition.

This Eulerian charge model has yielded sensible results in terms of the build-up of charge and resulting electric fields in the cyclone. The model presented here was formulated to be computationally inexpensive and thus has simplified reality. One such exclusion of physics is the polarity of the charged particles. This model has assumed that particles will charge positively through tribocharging and that particles will never obtain a negative charge. This was informed by the salt particles charging positively in the tribocharging experiments in Chapter 3. In reality, the particulate phase will contain negatively charged particles and a net neutral aerosol will have a mix of the two. To more accurately account for the negative particles, an additional charge transport equation could be implemented, with the summation of the two Eulerian fields used as the input for the electric potential Poisson equation. In order to prevent the two from cancelling-out, different tribocharging constants could be used for both polarities (the salt was found to more-readily charge positive from the neutraliser in Chapter 3). This would double the computational effort required after solving for the volume fraction and would represent a more expensive computational model.

Another consequence of assuming all-positive particles is that the electric field will always point away from regions of charge. If the particles were negatively charged, the field would point in the opposite direction. In spite of this deficiency, the net absolute charge would be the same and so the areas of net charge build-up presented here are still relevant and can inform where charge and electric breakdown are likely to occur within the domain.

Additionally, the tribocharging constants have been derived from collisions between sub-micron salt particles and a metal plate. For particle-particle collisions, these constants would be expected to differ somewhat. Obtaining such experimental data was not possible from the set-up in Chapter 3. With this additional data, a distinction could be made in the computational model between particle-wall and particle-particle charging. In the current simulations, the walls are modelled as grounded for electric potential. Determining a boundary condition on the walls which is consistent for both the charge and electric potential transport equations is predicted to be very difficult and beyond the scope of this work.

The last piece of missing charge physics in the model not yet discussed is the coupling between the volume fraction and the charge. In reality, a large build-up of positive charge in an area will repel more positive charge from entering the same area. This means that the build-up of charge in the boundary layers by the cyclone walls may act to repel additional charged particles from entering the boundary layer and being separated. This situation is made even more complex if the charge of each individual particle size is considered. Clearly such complex coupling makes the model intractable for solution. For the monodisperse case in a standard two-fluid model, this coupling could be relatively easily be implemented by the addition of electrostatic repulsion source terms in the Eulerian particle velocity momentum equations. In this work, there are no PDE's for the particle momenta and instead it is specified algebraically using the EE method. There is no clear approach with the addition of this electrostatic force into the EE velocity field and therefore this is not possible to be implemented here. This coupling requires solving the more computationally-involved two-fluid equations and is not explored in this work.

The results of the charge model implementation has provided suggestive results on both the charge distribution and the resulting electric field in the cyclone. For neutrally-charged particles entering the cyclone, charge is produced through collisions, especially in the cone tip region for all particle diameters considered. Charge is seen to travel along insulating walls and for small particles, this charge is transported by the lip-leakage flow towards the vortex finder. The resulting electric field is strongest by the cone tip as expected for the larger particles, however for the smallest particles the electric field is strongest near the vortex finder due to a combination of the lip-leakage flow and the transport of charge up the vortex core. Collisions from highly-charged particles entering the cyclone reduced the magnitude of charge present. This charging model assumed that the particulate phase had the same charging properties as small salt particles from experiments in Chapter 3. For silica-based test dust, charge levels are expected to be much larger and air breakdown is highly possible.

5.4 Conclusion

A compressible LES of a cyclone was presented with spatial and temporal resolution comparable to a direct numerical simulation, with flow rates matching experiment. The flow field is complex, 3D and highly-swirling and turbulent structures in the boundary layer were partially observed. An in-depth study on accurately computing the separation efficiency using Lagrangian particles was performed, with an excellent match to experiment observed for larger particles and for $d_{p,50}$. The separation efficiencies of the smallest particles were over-predicted due to missing physics including agglomeration. The Lagrangian particle tracking also provided useful statistics of Re_p and Stk along the particle trajectory, showing that both of these dimensionless quantities are small in this flow.

These statistics validated the use of a computationally efficient method of computing the Eulerian particle velocity field using the EE method. Solving for the volume fraction transport equation allowed estimation of a separation efficiency, which was an excellent match to the Lagrangian particle result for reflecting walls and including the effects of the filtered scales. The Eulerian results exhibited the same physics as observed for the Lagrangian particles: particle accumulation at the walls in the boundary layer and at the cone tip. Streaky bands of volume fraction were seen along the cyclone walls for the larger particles, matching experimental evidence from Chapter 1. This has provided strong evidence that this method is applicable to this highly-swirling flow and that the volume fraction distribution in the cyclone is accurate.

This was then used in speculative simulations of the charge and electric field in the cyclone. These results are only suggestive due to the lack of validation and/or data available for these quantities in a cyclone. However the charge model from literature was validated at these size ranges from experiments in Chapter 3, the Eulerian model was both tested and validated in strong streamline curvature in Chapter 4 and matched the Lagrangian separation efficiency in this chapter. Therefore there is good reason to examine the results. Collisions were seen to dominate at the cone tip as expected, with neutrally-charged particles charging the most in this region of the cyclone. The charge for small particles was seen to mimic the lip-leakage phenomenon and flow along the top of the cyclone wall towards the vortex finder. The charge and electric field strengths were very small for neutrally charged particles as the charging constants used were that of salt. Using silica-based powders is expected to produce much more charge than is observed for salt. Having charged particles enter the cyclone (with charge levels matching that from the neutraliser from experiments) resulted in much stronger electric fields in the cyclone, with the vector field pointed towards the walls. The electric field strength results for the salt were approximately 1% of the breakdown field strength for air. This suggests that corona discharge to air is likely at higher volume fractions and for more charge-prone particles.

Chapter 6

Conclusion

In this study, the relevant physics and methods of computationally modelling the multiphase system of a swirling, high-speed flow applied to a small cyclone has been investigated. Experimental evidence provided by the project sponsor appeared to show particles moving in streaky bands along the walls of the cyclone. This suggested that turbulent structures in the near-wall region were entraining particles into these bands, in which these dense clustering of particles are expected to exchange charge through collisions. An inexpensive computational model which is able to capture these physics was sought in the literature, which would enable predictions of both separation efficiency and charge in the cyclone.

From the literature, LES was found to be the most appropriate method to model the fluid flow in order to both capture the vortex core precession to match the experimental pressure drop and to attempt to resolve the near-wall structures which would be seen by the particles. The commonly-used RANS turbulence models used for cyclones in the literature will average-out these small-scale structures, for which the particles are expected to interact with due to their low Stokes numbers.

A simple model by Ireland for tribocharging enabled the charge transfer to be predicted from a binary particle collision by suitable choice of tune-able model constants. This model, along with many other tribocharging models present in the literature were validated for large $\approx 1mm$ particles; $3-4$ orders of magnitude larger than the particles seen by the cyclone of interest. This gap in the literature required experiments to be performed in order to both validate the model at these small scales and to estimate the tune-able model constants.

For low mass loadings, one-way coupling between the particle and the fluid was assumed. This allowed Lagrangian particles to be accurately tracked individually through the flow field which enabled estimates of separation efficiency to be made. As the volume fraction is expected to become moderate near the walls and cone tip, particle-particle collisions are expected to be significant in these regions. Capturing these collisions in a Lagrangian framework is not computationally feasible and so Eulerian particle models were explored. From these, the Equilibrium Eulerian model was selected as it does not require the solution of any additional PDEs for the particle momenta and is able to capture both preferential accumulation and turbophoresis for low Stokes number particles. This model was validated for use in isotropic turbulence but not for a highly-swirling flow. This necessitated validation to be performed of the model, which additionally provided useful testing for the Eulerian model.

The tribocharging experiments required fine control over sub-micron particles. Controlling individual particles of this size is difficult and so the combined effect of many particles had to be used instead. To maintain control over the particulate phase, an aerosol beam was used to aerodynamically focus particles. These were collided with a metal plate in experiments analogous to single particle experiments performed in the literature for much larger particles. The saturation of voltage on the plate due to particle-impact matched the literature for larger particles, with an exponential capacitor-like charging of the plate observed. This provided the validation required of the model at these small sizes along with the necessary constants for the charge model.

To validate the Eulerian model, an analytical flow field was used which featured strong streamline curvature and gradients in the flow to stress-test the model. A 2D Taylor-Green flow was used, with the eddy length and velocity scales indicative of the Kolmogorov scales of turbulence in the cyclone. The full discretisation of the volume fraction transport equation was shown for this flow, with methods of stabilising the solution explored. This centred around the decomposition of the particle velocity field using the definition of the Equilibrium Eulerian velocity into the sum of the fluid and relative velocity terms to split the convective term. This enabled the volume fraction to be convected by a divergence-free flow field, with the relative velocity providing a non-linear source term. Lagrangian particle tracking was performed in this flow to provide a reference with which to compare the Eulerian results to inform the choice of numerical integration scheme for use in the cyclone.

The Eulerian model was found to predict the preferential accumulation of particles as expected, with numerical issues observed as the Stokes number increased. These issues were identified as a direct result of neglecting the influence of collisions on the particles which would predict ever-increasing particle build-up as both Stk and the fineness of the grid increases. Diffusion coefficients were found to increase the stability of the system and extended the model to larger Stokes numbers.

An LES of a cyclone was performed with excellent spatial resolution and a temporal resolution comparable to a direct numerical simulation. The walls were well-resolved in the wall-normal direction, however the filter width is large in these regions due to the high aspect ratio cells in the inflation layers. The experimental pressure drop used as the boundary condition provided the correct mass flow rate observed from experiment and the tangential velocity profile matches the correct Rankine vortex-like form seen in the literature. The boundary layer normalised velocity profile was in good agreement with flat-plate theory, with the boundary layers along the concave walls being much thinner and stable. Streaky structures were observed in this concave boundary layer via the Q-criterion qualitatively matching the particle bands observed from experiment and thus suggesting that these near-wall structures are the cause of these particle bands.

Lagrangian particle tracking in the cyclone provided a good match to experimental evidence for the separation efficiency, especially for the match of $d_{p,50}$. The computational results over predicted the separation efficiency of particles $< 0.2\mu m$ which is expected to be due to missing physics of agglomeration at this size range. This additionally resulted in the gradient of the predicted separation curve being less steep than experiment. The statistics along particle trajectories provided the Stokes numbers which were used to test the Eulerian model in the Taylor-Green flow in order to make the validation representative. The particle position in the boundary layer along the trajectory was also examined, with larger particles found to sit deeper in the boundary layer due to larger centrifugal forces acting on them. Larger particles were found to become trapped in the boundary layers, whilst small particles possessed the ability to enter the boundary layer and leave shortly after. This entrapment is suggestive that the particle bands seen experimentally are caused by the larger particles in the flow.

The Eulerian model for a range of wall boundary conditions and diffusion coefficients was applied to the cyclone. A reflect wall boundary condition, along with including the effects of the unresolved SGS, provided an excellent match to the Lagrangian particle result for separation efficiency. The particle volume fraction along the walls featured a streaky pattern matching the experimental particle bands for the largest particles, with this pattern not clearly observed for the small particles. This was in further agreement with the Lagrangian results. Novel predictions for the charge, electric potential and electric field strength in the cyclone were made using the Eulerian particle model, with charge shown to accumulate by the cyclone walls and especially by the cone tip.

6.1 Suggestions For Future Work

The Modified Equilibrium Eulerian method, which was not utilised due to numerical instability of the model in regions of large compressive strain, may be able to provide a more accurate particle velocity field. This would also save the computational expense of solving PDEs for the particle momentum at the cost of a small matrix inversion at all points in the flow. Ferry *et al* discussed simply replacing any extreme values of particle velocity with a "reasonable" value, however this would result in a non-smooth velocity field which is problematic when derivatives of this flow field are taken for the transport equation [166]. Their suggested numerical fix has been shown to not work and thus future work could examine how to ensure the matrix inversion produces "reasonable" particle velocities whilst keeping the particle velocity field smooth.

The EE method has been used to track a monodisperse particulate phase in this work. The model could be extended to polydisperse systems using the method of moments. Particle collisions at a certain particle diameter can provide a source term for the creation of a larger diameter phase and thus effects of agglomeration can be included. This would be expected to cause small particles to agglomerate into larger particles which would result in increased separation efficiency, thus providing a better match to experiment for very small particles.

The aerosol beam provided a method of controlling sub-micron particles and aerodynamically focusing them onto a metal plate. The experimental set-up could be adapted to allow two aerosol beams to collide, with the pre and post-impact net charges measured on the aerosol. All collisions could be assumed to be particle-particle which would provide tribocharging data not present in the literature for these small particle sizes.

The Eulerian model presented in this work has assumed one-way coupling with the fluid influencing the particulate phase due to low mass fractions. The additional coupling between the resulting electric field on the transport of charged particles has been neglected. Including this coupling and retaining an algebraic relation for the particle momenta is unlikely to be feasible. If this coupling is expected to be significant, the computational saving associated with the EE method must be abandoned and the full two-fluid model used instead, with the electrostatic force from the electric field acting on the charged particles accounted for as a source term in the transport equations for the particle momentum.

Appendix A

Geometric Swirl Number Derivation

The swirl number is given by Eq. 1.3, repeated here as

$$Sw = \frac{L_\theta}{L_x D_e/2}.$$

To aid in the derivation of a simpler geometric swirl number, a relevant diagram is provided in Figure A.1.

It is assumed that $u_t \approx u_0$ and the effects of viscosity are negligible. The flow is also considered incompressible. The input flux of angular momentum leaving the cyclone is

$$L_\theta = \dot{m}_{in}\left(\rho_f u_v \frac{\pi D_e^3}{8}\right). \tag{A.1}$$

The input flux of linear momentum entering the cyclone is

$$L_z = \dot{m}_{in}\left(\rho_f u_0 a_h b\right). \tag{A.2}$$

Substitution into the definition of swirl number yields

$$Sw = \frac{u_v}{u_0}\frac{\pi D_e^2}{4a_h b}. \tag{A.3}$$

The velocities can be eliminated from conservation arguments. Angular velocity within the cyclone must be conserved giving

$$u_t D = u_v D_e. \tag{A.4}$$

Using $u_t \approx u_0$ and rearranging for $\frac{u_v}{u_0}$ provides

$$\frac{u_v}{u_0} = \frac{D}{D_e}.$$

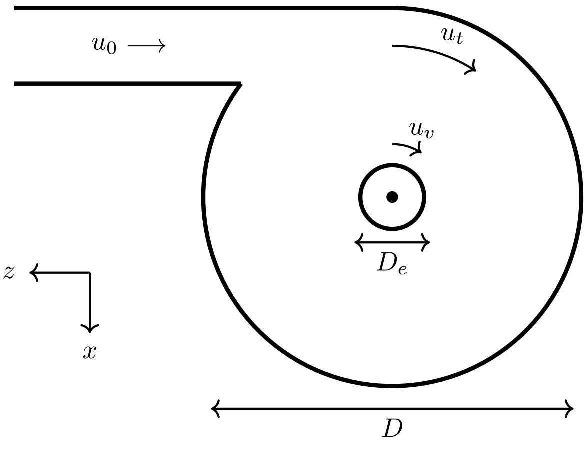

Figure A.1: 2D section of the cyclone geometry on the x-z plane with labelled representative velocities. The black central dot indicates the location of the origin of the coordinate system. The outer swirl velocity is denoted by u_t, with the swirl velocity of the vortex core within the vortex finder given by u_v.

Substitution of this velocity ratio into Eq. A.3 finally yields the equation for the geometric swirl number (Eq. 1.4)

$$Sw_g = \frac{\pi D D_e}{4 a_h b}. \tag{A.5}$$

Appendix B

Rankine Vortex

The fluid flow in a cyclone is commonly simplified to an analytical vortex flow to aid in analysis. The standard comparison flow is that of a Rankine vortex [11], with tangential velocity given by

$$\boldsymbol{u}_t(\boldsymbol{r}) = \begin{cases} C_r \boldsymbol{r}, & \text{if } |\boldsymbol{r}| < R \\ \frac{C_r}{R^2|\boldsymbol{r}|}\hat{\boldsymbol{r}} & \text{otherwise.} \end{cases} \tag{B.1}$$

Here $\boldsymbol{r}$ is the radial vector from the origin (with $\hat{\boldsymbol{r}}$ representing its unit vector), R is the radius at which point the flow changes character and C_r is a constant related to the circulation of the vortex and determines its strength. The tangential velocity profile for $|\boldsymbol{r}| < R$ represents a rigid body rotation of the fluid in this region, with the velocity profile outside this region given by an irrotational vortex [11]. The tangential velocity profiles for these vortices are provided in Figure B.1.

Away from the core of a "real" vortex ($|\boldsymbol{r}| > R$), viscosity effects from the fluid are negligible and the irrotational, potential flow solution is seen. This is inversely proportional to the radius and so the velocity decreases with increasing radial distance. As the radius decreases, the flow speeds up until a maximum value is reached where $|\boldsymbol{r}| = R$. For $|\boldsymbol{r}| \leq R$, viscosity effects become prominent and the angular momentum is dissipated in the "eye". If the effects of viscosity were ignored, the vortex would have a singularity at the origin which is unphysical.

The Rankine vortex represents an idealisation of the main cyclone flow, with the outer vortex flow given by an irrotational vortex and a solid body rotation modelling the viscosity effects within the vortex core. Being idealised, the Rankine vortex neglects the transfer of angular momentum between different radial layers due to both viscosity and from small turbulent structures [11]. Cyclones are also wall-bounded flows and as $\boldsymbol{r}$ approaches the local cyclone radius, viscosity at the wall dominates and a boundary layer is present. These additional phenomena will distort this ideal Rankine vortex which may cause wildly different particle trajectories in this flow, thus missing important physics required for predicting cyclone separation efficiency. A more complex CFD model is required to acquire the flow field in the cyclone accurately.

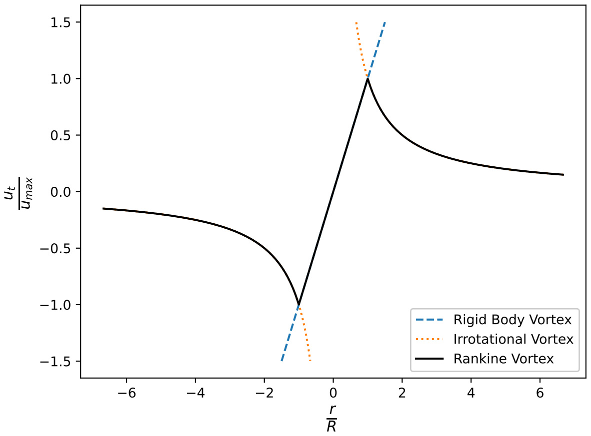

Figure B.1: Dimensionless tangential velocity profile for the rigid body, irrotational and Rankine vortices, each with common R and C. The radial distance is normalised with the cut-off radius R.

Appendix C

MEE Matrix Inversion: Proof by Contradiction

The matrix to be inverted in the MEE method is

$$\left(\boldsymbol{I} + \tau_p \left(\nabla \boldsymbol{u}\right)^T\right). \tag{C.1}$$

Following Ferry *et al.*, an interpolation factor ζ_f, where $0 \leq \zeta_f \leq 1$ is introduced as [166]

$$\left(\boldsymbol{I} + \zeta_f \tau_p \left(\nabla \boldsymbol{u}\right)^T\right). \tag{C.2}$$

To find a value for ζ_f to ensure invertibility, they require the second C_{i2} and third C_{i3} matrix invariants of $A = \left(\nabla \boldsymbol{u}\right)^T$ given as

$$C_{i2} = \begin{vmatrix} a_{22} & a_{23} \\ a_{32} & a_{33} \end{vmatrix} + \begin{vmatrix} a_{33} & a_{31} \\ a_{13} & a_{11} \end{vmatrix} + \begin{vmatrix} a_{11} & a_{12} \\ a_{21} & a_{22} \end{vmatrix}, \tag{C.3}$$

$$C_{i3} = \det\left(A\right), \tag{C.4}$$

where the lowercase a represents the elements of the matrix A. They then define a new variable θ_f as

$$\theta_f = \tau_p \left(8 \max\left(0, -C_{i2}\right)^3 + 8 \max\left(0, -C_{i3}\right)^2\right)^{\frac{1}{6}}, \tag{C.5}$$

which determines the interpolation factor as

$$\zeta_f = \begin{cases} 1, & \text{if } \theta_f \leq 1 \\ 0, & \text{if } \theta_f \geq 2 \\ \frac{1-\cos\left(\pi\theta_f\right)}{2} & \text{otherwise.} \end{cases} \tag{C.6}$$

Ferry *et al.* claim that this procedure guarantees that $\det\left(\boldsymbol{I} + \zeta_f \tau_p \left(\nabla \boldsymbol{u}\right)^T\right) > 0.207$ [166]. To prove that this is incorrect by contradiction we assume that this claim is true and look at a case where τ_p is unity and $\left(\nabla \boldsymbol{u}\right)^T$ is given by

$$\left(\nabla \boldsymbol{u}\right)^T = A = \begin{pmatrix} -0.8848029868419878 & -0.11105094208205613 & -0.02248538330710992 \\ -0.05733074797076698 & -0.9320998847607228 & -0.037804483047788606 \\ -0.20238846705879077 & -0.016504552412230145 & -0.13944578061155377 \end{pmatrix}. \tag{C.7}$$

The invariants of this matrix are

$$C_{i2} = 1.0665428393943164, \tag{C.8}$$

$$C_{i3} = -0.11019368317321844, \tag{C.9}$$

providing

$$\theta_f \approx 0.678. \tag{C.10}$$

From Eq. C.6, as $\theta_f < 1$, the interpolation factor produced would be unity and no interpolation is required from the MEE result. The matrix to invert is therefore

$$\left(\boldsymbol{I} + \tau_p \left(\nabla \boldsymbol{u}\right)^T\right) = \begin{pmatrix} 0.115197013158012 23 & -0.11105094208205613 & -0.02248538330710992 \\ -0.05733074797076698 & 0.06790011523927719 & -0.037804483047788606 \\ -0.20238846705879077 & -0.016504552412230145 & 0.8605542193884462 \end{pmatrix}. \tag{C.11}$$

The determinant of this matrix is $\approx 5.04 \times 10^{-7}$. This is a contradiction to the original assumption and thus this method does not guarantee that det $\left(\boldsymbol{I} + \zeta_f \tau_p \left(\nabla \boldsymbol{u}\right)^T\right) > 0.207$. This matrix along with many others disproving the claim were found from a brute-force search using 1×10^6 matrices with elements drawn from a uniform random distribution between 0 and 1, of which over 99% of these random matrices invalidated the claim made by Ferry *et al.*

Appendix D

Scanning Mobility Particle Sizer Theory of Operation

The Scanning Mobility Particle Sizer (SMPS) is used to measure the size distribution of an aerosol sample. The SMPS consists of three pieces of equipment: a TSI Electrostatic Classifier, a long Differential Mobility Analyser (DMA) and a Condensation Particle counter (CPC). The aerosol stream enters the classifier and is passed through an impactor. This removes larger particles by inertial impaction. The aerosol then enters a Krypton-85 neutraliser which produces a known charge state on the aerosol. The charged aerosol enters the DMA, where the particles are separated by electrical mobility. Particles of a selected electrical mobility then enter the CPC to be counted optically.

At the front of the classifier is an impactor, which removes particles larger than a known aerodynamic diameter in order to remove their contribution to multiply-charged aerosols by inertial impaction [193]. The cut diameter of the impactor, $d_{p,50}$, is the aerodynamic diameter for which the impactor has an efficiency of 50%. This cut diameter is calculated by considering the Stokes number of a cut-sized particle passing through the impactor

$$Stk_{50} = \frac{\tau_{p,50}}{\tau_f}, \tag{D.1}$$

with

$$\tau_{p,50} = \frac{\rho_p d_{p,50}^2 C_c}{18\mu_f}, \tag{D.2}$$

$$\tau_f = \frac{D_n}{2u_n}, \tag{D.3}$$

where D_n is the impactor nozzle diameter and u_n is the velocity through the impactor nozzle. Rearrangement and substitution of the fluid volumetric flow rate $\dot{V}_f = \frac{\pi D_n^2 u_n}{4}$ yields

$$d_{p,50} = \sqrt{\frac{9\pi Stk_{50}\mu_f D_n^3}{4\rho_p C_c \dot{V}_f}}, \tag{D.4}$$

where $Stk_{50} = 0.23$ and the nozzle diameter $D_n = 4.57 \times 10^{-4} m$. The Cunningham slip correction factor is defined in Eq. 1.25, the volumetric flow rate through the impactor was $\dot{V}_f = 0.3$lpm and the particles were salt with a density of $2170 kgm^{-3}$. The equation for the cut-off diameter is implicit due to the Cunningham slip term and for the experiments detailed in Chapter 3 the cut-off diameter of the impactor was $d_{p,50} = 459nm$.

After the impactor, the aerosol is passed through a Krypton-85 radioactive source which undergoes beta decay to create a well-defined charged distribution on the aerosol. This distribution is given by Fuchs' diffusion theory [55] and is modelled for particles under a micron from the model by Wiedensohler *et al.* [194]. This calculates the fraction f_p of particles with N elementary charges as

$$f_p(N) = 10^{\sum_{i=0}^{5} a_i(N)\left(ln\left(\frac{d_p}{1\times 10^{-9}}\right)\right)^i}. \tag{D.5}$$

This equation is valid for the size ranges $1nm \leq d_p \leq 1\mu m$ for $N = -1, 0, 1$ and $20nm \leq d_p \leq 1\mu m$ for

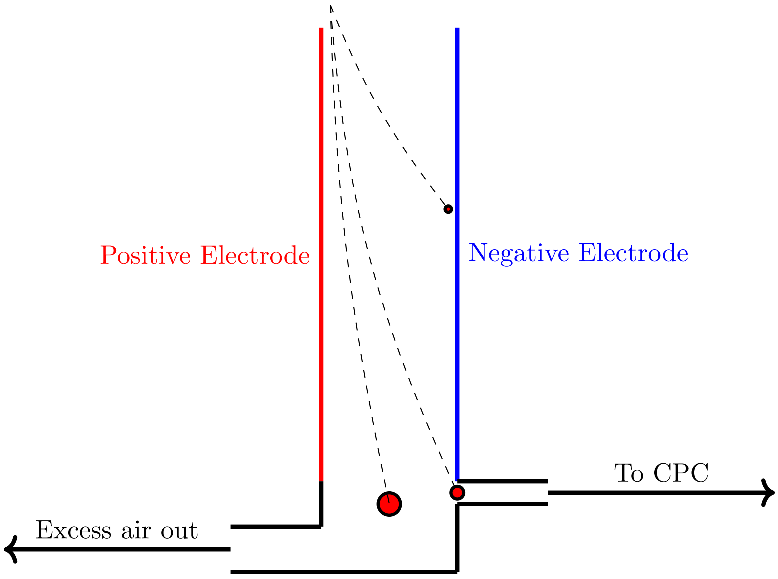

Figure D.1: DMA principle of operation. Three positively charged particles of different diameters (and therefore different mobilities) migrate through the DMA with different trajectories as shown by the dashed line. One particle has the correct electrical mobility to leave through the thin slit to be counted downstream.

$N = -2, 2$. For particles carrying 3 or more charges, the derivation by Gunn and Woessner is used [195]

$$f_p(N) = \frac{e}{\sqrt{4\pi^2\epsilon_0 d_p k_B T_f}} \exp\left(- \frac{\left[N - \frac{2\pi\epsilon_0 d_p k_B T_f}{e^2} \ln\left(\frac{Z_{i+}}{Z_{i-}}\right)\right]^2}{2\frac{2\pi\epsilon_0 d_p k_B T_f}{e^2}} \right), \tag{D.6}$$

where $\frac{Z_{i+}}{Z_{i-}}$ is the ion mobility ratio. The electrical mobility of a particle Z_p is defined as

$$Z_p = \frac{neC_c}{3\pi\mu_f d_p}. \tag{D.7}$$

The aerosol, with known charge state, is then injected into the top of the DMA and travels down the DMA due to the sheath flow. An electric field is set-up along the DMA which causes the charged particles to migrate horizontally due to the electrostatic force. Particles of a narrow range of electrical mobilities are able to leave through a thin slit by the base of the DMA to flow further downstream. Figure D.1 illustrates the working principle of the DMA.

The set electrical mobility Z_p^* on the DMA is given by

$$Z_p^* = \frac{\dot{V}_{sh}}{2\pi\bar{V}_c L} \ln\frac{r_2}{r_1}, \tag{D.8}$$

where $\dot{V}_{sh} = 3$lpm is the sheath flow rate, $L = 0.44369m$ is the length between the inlet and the exit slit, $r_1 = 0.00937m$ is the inner radius of the annular space, $r_2 = 0.01961m$ is the outer radius of the annular space and $\bar{V}_c$ is the average voltage of the inner collector rods. This voltage is swept through a range of values during a scan to allow the CPC to measure the concentration of particles with various electrical mobility. This voltage sweep as a function of time is given by

$$V_c(t) = V_{c,tf}\left(\frac{V_{c,max}}{V_{c,tf}}\right)^{\frac{t-t_f}{t_{\text{scan}}-t_f}}, \tag{D.9}$$

where $V_{c,tf}$ is the starting voltage, $V_{c,max}$ is the end voltage, t_{tf} is the time particles need to pass through the DMA and $t_{\text{scan}} = 90s$ is the scan time. Particles with a known electrical mobility exiting the DMA then travel to the CPC to be counted. The CPC consists of an aerosol beam which fires particles perpendicular to a laser pointed at a photodetector. When a particle passes through the laser beam, a drop in voltage is observed at the photodetector and a particle is counted. At higher particle concentrations, two particles may pass through the laser at the same time (coincidence). A coincidence correction is used to extend the range of concentrations which can be counted in this manner. The manufacturer's maximum stated error for this method of counting is 5%.

For concentrations larger than $5 \times 10^5 p/cc$, single particle counting is not possible due to coincidence and instead the light scattered by the particles from the laser beam is measured to determine the concentration. The scattered light is focused by lenses, which are perpendicular to both the laser and the aerosol beam, onto another photodetector which determines concentration through calibration. This method of determining concentration is less accurate than single particle counting (maximum error of 10%) and was not used during the experiments performed.

The CPC is connected to the DMA by conductive tubing. The transport time for the particles through this tubing, along with the internal response time of the detector is the delay time t_d. Particles $k_C(t)$ counted during a scan by the CPC at time t will have an electrical mobility corresponding to $t - t_d$

$$k_C(t) = k_C(Z(t - t_d)). \tag{D.10}$$

The classifier records the number of counted particles in time intervals of $\Delta t = 0.02s$ whilst the DMA voltage raises exponentially during a scan. All further calculations are made in 192 size bins j. These are either geometrically or logarithmically distributed between $1nm$ and $1\mu m$. The particle counts are first mapped from time intervals i into size bins j by

$$K_{c,j} = \sum_i k_{c,i} \frac{\Delta t_j \in \Delta t_i}{\Delta t_i}. \tag{D.11}$$

The raw particle counts $k_{c,j}$ for the size bins j are used to calculate the particle number concentration dn_j in each size bin at the inlet of the SMPS (assuming all particles were singly charged)

$$dn_j = \frac{k_{c,j}}{\dot{V}_{\text{sensor}} t_{bin,j}} \frac{\Phi_d}{f_{1,j} \eta_{det,j} P_j} \frac{Z(d_{low,j}) - Z(d_u p, j)}{\Delta Z(d_m, j)}, \tag{D.12}$$

where $\dot{V}_{\text{sensor}}$ is the volumetric flow rate through the sensor of the CPC (m^3/s), $t_{bin,j}$ is the sampling time interval during which a size bin j can receive particles during a scan (s), Φ_d is the eventual dilution due to DMA bypass flow, $f_{1,j}$ is the fraction of singly charged particles for the midpoint diameter $d_{m,j}$ of each size bin j, $d_{m,j}$ is the midpoint diameter of each size bin j (m), $\eta_{det,j}$ is the detection efficiency of the particle detector for each size bin j, P_j is the penetration of particles with size $d_{m,j}$ to correct for diffusion losses.

The data inversion assumes that all particles leaving the DMA and counted by the CPC are singly charged. There will be particles with more than one charge in the monodisperse flow (especially larger ones) to be counted. A correction is needed to eliminate this error, known as the multiple charge correction (MCC). The requirement for this correction to be valid is that the largest bin containing particles may only contain singly charged particles. This is true either if the size distribution does not contain particles larger than the upper boundary of the selected SMPS measurement range, or if the impactor removes such larger particles. Starting from the topmost size bin j, the multiple charge correction for up to 6 charges is given by

$$dn_{MCC,j} = dn_j - \sum_{i=j-1}^{1} \sum_{l=2}^{6} \frac{f_{p,l,j}}{f_{p,1,i}} dn_i. \tag{D.13}$$

The measured size distribution under-represents small particles due to diffusion losses in transit. These losses are characterised in terms of penetration $\mathcal{P}$ through a tube

$$\mathcal{P} = \frac{n_{out}}{n_{in}}. \tag{D.14}$$

Diffusion losses through a tube at fixed volumetric flow rate and laminar flow is not a function of tubing diameter as the additional distance the particles must travel to the walls in a wider tube is offset by a longer residence time. The Reynolds number of the flow through the conductive tubing is $Re \approx 90$ suggesting the flow is laminar. Circular tube penetrations are given by Gormley and Kennedy [196].

Appendix E

Aerosol Beam Drawing

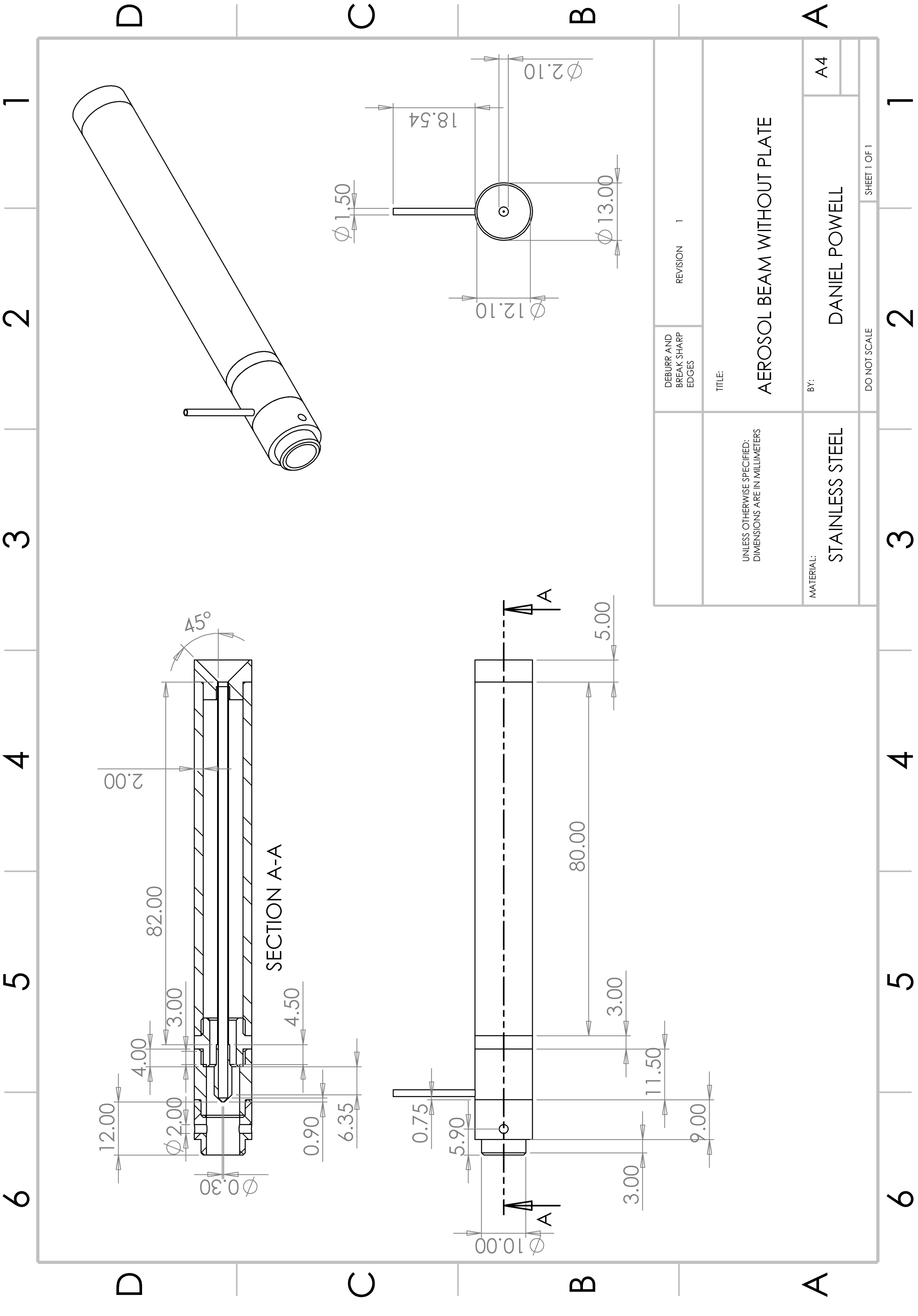
DEBURR AND BREAK SHARP EDGES
REVISION 1
TITLE:
AEROSOL BEAM WITHOUT PLATE
BY:
DANIEL POWELL
A4
SHEET 1 OF 1
DO NOT SCALE
UNLESS OTHERWISE SPECIFIED: DIMENSIONS ARE IN MILLIMETERS
MATERIAL:
STAINLESS STEEL
SECTION A-A
45°
2.00
82.00
3.00
4.00
12.00
Ø2.00
Ø0.30
4.50
0.90
6.35
0.75
5.90
3.00
80.00
5.00
3.00
11.50
9.00
Ø10.00
A
A
Ø12.10
Ø13.00
Ø1.50
18.54
Ø2.10
A B C D
1 2 3 4 5 6

Appendix F

LES Governing Equations

The compressible, spatially-filtered Navier-Stokes equations are given by [197]

$$\frac{\partial \tilde{\rho}_f}{\partial t} + \frac{\partial (\tilde{\rho}_f \hat{u}_j)}{\partial x_j} = 0, \tag{F.1}$$

$$\frac{\partial \tilde{\rho}_f \hat{u}_i}{\partial t} + \frac{\partial (\tilde{\rho}_f \hat{u}_i \hat{u}_j)}{\partial x_j} = -\frac{\partial \hat{P}}{\partial x_i} + \frac{\partial \hat{\tau}_{ij}}{\partial x_j} - \frac{\partial \left(\tilde{\rho}_f \widehat{u_i u_j} - \tilde{\rho}_f \hat{u}_i \hat{u}_j \right)}{\partial x_j}, \tag{F.2}$$

$$\frac{\partial \tilde{\rho}_f \hat{E}_g}{\partial t} + \frac{\partial \left(\rho_f \hat{u}_i \hat{E}_g \right)}{\partial x_j} = \frac{\partial}{\partial x_j} \left(\hat{E}_g \hat{u}_i - \widehat{E_g u_i} + \hat{P} \hat{u}_i - \widehat{P u_i} - q_{h,i} \right) + \frac{\partial \hat{\tau}_{ij} \hat{u}_i}{\partial x_j}, \tag{F.3}$$

$$\hat{\tau}_{ij} = \tilde{\mu}_f \left(\frac{\partial \hat{u}_i}{\partial x_j} + \frac{\partial \hat{u}_j}{\partial x_i} - \frac{2}{3} \delta_{ij} \frac{\partial \hat{u}_k}{\partial x_k} \right), \tag{F.4}$$

$$q_{\hat{h},i} = -\frac{\hat{k}_t}{\tilde{\rho}_f C_p} \frac{\partial \hat{T}_f}{\partial x_i}, \tag{F.5}$$

$$\hat{P} = \tilde{\rho}_f R \hat{T}_f, \tag{F.6}$$

$$\hat{e}_t = C_v \hat{T}_f, \tag{F.7}$$

$$\hat{E}_g = \hat{e}_t + \frac{\hat{u}_k \hat{u}_k}{2}. \tag{F.8}$$

In these equations, τ_{ij} is the deviatoric stress tensor, E_g is the total energy, q_h is the heat flux, δ_{ij} is the Kronecker delta, k_t is the thermal conductivity, C_p is the specific heat at constant pressure, T_f is the temperature, C_v is the specific heat at constant volume and e is the internal energy. Variables with a $\tilde{}$ and a $\hat{}$ represent Favre-averaged and spatially filtered quantities (Eq. 1.12) respectively.

The unresolved or sub-grid scales (SGS) of the LES require modelling. As the larger scales are resolved in the LES, only the small scales are expected to modelled. From Kolmogorov's hypotheses, these eddies are isotropic and have a universal form. The SGS models are based on these hypotheses, leading to relatively simple eddy-viscosity models. Here we present the wall-adapting local eddy-viscosity (WALE) model. The WALE subgrid model is based on the Boussinesq hypothesis [30] (Eq. F.9) and provides the correct wall asymptotic behaviour for wall bounded flows such as a cyclone. The WALE model also returns zero turbulent viscosity for laminar zones in the domain and at the wall, and accounts for the contribution of regions where vorticity is more dominant than strain; making the model more appropriate than other "sub-grid" models such as Smagorinsky-Lilly [198]. The modelled term is

$$-\tilde{\rho}_f \widehat{u_i' u_j'} = \tilde{\mu}_t \left(\frac{d\hat{u}_i}{dx_j} + \frac{d\hat{u}_j}{dx_i} \right) - \frac{2}{3} \tilde{\mu}_t \frac{d\hat{u}_k}{dx_k} \delta_{ij}. \tag{F.9}$$

The mixing length is calculated by

$$L_s = \min \left(\kappa d, C_w \Delta \right), \tag{F.10}$$

where the Von Karman constant $\kappa = 0.41$ [199], d is the distance to the nearest wall, the local grid scale $\Delta = V^{\frac{1}{3}}$ [200] where V is the volume of the computational cell and the WALE constant C_w has been set to 0.325 for its suitability for a large range of flows [201]. The turbulent viscosity in the WALE model [198] is modelled as Eq.

F.11

$$\tilde{\mu}_t = \tilde{\rho}_f L_s^2 \frac{\left(\hat{S}_{ij}^d \hat{S}_{ij}^d\right)^{\frac{3}{2}}}{\left(\hat{S}_{ij}\hat{S}_{ij}\right)^{\frac{5}{2}} \left(\hat{S}_{ij}^d \hat{S}_{ij}^d\right)^{\frac{5}{4}}}, \tag{F.11}$$

with the second bracket in the denominator of Eq. F.11 given by [198]

$$\hat{S}_{ij}^d \hat{S}_{ij}^d = \frac{1}{6}\left(\hat{S}^2\hat{S}^2 + \hat{\Omega}^2\hat{\Omega}^2\right) + \frac{2}{3}\left(\hat{S}^2\hat{\Omega}^2\right) + 2\hat{J}, \tag{F.12}$$

where

$$\hat{\Omega}_{ij} = \frac{1}{2}\left(\frac{d\hat{u}_i}{dx_j} - \frac{d\hat{u}_j}{dx_i}\right), \tag{F.13}$$

$$\hat{S}^2 = \hat{S}_{ij}\hat{S}_{ij}, \tag{F.14}$$

$$\hat{\Omega}^2 = \hat{\Omega}_{ij}\hat{\Omega}_{ij}, \tag{F.15}$$

$$\hat{J} = \hat{S}_{ik}\hat{S}_{kj}\hat{\Omega}_{jl}\hat{\Omega}_{li}. \tag{F.16}$$

References

[1] W. Mazyan, A. Ahmadi, J. Brinkerhoff, H. Ahmed, M. Hoorfar, Enhancement of cyclone solid particle separation performance based on geometrical modification: Numerical analysis, Separation and Purification Technology 191 (Supplement C) (2018) 276 – 285. `doi:https://doi.org/10.1016/j.seppur.2017.09.040`.
URL `http://www.sciencedirect.com/science/article/pii/S1383586617312212`

[2] F. Parvaz, S. H. Hosseini, G. Ahmadi, K. Elsayed, Impacts of the vortex finder eccentricity on the flow pattern and performance of a gas cyclone, Separation and Purification Technology 187 (Supplement C) (2017) 1 – 13. `doi:https://doi.org/10.1016/j.seppur.2017.06.046`.
URL `http://www.sciencedirect.com/science/article/pii/S1383586617313692`

[3] A. Hoekstra, J. Derksen, H. V. D. Akker, An experimental and numerical study of turbulent swirling flow in gas cyclones, Chemical Engineering Science 54 (13) (1999) 2055 – 2065. `doi:https://doi.org/10.1016/S0009-2509(98)00373-X`.
URL `http://www.sciencedirect.com/science/article/pii/S000925099800373X`

[4] X. Sun, S. Kim, S. D. Yang, H. S. Kim, J. Y. Yoon, Multi-objective optimization of a stairmand cyclone separator using response surface methodology and computational fluid dynamics, Powder Technology 320 (2017) 51 – 65. `doi:https://doi.org/10.1016/j.powtec.2017.06.065`.
URL `http://www.sciencedirect.com/science/article/pii/S0032591017305338`

[5] M. Narasimha, M. Brennan, P. N. Holtham, A review of cfd modelling for performance predictions of hydrocyclone, Engineering Applications of Computational Fluid Mechanics 1 (2) (2007) 109–125. `arXiv:https://doi.org/10.1080/19942060.2007.11015186`, `doi:10.1080/19942060.2007.11015186`.
URL `https://doi.org/10.1080/19942060.2007.11015186`

[6] C. Cortés, A. Gil, Modelling the gas and particle flow inside cyclone separators, Progress in Energy and Combustion Science 33 (5) (2007) 409 – 452. `doi:http://dx.doi.org/10.1016/j.pecs.2007.02.001`.
URL `http://www.sciencedirect.com/science/article/pii/S036012850700010X`

[7] A.-N. Huang, K. Ito, T. Fukasawa, H. Yoshida, H.-P. Kuo, K. Fukui, Classification performance analysis of a novel cyclone with a slit on the conical part by cfd simulation, Separation and Purification Technology 190 (Supplement C) (2018) 25 – 32. `doi:https://doi.org/10.1016/j.seppur.2017.08.047`.
URL `http://www.sciencedirect.com/science/article/pii/S1383586617310018`

[8] S. K. Shukla, P. Shukla, P. Ghosh, The effect of modelling of velocity fluctuations on prediction of collection efficiency of cyclone separators, Applied Mathematical Modelling 37 (8) (2013) 5774 – 5789. `doi:https://doi.org/10.1016/j.apm.2012.11.019`.
URL `http://www.sciencedirect.com/science/article/pii/S0307904X12007354`

[9] BS EN 1822-1:2009, High efficiency air filters (epa, hepa and ulpa), Tech. rep., European Committee for Standardization, Avenue Marnix 17, B-1000 Brussels (10 2009).

[10] P. Wadhwani, P. Saha, Household vacuum cleaners market size by product (cordless/stick, upright, canister, central, drum, wet/dry, robotic), by sales channel (offline, online), industry analysis report, regional outlook, growth potential, competitive market share & forecast, 2020 – 2026, Tech. rep., Global Market Insights (02 2020).

[11] A. Hoffmann, L. Stein, Gas cyclones and swirl tubes: Principles, design and operation, Springer Berlin Heidelberg, 2008.

[12] P. M. Ireland, Impact tribocharging of soft elastic spheres, Powder Technology 348 (2019) 70 – 79. `doi:https://doi.org/10.1016/j.powtec.2019.03.019`.
URL `http://www.sciencedirect.com/science/article/pii/S003259101930186X`

[13] J. S. Shrimpton, A review of the physics, model methods and computational prediction tools relevant to separation of particles in the range 1 > d > $0.1\mu m$ using cyclone technology, Tech. rep., University of Southampton (11 2015).

[14] S. Naik, R. Mukherjee, B. Chaudhuri, Triboelectrification: A review of experimental and mechanistic modelling approaches with a special focus on pharmaceutical powders, International Journal of Pharmaceutics 510 (1) (2016) 375 – 385. `doi:https://doi.org/10.1016/j.ijpharm.2016.06.031`.
URL `http://www.sciencedirect.com/science/article/pii/S0378517316305075`

[15] G. A. Cottrell, J. Lowell, A. C. Rose-Innes, Charge transfer in metal-polymer contacts and the validity of "contact charge spectroscopy", Journal of Applied Physics 50 (1) (1979) 374–376. `arXiv:https://doi.org/10.1063/1.325673`, `doi:10.1063/1.325673`.
URL `https://doi.org/10.1063/1.325673`

[16] M. G. Rowland, Electrostatic properties of particles for inhalation, Ph.D. thesis, Department of Pharmacy and Pharmacology, University of Bath (2014).

[17] F. Podczeck, Particle-particle Adhesion in Pharmaceutical Powder Handling, 1st Edition, Imperial College Press, 1998.

[18] T. Matsuyama, M. Ogu, H. Yamamoto, J. C. Marijnissen, B. Scarlett, Impact charging experiments with single particles of hundred micrometer size, Powder Technology 135-136 (2003) 14–22. `doi:10.1016/S0032-5910(03)00154-2`.

[19] S. J. Scott, A pdf based method for modelling polysized particle laden turbulent flows without size class discretisation, Ph.D. thesis, Department of Mechanical Engineering, Imperial College London (2006).

[20] J. Ferry, S. Balachandar, A fast eulerian method for disperse two-phase flow, International Journal of Multiphase Flow 27 (7) (2001) 1199 – 1226. `doi:https://doi.org/10.1016/S0301-9322(00)00069-0`.
URL `http://www.sciencedirect.com/science/article/pii/S0301932200000690`

[21] I. G. Currie, Fundamental mechanics of fluids, New York : McGraw-Hill, 1974.
URL `http://search.ebscohost.com/login.aspx?direct=true&db=cat02326a&AN=usl.59628&site=eds-live`

[22] A. Hoekstra, Gas flow field and collection efficiency of cyclone separators, Ph.D. thesis, Delft University of Technology (12 2000).

[23] K. Chu, J. Chen, B. Wang, A. Yu, A. Vince, G. Barnett, P. Barnett, Understand solids loading effects in a dense medium cyclone: Effect of particle size by a cfd-dem method, Powder Technology 320 (2017) 594 – 609. `doi:https://doi.org/10.1016/j.powtec.2017.07.032`.
URL `http://www.sciencedirect.com/science/article/pii/S0032591017305697`

[24] B. Pei, L. Yang, K. Dong, Y. Jiang, X. Du, B. Wang, The effect of cross-shaped vortex finder on the performance of cyclone separator, Powder Technology 313 (2017) 135 – 144. `doi:https://doi.org/10.1016/j.powtec.2017.02.066`.
URL `http://www.sciencedirect.com/science/article/pii/S003259101730205X`

[25] A. Gupta, D. Lilley, N. Syred, Swirl Flows, Abacus Press, 1984.

[26] M. O. Vigueras-Zúñiga, C. A. Ramírez-Ruíz, A. L. Herrera-May, M. E. Tejeda-del Cueto, Numerical and experimental analysis of the effect of a swirler with a high swirl number in a biogas combustor, Energies 14 (10) (2021). `doi:10.3390/en14102768`.
URL `https://www.mdpi.com/1996-1073/14/10/2768`

[27] P. A. Yazdabadi, A. J. Griffiths, N. Syred, Characterization of the pvc phenomena in the exhaust of a cyclone dust separator, Experiments in Fluids 17 (1) (1994) 84–95. `doi:10.1007/BF02412807`.
URL `http://dx.doi.org/10.1007/BF02412807`

[28] W. Peng, A. Hoffmann, H. Dries, M. Regelink, L. Stein, Experimental study of the vortex end in centrifugal separators: The nature of the vortex end, Chemical Engineering Science 60 (24) (2005) 6919 – 6928. `doi:http://dx.doi.org/10.1016/j.ces.2005.06.009`.
URL `http://www.sciencedirect.com/science/article/pii/S0009250905005427`

[29] T. A. Grimble, A. Agarwal, M. P. Juniper, Local linear stability analysis of cyclone separators, Journal of Fluid Mechanics 816 (2017) 507–538. `doi:10.1017/jfm.2017.89`.

[30] S. B. Pope, Turbulent Flows, Cambridge University Press, 2000.

[31] Y. Zhang, P. Cai, F. Jiang, K. Dong, Y. Jiang, B. Wang, Understanding the separation of particles in a hydrocyclone by force analysis, Powder Technology (2017) –`doi:https://doi.org/10.1016/j.powtec.2017.09.031`.
URL `http://www.sciencedirect.com/science/article/pii/S0032591017307623`

[32] J. H. Ferziger, M. Periĉ, Computational Methods for Fluid Dynamics, Springer-Verlag Berlin Heidelberg New York, 2002.

[33] F. Boysan, W. Ayers, J. Swithenbank, A fundamental mathematical modelling approach to cyclone design, TRANS INST CHEM ENG 60 (1982) 222–230.

[34] M. Wasilewski, L. S. Brar, Effect of the inlet duct angle on the performance of cyclone separators, Separation and Purification Technology 213 (2019) 19 – 33. `doi:https://doi.org/10.1016/j.seppur.2018.12.023`.
URL `http://www.sciencedirect.com/science/article/pii/S1383586618333549`

[35] K. Chu, B. Wang, D. Xu, Y. Chen, A. Yu, Cfd–dem simulation of the gas–solid flow in a cyclone separator, Chemical Engineering Science 66 (5) (2011) 834 – 847. `doi:https://doi.org/10.1016/j.ces.2010.11.026`.
URL `http://www.sciencedirect.com/science/article/pii/S0009250910006883`

[36] K. Elsayed, C. Lacor, The effect of cyclone inlet dimensions on the flow pattern and performance, Applied Mathematical Modelling 35 (4) (2011) 1952 – 1968. `doi:https://doi.org/10.1016/j.apm.2010.11.007`.
URL `http://www.sciencedirect.com/science/article/pii/S0307904X10004178`

[37] J. S. Shrimpton, An Introduction to Engineering Thermofluids, 1st Edition, Pnume Publishing, 2013.

[38] J. Floryan, On the görtler instability of boundary layers, Progress in Aerospace Sciences 28 (3) (1991) 235 – 271. `doi:https://doi.org/10.1016/0376-0421(91)90006-P`.
URL `http://www.sciencedirect.com/science/article/pii/037604219190006P`

[39] A. Ducoin, M. Shadloo, S. Roy, Direct numerical simulation of flow instabilities over savonius style wind turbine blades, Renewable Energy 105 (Supplement C) (2017) 374 – 385. `doi:https://doi.org/10.1016/j.renene.2016.12.072`.
URL `http://www.sciencedirect.com/science/article/pii/S0960148116311326`

[40] S. Winoto, H. Mitsudharmadi, D. Shah, Visualizing görtler vortices, Journal of Visualization 8 (2005) 315–322. `doi:10.1007/BF03181550`.

[41] J. D. Anderson, Fundamentals of aerodynamics, 5th Edition, McGraw Hill, 2011.

[42] M. R. Maxey, J. J. Riley, Equation of motion for a small rigid sphere in a nonuniform flow, The Physics of Fluids 26 (4) (1983) 883–889. `arXiv:https://aip.scitation.org/doi/pdf/10.1063/1.864230`, `doi:10.1063/1.864230`.
URL `https://aip.scitation.org/doi/abs/10.1063/1.864230`

[43] L. B. Esteban, Dynamics of Non-Spherical Particles in Turbulence, Springer, Cham, 2020. `doi:https://doi.org/10.1007/978-3-030-28136-6`.

[44] M. R. Maxey, the gravitational settling of aerosol particles in homogeneous turbulence and random flow fields, Journal of Fluid Mechanics 174 (1987) 441–465. `doi:10.1017/50022112087000193`.

[45] S. K. Friedlander, Smoke, Dust, and Haze, 2nd Edition, Oxford University Press, 2000.

[46] C. T. Crowe, Multiphase Flow Handbook, CRC Press, 2006.

[47] T. I. Gombosi, Gaskinetic theory, Cambridge University Press, 1994.

[48] C. N. Davies, Definitive equations for the fluid resistance of spheres, Proceedings of the Physical Society 57 (4) (1945) 259–270. `doi:10.1088/0959-5309/57/4/301`.
URL `https://doi.org/10.1088%2F0959-5309%2F57%2F4%2F301`

[49] E. Cunningham, On the velocity of steady fall of spherical particles through fluid medium, Proc. R. Soc, Lond A 83 (1910) 357 – 365. `doi:https://doi.org/10.1098/rspa.1910.0024`.

[50] S. Jennings, The mean free path in air, Journal of Aerosol Science 19 (2) (1988) 159 – 166. `doi:https://doi.org/10.1016/0021-8502(88)90219-4`.
URL `http://www.sciencedirect.com/science/article/pii/0021850288902194`

[51] S. Balachandar, J. K. Eaton, Turbulent dispersed multiphase flow, Annual Review of Fluid Mechanics 42 (1) (2010) 111–133. `arXiv:https://doi.org/10.1146/annurev.fluid.010908.165243`, `doi:10.1146/annurev.fluid.010908.165243`.
URL `https://doi.org/10.1146/annurev.fluid.010908.165243`

[52] S. Elghobashi, On predicting particle-laden turbulent flows, Applied Scientific Research 52 (1994) 309 – 329. `doi:https://doi.org/10.1007/BF00936835`.

[53] L. I. Zaichik, V. M. Alipchenkov, Pair dispersion and preferential concentration of particles in isotropic turbulence, Physics of Fluids 15 (6) (2003) 1776–1787. `arXiv:https://aip.scitation.org/doi/pdf/10.1063/1.1569485`, `doi:10.1063/1.1569485`.
URL `https://aip.scitation.org/doi/abs/10.1063/1.1569485`

[54] A. Einstein, Investigations on the theory of the brownian movement, Ann. der Physik (1905).
URL `http://www.physik.fu-berlin.de/~{}kleinert/files/eins_brownian.pdf`

[55] N. Fuchs, The mechanics of aerosols, by N. A. Fuchs. Translated from the Russian by R. E. Daisley and Marina Fuchs. Translation edited by C. N. Davies., Pergamon Press: Oxford, 1964.

[56] G. K. Batchelor, Brownian diffusion of particles with hydrodynamic interaction, Journal of Fluid Mechanics 74 (1) (1976) 1–29. `doi:10.1017/S0022112076001663`.

[57] P. G. Saffman, J. S. Turner, On the collision of drops in turbulent clouds, Journal of Fluid Mechanics 1 (1) (1956) 16–30. `doi:10.1017/S0022112056000020`.

[58] P. S. H. Henry, Survey of generation and dissipation of static electricity, British Journal of Applied Physics 4 (S2) (1953) S6.
URL `http://stacks.iop.org/0508-3443/4/i=S2/a=302`

[59] W. R. Harper, Contact and frictional electrification, Oxford University Press, 1967.

[60] Z. Gu, W. Wei, Electrification of Particulates in Industrial and Natural Multiphase Flows, 1st Edition, Springer Nature, 2017.

[61] J. M. Crowley, Fundamentals of Applied Electrostatics, Laplacian Press, 1999.

[62] J. C. Wilcke, Disputatio physica experimentalis, de electricitatibus contrariis, Thesis, University of Rostock (1757).

[63] L. McCarty, G. Whitesides, Electrostatic charging due to separation of ions at interfaces: Contact electrification of ionic electrets, Angewandte Chemie International Edition 47 (12) (2008) 2188–2207. `doi:10.1002/anie.200701812`.
URL `http://dx.doi.org/10.1002/anie.200701812`

[64] W. R. Harper, The volta effect as a cause of static electrification, Proceedings of the Royal Society of London A: Mathematical, Physical and Engineering Sciences 205 (1080) (1951) 83–103. `doi:10.1098/rspa.1951.0019`.
URL `http://rspa.royalsocietypublishing.org/content/205/1080/83`

[65] C. Kittel, Introduction to Solid State Physics, 7th Edition, Wiley India Pvt. Limited, 2007.

[66] J.-S. Chang, A. J. Kelly, J. M. Crowley, Handbook of Electrostatic Processes, Marcel Dekker, Inc., 1995.

[67] M. Springford, Electron : a centenary volume, Cambridge ; New York : Cambridge University Press, 1997.

[68] BIPM, Le Système international d'unités / The International System of Units ('The SI Brochure'), ninth Edition, Bureau international des poids et mesures, 2019.
URL `http://www.bipm.org/en/si/si_brochure/`

[69] E. Fukada, J. F. Fowler, Triboelectricity and electron traps in insulating materials: Some correlations, Nature 181 (1958) 693–694. `doi:10.1038/181693b0`.

[70] A. Einstein, Über einen die erzeugung und verwandlung des lichtes betreffenden heuristischen gesichtspunkt, Annalen der Physik 322 (6) (1905) 132–148. `arXiv:https://onlinelibrary.wiley.com/doi/pdf/10.1002/andp.19053220607`, `doi:10.1002/andp.19053220607`.
URL `https://onlinelibrary.wiley.com/doi/abs/10.1002/andp.19053220607`

[71] M. L. Burns, Modern Physics for Science and Engineering, 1st Edition, Physics Curriculum & Instructtion Inc., 2012.

[72] S. G. Bogodage, A. Y. Leung, Cfd simulation of cyclone separators to reduce air pollution, Powder Technology 286 (2015) 488 – 506. `doi:https://doi.org/10.1016/j.powtec.2015.08.023`.
URL `http://www.sciencedirect.com/science/article/pii/S0032591015300231`

[73] O. L. Sgrott, D. Noriler, V. R. Wiggers, H. F. Meier, Cyclone optimization by complex method and cfd simulation, Powder Technology 277 (2015) 11–21. `doi:https://doi.org/10.1016/j.powtec.2015.02.039`.
URL `https://www.sciencedirect.com/science/article/pii/S0032591015001606`

[74] C. Haig, A. Hursthouse, S. McIlwain, D. Sykes, The effect of particle agglomeration and attrition on the separation efficiency of a stairmand cyclone, Powder Technology 258 (2014) 110 – 124. `doi:https://doi.org/10.1016/j.powtec.2014.03.008`.
URL `http://www.sciencedirect.com/science/article/pii/S0032591014002083`

[75] Z. Liu, Y. Zheng, L. Jia, J. Jiao, Q. Zhang, Stereoscopic piv studies on the swirling flow structure in a gas cyclone, Chemical Engineering Science 61 (13) (2006) 4252–4261, the John Bridgwater Symposium: “Shaping the Future of Chemical Engineering”. `doi:https://doi.org/10.1016/j.ces.2006.01.024`.
URL `https://www.sciencedirect.com/science/article/pii/S0009250906000601`

[76] M. Raffel, C. E. Willert, S. T. Wereley, J. Kompenhans, Particle Image Velocimetry, 2nd Edition, Springer-Verlag Berlin Heidelberg, 2007.

[77] W. Barth, Berechnung und auslegung von zyklonabscheidern auf grund neuerer untersuchungen, bund der ingenieure für wasserwirtschaft, Abfallwirtschaft und Kulkurbau 8 (1956) 1–9.

[78] S. Altmeyer, V. Mathieu, S. Jullemier, P. Contal, N. Midoux, S. Rode, J.-P. Leclerc, Comparison of different models of cyclone prediction performance for various operating conditions using a general software, Chemical Engineering and Processing: Process Intensification 43 (4) (2004) 511–522. `doi:https://doi.org/10.1016/S0255-2701(03)00079-5`.
URL `https://www.sciencedirect.com/science/article/pii/S0255270103000795`

[79] J. Dirgo, D. Leith, Cyclone collection efficiency: Comparison of experimental results with theoretical predictions, Aerosol Science and Technology 4 (4) (1985) 401–415. `arXiv:https://doi.org/10.1080/02786828508959066`, `doi:10.1080/02786828508959066`.
URL `https://doi.org/10.1080/02786828508959066`

[80] K. Chu, J. Chen, A. Yu, Applicability of a coarse-grained cfd–dem model on dense medium cyclone, Minerals Engineering 90 (2016) 43 – 54, computational Modelling. `doi:https://doi.org/10.1016/j.mineng.2016.01.020`.
URL `http://www.sciencedirect.com/science/article/pii/S0892687516300188`

[81] J. Gimbun, T. Chuah, T. S. Choong, A. Fakhru’l-Razi, Prediction of the effects of cone tip diameter on the cyclone performance, Journal of Aerosol Science 36 (8) (2005) 1056 – 1065. `doi:https://doi.org/10.1016/j.jaerosci.2004.10.014`.
URL `http://www.sciencedirect.com/science/article/pii/S0021850204003842`

[82] F. Parvaz, S. H. Hosseini, K. Elsayed, G. Ahmadi, Numerical investigation of effects of inner cone on flow field, performance and erosion rate of cyclone separators, Separation and Purification Technology 201 (2018) 223 – 237. `doi:https://doi.org/10.1016/j.seppur.2018.03.001`.
URL `http://www.sciencedirect.com/science/article/pii/S1383586617335591`

[83] D. Winfield, M. Cross, N. Croft, D. Paddison, I. Craig, Performance comparison of a single and triple tangential inlet gas separation cyclone: A cfd study, Powder Technology 235 (2013) 520–531. `doi:https://doi.org/10.1016/j.powtec.2012.10.026`.
URL `https://www.sciencedirect.com/science/article/pii/S0032591012007036`

[84] Q. Wei, G. Sun, C. Gao, Numerical analysis of axial gas flow in cyclone separators with different vortex finder diameters and inlet dimensions, Powder Technology 369 (2020) 321–333. `doi:https://doi.org/10.1016/j.powtec.2020.05.038`.
URL `https://www.sciencedirect.com/science/article/pii/S0032591020304010`

[85] F. J. de Souza, R. de Vasconcelos Salvo, D. A. de Moro Martins, Large eddy simulation of the gas–particle flow in cyclone separators, Separation and Purification Technology 94 (2012) 61 – 70, cO2 Capture and Storage. `doi:https://doi.org/10.1016/j.seppur.2012.04.006`.
URL `http://www.sciencedirect.com/science/article/pii/S1383586612002171`

[86] H. Shalaby, K. Wozniak, G. Wozniak, Numerical calculation of particle-laden cyclone separator flow using les, Engineering Applications of Computational Fluid Mechanics 2 (4) (2008) 382–392. `arXiv:http://dx.doi.org/10.1080/19942060.2008.11015238`, `doi:10.1080/19942060.2008.11015238`.
URL `http://dx.doi.org/10.1080/19942060.2008.11015238`

[87] J. J. Derksen, Separation performance predictions of a stairmand high-efficiency cyclone, AIChE Journal 49 (6) (2003) 1359–1371. `arXiv:https://aiche.onlinelibrary.wiley.com/doi/pdf/10.1002/aic.690490603`, `doi:https://doi.org/10.1002/aic.690490603`.
URL `https://aiche.onlinelibrary.wiley.com/doi/abs/10.1002/aic.690490603`

[88] D. Misiulia, G. Lidén, S. Antonyuk, Evolution of turbulent swirling flow in a small-scale cyclone with increasing flow rate: A les study, Flow, Turbulence and Combustion 107 (2021) 575–608. `doi:10.1007/s10494-021-00253-2`.
URL `https://doi.org/10.1007/s10494-021-00253-2`

[89] H. Safikhani, P. Mehrabian, Numerical study of flow field in new cyclone separators, Advanced Powder Technology 27 (2) (2016) 379–387. `doi:https://doi.org/10.1016/j.apt.2016.01.011`.
URL `https://www.sciencedirect.com/science/article/pii/S0921883116000133`

[90] G. Zhu, J.-L. Liow, A. Neely, Computational study of flow in a micro-sized hydrocyclone, 17th Australasian Fluid Mechanics Conference, Auckland, New Zealand (2010) 1 – 4.

[91] G. Zhu, J.-L. Liow, A. Neely, Computational study of the flow characteristics and separation efficiency in a mini-hydrocyclone, Chemical Engineering Research and Design 90 (12) (2012) 2135 – 2147. `doi:https://doi.org/10.1016/j.cherd.2012.05.020`.
URL `http://www.sciencedirect.com/science/article/pii/S0263876212002432`

[92] Q.-C. Wang, Z.-G. Wang, M.-B. Sun, R. Yang, Y.-X. Zhao, Z. Hu, The amplification of large-scale motion in a supersonic concave turbulent boundary layer and its impact on the mean and statistical properties, Journal of Fluid Mechanics 863 (2019) 454–493. `doi:10.1017/jfm.2018.1004`.

[93] M. Sun, N. D. Sandham, Z. Hu, Turbulence structures and statistics of a supersonic turbulent boundary layer subjected to concave surface curvature, Journal of Fluid Mechanics 865 (2019) 60–99. `doi:10.1017/jfm.2019.19`.

[94] S. Schmidt, H. M Blackburn, M. Rudman, Impact of outlet boundary conditions on the flow properties within a cyclone, 5th Australasian Fluid Mechanics Conference (12 2004).

[95] D. Misiulia, S. Antonyuk, A. G. Andersson, T. S. Lundström, Effects of deswirler position and its centre body shape as well as vortex finder extension downstream on cyclone performance, Powder Technology 336 (2018) 45 – 56. `doi:https://doi.org/10.1016/j.powtec.2018.05.034`.
URL `http://www.sciencedirect.com/science/article/pii/S0032591018303991`

[96] L. S. Brar, K. Elsayed, Analysis and optimization of cyclone separators with eccentric vortex finders using large eddy simulation and artificial neural network, Separation and Purification Technology 207 (2018) 269–283. `doi:https://doi.org/10.1016/j.seppur.2018.06.013`.
URL `https://www.sciencedirect.com/science/article/pii/S1383586618302934`

[97] R. Shastri, L. Singh Brar, K. Elsayed, Multi-objective optimization of cyclone separators using mathematical modelling and large-eddy simulation for a fixed total height condition, Separation and Purification Technology 291 (2022) 120968. `doi:https://doi.org/10.1016/j.seppur.2022.120968`.
URL `https://www.sciencedirect.com/science/article/pii/S1383586622005251`

[98] Z.-W. Gao, Z.-X. Liu, Y.-D. Wei, C.-X. Li, S.-H. Wang, X.-Y. Qi, W. Huang, Numerical analysis on the influence of vortex motion in a reverse stairmand cyclone separator by using les model, Petroleum Science (2021). `doi:https://doi.org/10.1016/j.petsci.2021.11.009`.
URL `https://www.sciencedirect.com/science/article/pii/S1995822621001436`

[99] S. Pandey, L. S. Brar, Large-eddy simulations of cyclone separator based on the lattice-boltzmann method, AIP Conference Proceedings 2341 (1) (2021) 030020. `arXiv:https://aip.scitation.org/doi/pdf/10.1063/5.0050107`, `doi:10.1063/5.0050107`.
URL `https://aip.scitation.org/doi/abs/10.1063/5.0050107`

[100] O. R. Nassaj, D. Toghraie, M. Afrand, Effects of multi inlet guide channels on the performance of a cyclone separator, Powder Technology 356 (2019) 353–372. `doi:https://doi.org/10.1016/j.powtec.2019.08.038`.
URL `https://www.sciencedirect.com/science/article/pii/S0032591019306382`

[101] D. Powell, Evaluation of particle models for small, high-speed cyclones, Master's thesis, Faculty of Engineering and the Environment, University of Southampton (2017).

[102] P. G. Saffman, The lift on a small sphere in a slow shear flow, Journal of Fluid Mechanics 22 (2) (1965) 385–400. `doi:10.1017/S0022112065000824`.

[103] I. Akhatov, J. Hoey, O. Swenson, D. Schulz, Aerosol focusing in micro-capillaries: Theory and experiment, Journal of Aerosol Science 39 (8) (2008) 691–709. `doi:https://doi.org/10.1016/j.jaerosci.2008.04.004`.
URL `https://www.sciencedirect.com/science/article/pii/S0021850208000773`

[104] I. Akhatov, J. Hoey, O. Swenson, D. Schulz, Aerosol flow through a long micro-capillary: Collimated aerosol beam, Microfluidics and Nanofluidics 5 (2007) 215–224. `doi:10.1007/s10404-007-0239-3`.

[105] A. Li, G. Ahmadi, Dispersion and deposition of spherical particles from point sources in a turbulent channel flow, Aerosol Science and Technology 16 (4) (1992) 209–226. `arXiv:https://doi.org/10.1080/02786829208959550`, `doi:10.1080/02786829208959550`.
URL `https://doi.org/10.1080/02786829208959550`

[106] L. Xiaodong, Y. Jianhua, C. Yuchun, N. Mingjiang, C. Kefa, Numerical simulation of the effects of turbulence intensity and boundary layer on separation efficiency in a cyclone separator, Chemical Engineering Journal 95 (1) (2003) 235 – 240. `doi:https://doi.org/10.1016/S1385-8947(03)00109-8`.
URL `http://www.sciencedirect.com/science/article/pii/S1385894703001098`

[107] T. Wittemeier, J. S. Shrimpton, Explanation of differences in experimental and computational results for the preferential concentration of inertial particles, Computers & Fluids 173 (2018) 37–41. `doi:https://doi.org/10.1016/j.compfluid.2018.03.078`.
URL `https://www.sciencedirect.com/science/article/pii/S0045793018301828`

[108] J. Eaton, J. Fessler, Preferential concentration of particles by turbulence, International Journal of Multiphase Flow 20 (1994) 169–209. `doi:https://doi.org/10.1016/0301-9322(94)90072-8`.
URL `https://www.sciencedirect.com/science/article/pii/0301932294900728`

[109] K. D. Squires, J. K. Eaton, Preferential concentration of particles by turbulence, Physics of Fluids A: Fluid Dynamics 3 (5) (1991) 1169–1178. `arXiv:https://doi.org/10.1063/1.858045`, `doi:10.1063/1.858045`.
URL `https://doi.org/10.1063/1.858045`

[110] S. J. Scott, A. Karnik, J. Shrimpton, On the quantification of preferential accumulation, International Journal of Heat and Fluid Flow 30 (2009) 789–795. `doi:10.1016/j.ijheatfluidflow.2009.02.002`.

[111] M. Caporaloni, F. Tampieri, F. Trombetti, O. Vittori, Transfer of particles in nonisotropic air turbulence, Journal of Atmospheric Sciences 32 (1975) 565–568. `doi:https://doi.org/10.1175/1520-0469(1975)032<0565:TOPINA>2.0.CO;2`.

[112] J. YOUNG, A. LEEMING, A theory of particle deposition in turbulent pipe flow, Journal of Fluid Mechanics 340 (1997) 129–159. `doi:10.1017/S0022112097005284`.

[113] J. Bec, H. Homann, S. S. Ray, Gravity-driven enhancement of heavy particle clustering in turbulent flow, Physical Review Letters 112 (18) (May 2014). `doi:10.1103/physrevlett.112.184501`.
URL `http://dx.doi.org/10.1103/PhysRevLett.112.184501`

[114] M. Wasilewski, L. S. Brar, Optimization of the geometry of cyclone separators used in clinker burning process: A case study, Powder Technology 313 (2017) 293–302. `doi:https://doi.org/10.1016/j.powtec.2017.03.025`.
URL `https://www.sciencedirect.com/science/article/pii/S0032591017302310`

[115] J. Wei, H. Zhang, Y. Wang, Z. Wen, B. Yao, J. Dong, The gas-solid flow characteristics of cyclones, Powder Technology 308 (2017) 178–192. `doi:https://doi.org/10.1016/j.powtec.2016.11.044`.
URL `https://www.sciencedirect.com/science/article/pii/S0032591016308361`

[116] S.-Y. Noh, J.-E. Heo, S.-H. Woo, S.-J. Kim, M.-H. Ock, Y.-J. Kim, S.-J. Yook, Performance improvement of a cyclone separator using multiple subsidiary cyclones, Powder Technology 338 (2018) 145 – 152. `doi:https://doi.org/10.1016/j.powtec.2018.07.015`.
URL `http://www.sciencedirect.com/science/article/pii/S0032591018305072`

[117] E. W. Cheney, D. R. Kincaid, Numerical Mathematics and Computing, 6th Edition, Brooks/Cole Publishing Co., USA, 2007.

[118] W. B. Kunkel, The static electrification of dust particles on dispersion into a cloud, Journal of Applied Physics 21 (8) (1950) 820–832. `doi:10.1063/1.1699765`.

[119] D. K. Davies, Charge generation on dielectric surfaces, Journal of Physics D: Applied Physics 2 (11) (1969) 1533.
URL `http://stacks.iop.org/0022-3727/2/i=11/a=307`

[120] J. Lowell, Contact electrification of metals, Journal of Physics D: Applied Physics 8 (1) (1975) 53.
URL `http://stacks.iop.org/0022-3727/8/i=1/a=013`

[121] J. Lowell, The electrification of polymers by metals, Journal of Physics D: Applied Physics 9 (11) (1976) 1571.
URL `http://stacks.iop.org/0022-3727/9/i=11/a=006`

[122] J. Lowell, The role of material transfer in contact electrification, Journal of Physics D: Applied Physics 10 (17) (1977) L233.
URL `http://stacks.iop.org/0022-3727/10/i=17/a=001`

[123] T. Matsuyama, H. Yamamoto, Charge transfer between a single polymer particle and metal plate by impact, J. Soc. Powder Technology, Japan 24 (1987) 765–770.

[124] T. Matsuyama, H. Yamamoto, Characterizing the electrostatic charging of polymer particles by impact charging experiments, Advanced Powder Technology 6 (1995) 211–220. `doi:10.1016/S0921-8831(08)60529-4`.

[125] H. Watanabe, M. Ghadiri, T. Matsuyama, Y. L. Ding, K. G. Pitt, H. Maruyama, S. Matsusaka, H. Masuda, Triboelectrification of pharmaceutical powders by particle impact, International Journal of Pharmaceutics 334 (2007) 149–155. `doi:10.1016/j.ijpharm.2006.11.005`.

[126] E. Šupuk, C. Seiler, M. Ghadiri, Analysis of a simple test device for tribo-electric charging of bulk powders, Particle & Particle Systems Characterization 26 (1-2) (2009) 7–16. `doi:10.1002/ppsc.200800015`.
URL `http://dx.doi.org/10.1002/ppsc.200800015`

[127] J. Wu, H. T. Bi, Addition of fines for the reduction of powder charging in particle mixers, Advanced Powder Technology 22 (3) (2011) 332 – 335. `doi:https://doi.org/10.1016/j.apt.2010.04.009`.
URL `http://www.sciencedirect.com/science/article/pii/S0921883110000762`

[128] A. Schella, S. Herminghaus, M. Schroter, Influence of humidity on tribo-electric charging and segregation in shaken granular media, Soft Matter 13 (2017) 394–401. `doi:10.1039/C6SM02041K`.
URL `http://dx.doi.org/10.1039/C6SM02041K`

[129] S. Alois, J. Merrison, J. J. Iversen, J. Sesterhenn, Quantifying the contact electrification of aerosolized insulating particles, Powder Technology 332 (2018) 106 – 113. `doi:https://doi.org/10.1016/j.powtec.2018.03.059`.
URL `http://www.sciencedirect.com/science/article/pii/S0032591018302523`

[130] G. W. Israel, S. Friedlander, High-speed beams of small particles, Journal of Colloid and Interface Science 24 (3) (1967) 330 – 337. `doi:https://doi.org/10.1016/0021-9797(67)90258-5`.
URL `http://www.sciencedirect.com/science/article/pii/0021979767902585`

[131] I. Currie, Fundamental Mechanics of Fluids, Third Edition, Dekker Mechanical Engineering, Taylor & Francis, 2002.

[132] B. Dahneke, S. Friedlander, Velocity characteristics of beams of spherical polystyrene particles, Journal of Aerosol Science 1 (4) (1970) 325 – 339. `doi:https://doi.org/10.1016/0021-8502(70)90006-6`.
URL `http://www.sciencedirect.com/science/article/pii/0021850270900066`

[133] S. A. Schaaf, P. L. Chambre, Flow of Rarefied Gases, Princeton University Press, 1958.
URL `http://www.jstor.org/stable/j.ctt1m32248`

[134] D. Zwillinger, S. Kokoska, CRC Standard Probability and Statistics Tables and Formulae, Chapman & Hall/CRC, 2000.

[135] B. Bhushan, Modern Tribology Handbook, The mechanics and materials science series, CRC Press, 2001.
URL `https://books.google.co.uk/books?id=io9UAAAAMAAJ`

[136] H. Hertz, Uber die berührung fester elastischer körper. (on the contact of elastic solids), J. reine und an-gewandte Mathematik 92 (1882) 156–171.

[137] J. Kolehmainen, A. Ozel, S. Sundaresan, Eulerian modelling of gas–solid flows with triboelectric charging, Journal of Fluid Mechanics 848 (2018) 340–369. `doi:10.1017/jfm.2018.361`.

[138] S. Timoshenko, J. Goodier, Theory of Elasticity, 2nd Edition, Mcgraw-Hill Book Company Inc, 1951.

[139] S. Matsusaka, M. Ghadiri, H. Masuda, Electrification of an elastic sphere by repeated impacts on a metal plate, Journal of Physics D: Applied Physics 33 (18) (2000) 2311.
URL `http://stacks.iop.org/0022-3727/33/i=18/a=316`

[140] M. Perkins, S. J. Ebbens, S. Hayes, C. J. Roberts, C. E. Madden, S. Y. Luk, N. Patel, Elastic modulus measurements from individual lactose particles using atomic force microscopy, International Journal of Pharmaceutics 332 (1) (2007) 168–175. `doi:https://doi.org/10.1016/j.ijpharm.2006.09.032`.
URL `https://www.sciencedirect.com/science/article/pii/S037851730600785X`

[141] S. K. Ahuja, A collision model of charge exchange between metal and polymer spheres, Journal of Physics D: Applied Physics 9 (9) (1976) 1305.
URL `http://stacks.iop.org/0022-3727/9/i=9/a=007`

[142] T. Matsusyama, H. Yamamoto, Impact charging of particulate materials, Chemical Engineering Science 61 (2006) 2230–2238. `doi:10.1016/j.ces.2005.05.003`.

[143] T. Matsuyama, H. Yamamoto, Charge relaxation process dominates contact charging of a particle in atmospheric conditions, Journal of Physics D: Applied Physics 28 (12) (1995) 2418.
URL `http://stacks.iop.org/0022-3727/28/i=12/a=005`

[144] P. M. Ireland, Some comments on contact charge relaxation, Applied Physics Letters 91 (9) (2007) 091501. `arXiv:https://doi.org/10.1063/1.2776021`, `doi:10.1063/1.2776021`.
URL `https://doi.org/10.1063/1.2776021`

[145] P. M. Ireland, The role of changing contact in sliding triboelectrification, Journal of Physics D: Applied Physics 41 (2) (2008) 025305.
URL `http://stacks.iop.org/0022-3727/41/i=2/a=025305`

[146] P. M. Ireland, Contact charge accumulation and separation discharge, Journal of Electrostatics 67 (2) (2009) 462 – 467, 11th International Conference on Electrostatics. `doi:https://doi.org/10.1016/j.elstat.2009.01.014`.
URL `http://www.sciencedirect.com/science/article/pii/S0304388609000503`

[147] P. M. Ireland, Triboelectrification of particulate flows on surfaces: Part i — experiments, Powder Technology 198 (2) (2010) 189 – 198. `doi:https://doi.org/10.1016/j.powtec.2009.11.017`.
URL `http://www.sciencedirect.com/science/article/pii/S0032591009006172`

[148] P. M. Ireland, Triboelectrification of particulate flows on surfaces: Part ii — mechanisms and models, Powder Technology 198 (2010) 199–210. `doi:10.1016/j.powtec.2009.11.008`.

[149] ChemBK, alpha-lactose monohydrate, [Online; accessed 15/06/21] (2015).
URL `https://www.chembk.com/en/chem/alpha-Lactose%20monohydrate`

[150] J. Laurentie, P. Traoré, L. Dascalescu, Discrete element modelling of triboelectric charging of insulating materials in vibrated granular beds, Journal of Electrostatics 71 (6) (2013) 951 – 957. `doi:https://doi.org/10.1016/j.elstat.2013.08.001`.
URL `http://www.sciencedirect.com/science/article/pii/S0304388613001034`

[151] F. A. Williams, Spray combustion and atomization, The Physics of Fluids 1 (6) (1958) 541–545. `arXiv:https://aip.scitation.org/doi/pdf/10.1063/1.1724379`, `doi:10.1063/1.1724379`.
URL `https://aip.scitation.org/doi/abs/10.1063/1.1724379`

[152] O. Simonin, Second-moment prediction of dispersed phase turbulence in particle-laden flows, in: 8th Symposium on Turbulent Shear Flows, Volume 1, Vol. 1, 1991, pp. 741 – 746.

[153] E. Deutsch, O. Simonin, Large eddy simulation applied to the modelling of particulate transport coefficients in turbulent two-phase flows, Proc. 8th Symp. Turbulent Shear Flows 1 (1991) 10–1.

[154] O. Druzhinin, S. Elghobashi, Direct numerical simulations of bubble-laden turbulent flows using two-fluid formulation, Physics of Fluids 10 (1998) 685–697. `doi:10.1063/1.869594`.

[155] M. Icardi, D. Marchisio, C. Narayanan, R. Fox, Equilibrium-eulerian les model for turbulent poly-dispersed particle-laden flow, International Journal of Nonlinear Sciences and Numerical Simulation 14 (2013) 139–158. `doi:10.1515/ijnsns-2012-0086`.

[156] L. Mazzei, D. L. Marchisio, P. Lettieri, Direct quadrature method of moments for the mixing of inert polydisperse fluidized powders and the role of numerical diffusion, Industrial & Engineering Chemistry Research 49 (11) (2010) 5141–5152. `arXiv:https://doi.org/10.1021/ie901116y`, `doi:10.1021/ie901116y`.
URL `https://doi.org/10.1021/ie901116y`

[157] S. Chapman, T. Cowling, D. Burnett, C. Cercignani, The Mathematical Theory of Non-uniform Gases: An Account of the Kinetic Theory of Viscosity, Thermal Conduction and Diffusion in Gases, 3rd Edition, Cambridge Mathematical Library, Cambridge University Press, 1990.
URL `https://books.google.co.uk/books?id=y2Yyy798WzIC`

[158] D. Gidaspow, Multiphase flow and fluidization: Continuum and kinetic theory descriptions, Academic Press, New York, 1994.

[159] J. Ding, D. Gidaspow, A bubbling fluidization model using kinetic theory of granular flow, AIChE Journal 36 (4) (1990) 523–538. `arXiv:https://aiche.onlinelibrary.wiley.com/doi/pdf/10.1002/aic.690360404`, `doi:https://doi.org/10.1002/aic.690360404`.
URL `https://aiche.onlinelibrary.wiley.com/doi/abs/10.1002/aic.690360404`

[160] M. Loomans, W. van Houdt, A. Lemaire, J. Hensen, Performance assessment of an operating theatre design using cfd simulation and tracer gas measurements, Indoor and Built Environment 17 (4) (2008) 299–312. `arXiv:https://doi.org/10.1177/1420326X08094948`, `doi:10.1177/1420326X08094948`.
URL `https://doi.org/10.1177/1420326X08094948`

[161] C. Beauchêne, N. Laudinet, F. Choukri, J.-L. Rousset, S. Benhamadouche, J. Larbre, M. Chaouat, M. Benbunan, M. Mimoun, J.-P. Lajonchère, V. Bergeron, F. Derouin, Accumulation and transport of microbial-size particles in a pressure protected model burn unit: Cfd simulations and experimental evidence, BMC infectious diseases 11 (2011) 58. `doi:10.1186/1471-2334-11-58`.

[162] M. Manninen, V. Taivassalo, S. Kallio, On the mixture model for multiphase flow, in: VTT Publications, Vol. 288, 1996, p. 67.

[163] V. A. Aketi, T. Vakamalla, M. Narasimha, G. Sreedhar, R. Shivakumar, RajanKumar, Computational fluid dynamic study on the effect of near gravity material on dense medium cyclone treating coal using discrete phase model and algebraic slip mixture multiphase model, The Journal of Computational Multiphase Flows 9 (2) (2017) 58–70. `arXiv:https://doi.org/10.1177/1757482X16677755`, `doi:10.1177/1757482X16677755`.
URL `https://doi.org/10.1177/1757482X16677755`

[164] S. Grady, G. Wesson, M. Abdullah, E. Kalu, Prediction of 10-mm hydrocyclone separation efficiency using computational fluid dynamics, Filtration & Separation 40 (9) (2003) 41–46. `doi:https://doi.org/10.1016/S0015-1882(03)00930-3`.
URL `https://www.sciencedirect.com/science/article/pii/S0015188203009303`

[165] J. Ferry, S. Balachandar, Equilibrium expansion for the eulerian velocity of small particles, Powder Technology 125 (2) (2002) 131 – 139, the fourth international conference on multiphase Flow. `doi:https://doi.org/10.1016/S0032-5910(01)00499-5`.
URL `http://www.sciencedirect.com/science/article/pii/S0032591001004995`

[166] J. Ferry, S. L. Rani, S. Balachandar, A locally implicit improvement of the equilibrium eulerian method, International Journal of Multiphase Flow 29 (6) (2003) 869 – 891. `doi:https://doi.org/10.1016/S0301-9322(03)00064-8`.
URL `http://www.sciencedirect.com/science/article/pii/S0301932203000648`

[167] S. L. Rani, S. Balachandar, Evaluation of the equilibrium eulerian approach for the evolution of particle concentration in isotropic turbulence, International Journal of Multiphase Flow 29 (12) (2003) 1793 – 1816. `doi:https://doi.org/10.1016/j.ijmultiphaseflow.2003.09.005`.
URL `http://www.sciencedirect.com/science/article/pii/S0301932203001721`

[168] B. Shotorban, S. Balachandar, A eulerian model for large-eddy simulation of concentration of particles with small stokes numbers, Physics of Fluids 19 (11 2007). `doi:10.1063/1.2804956`.

[169] S. Stolz, N. A. Adams, L. Kleiser, An approximate deconvolution model for large-eddy simulation with application to incompressible wall-bounded flows, Physics of Fluids 13 (4) (2001) 997–1015. `arXiv:https://doi.org/10.1063/1.1350896`, `doi:10.1063/1.1350896`.
URL `https://doi.org/10.1063/1.1350896`

[170] S. Badawy, Laboratory freezing desalination of seawater, Desalination and water treatment 57 (2015) 11040–11047. `doi:10.1080/19443994.2015.1041163`.

[171] W. H. Finlay, The Mechanics of Inhaled Pharmaceutical Aerosols, 1st Edition, Academic Press, 2001.

[172] G. I. Taylor, A. E. Green, Mechanism of the production of small eddies from large ones, Proceedings of the Royal Society of London. Series A - Mathematical and Physical Sciences 158 (895) (1937) 499–521. `arXiv:https://royalsocietypublishing.org/doi/pdf/10.1098/rspa.1937.0036`, `doi:10.1098/rspa.1937.0036`.
URL `https://royalsocietypublishing.org/doi/abs/10.1098/rspa.1937.0036`

[173] J. DeBonis, Solutions of the taylor-green vortex problem using high-resolution explicit finite difference methods, in: 51st AIAA Aerospace Sciences Meeting including the New Horizons Forum and Aerospace Exposition, 2013, pp. 1 – 20. `arXiv:https://arc.aiaa.org/doi/pdf/10.2514/6.2013-382`, `doi:10.2514/6.2013-382`.
URL `https://arc.aiaa.org/doi/abs/10.2514/6.2013-382`

[174] S. V. Patankar, Numerical heat transfer and fluid flow, Series on Computational Methods in Mechanics and Thermal Science, Hemisphere Publishing Corporation (CRC Press, Taylor & Francis Group), 1980.
URL `http://www.crcpress.com/product/isbn/9780891165224`

[175] B. Leonard, A stable and accurate convective modelling procedure based on quadratic upstream interpolation, Computer Methods in Applied Mechanics and Engineering 19 (1) (1979) 59–98. `doi:https://doi.org/10.1016/0045-7825(79)90034-3`.
URL `https://www.sciencedirect.com/science/article/pii/0045782579900343`

[176] K. Stewartson, Vectors, tensors, and the basic equations of fluid mechanics.rutherford aris. prentice-hall, london. 1962. 286 pp. illustrated. 42s., The Journal of the Royal Aeronautical Society 67 (632) (1963) 532–532. `doi:10.1017/S0001924000062679`.

[177] H. Jasak, Error analysis and estimation for the finite volume method with applications to fluid flows, Ph.D. thesis, Department of Mechanical Engineering, Imperial College London (1996).

[178] T. BARTH, D. JESPERSEN, The design and application of upwind schemes on unstructured meshes, in: 27th Aerospace Sciences Meeting, 1989, pp. 1–12. `arXiv:https://arc.aiaa.org/doi/pdf/10.2514/6.1989-366`, `doi:10.2514/6.1989-366`.
URL `https://arc.aiaa.org/doi/abs/10.2514/6.1989-366`

[179] W. H. Press, S. A. Teukolsky, W. T. Vetterling, B. P. Flannery, Numerical Recipes 3rd Edition: The Art of Scientific Computing, 3rd Edition, Cambridge University Press, New York, NY, USA, 2007.

[180] P. H. Westfall, Kurtosis as peakedness, 1905–2014. r.i.p., The American Statistician 68 (3) (2014) 191–195. `arXiv:https://doi.org/10.1080/00031305.2014.917055`, `doi:10.1080/00031305.2014.917055`.
URL `https://doi.org/10.1080/00031305.2014.917055`

[181] Y. Tominaga, T. Stathopoulos, Turbulent schmidt numbers for cfd analysis with various types of flowfield, Atmospheric Environment 41 (37) (2007) 8091 – 8099. `doi:https://doi.org/10.1016/j.atmosenv.2007.06.054`.
URL `http://www.sciencedirect.com/science/article/pii/S1352231007006036`

[182] J. Cash, A. Karp, A variable order runge—kutta method for value problems with rapidly varying right-hand sides, ACM Trans. Math. Softw. 16 (1990) 201–222. `doi:10.1145/79505.79507`.

[183] F. Holland, Fluid flow for chemical engineers, Edward Arnold, 1973.

[184] B. Cui, C. Zhang, D. Wei, S. Lu, Y. Feng, Effects of feed size distribution on separation performance of hydrocyclones with different vortex finder diameters, Powder Technology 322 (2017) 114 – 123. `doi:https://doi.org/10.1016/j.powtec.2017.09.010`.
URL `http://www.sciencedirect.com/science/article/pii/S0032591017307453`

[185] B. Leonard, The ultimate conservative difference scheme applied to unsteady one-dimensional advection, Computer Methods in Applied Mechanics and Engineering 88 (1) (1991) 17 – 74. `doi:https://doi.org/10.1016/0045-7825(91)90232-U`.
URL `http://www.sciencedirect.com/science/article/pii/004578259190232U`

[186] C. M. Rhie, W. L. Chow, Numerical study of the turbulent flow past an airfoil with trailing edge separation, AIAA Journal 21 (11) (1983) 1525–1532. `arXiv:https://doi.org/10.2514/3.8284`, `doi:10.2514/3.8284`.
URL `https://doi.org/10.2514/3.8284`

[187] T. Chan, H. Van, H. Van der Vorst, Approximate and Incomplete Factorizations. In: Keyes D.E., Sameh A., Venkatakrishnan V. (eds) Parallel Numerical Algorithms, Springer, Dordrecht, 1970. `doi:https://doi.org/10.1007/978-94-011-5412-3_6`.

[188] A. Smirnov, S. Shi, I. Celik, Random flow generation technique for large eddy simulations and particle-dynamics modelling, Journal of Fluids Engineering 123 (2) (2001) 359–371. `arXiv:https://asmedigitalcollection.asme.org/fluidsengineering/article-pdf/123/2/359/5591369/359\_1.pdf`, `doi:10.1115/1.1369598`.
URL `https://doi.org/10.1115/1.1369598`

[189] F. Russo, N. Basse, Scaling of turbulence intensity for low-speed flow in smooth pipes, Flow Measurement and Instrumentation 52 (10 2016). `doi:10.1016/j.flowmeasinst.2016.09.012`.

[190] M. Gibson, C. Verriopoulos, N. Vlachos, Turbulent boundary layer on a mildly curved convex surface., Experiments in Fluids 2 (1984) 17–24. `doi:10.1007/BF00266314`.

[191] J. Hunt, A. Wray, P. Moin, Eddies, streams, and convergence zones in turbulent flows, Studying Turbulence Using Numerical Simulation Databases -1 (1988) 193–208.

[192] G. Haller, An objective definition of a vortex, Journal of Fluid Mechanics 525 (2005) 1–26. `doi:10.1017/S0022112004002526`.

[193] W. Hinds, Aerosol Technology: Properties, Behavior, and Measurement of Airborne Particles, New York: John Wiley & Sons, 1982.

[194] A. Wiedensohler, E. Lütkemeier, M. Feldpausch, C. Helsper, Investigation of the bipolar charge distribution at various gas conditions, Journal of Aerosol Science 17 (3) (1986) 413 – 416. `doi:https://doi.org/10.1016/0021-8502(86)90118-7`.
URL `http://www.sciencedirect.com/science/article/pii/0021850286901187`

[195] R. Gunn, R. Woessner, Measurements of the systematic electrification of aerosols, Journal of Colloid Science 11 (3) (1956) 254 – 259. `doi:https://doi.org/10.1016/0095-8522(56)90050-2`.
URL `http://www.sciencedirect.com/science/article/pii/0095852256900502`

[196] P. G. Gormley, M. Kennedy, Diffusion from a stream flowing through a cylindrical tube, Proceedings of the Royal Irish Academy. Section A: Mathematical and Physical Sciences 52 (1949) 163–169.
URL `http://www.jstor.org/stable/20488498`

[197] B. W. Green, F. Zhang, Idealized large-eddy simulations of a tropical cyclone-like boundary layer (2015). `arXiv:http://dx.doi.org/10.1175/JAS-D-14-0244.1`, `doi:10.1175/JAS-D-14-0244.1`.
URL `http://dx.doi.org/10.1175/JAS-D-14-0244.1`

[198] F. Nicoud, F. Ducros, Subgrid-scale stress modelling based on the square of the velocity gradient tensor, Flow, Turbulence and Combustion 62 (3) (1999) 183–200. `doi:10.1023/A:1009995426001`.
URL `https://doi.org/10.1023/A:1009995426001`

[199] M. Weickert, G. Teike, O. Schmidt, M. Sommerfeld, Investigation of the les wale turbulence model within the lattice boltzmann framework, Computers & Mathematics with Applications 59 (7) (2010) 2200 – 2214, mesoscopic Methods in Engineering and Science. `doi:https://doi.org/10.1016/j.camwa.2009.08.060`.
URL `http://www.sciencedirect.com/science/article/pii/S089812210900652X`

[200] R. K. Moghadam, K. Javadi, F. Kiani, Assessment of the les-wale and zonal-des turbulence models in simulation of the flow structures around the finite circular cylinder., Journal of Applied Fluid Mechanics 9 (2) (2016) 909 – 923.
URL `http://search.ebscohost.com/login.aspx?direct=true&db=iih&AN=113635692&site=eds-live`

[201] D. Mylonas, S. Turkmen, M. Khorasanchi, Numerical study of asymmetric keel hydrodynamic performance through advanced cfd, in: Third International Conference On Innovation In High Performance Sailing Yachts, 2013, pp. 1 – 12.
URL `https://strathprints.strath.ac.uk/47155/`